Thèse de doctorat

Universitat Politècnica de Valencia (UPV)

En cotutelle avec
École Nationale Supérieure d'Ingénieurs de Tunis (ENSIT)
Université de Tunis

Spécialité : Physique

Préparation et performances d'une cellule photo-catalytique à base d'hématite pour la génération d'hydrogène

Présenté par

Feriel Bouhjar

Pour obtenir le grade de Docteur

de l'Université de Tunis et de la Universitat Politècnica de Valencia

Juin 2018

Directeur de thèse :
Dr.Bernabé Mari Soucase (UPV - SPAIN)

Laboratoire de Photovoltaïque (LPV), Centre de Recherches et des Technologies de l'Energie, Technopole de Borj Cédria
Group d'optoelectronica i semiconductorsDepartament de FísicaAplicada – Institut de Disseny i Fabricació (IDF)

“We are like tenant farmers chopping down the fence around our house for fuel when we should be using Natures inexhaustible sources of energy — sun, wind and tide. ... I’d put my money on the sun and solar energy. What a source of power! I hope we don’t have to wait until oil and coal run out before we tackle that.”

Thomas Alva Edison, in conversation with Henry Ford. 1931

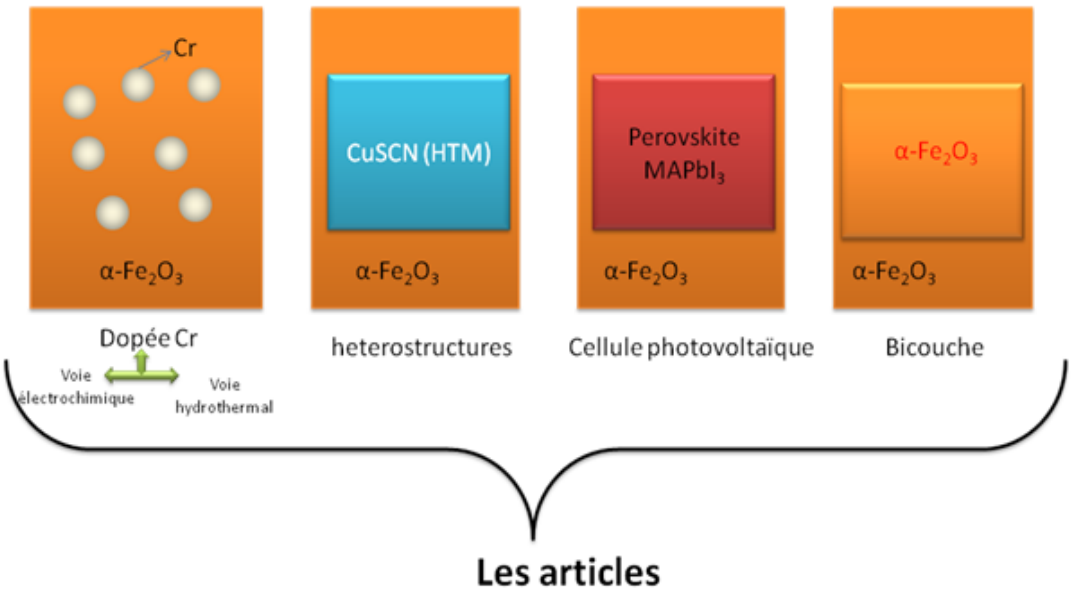
Cr
α-Fe2O3
CuSCN (HTM)
α-Fe2O3
Perovskite
MAPbI3
α-Fe2O3
α-Fe2O3
α-Fe2O3
Dopée Cr
Voie
électrochimique
Voie
hydrothermal
heterostructures
Cellule photovoltaïque
Bicouche
Les articles

Sommaire

Remerciements

Je dois mes profonds remerciements et ma profonde gratitude au Tout-Puissant **ALLAH**, Créateur de l'univers, et digne de toutes les louanges, qui m'ont béni avec le potentiel, la capacité et la détermination nécessaires pour mener à bien ce travail de recherche.

Au terme de ce travail, je tiens à remercier tous ceux qui y ont contribué, directement ou indirectement, lors des deux années et 6 mois de la thèse en cotutelle.

Je souhaiterais tout d'abord remercier l'Ecole Doctorale Tunis ainsi que L'École nationale supérieure d'ingénieurs de Tunis ,Laboratoire de Photovoltaïque (LPV) Centre de Recherches et des Technologies de l'Energie Technopole Borj Cédria et l'université polytechnique de valence (UPV) Groupe d'optoélectronique et semi-conducteurs département de Física Aplicada – Institut de Disseny i Fabricació (IDF) qui m'ont offert l'opportunité d'effectuer ce travail de thèse dans les meilleures conditions.

Je souhaite exprimer mes sincères remerciements, mon respect et mon admiration au directeur de l'école de physique appliquée, et à l'université polytechnique de Valence pour m'avoir accepté comme chercheuse dans son groupe de recherche admiré.

Je remercie **Monsieur le professeur Soto Camino Juan** Universitat Politècnica de València (UPV - SPAIN), qui m'a fait l'honneur de présider mon jury de thèse.

Je tiens également à remercier **Monsieur le professeur Ennaoui Ahmed**, Institut de recherche informatique (Qatar), pour leur participation à l'évaluation scientifique de ces travaux en tant que rapporteurs et puis en tant que membres dans le jury. Je le remercie aussi pour la rédaction de rapport dans les délais très contraignants.

J'adresse mes remerciements à **Monsieur le Professeur Mongi Bouaicha**, chef de laboratoire photovoltaïque au Centre de Recherches et des Technologies de l'Energie, Technopole de Borj Cédria, d'avoir accepté de participer au jury de thèse.

J'aimerai exprimer mon admiration sans limite pour **Monsieur le Professeur Brahim Bessais**, directeur de cette thèse. Qui m'a encadré pendant toute la durée de cette thèse. Il a toujours su m'indiquer les bonnes directions tout en me laissant beaucoup de liberté. Il possède ce talent de pouvoir expliquer les concepts les plus techniques de manière très simple et pédagogique. J'ai sincèrement appréciée de travailler avec lui et je lui suis extrêmement reconnaissante pour tout le temps qu'il m'a consacré, toute la patience dont

il a fait preuve et toutes les qualités humaines qu'il possède. Les mots ne pourront, hélas, jamais exprimer toute l'ampleur de ma reconnaissance. Je n'oublierai pas ses efforts tout au long de ma vie.

Je souhaiterais exprimer ma gratitude à **Monsieur le Professeur Bernabé Marí Soucase**, directeur du laboratoire de Physique Appliquée à l'Université polytechnique de valence pour avoir dirigé ma thèse. L'existence et la reconnaissance nouvelle du laboratoire doivent beaucoup à son dynamisme et son engagement qui ont peu d'égal. Sa conception des relations humaines contribue à créer un climat de travail très agréable. Sans lui, cette thèse n'aurait jamais été.

J'ai eu la chance de travailler avec **Monsieur le Professeur Miguel Alfonso Mollar** qui m'a beaucoup appris sur le plan expérimental. Ses connaissances dans le domaine de l'électrochimique m'ont aidé tout au long de ma thèse, sans oublier nos discussions scientifiques qui ont toujours été fructueuses.

Je remercie également **monsieur Dr.Lassaad mohamed Chourou** Maître Assistant (CRTEn) pour sa disponibilité et ses conseils avisés concernant l'électrochimie.

Mes sincères remerciements vont au parrainage du Ministère de l'Enseignement Supérieur et de la Recherche Scientifique Tunisie (Université de Tunis), pour mener des recherches pendant 9 mois à l'Universitat Politècnica de Valencia (UPV) Espagne. Cette étude n'aurait pas été possible sans ce soutien financier.

De plus, j'aimerais remercier chaleureusement **Dr. Shafi ullah** pour son aide et son soutien, grâce à sa bonté et sa gentillesse, il a rendu mon séjour à valence possible et sans aucun problèmes.

La reconnaissance ne serait jamais complète sans exprimer ma gratitude à ma famille : mes frères et mes sœurs (Fahmi, Faten, Fares et Farah) évidemment, Anis, Ines et Manel et leur soutien inconditionnel a joué un rôle clé dans mes efforts de recherche et sans oublier mes 7 petits adorables (Farihène ,Fakhredine, Rayan, Fahed, Adam, Fadi et Anas) que dieu les protège.

Je remercie du fond du cœur mes parents **Jilani et Jamila** pour m'avoir toujours permis de suivre le chemin des études. Merci pour leur soutient, leurs encouragements et surtout leur amour qui a toujours été une source motivante. Je remercie spécialement **Ma mère Jamoula** pour tout ce qu'elle a fait pour moi. Elle a beaucoup sacrifié pour m'offrir toutes les conditions nécessaires afin que je puisse devenir ce je suis. Ma reconnaissance envers elle est inexprimable.

Milles excuses à tous ceux que j'aurais oublié.

RÉSUMÉ(Français)

L’hydrogène est un vecteur énergétique qui a déjà démontré ses capacités à pouvoir remplacer le pétrole en tant que carburant.Cependant, les moyens de production actuellement mis en œuvre restent fortement émetteurs de gaz à effet de serre. La photo-électrolyse de l’eau est un procédé permettant, à partir d’énergie solaire, de séparer les composés élémentaires de l’eau que sont l’hydrogène et l’oxygène en utilisant un semi-conducteur aux propriétés physiques adéquates.L'hématite (α-Fe_2O_3) est un matériau prometteur pour cette application en raison de sa stabilité chimique et de sa capacité à absorber une partie importante de la lumière (avec une bande interdite comprise entre de 2.0 – 2.2 eV). Malgré ces propriétés avantageuses, il existe des limites intrinsèques à l'utilisation de l’oxyde de fer pour le craquage photoélectrochimique de l'eau. La première contrainte est la position de sa bande de conduction qui est inférieure au potentiel de réduction de l'eau. Cette contrainte peut être surmontée par l'ajout en série d'un second matériau, en tandem, qui absorbera une partie complémentaire du spectre solaire et amènera les électrons à un niveau énergétique plus élevé que le potentiel de dégagement de l'hydrogène. Le second obstacle provient du désaccord entre la courte longueur de diffusion des porteurs de charges et la longue profondeur de pénétration de la lumière. Il est donc nécessaire de contrôler la morphologie des électrodes d’hématite sur une échelle de taille similaire à la longueur de transport du trou.

Dans cette thèseun nouveau conceptest introduit pour améliorer les performances photoélectrochimiques. En utilisant la méthode hydrothermale nous avons déposé des couches minces d'hématite dopées au Cr sur des substrats en verre conducteur. Nous avons aussi préparépar voie électrochimique une hétérojonctionp-CuSCN/n-Fe_2O_3 en déposant séquentiellement du α-Fe_2O_3 et des films de CuSCN sur des substrats FTO (SnO_2: F).Enfin nous avons utilisédes couches minces uniformes et denses d'oxyde de fer (α-Fe_2O_3) comme couche de transport d'électrons (ETL) à la place du dioxyde de titane (TiO_2) conventionnellement utilisé dans des cellules photovoltaïques à base de pérovskites $CH_3NH_3PbI_3$ (PSC). Ce dernier concept a montré une augmentation du photocourant de 20% et d’un IPCE30 fois plus grand que l’hématite simple, suggérant une meilleure conversion des longueurs d'onde élevées (> 500 nm).

Mots clés:

Photoélectrochimie, division de l'eau, production d'hydrogène, évolution de l'oxygène, semi-conducteurs métal-oxyde, hématite, oxyde de fer, nanostructures, surface.

ABSTRACT (Anglais)

Hydrogen is an energy carrier that has already demonstrated its ability to replace oil as a fuel. However, the means of production currently used remain highly emitting greenhouse gases. Photo-electrolysis of water is a process that uses solar energy to separate the elemental compounds of water such as hydrogen and oxygen using a semiconductor with adequate physical properties. Hematite (α-Fe_2O_3) is a promising material for this application because of its chemical stability and ability to absorb a significant portion of light (with a band-gap between 2.0 - 2.2 eV). Despite these advantageous properties, there are intrinsic limitations to the use of iron oxide for the photoelectrochemical cracking of water. The first constraint is the position of its conduction band, which is lower than the water reduction potential. This constraint can be overcome by the addition in series of a second material, in tandem, which will absorb a complementary part of the solar spectrum and bring the electrons to a higher energy level than the potential of hydrogen release. The second obstacle comes from the disagreement between the short diffusion length of the charge carriers and the long light penetration depth. It is therefore necessary to control the morphology of the hematite electrodes on a scale of similar size to the transport length of the hole.

In this thesis a new concept is introduced to improve the photoelectrochemical performances. Using the hydrothermal method we deposited thin layers of Cr-doped hematite on conductive glass substrates. We also electrochemically prepared a p-CuSCN / n-Fe_2O_3 heterojunction by sequentially depositing α-Fe_2O_3 and CuSCN films on FTO (SnO_2: F) substrates. Finally, we have used uniform and dense thin layers of iron oxide (α-Fe_2O_3) as an electron transport layer (ETL) in place of titanium dioxide (TiO_2) conventionally used in photovoltaic cells based on perovskites $CH_3NH_3PbI_3$ (PSC). This latter concept showed a 20% increase of the photocurrent and an IPCE 30 times greater than the simple hematite, suggesting better conversion of high wavelengths (> 500 nm).

Keywords:

Photoelectrochemistry, Water Splitting, Hydrogen Production, Oxygen Evolution, Metal-Oxide Semiconductors, Hematite, Iron Oxide, Nanostructures, Surface.

RESUM (Valencià)

L'hidrogen és un proveïdor d'energia que ja ha demostrat la seva capacitat per reemplaçar el petroli com a combustible, però els mitjans de producció actuals continuen essent fortament emissors dels gasos responsables d'efecte hivernacle. La fotoelectròlisi de l'aigua és un procés que, a partir de l'energia solar, separa els compostos elementals d'aigua com l'hidrogen i l'oxigen utilitzant un semiconductor amb propietats físiques adequades. La hematita (α-Fe_2O_3) és un material prometedor per a aquesta aplicació a causa de la seva estabilitat química i capacitat d'absorbir una porció significativa de la llum (amb un gap entre 2,0 i 2,2 eV). Malgrat aquestes propietats avantatjoses, hi ha limitacions intrínseques per a l'ús d'òxid de ferro per a la descomposició fotoelectroquímica de l'aigua. La primera restricció és la posició de la seva banda de conducció que és inferior al potencial de reducció d'aigua. Aquesta limitació es pot superar mitjançant l'addició en sèrie d'un segon material, en tàndem, que absorbirà una part complementària de l'espectre solar i portar els electrons a un nivell d'energia més alt que el potencial per a l'alliberament d'hidrogen. El segon obstacle prové del desacord entre la curta durada de la difusió dels portadors de càrrega i la llarga profunditat de penetració de la llum. Per tant, és necessari controlar la morfologia dels elèctrodes d'hematita en una escala de mida similar a la longitud del forat del transport.

En aquesta tesi, es presenta un nou concepte per millorar el rendiment fotoelectroquímic. Mitjançant el mètode hidrotermal es van dipositar capes primes de hematita Cr-doped sobre substrats de vidre conductor. També s'han preparat electroquímicamentheterounions de tipus p-CuSCN/n-Fe_2O_3 dipositant seqüencialment una capa de α-Fe_2O_3 i altra de CuSCN sobre substrats FTO (SnO_2: F).Finalment, s'han produït cél·lules solars de perovskitesi óxid de ferro. Per això es va depositaruna capa prima,densai uniforme d'òxid de ferro (α-Fe_2O_3) com a capa de transport d'electrons (ETL) en lloc de diòxid de titani (TiO_2) que s'utilitza convencionalment en les cèl·lules fotovoltaiques de perovskita híbrida del tipus $CH_3NH_3PbI_3$ (SGP). Aquest últim dispositiu va mostrar un augment del fotocorrent del 20% i una IPCE30 vegades superior a la hematita simple, la qual cosa suggereix una millor conversió a longitud d'ones per sobre de 500 nm.

Paraules clau:Fotoelectroquímica, divisió d'aigua, producció d'hidrogen, evolució d'oxigen, semiconductors d'òxids metàl·lics, hematita, òxid de ferro, nanoestructures.

RESUMEN (Castellano)

El hidrógeno es un portador de energía que ya ha demostrado su capacidad para reemplazar el petróleo como combustible. Sin embargo, los medios de producción actualmente en uso siguen siendo altamente emisores de gases de efecto invernadero. La foto-electrólisis del agua es un proceso que, a partir de la energía solar, separa los compuestos elementales del agua como el hidrógeno y el oxígeno utilizando un semiconductor con propiedades físicas adecuadas. La hematita (α-Fe_2O_3) es un material prometedor para esta aplicación debido a su estabilidad química y su capacidad para absorber una porción significativa de la luz (con una banda prohibida entre 2.0 - 2.2 eV). A pesar de estas propiedades ventajosas, existen limitaciones intrínsecas al uso de óxido de hierro para la descomposición fotoelectroquímica del agua. La primera restricción es la posición de su banda de conducción que es menor que el potencial de reducción de agua. Esta limitación se puede superar mediante la adición en serie de un segundo material, en tándem, que absorberá una parte complementaria del espectro solar y llevar a los electrones a un nivel de energía más alto que el potencial para la liberación de hidrógeno. El segundo obstáculo proviene del desacuerdo entre la corta longitud de difusión de los portadores de carga y la profundidad de penetración larga de la luz. Por lo tanto, es necesario controlar la morfología de los electrodos de hematita en una escala de tamaño similar a la longitud de transporte del orificio.

En esta tesis, se introduce un nuevo concepto para mejorar el rendimiento fotoelectroquímico de la hematita. Usando el método hidrotermal depositamos capas delgadas de hematita dopada con Cr en sustratos de vidrio conductivo. También se ha preparado por medios electroquímicos una heterounión del tipo p-CuSCN/n-Fe_2O_3 depositando secuencialmente una capa de α-Fe_2O_3 y una película de CuSCNsobre sustratos de FTO (SnO_2: F).Finalmente, se ha preparado células solares de perovskitas y óxido de hierro. Para ello se depositó una capa delgada, densa y uniformede óxido de hierro (α-Fe_2O_3) como capa de transporte de electrones (ETL) en lugar de dióxido de titanio (TiO_2) que se utiliza convencionalmente en las células fotovoltaicas perovskitastipo$CH_3NH_3PbI_3$ (SGP). Este último dispositivo mostró un aumento en la fotocorriente del 20% y un IPCE30 veces mayor que la hematita simple, lo que sugiere una mejor conversión de las longitudes de onda por encima de 500 nm.

Palabras clave:

Fotoelectroquímica, división de agua, producción de hidrógeno, evolución de oxígeno, semiconductores de óxido de metal, hematita, óxido de hierro, nanoestructuras

Liste des figures

Figure Captions (chapitre I)

Figure Captions (chapitre II)

Figure Captions (chapitre III)

Figure III.6 :Image de la microscopie électronique à transmission (TEM) JEOL JEM 2100F

Figure III.7 : Diagramme schématique d'une cellule photoélectrochimique (PEC).

Figure III.8 : Exemple de courbes J-V pour une cellule solaire dans l'obscurité et pour la même cellule solaire sous éclairement.

Figure Captions (chapitre IV)

Article 1 :

Figure1:Schematic illustration of Cr-doped hematite photoanodes synthesized by the hydrothermal method

Figure2A: FESEM of hydrothermal deposited α-Fe_2O_3 (a) undoped, (b) 4 at. % Cr, (c) 8 at.% Cr, (d) 16 at.% Cr, and (e) 20 at.% Cr (1µm and 200nm).

Figure2B:FESEM of hydrothermally deposited α-Fe_2O_3 (a and b) undoped, (c) 16% Cr.

Figure 3:HRTEM of hydrothermally deposited undoped α-Fe_2O_3

Figure 4:XRD patterns of α-Fe_2O_3 and Cr-doped α-Fe_2O_3films at different Cr %.

Figure 5: EDX spectrum of (a) undoped α-Fe_2O_3, (b) 4 at. % Cr-doped α-Fe_2O_3, (c) 8 at.% Cr-doped α-Fe_2O_3 (d) 16 at.% Cr-doped α-Fe_2O_3 and (e) 20 at.% Cr-doped α-Fe_2O_3.

Figure 6: Transmittance spectra of undoped and Cr doped α-Fe_2O_3

Figure 7: Absorbance spectra of undoped and Cr doped α-Fe_2O_3

Figure 8:Tauc plot of undoped and Cr-doped α-Fe_2O_3

Figure 9: (a) Photocurrent intensity of Cr-doped Fe_2O_3 electrodes under on/off illumination, measured in 1M NaOH electrolyte under a bias potential of +0.1 V (vs. Ag/AgCl) under successive illumination cycles with an interval of 20 s (b) enlarged current time curves of (a).

Figure 10: IPCE for α-Fe_2O_3 films with and without Cr-doping at an applied potential of +0.4 V (vs. Ag/AgCl) in 1 M NaOH.

Figure 11: Energy diagram of the n-type hematite photoanode and schematic illustration of the photoelectrochemical water splitting on photoanode and cathode.

Article 2 :

Figure 1: Schematic cross-sectional view of heterojunction: FTO glass, compact α-Fe_2O_3, and CuSCN (HTM).

Figure2.a: linear sweep voltammetry of Fe_2O_3 precursor solution in the range of -1V to 1V on the indium fluoride oxide electrode at a rate 50mVs-1.

Figure 2.b: linear sweep voltammetry of CuSCN precursor solution in the range of -0.8V to 0.6V at a rate of 200 mVs^{-1}.

Figure 3: Chronoamperometry of CuSCN with a Cu: SCN ratio of 1:1.5.

Figure 4:FESEM images for (a) CuSCN (b) α-Fe_2O_3 (c) α-Fe_2O_3/CuSCN (1µm) (d) α-Fe_2O_3/CuSCN (10µm).

Figure 5: Vertical cross section of (a-b) α-Fe_2O_3, (c) CuSCN and (d) heterojunction thin films.

Figure 6: Figure 6: (a) EDX spectrum for α-Fe_2O_3, (b) EDX spectrum for CuSCN thin films.

Figure 7: XRD spectra of FTO, α-Fe_2O_3, CuSCN and the Fe_2O_3/CuSCN bilayer.

Figure 8: Transmittance and absorbance spectra of CuSCN (a) and α-Fe_2O_3 (b).

Figure 9:Tauc plot of CuSCN and α-Fe_2O_3.

Figure 10: PL spectrum of α-Fe_2O_3, CuSCN and Fe_2O_3/CuSCN.

Figure 11: (a) Energy band diagram of α-Fe_2O_3 and CuSCN before and after the formation p-n junction,(b)schematic energy band diagram of the α-Fe_2O_3 and CuSCN heterojunction with the band bending and alignment due to the solution.

Figure 12: I-V characteristics of the α-Fe_2O_3 and CuSCN electrode in dark and illumination (0 V-0.8 V).

Figure 13: (a) Photocurrent intensity for α-$Fe_2O_3$and α-Fe_2O_3/CuSCN electrodes under on/off illumination, measured in 1M NaOH electrolyte under a bias potential of +0.1 V, (b) Time dependence of the photocurrent intensities for α-$Fe_2O_3$and α-Fe_2O_3/CuSCN electrodes under successive illumination cyclesand (c) Time dependence of the photocurrent intensities for α-Fe_2O_3/CuSCN electrode under on/off illumination cycles (white light and λ >400 nm).

Figure 14: Mott–Schottky plot for (a) α-Fe_2O_3 (b) CuSCN (c) α-Fe_2O_3 /CuSCN.

Article 3 :

Figure 1: Schematic representations of a typical three-electrode electrochemical cell

Figure 2: Schematic representations of the syntheses methods adopted for α-Fe_2O_3 hematite photoanode film electrodeposited on α-Fe_2O_3 (A) substrate.

Figure 3: Solvent engineering procedure for preparing the uniform and dense perovskite film

Figure 4 A: Scheme of the perovskite solar cell

Figure 4 B: Energy-level diagram for each component of the device

Figure 5 (a): XRD spectra of α-Fe_2O_3 (A), α-Fe_2O_3 (B) and α-Fe_2O_3/α-Fe_2O_3bilayer.

Figure 5 (b): XRD patterns of $MAPbI_3$ and α-Fe_2O_3 (A)/α-Fe_2O_3(B)/$MAPbI_3$/FTO.

Figure 5 (c): Scheme of $MAPbI_3$ perovskite crystallization

Figure 6: FESEM images of (a) α- Fe_2O_3(A), (b) α-Fe_2O_3(B), (c) α- Fe_2O_3(A)/α-Fe_2O_3(B), (d)$MAPbI_3$, (e) α-Fe_2O_3(A)/α-Fe_2O_3(B)/$MAPbI_3$ and (f) solar cell.

Figure 7: Vertical cross section of (a) α-Fe_2O_3 (A), (b) α-Fe_2O_3/α-Fe_2O_3 thin films.

Figure 8 A: EDX spectrum for (a) $MAPbI_3$, (b) α-Fe_2O_3 (A)/α-Fe_2O_3(B), (c) α-Fe_2O_3(A)/α-Fe_2O_3(B)/$MAPbI_3$, and (d) solar cell.

Liste des tableaux

(Article 1) :

(Article 2):

(Article 3):

Liste des Abréviations et des Symboles

A	Absorption coefficient
AC	Alternatingcurrent
AFM	Microscopie à force atomique
ALD	Atomic layer deposition
APCVD	Atmospheric pressure CVD
C	Capacitance (in F)
CVD	Chemical vapor deposition
DSC	Dye-sensitized solar cell
DRX	Diffraction des Rayons X
E	Elementary charge (= 1.602 10^{-19} C)
E_C	Potential of the edge of the conduction band (in V)
EDS	Spectroscopie à Dispersion d'Energie
E_F	Fermi energylevel (in eV)
Eg	Bandgap energy (in eV)
E_{Redox}	Redox potential or electrolyte energy mediator (in V)
EV	Potential of the edge of the valence band (in V)
ΔJmax	Maximum of the photocurrent transient (in mA cm^{-2})
ΔJSS	Photocurrent transient amplitudes in NaOH, difference between steady state values (in mA cm^{-2})
ΔJSS, H_2O_2	Photocurrent transient amplitudes in NaOH + H_2O_2, difference between steady state values (in mA cm^{-2})
ΔNIPCE	Difference in normalized IPCE measurements
ΔVSS, H_2O_2	Photovoltage transient amplitudes in NaOH + H_2O_2, differencebetween steady state values (in V)
ε_0	Permittivity of free space (= 8.85419 10^{-12} F m^{-1})
ε, ε_{SC}	Dielectric constant
H_2	dihydrogène
EIS	Electrochemicalimpedancespectroscopy
ETL	couche de transport d'électrons (Electronic Transport Layer)
FTO	Oxyde d'étain dopé au Fluor (F doped SnO_2)

FESEM	Microscopie Electronique à Balayage à Emission de Champ
IPCE	Incident Photon to Charge carrier Efficiency (rendement quantique externe)
α-Fe_2O_3	Hematite
J	Current density (in A cm^{-2} or mA cm^{-2})
k_B	Boltzmann constant (= 1.380 10–23 J K^{-1})
L_D	Diffusion length (in nm)
L_D, eff.	Effective diffusion length (in nm)
LSV	Voltammétrie à balayagelinéaire
λ	Wavelength (in nm)
M_S	Mott–Schottky
Nd	Donor density
OER	Oxygen evolution reaction
PC	Photocatalytic
PEC	cellule photoélectrochimique
PV	Photovoltaic
PSC	cellules photovoltaïques à base de pérovskites
R	Resistance (in Ω)
RHE	Reversible hydrogen electrode
SCE	Saturated calomel electrode
STH	Solar-to-hydrogen conversion efficiency
τ	Lifetime (in s)
T	Temperature (in K or °C)
TEM	Analyse par microscopie électronique à transmission
UV-vis	Ultraviolet-visible
V_b or $V_{Appl.}$	Applied bias potential (in V)
$V_{Eq.}$	Potential at equilibrium (in V)
V_{fb}	Flat-band potential (in V)
V_{RHE}	Volts vs. RHE
V_{SCE}	Volts vs. SCE

Chapitre I
Introduction

I. Introduction et problématique

I.1 Contexte général

La crise énergétique est devenue un mot qu'on entend presque tous les jours. La vulnérabilité des prix des ressources énergétiques fossiles a souvent augmenté durant les dernières années. Toutefois il y a des débats sur l'origine de cette crise, réserves manquantes ou causées par des spéculations. Afin de surmonter cette crise apparente et prévisible, il y a des recherches intenses sur des énergies alternatives. Les philosophies majeures derrière ces approches sont la durabilité et l'omniprésence de fournir éternellement de l'énergie avec les ressources domestiques. Ainsi les formes d'énergies préférées sont celles collectées naturellement comme les énergies solaires, éolienne et géothermique. Ces sources d'énergie primaires sont difficiles de les utiliser telles qu'elles, en effet elles doivent être converties sous une forme secondaire adéquate et facilement utilisable.

De plus ces sources d'énergie naturelles existent avec des aspects de basse densité dans le milieu urbain, nécessitant parfois des conditions environnementales extrêmes pour un maximum d'efficacité. Ainsi, les installations d'énergie solaire dans le désert ou les éoliennes en pleine mer en sont de bons exemples.

Pour ces raisons, l'électricité est typiquement générée sur des sites lointains des agglomérations et est prête à être transportée et distribuée à travers le réseau vers les consommateurs finaux. Ainsi, à quoi bon est-on amené à produire et délivrer l'énergie sous forme chimique?

I.2 Nécessité de l'énergie chimique renouvelable

La figure1 montre les prévisions par secteur d'utilisation de l'énergie primaire aux Etats Unis comme exemple[
1].

La plupart de la consommation industrielle, commerciale et résidentielle est consommée par des installations fixes, opérant donc en puisant leurs énergies sur le réseau de distribution électrique. Toutefois, une large part de la consommation énergétique est sous forme d'énergies stockées, ou bien énergies hors du réseau.

Un bon exemple est le transport qui compte plus que 25% du total de la consommation comme le montre la figure1, en plus les installations de secours, les installations physiquement séparées, les appareils mobiles nécessitent des matrices de stockage d'énergie pour des opérations hors du réseau. Ceci amène à prendre des mesures pour satisfaire la

demande des opérations hors du réseau en plus de la demande en relation avec le réseau de distribution.

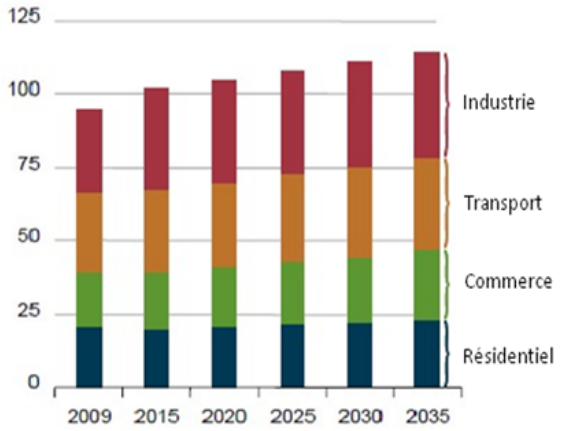

Figure I.1 : Utilisation de l'énergie primaire par secteur [1], 2009-2035 (quadrillion btu)

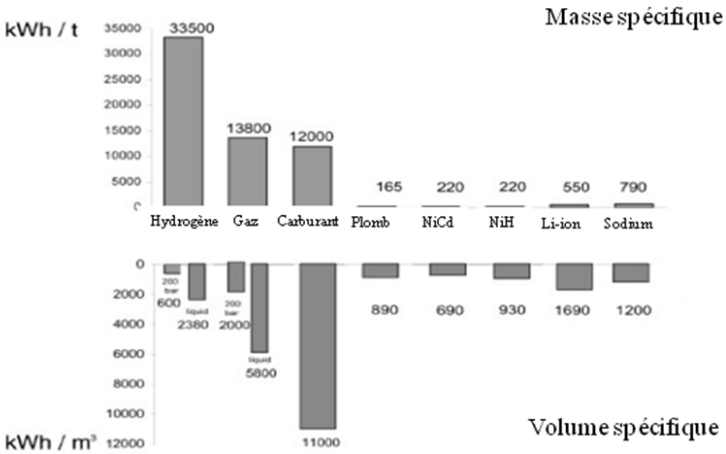

FigureI.2 : Énergie théorique spécifique d'une sélection de matériaux

En considérant que le réseau électrique constitue le cœur de notre infrastructure, la batterie semble mériter alors d'être un choix de premier ordre. La figure2 [2] présente une liste de matrices de stockages en fonction de leurs énergies spécifiques. Bien qu'il soit clair d'après la figure2 que les batteries ont une plus basse énergie spécifique comparée aux sources d'énergie d'origine chimique, leur fabrication simple leur donne de grands avantages incluant la miniaturisation des construits et une incorporation facile dans les appareillages. En plus, comme il n'y a pas une nécessité d'échange physique de matière alors les batteries sont appropriées pour les appareils portatifs comme les outils électroniques essentiellement.

Il y a des essais en cours pour étendre l'usage des batteries dans des applications plus énergivores tel que le transport. Toutefois, comme le montre la figure2, malgré que les chercheurs aient développé des batteries à haute énergie spécifique, leurs contenus énergétiques sont encore plus bas que les combustibles chimiques conventionnels. Cela montre que les technologies actuelles des batteries ne peuvent pas complètement répondre à toutes les demandes du transport terrestre par exemple. Ceci est plus problématique dans le transport aérien et maritime. Malgré la perte énorme d'énergie sous forme de chaleur, la turbo propulsion est le choix dominant pour les moteurs d'avions à cause de sa haute poussée spécifique. Selon ces aspects l'idée de remplacer les combustibles chimiques avec les batteries est encore prématurée dans les domaines à utilisation intensifs en énergie. Le rechargement des batteries est un autre sujet à considérer sur le plan pratique. En effet, tandis que le combustible chimique peut être rechargé pendant quelques minutes, le rechargement des batteries prend des heures d'alimentation continue. Enfin la dégradation à long terme des batteries augmente le coût global de leur exploitation.

Malgré que l'hydrogène ait une excellente énergie massique spécifique, sa basse densité volumique lui donne le titre de la plus mauvaise matrice énergétique en volume spécifique. En plus, sa nature explosive fait apparaître des contraintes de sécurité pour le stockage. Dans la pratique il est stocké sous forme de gaz compressé ou combiné à une phase appropriée à travers des liaisons chimiques. Les premières méthodes étaient accompagnées de problèmes de sécurité et pour les dernières solutions, les technologies sont encore dans un stade peu avancé. Une dernière alternative de stockage, qui semble la plus intéressante, consiste à intégrer l'hydrogène solaire dans les procédés de synthèse d'hydrocarbures synthétiques [3,4,5](procédés Fisher-Tropsch). Dans ce procédé, largement utilisé, des liquides synthétiques d'hydrocarbures sont fabriqués à partir d'hydrogène. En utilisant l'hydrogène issu, de la photo-électrolyse de l'eau dans le procédé Fisher-Tropsch, on arrive à le stocker sous une autre forme chimique très stable. Cette option de stockage est très convenable non seulement parce qu'elle fournit une phase condensée sécurisée semblable aux hydrocarbures déjà utilisés, mais aussi elle permet d'intégrer facilement les vastes infrastructures de l'économie basée sur les énergies fossiles déjà existantes (stations de carburants, fabrication de plusieurs dérivés du pétrole ...). En conclusion, l'utilisation de l'hydrogène et son stockage devraient être pensés simultanément.

Structure de la thèse

Le **chapitre 1**consiste en uneintroduction, dans laquelle le cadre de la thèse est défini.

Le **chapitre 2** consiste en une étude bibliographique, consacréeessentiellement à la présentation del'aspect fondamental de l'échange et de transfert de charge dans un système photo-électrochimique (PEC) et regroupe les différentes propriétés des matériaux étudiés dans le courant de ce travail. Le chapitre 2est divisé en trois parties. Dans la première partie, nous donnons des notions sur la photoelectrolyse de l'eau et le système photoélectrochimique avant d'aborder la description des phénomènes ayant lieu à l'interface semiconducteur/électrolyte à l'obscurité et sous éclairement. Dans la deuxième partie, on a parlé du choix des semi-conducteurs pour les mesures PEC. La troisième partie présente les matériaux étudiés en donnant leurs propriétés structurales, électriques et optiques, les techniques de préparation de ces matériaux sous forme nanométrique ainsi que leurs domaines d'application qui sont en lien direct avec leurs propriétés et leur morphologie.

Le Chapitre 3concerne la partie expérimentale, les techniques et les caractérisationsutilisées au cours de ce travail.

Le chapitre 4comprend trois articles publiés dans des revues scientifiques indexées, et constitue le corps principal de la thèse. Dans le premier article, nous avons déposé des couches minces d'hématite sur des substrats en verre conducteur dopées au Cr en utilisant la méthode hydrothermale. Dans le deuxième article nous avonspréparé une hétérojonctionp-CuSCN/n-Fe_2O_3 en déposant séquentiellement α-Fe_2O_3 et des films de CuSCN sur des substrats FTO (SnO_2: F).Dans le troisième article, des couches minces d'oxyde de fer α-Fe_2O_3 uniformes et denses sont utilisées comme couche de transport d'électrons (ETL) dans des cellules photovoltaïques à base de pérovskites $CH_3NH_3PbI_3$ (PSC).

Les publications de cette thèse :

Le premier article estintitulé "*Hydrothermal synthesis of Nanostructured Cr-doped hematite with enhanced photoelectrochemical activity*" [6].Cet article a été publié le 10 janvier 2018dans « Electrochimica Acta »(Volume 260, 10 January 2018, Pages 838-846),le facteur d'impact en 2017 était de 4.798. Dans cet article nous avons utilisé la méthode hydrothermale, pour préparer des couches minces d'hématite dopées au Cr sur des substrats en verre conducteur. La réponse photoélectrochimique montre que les échantillons sont efficaces pour la décomposition de l'eau et que le niveau de dopage affecte le rendement photocatalytique des films. L'échantillon optimal est α-Fe_2O_3 dopé avec 16% de Cr. On pense que ce résultat

pourrait être bénéfique dans les domaines de la photocatalyse et des dispositifs photoélectriques.

Le deuxième article présenté dans cette thèse est intitulé "*Electrochemical fabrication and characterization of p-CuSCN/n-Fe_2O_3heterojunctiondevices for hydrogen production* " [7].Cet article a été publié dans « Journalof the ElectrochemicalSociety » en 2017 (Volume 164, issue 13, H936-H945).Le facteur d'impact en 2017 était de 3.25.Dans ce travail, nous décrivons la fabrication d'une hétérojonction à travers le dépôt électrochimique de films α-Fe_2O_3/CuSCN. Ayant diverses compositions, les films de CuSCN ont été déposés sur des surfaces lisses de α- Fe_2O_3. La caractérisation des films a été réalisée en utilisant des techniques de diffraction des rayons X (XRD) et FESEM.

Le troisième article intitulé « *Influence of a compact α-Fe_2O_3 layer on the photovoltaic performance of perovskite-basedsolarcells*» [8] a été publié dans « Journalof the Electrochemical Society» en 2018(Volume 165(2) H30-H38).

Cet article se concentre principalement sur le dépôt d'un film compact de α-Fe_2O_3 et son impact sur la croissance de la couche de perovskite, fournissant une compréhension globale des propriétés de l'interface α-Fe_2O_3 / perovskite. L'impact de la croissance du film α-Fe_2O_3 sur les propriétés de l'interface α-Fe_2O_3 / perovskite et sur les performances des PSC est étudié. Un film α-Fe_2O_3 morphologiquement uniforme permet d'obtenir un PEC de 5,7%. Ces résultats montrent la possibilité d'application de α-Fe_2O_3 dans les PSC et fournissent le principe du choix de la couche de transport d'électrons pour des PSC efficaces.

Après la compilation des articles, **le chapitre 5** présente une brève discussion sur les principaux résultats obtenus tandis que **le chapitre 6** présente les conclusions finales de la thèse ainsi que la réalisation des objectifs proposés et les futures lignes de travail.

Références chapitre 1

[1] Annual Energy Outlook, U.S. Energy Information Administration. 2011

[2]Winter, M.; Brodd, R. J., What Are Batteries, Fuel Cells, and SupercapacitorsChemical Reviews 2004, 104 (10), 4245-4270

[3]Jager, B.; Dry, M. E.; Shingles, T.; Steynberg, A. P., Experience with a new type of reactor for Fischer-Tropsch synthesis. Catalysis Letters 1990, 7 (1), 293-301.

[4] van Dyk, J. C.; Keyser, M. J.; Coertzen, M., Syngas production from South African coal sources using Sasol-Lurgi gasifiers. International Journal of Coal Geology 2006, 65 (3-4), 243-253.

[5] Steynberg, A. P.; Nel, H. G., Clean coal conversion options using Fischer-Tropsch technology. Fuel 2004, 83 (6), 765-770.

[6] Bouhjar F, Mollar M, Chourou ML, Marí B, and Bessaïs B. (2018) Hydrothermal synthesis of nanostructured Cr-doped hematite with enhanced photoelectrochemical activity. Electrochim Acta 260:838–846

[7] Bouhjar F, Ullah S, Chourou ML, Mollar M, Marí B, and Bessaïs B. (2017) Electrochemical Fabrication and Characterization of p-CuSCN/n-Fe2O3 Heterojunction Devices for Hydrogen Production. J ElectrochemSoc 164:936–945.

[8] F. Bouhjar,M. Mollar,ShafiUllah, B. Marí and B.Bessaïs. Influence of a Compact α-Fe2O3 Layer on the Photovoltaic Performance of Perovskite-Based Solar Cells Journal of The Electrochemical Society,165(2) H30-H38 (2018).

Chapitre II

Etude bibliographique

I .Photoélectrolyse de l'eau

I.1.Principe de base et détails de la technologie

Le principe de la décomposition photoélectrochimique de l'eau est basé sur la conversion de l'énergie lumineuse en électricité dans une cellule impliquant deux électrodes, immergées dans une solution aqueuse électrolytique, où aumoins une électrode est composée d'un semi-conducteur exposé à la lumière et capable de l'absorber. Cette électricité est ensuite utilisée pour l'électrolyse de l'eau.

Par définition, la photoélectrolyse de l'eau consiste à dissocierla molécule d'eau par le courantélectrique généré pour donner suite àl'éclairement d'un semi-conducteur qui joue le rôle d'un photocatalyseur. En effet, les cellules photoélectrochimiques (PEC) immergées dans un électrolyte aqueux et illuminées par la lumière solaire peuvent décomposer l'eau en hydrogène et en oxygène. Sous leur forme la plus simple, elles peuvent être décrites comme des dispositifs photovoltaïques/électrolytiques intégréesou monolithiques. Une large variété de processus PEC et de photocatalyse susceptibles de dissocier l'eau sont étudiés de par le monde. Quatre étapes principales sont mises en jeu dans le processus photoélectrochimique de la dissociation de l'eau. La figure 1 résume les quatre étapes.

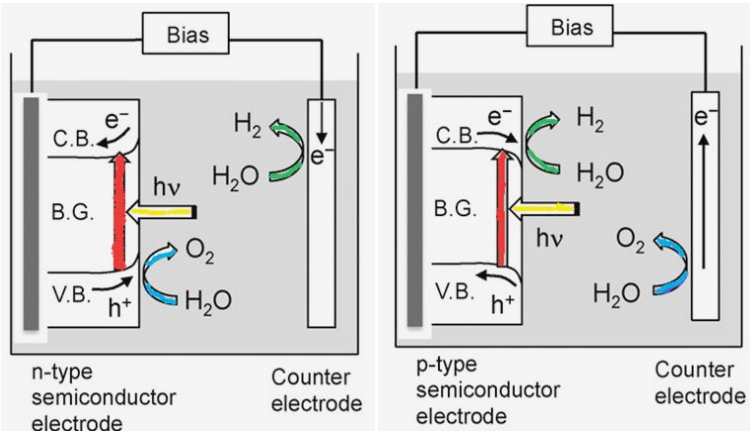

Figure II.1 : Schémas de principe de la photoélectrolyse de l'eau

- La première étape consiste à générer des paires d'électrons-trousà la surface du semi-conducteur (photoanode ou photocathode) lorsque celui-ci est soumis à la lumière visible.
- La deuxième étape correspond à l'oxydation de l'eau à la surface de la photoanode (ou réduction de l'eau à la surface de la photocathode) suite à la création des pairs électrons-trous.

- La troisième étape englobe le transport des ions hydrogène (H^+) et des électrons de la photoanode à la cathode (ou de l'anode à la photocathode) respectivementvia l'électrolyte et la connexion électrique.
- Enfin, les électrons présents à la cathode (ou à la photocathode) réduisent les ions H^+ pour former des molécules d'hydrogène (H_2).

I.2. Description du processus

Le courant électrique dissocie la molécule d'eau (H_2O) en ions hydroxyde (HO^-) et hydrogène H^+ : dans la cellule électrolytique, les ions hydrogène acceptent des électrons à la cathode dans une réaction d'oxydoréduction en formant du dihydrogène gazeux (H_2), selon la réaction de réduction :

$$2H^+ + 2e^- \rightarrow H_2(g) \qquad (1)$$

Du coté de l'anode des ions hydroxyde sont oxydésperdant ainsides électrons, ce qui permetde « fermer » le circuit électrique (équilibre de la réaction chimique en charge) :

$$2H_2O(l) \rightarrow O_2(g) + 4H^+(aq) + 4e^- \qquad (2)$$

Ce qui donne l'équation de décomposition par électrolyse suivante :

$$2H_2O(l) \rightarrow 2H_2(g) + O_2(g) \qquad (3)$$

La quantité de dihydrogène gazeux produite est donc deux fois celle dudioxygène. Selon la loi d'Avogadro, le volume récupéré de dihydrogène produit est aussi deux fois plus important que celui dudioxygène.

En utilisant l'équation de Nernst, il est possible de déterminer le potentiel des réactions d'oxydation et de réduction de l'eau en fonction du pH :

$$EH_3O^+/H_2 = -0.06 \times pH // EO_2/H_2O = 1.23 - 0.06 \times pH \qquad (4)$$

Lors de l'électrolyse de l'eau, deux électrodes métalliques sont plongées dans une solution d'eau et une différence de potentiel est appliquée entre ces électrodes. La Figure 2 montre que le courant obtenu varie fortement lors de la réduction de l'eau pour un potentiel de ~0V, puis lors de l'oxydation de l'eau pour un potentiel ~1.23V à un pH de l'ordre de 0. Dans le cas où on utilise un solvant, la différence de réaction cinétique entre le solvant et le métal pour l'oxydation et la réduction de l'eau provoque des décalages de potentiels réactionnels. Les

domaines définis autour du potentiel d'oxydation ou de réduction sont nommés « domaine de surtension » et sont caractérisés par une augmentation de type exponentielle du courant pour l'oxydation et une diminution du même type pour la réduction.

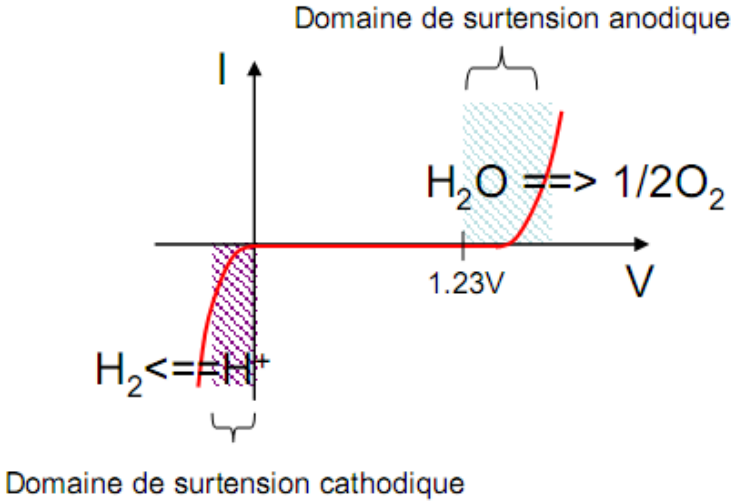

Figure II.2 : Courbe I(V) observée lors de l'électrolyse de l'eau à pH = 0.

I.3.Cellule Photoélectrochimique (PEC)

I.3.1. Définition

Laphotoélectrochimie est la partie de la chimie qui étudie les processus d'échanges électroniques qui sont initiés ou induits par uneradiation lumineuse arrivant sur un matériau. Honda [1] a définila photoélectrochimie comme étant l'ensemble des réactions mises en jeu sur une électrode dansun état excité. L'excitation peut concerner directement l'électrode métallique ou semi-conductrice ou les molécules adsorbées à la surface d'une électrode ou bien à l'interface électrode/électrolyte. Cesréactions peuvent être une suite d'excitations des composés réactifs en solution. La photoélectrochimie concerne plus les matériaux semi-conducteurs. C'est une technique puissante permettant d'évaluer la photoactivité ou l'activité sous radiationappropriée des matériauxsemi-conducteurscristallins ou nanocristallins, tels que le TiO_2[2]ou autres. Ainsi, une réaction photoélectrochimique est l'ensemble des phénomènes qui permettent la conversion de l'énergie des photons d'une radiation lumineuse en énergie électrique (paires électron-trou), cette dernière énergie pouvant induire ensuite des réactions chimiques telles que les réactions d'oxydation et de réduction. La nature du courant et du potentiel rend compte des réactions qui se déroulent à l'interface de l'électrode de travail (ET) et l'électrolyte. Les réactions qui ont lieu à la surface de l'électrode de travail en contact avec l'électrolyte dépendent de la nature de l'électrode oudu matériau, mais aussi des entités que

comportent l'électrolyte. En variant le potentiel, le courant varie. Le potentiel est varié entre un premier potentielE_1 et un deuxième E_2 et ce domaine de potentiels définit alors la zone d'électro-activité. Ce domaine est souvent petit de l'ordre de 1V afin de pouvoir détecter les réactions d'oxydation et de réduction soit du matériau soit des composés présents dans l'électrolyte.Dans le domaine d'électro-activité, l'ensemble des phénomènes peuvent être élucidés par la chimie des interfaces qui explique lemouvement ou le transfert des charges et la variation d'énergie des bandes aux interfaces semi-conducteur/électrolyte et interfaces métal/électrolyte.

I.3.2 Interfaces semi-conducteur/électrolyte

L'étude des processus aux interfaces semi-conducteur/électrolyte s'avèretrèsintéressante et importante pourlestechnologiesportantsurlacorrosion, l'électro-catalyse la détection, les batteries et la photocatalyse etc. [3]. La grande particularité des semi-conducteursestlapossibilitéd'introduction de certaines impuretésquipeuventaugmenterlenombredeporteurs decharges deplusieursordresde grandeur.
L'oxyde de Fer est un semi-conducteur naturellement de type n car les porteurs négatifs sont plus nombreux que les porteurs positifs. Si n_i représente la densité intrinsèque de porteursdechargespositives ou négatives, les approximations de Maxwell Boltzmann donnent

$$\boldsymbol{n \times p = n_i^2} \qquad \textbf{(5)}$$

Avec :

$$\mathbf{n = N_c \exp\left(-\frac{E_c - E_f}{k_B T}\right)} \qquad \textbf{(6)}$$

$$\mathbf{p = N_v \exp\left(-\frac{E_f - E_v}{k_B T}\right)} \ldots\ldots\ldots\ldots\ldots\ldots\ldots \ldots \textbf{(7)}$$

où N_c et N_v représentent respectivement les densités d'états dans la bande de conduction et dans la bande de valence, k_B est la constante de Boltzmann et E_f est le niveau de Fermi défini comme étant lepotentielderéférencepourl'occupationdesniveaux d'énergie:c'estlepotentielélectrochimiquedesélectronsdansun matériau il estconstantà l'équilibre (pas de tension imposée ni d'injection ou création de porteurs).

I.3.3 Choix des électrodes pour le système PEC

Deux critères sont essentiels pour le choix des matériaux semi-conducteurs des cellules PEC: l'existence d'une bande interdite "parfaite" (large gap) et la possibilité d'éviter la recombinaisondesporteursde charge. L'énergie minimale théorique du photon devant être

absorbée par une photoanode "parfaite" est de 1.23 eV.C'estlaforceélectromotriceminimalethéoriquenécessaireauxcellulesPECpour dissocier la molécule d'eau.

Trois concepts de système peuventêtre envisagés pour dissocierl'eau : lessystèmesà photoélectrode simple, à double photoélectrodes et les systèmes hybrides photoélectrode/photovoltaïque.Du point de vue matériaux, des semi-conducteurs àlarge gap (comme le ZnO, TiO_2 et Fe_2O_3) fournissentla tensionsuffisante pour assurerla décomposition de l'eau. En effet, le dioxyde de titane (TiO_2) est le matériau photoélectrode le plus étudié ; il a été testé avec succès dans des cellules PEC par Honda et Fujishima dès le début des années 1970. Toutefois, le champ d'investigations'estélargiàl'utilisationd'autresmatériauxsemi-conducteurs,plusparticulièrementl'oxyde de Fer hématite (Fe_2O_3), le vanadate de bismuth ($BiVO_4$), l'oxyde de zinc (ZnO) et le trioxyde de tungstène (WO_3). La phototension des cellules PEC qui s'applique à chacun de ces matériaux photoanodes étant inférieure à 1.23eV, latension de polarisation nécessaire pour dissocier l'eau.L'Université des Sciences de Tokyo a fait part, début janvier 2007, des progrès dans cette technologie en utilisant un photocatalyseur réalisé à partir d'un sulfure mixte Ag-Cu-In avec du Ru en surface. Ce photocatalyseur captetoutelalumière visible dansla gamme 400 – 800 nm. De l'hydrogène estformé avec un débit de 3.1 l/h.m². [4].Desprototypesàmulti-jonctionsontpermisdesrendementsdel'ordrede12à14%, maisavecdes instabilités de système [12].Enrevanche,desrendementsstablesde10%devraientpouvoirêtreatteints. Unsystème, étudié en Suisse appelé dual-bed, comporte des zones de production d'hydrogène et d'oxygène séparées, afin de permettre une meilleure optimisation des deux réactions. Ce système comprend une photoanode en couche mince de WO_3 polycristallin et une cellulesolairecathode en TiO_2 avec un colorant DSC, en 1999 le rendement global a atteint 5 %. Des travaux de développement en cours sur ce système sont orientés sur la recherche de nouveaux matériauxd'électrodes,commel'hématite(α-Fe_2O_3)entant que photoanode, ou encore sur le développement de pigments organiques [12].

I.3.4 Courant d'oxydation et courant de réduction

Les électrons etlestrous peuvent diffuser del'interface oùils sont produits versl'intérieur selon le niveau de Fermi du semi-conducteur. Uncourantd'oxydationoucourantanodiqueestcomptéparconventionpositivement.Il correspondàladiffusiondesélectronslorsqu'ilssontmajoritairesalorsquel'onauraun courant cathodique dans le cas où se sont les trous majoritaires qui diffusent. C'est-à-dire que le

courant anodique se produit lorsqu'une oxydation a lieu à la surface de l'électrode. Le courant cathodique va correspondre au phénomène de réduction à la surface de l'électrode. Dans le cas d'un semi-conducteur illuminé, la densité totale de photocourant est donnée par la relation :

$$J = e(J_n(d) - J_p(d)) \qquad (7)$$

$$J = e[\, D_n(\frac{d_n(x)}{dx})_{x=d} - D_p(\frac{d_p(x)}{dx})_{x=d}] \qquad (8)$$

Où*n*et*p*sontlesconcentrationsd'électronsetdetrous,*d*estl'épaisseurdelacouchedu photocatalyseur, D_n et D_p sont les coefficients de diffusion respectivement des électrons et des trous, *e* est la charge élémentaire. À l'équilibre, les deux types de porteurs de charge obeissent aux relations suivantes:

$$D_n \frac{d^2n}{dx^2} + G_n(x) - R_n(x) = 0 \qquad (9)$$

$$D_p \frac{d^2p}{dx^2} + G_p(x) - R_p(x) = 0 \qquad (10)$$

G(x) est le taux degénération et R(x) est le taux de ecombinaison des paires électron-trou. Enl'absencedetoutemoléculeorganique,lagénérationestlamêmepourlestrousetles électrons, mais les termes de transport et de recombinaison sont différents.

I.3.5 Électrolytes

Les électrolytes sont des conducteurs ioniques. Les charges sont localisées dans les orbitales moléculaires des espècesioniques. Un électrolyte peut êtreinerte c'est-à-dire qu'il ne participe pas aux réactions de transfert de charges. Un électrolyte est défini par un couple redox Ox/Red. Les réactions entre les deux espèces sont les suivantes:

$$Ox^{(z+1)} + e^- \rightarrow Red^{(z+1)} \qquad (11)$$

$$Red^{(z+1)} \rightarrow Ox^{(z+1)} + e^- \qquad (12)$$

Le modèle de Gerischer-Marcus décrit les espèces ioniques comme des états électroniques vides et remplis :$Ox^{(z+1)}$ est l'état vide et l'état occupé correspond à $Red^{(z+1)}$.

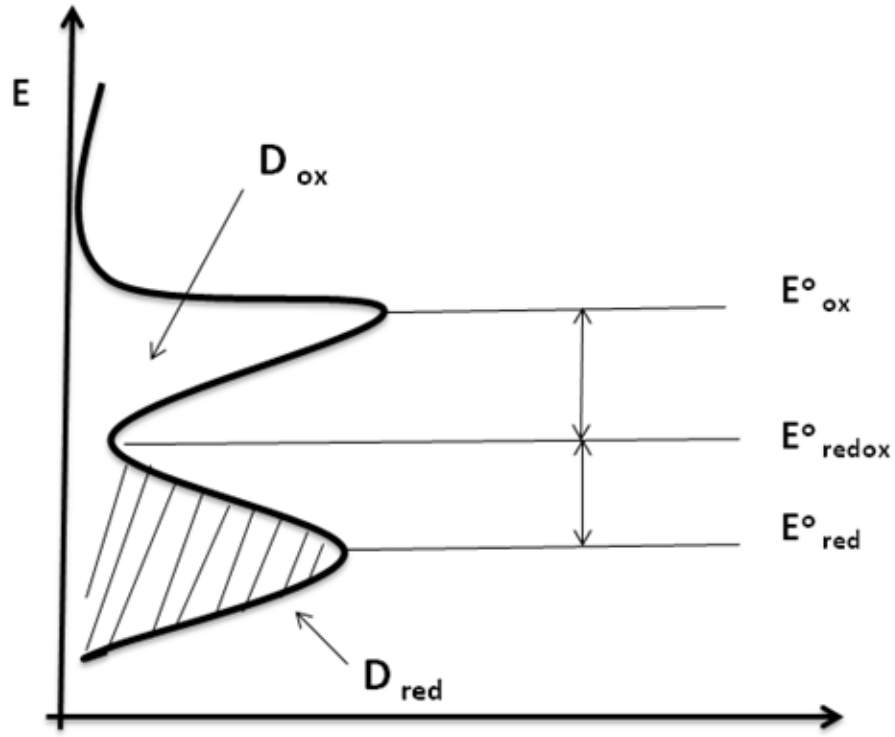

FigureII.3: Fonction de distribution des états d'énergie pour des électrons dans un électrolyte.

Les densités de ces espèces sont calculées par les expressions suivantes:

$$\boldsymbol{D_{ox}(E) = C_{ox} \times W_{ox}(E)} \qquad \textbf{(13)}$$

$$\boldsymbol{D_{red}(E) = C_{red} \times W_{red}(E)} \qquad \textbf{(14)}$$

C_{ox} et C_{red} représentent les concentrations alors que W_{ox} et W_{red} sont des fonctions de densités d'états des espèces oxydées et réductrices. Cette fonction d'état est donnée par la formule :

$$\boldsymbol{W(E) = (4\pi\lambda T^{\frac{-1}{2}})\ \exp\ (-\frac{(E_t - E)^2}{4\pi\lambda T})} \qquad \textbf{(15)}$$

$\boldsymbol{\lambda}$ estl'énergie deréorganisation, $\boldsymbol{e_t}$estla probabilité detrouver une espèce *Ox* ou *Red* à un niveau t. Le modèle est une approximation qui considère le potentiel redox comme le niveau de Fermi de l'électrolyte. C'est un modèle de transfert isoélectronique appliqué par de nombreux électrochimistes des semi-conducteurs, car à partir d'un tel schéma d'énergie il est

possible de prédire la bande d'énergie mise en jeu au cours du processus de transfert de charge aux interfaces.

I.3.6Comportement d'un semi-conducteur sous éclairement

L'absorption d'un photon d'une énergie supérieur à Eg engendre la création d'une paire électron/trou. Cette paire, lorsqu'elle est séparée, va augmenter la quantité de porteurs de charges libre dans la bande de conduction ainsique dans la bande de valence. Lors de la séparation de la paire électron/trou, une augmentation des densités de charge de chacun des deux types de porteurs est observée. La densité des porteurs de charge majoritaires va être légèrement augmentée du fait qu'elle est déjà forte. La densité de porteurs de charge minoritaire sera augmentée fortement par rapport à sa valeur initiale avant illumination. Cette évolution est représentée schématiquement sur la Figure II-4.

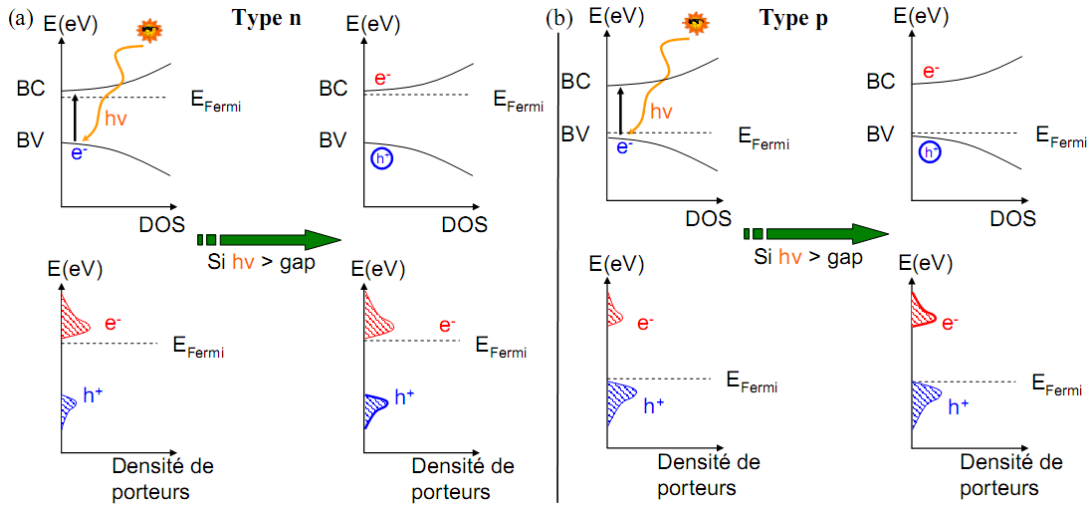

Figure II.4 : Création d'une paire électron/trou dans un semi-conducteur de type n/p (a/b) et effet sur les pseudos niveaux d'énergies des porteurs et sur la densité des porteurs. [5]

I. 3.7 Electrode semi-conductrice plongée dans un électrolyte

On discute dans ce qui suit le cas d'une électrode semi-conductrice. Lors de la mise en contact du semi-conducteur avec l'électrolyte, une égalisation du niveau de Fermi se produit à l'interface entre les deux. La quantité d'espèces oxydées ou réduites présente en solution suit une loi de probabilité autour du potentiel de réaction que l'on peut comparer à la loi de Fermi Dirac et qui est présenté sur la Figure II-5a. Selon le potentiel imposé à la solution, la majorité des espèces présentes seront soit oxydées soit réduites. Elles peuvent participer à une réaction électrochimique si des charges sont transmises via l'interface électrode/solvant. Le niveau de Fermi du semi-conducteur s'ajuste au niveau de Fermi de la solution, donc au potentiel fixé par l'appareillage. L'interface entre le semi-conducteur et l'électrolyte est définie

schématiquement comme présentéedans laFigure II-5a. Sur ce schéma, un semi-conducteur de type p en désertion est présenté, c'est le régime de fonctionnement commun d'une électrode semi-conductrice dans un montage d'électrochimie. Ainsi, les bandes sont courbées de telle façon queles porteurs de charge majoritaires sont entraînés vers le cœur du matériau, et les porteurs minoritaires ont tendance à rester en surface.

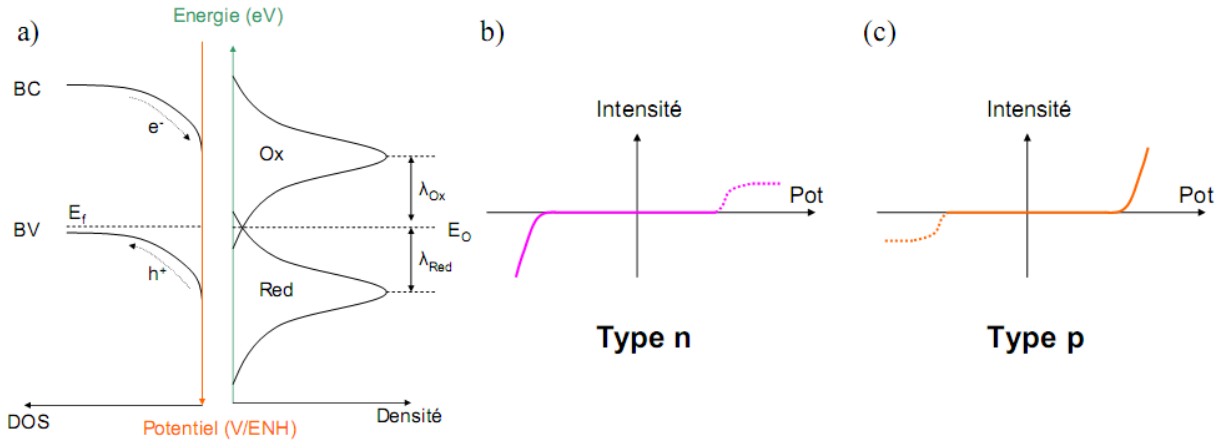

Figure II.5 : (a) Distribution des états énergétiques d'un couple oxydo-réducteur en solution et représentation du diagramme énergétique d'un semi-conducteur de type p. Courbes I(V) obtenues par une jonction électrolyte/semi-conducteur sous obscurité en fonction du type de semi-conducteur : n (b) et p (c). [13]

L'utilisation d'une électrode semi-conductrice permet d'effectuer l'électrolyse de l'eau sous potentiel grâce aux porteurs libres du semi-conducteur. Une limitation du courant existe cependant pour les courants générés par les porteurs minoritaires du semi-conducteur. La faible présence de ces porteurs ne permettra pas d'obtenir une augmentation exponentielle du courant d'oxydation pour un type n et de réduction pour un type p. Un palier de courant sera atteint pour de forts potentiels. Les courants obtenus sont représentés sur la Figure II-5b et c. On observe ici les courants d'oxydations et de réduction de l'eau.

Sous illumination, le semi-conducteur utilisé comme électrode subit des variations de densité de porteurs de charges majoritaires et minoritaires. Dans une situation de désertion au cœur du semi-conducteur, induisant une gamme de potentiel avec très peu de courant généré sous obscurité, les porteurs minoritaires générés par l'illumination au sein du matériau vont migrer vers la surface, et les porteurs majoritaires générés vont migrer vers lecœur du matériau. Les mouvements de porteurs au sein du matériau vont créer une différence de potentiel en surface qui sera notée photopotentiel. Ce photopotentiel s'accompagne d'un photocourant généré par la paire électron-trou une fois séparé. Le semi-conducteur étant dans une situation de désertion, lors de l'illumination de celui-ci ; dans ce cas une augmentation de la quantité de porteurs de charges minoritaires a lieu, avec possibilité de réaction d'oxydoréduction entre les

porteurs minoritaires et l'électrolyte. Au courant visible lors du test sous obscurité (courbes rouges sur la Figure II-6) va s'ajouter une contribution positive (semi-conducteur de type n) ou négative (semi-conducteur de type p). Le photocourant généré est dépendant de la cinétique de transfert de porteurs minoritaires du semi-conducteur vers la solution d'électrolyte. Ainsi, lors d'une manipulation avec un potentiostat, les courants visibles àl'obscurité ou sous illumination sont représentés sur la Figure II-6.

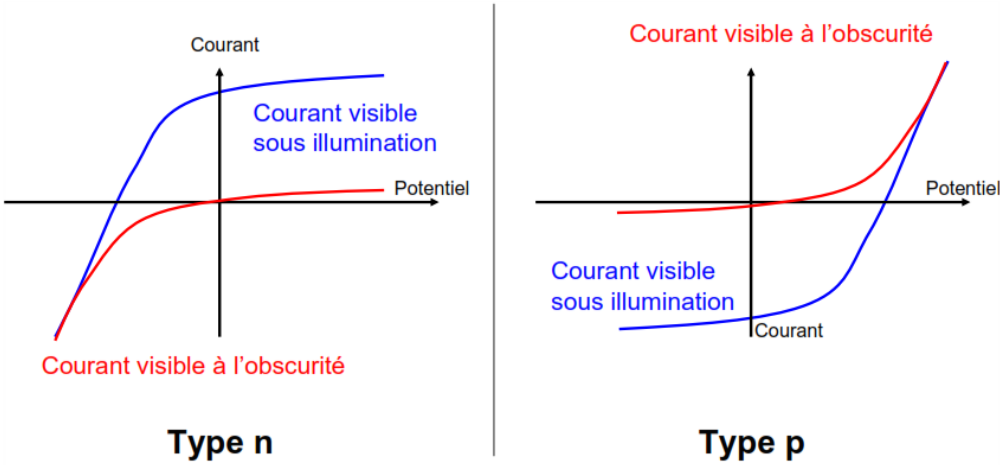

Figure II.6 : Caractéristiques courant/tension d'une jonction entre un semi-conducteur et un électrolyte sous illumination. En rouge : le courant issu des porteurs majoritaires (sous obscurité et sous illumination), en bleu : le courant sous illumination issu des porteurs minoritaires. [13]

Ces différences de signe sous éclairement et à l'obscurité seront utilisées afin de caractériser la nature des semi-conducteurs obtenus. La différence de courant dans la zone de désertion du semi-conducteur sera utilisée pour déterminer si le courant photogénéré est anodique ou cathodique.

I.3.8Effets de la nature de semi-conducteur sur la réponse PEC

Selon la nature des semi-conducteurs, deux types de comportements peuvent être observés sous potentiel dans un électrolyte (ici l'eau). Dans la méthode présentée ici, des variations de courant induites par l'augmentation des porteurs minoritaires de chacun des semi-conducteurs peuvent être observées. Pour cela une variation de l'éclairement dans la zone de désertion des semi-conducteurs est établie, soit entre les potentiels d'oxydation et de réduction de l'eau. Dans ce cas, onobserve une oscillation des courants vers des courants positifs pour un semi-conducteur de type n et négatifs pour un semi-conducteur de type p. Les résultats théoriques de cette analyse en fonction de chaque type de semi-conducteur sont indiqués sur la Figure II-7.

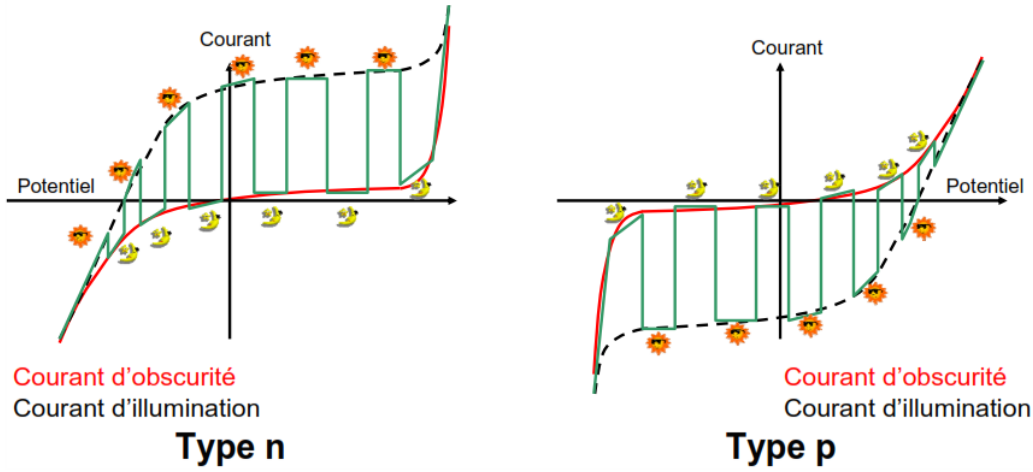

Figure II.7 : Résultats de la caractérisationcourant/tension selon le type de semi-conducteur sous éclairement alternatif [13].

Les deux types de résultats attendus permettront de conclure clairement sur le type n ou p des semi-conducteurs testés. Cette méthode s'applique sur toustypes d'échantillons, même très résistifs. Il suffit d'utiliser un potentiostat ayant une précision de l'ordre du nano ampère.

II. Choix des semi-conducteurs pour les photoélectrodes (PEC)

Les matériaux semi-conducteurs appropriés pour les photo-anodes destinées à la séparation de la molécule d'eau doivent satisfaire à plusieurs exigences. Cependant, il est très difficile de fabriquer une électrode idéale tant que la configuration du dispositif final dépend des techniques de traitement du matériau. Dans cette section, les propriétés fonctionnelles les plus importantes d'une électrode appropriée sont discutées.

II.1. Bande interdite et position des limites de bandes

Une exigence fondamentale pour uneélectrode semi-conductrice est que le niveau d'énergie de sa bande interdite ne doit pas être inférieur à 1.23 V (par rapport à l'électrode réversible d'hydrogène (V_{ERH}) dans des conditions standard),lepotentiel nécessaire pour briser une molécule d'eau en hydrogène et oxygène. Cependant, il a été montré qu'un matériau semi-conducteur avec une bande interdite d'environ 2 eV est le meilleur matériau pour les photoanodes. Bolton[6] a montré que dans un système idéal, la perte d'énergie réelle U_{loss} par molécule d'hydrogène (H_2) dans le processus PEC global est de ~ 0.3 - 0.4 eV tandis qu'un U_{loss}de ~ 0.8 eV pourrait être considéré comme une bonne estimation dans un système pratique. U_{loss} ne peut pas être nulparce que l'énergie de l'ensemble des paires d'électrons-trous photo-générés est thermodynamiquement l'énergie interne et non l'énergie de Gibbs, par

conséquent, les considérations entropiques imposent une perte d'énergie minimale de l'ordre de 0.3 à 0.4 eV. Un autre paramètre important est la position des extrémitésde la bande de conduction et de la bande de valence dusemi-conducteur. Le matériau idéal devrait avoir un gap de ~ 2 eV tandis que les extrémités de ses bandes doivent chevaucher les potentiels redox de la dissociation de l'eau. Par exemple, comme le montre la Figure 8, les bords de bande de $SrTiO_3$ satisfont à cette exigence, cependant, il s'agit d'un matériau à large bande interdite et, par conséquent, seulement environ 4 % du spectre solaire visible est absorbé.

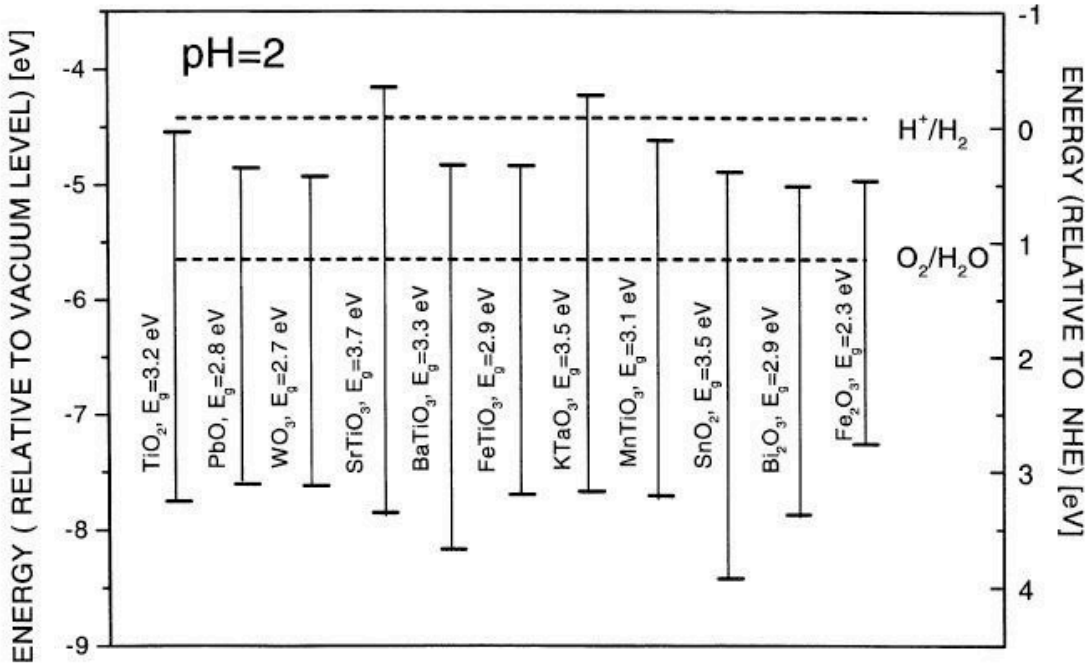

FigureII.8 :Schéma des bandes de quelquesmatériaux semi-conducteurs et positions de leurs limites de bandes en fonction du potentiel redox de l'hydrogène et l'oxygène [7]

D'autre part, Fe_2O_3 a unebande interdite presque idéale. Cependant, sa limite de bande de conduction est situéelégèrement en hautdu potentiel d'évolution de l'hydrogène, par conséquent, un potentiel de polarisation est nécessaire pour conduire la réaction de réduction.
Dans les semi-conducteurs de type n et de type p, le potentiel de bande plate peut être utilisé comme indicateur pour les positions de bord de bande de conduction et de valence. La division photoélectrochimique de l'eau peut avoir lieu sans l'imposition d'un potentiel, si le potentiel de bande plate d'un semi-conducteur de type n se situe au-dessus du potentiel redox de la réaction H^+/H_2. En d'autres termes, les photoanodes avec un potentiel de bande plate négatif, relativement au potentiel redox de la réaction H^+/ H_2,n'ont pas besoin d'un potentiel de polarisation pour décomposer l'eau. La figure 9 illustre les potentiels de bandes plates de plusieurs oxydes par rapport aux potentiels de bandes interdites E_g.

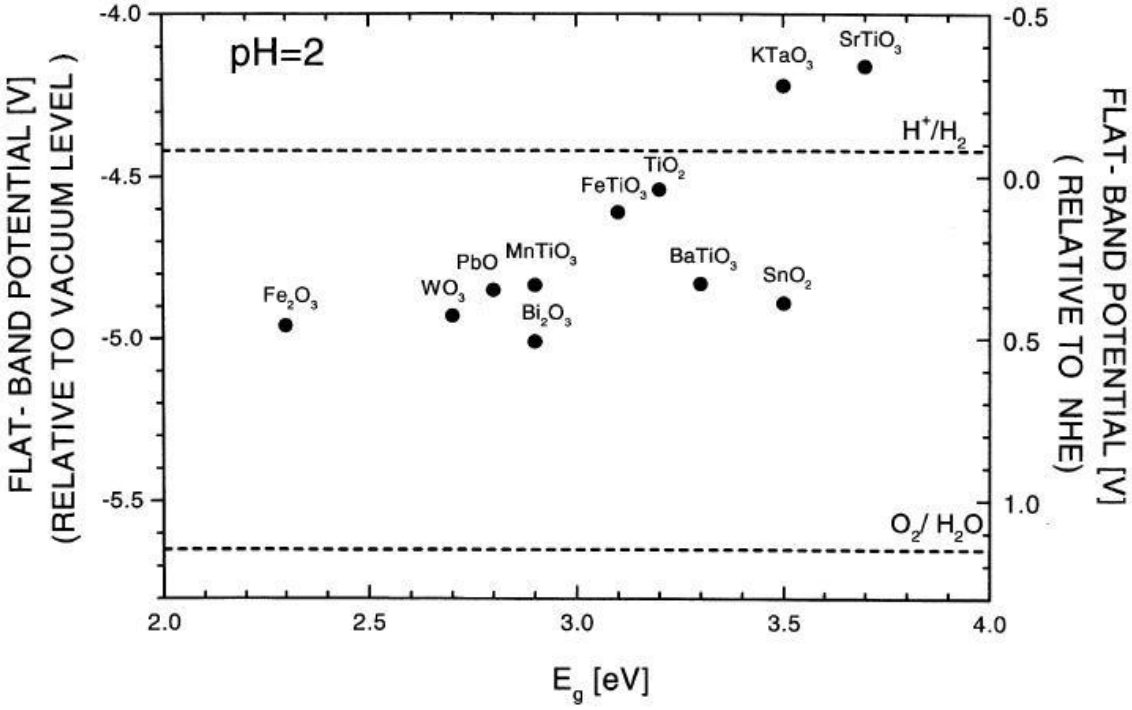

Figure II.9. Potentiel de bande plate de quelques oxydes métalliques par rapport à l'énergie de bande interdite [8]

II. 2.Stabilité

Lorsque l'électrode semi-conductrice est éclairée, des paires électron-trou sont générées. Ces électrons et trous ont de forts potentiels,respectivement oxydants et réducteurs. S'ils ne sont pas injectés dans l'électrolyte ou transférés au substrat conducteur, alors sous certaines circonstances, ils peuvent oxyder ou réduire le semi-conducteur lui-même. Cependant, ceci est seulement un côté du problème. Une électrode semi-conductrice idéale ne doit pas seulement résister à la corrosion associée aux électrons et trous photogénérés, mais elledoit également être résistante à la corrosion et à la dissolution électrochimique. Généralement, la plupart des oxydes sont stables dans ces conditions, et par conséquent, considérés de bons candidats en tant que matériaux photoélectrodes dans les électrolytes aqueux dans des cellules photoélectrochimiques.

II.3. Propriétés électriques

Lorsqu'une électrode semi-conductrice est éclairée, les porteurs de charges photogénérés doivent être transportés efficacement. Généralement, la conductivité électrique d'un semi-conducteur est plus petite que celle d'un métal de plusieurs ordres de grandeur. La conductivité électrique (σ) d'un semi-conducteur est décrite parl'équation 16:

$$\sigma = en\mu_n + ep\mu_p + Z_i ei\mu_i \qquad (16)$$

Où n est la concentration des électrons, p est la concentration destrous, ***i*** est la concentration des ions, $Z_i$est le nombre de charges des ions, μ_n, μ_p et μ_i sont respectivement les mobilités des électrons, des trous et des ions. Il faut noter qu'à la température ambiante, le composant ionique de l'équation ci-dessus peut être ignoré.

Lorsque la concentration des porteurs de charge augmente, la mobilité des porteurs diminue, pour donner suite à l'interaction coulombienneentre les électrons et les trous. Par conséquent, la conductivité optimale est obtenue lorsqu'on atteint un équilibre entre la concentration des porteurs et leur mobilité. L'introduction de défauts dans le semi-conducteur peut améliorer la conductivité. Cela est réalisé en incorporant des cations donneurs ou accepteurs dans la structure semi-conductrice et par le contrôle de la pression partielle d'oxygène pendant la préparation d'un matériau semi-conducteur [16].

Le mécanisme de transport des porteurs de charge dans l'électrode nanostructurée est généralement considéré être dominée par la diffusion. Par conséquent, la longueur de diffusion des électrons et des trous est un paramètre important pour un semi-conducteur. Elle peut être optimisée par la modification de la composition chimique [9].De plus, une nanostructure modifiée peut permettre un meilleur transport de charge, par exemple, si la taille des nanostructures (exemple : des nanoparticules) est inférieure à la longueur de diffusion des transporteurs, alors ceci conduira relativement à une faible recombinaison dans lamasse. Cependant, il peut également être désavantageux, car il pourrait augmenter la recombinaison aux limites interparticulaires particulièrement au niveau des joints de grains.

II.4 Généralités sur l'oxyde de Fer (Fe_2O_3)

II.4.1. Historique du Fe_2O_3

Au cours des dernières décennies, une large gamme de matériaux tels que les oxydes métalliques, les nitrures métalliques et les sulfures ont été utilisés comme photoélectrodes. Comme les premiers rapports sur la dissociation de l'eau par voie PEC ont émergé au début des années 1970, différents groupes de recherche ont commencé à chercher unmatériau semi-conducteur à utiliser comme photoélectrode. Les premières investigations ont impliqué des semi-conducteurs à large bande interdite tels que TiO_2, [9]$SrTiO_3$, [10] et SnO_2,[11]. Comme présenté ci-haut, TiO_2 et $SrTiO_3$ possèdent des positions de limites de bande idéales puisque les limites des bandes deconduction et de valence couvrent les potentiels redox de l'évolution de H_2 et O_2, (voir Figure III-1). Cependant, leurs inconvénients sont qu'ils absorbent seulement une petite quantité de l'énergie solaire (environ 3-4 %),étant donné que leur limited'absorption se situe dans la gamme des longueurs d'onde comprise entre 360-410 nm.

Les matériaux avec une énergie de bande plus basse vont absorber une plus grande partie du spectre solaire suscitant un espoir de conversion efficacede l'énergie solaire.

Les sulfures métalliques sont un autre groupe de matériaux qui ont suscité un intérêt considérable dans la préparation des électrodes PEC. Le CdS est l'un des sulfures métalliques qui a été étudié de manière approfondie[19,12]. Le CdS a une bande interdite de ~ 2.4 eV qui est un niveau énergétique approprié pourune électrode PEC. Les positions d'énergie des bords de bande de conduction et de valence duCdS permettent la photodissociation de l'eau sans avoir besoin d'un potentiel de polarisation externe.

Cependant, il a tendance à subir une photo-corrosion sous une irradiation prolongée puisqu'il se convertit en Cd^{2+} et sulfate (en présence d'oxygène) [13].

La plupart des nouvelles technologies énergétiques respectueuses de l'environnement sont généralement soit très cher en raison du coût du matériau de départ ou à cause du processus de fabrication coûteux. Par conséquent, ils sont constamment en concurrence avecles technologies bien établies déjà existantes. Donc, le coût de production et la facilité de fabrication sont les facteurs déterminants dans le processus de sélection des matériaux utilisés dans la photodissociation de l'eau.

L'hématite (α-Fe_2O_3) est un matériau candidat fort en tant qu'électrode PEC pour le clivage de l'eau. En effet l'hématite remplit la plupart des critères de sélection d'un matériau photocatalytique approprié pour le fractionnement de l'eau tel que la bande interdite, la stabilité chimique et photoélectrochimique et la facilité de fabrication.

Les premiers rapports sur l'application d'électrodes d'hématite dans des cellules PEC ont été publiés par Hardee et Bard [14,15] en 1976 et 1977. Ils ont préparé des électrodes polycristallines d'hématite en utilisant la CVD et l'acétylacétonate de fer comme précurseur. Quinn et. al. [16] ont préparé une électrode formée d'un monocristal d'hématite. Le comportement du monocristal était similaire aux électrodes polycristallines rapportées par Hardee et Bard atteignant une densité de photocourant de ~ 80 $\mu A.cm^{-2}$ à la longueur d'onde 400 nm et 0.5 V vs. SCE en utilisant un électrolyte NaOH à 2 M.

D'autres études sur les performances PEC des électrodes d'hématiteont été effectuées par Kennedy et al.[17] sur des poudres d'hématite. Leurs travaux incluaient la détermination du potentiel de la bande plate et de l'effet de la densité de l'électrolyte et des donneurs en fonction de l'efficacité de conversion de l'énergie solaire. Ils ont montré que le potentiel de bande plate descend vers des valeurs négatives lorsque le pH de l'électrolyte augmente. Ils ont également calculé la longueur diffusion dans l'électrode d'hématite qui était d'environ 2-4 nm, ce qui était considérablement plus faible que les valeurs duTiO_2 (100 nm).

La conductivité des électrodes semi-conductrices est significativement plus faible que celle des électrodes métalliques. L'hématite en phase pure est un isolant de Mott et a une faible conductivité qui limite son efficacité quantique dans les processus photoélectrochimiques à de très petites valeurs [18].Le dopage est largement considéré comme une solution à ce problème. L'effet de différents agents dopants a été abondamment étudié dans la littérature. Un des premiers rapports sur l'effet de dopage sur la photoactivité des électrodes d'hématite a été publié par Shinar et Kennedy [19] en 1982. Ils ont étudié l'effet de différents oxydes tels que ZrO_2, CeO_2, V_2O_5, Nb_2O_5 et également Al_4C_3 sur la photoactivité des électrodes d'hématite préparées à l'aide de traitement conventionnel de poudre.

Une de leurs découvertes intéressantes était que la meilleure performance obtenue n'était pas nécessairement pour l'échantillon avec le plus bas niveau de dopage, alors qu'on s'attendait que les niveaux de dopage faibles conduisent à la formation d'une large couche d'appauvrissement, et par conséquent, à une efficacité quantique plus élevée [27].

Cependant, le niveau de dopage idéal était différent pour chaque dopant. Merchant et. al.[20] ont rapporté une amélioration de l'efficacité de l'électrode d'hématite en présence de Fe_3O_4 à la surface des films d'hématite et ontaffirmé que cela était dû à la présence de Fe^{2+} qui agissent comme des centres donneurs pouvant fournir des électrons par voie d'excitation thermique. Cependant, les ions Fe^{2+} peuvent fonctionner comme des centres de piégeage d'électrons qui ne contribuerait pas au photocourant [21].

En 1999 Khan et Akikusa [22]ont rapporté une photoélectrode d'hématite très efficace préparée en utilisant la méthode de pyrolyse par pulvérisation atteignant une efficacité de conversion pratique de 1.84% et la valeur IPCE maximale de 22.5% à 370 nm. Leurs résultats ont montré une amélioration de la densité apparente des donneurs (2.2×10^{20} cm^{-3} à la fréquence AC de 1000 Hz et dans un électrolyte1M NaOH), laquellea été attribuée à la méthode de préparation qui serait responsable de l'amélioration de l'efficacité de la conversion. La densité des donneurs rapportée était presque trois fois plus élevée que celledes échantillons au TiO_2 dopés rapporté par Kennedy et. al.[30] (~ 7.3 x 10^{19} cm^{-3} à 1000 Hz et NaOH 1 M). Beermann et. al.[29] ontétudié l'effet de la nanostructure sur l'efficacité de la conversion des électrodes d'hématite. Ils ont préparé des électrodes comprenant des nanotiges d'hématite parallèles et perpendiculaires à la surface du substrat. L'IPCE rapporté est d'environ 18% à 360 nm à un pH = 12. Le même groupe a étudié l'effet de l'intensité lumineuse sur l'efficacité de la conversion et a conclu que l'IPCE des électrodes en forme de nano-bâtonnets était indépendante de l'intensité lumineuse [23].

Bien que l'hématite ait une bande interdite idéale de ~ 2.1-2.3 eV son bord de bande de conduction est positionné en dessous du potentiel redox de l'hydrogène nécessitant donc un potentielexterne pour initier la réaction de fractionnement de l'eau. De plus, les efficacités des photocourants rapportées pour l'hématite étaient la plupart du temps bien en dessous des niveaux attendus. La mauvaise performance des électrodes d'hématite a été attribuée à sa cinétique de transfert de charge relativement lente et à un taux élevé de recombinaison électron-trou due à sa courte longueur de diffusion.

II.4.2 Propriétés structurales

Le α-Fe_2O_3 est un minéral commun largement connu sous la dénomination commune d'hématite et est répandu dans le sol et les roches. Son nom "hématite" vient du nom grec "haima = sang" en raison de sa couleur rouge. Cependant, s'il est formé de gros grains cristallins, il apparaît comme noir ou gris brillant.

L'hématite est une source majeure dans l'industrie des pigments inorganiques en tant que pigment rouge. Comme il s'agit d'un produit majeur de la corrosion du fer et de l'acier, il a fait l'objet d'études approfondies.

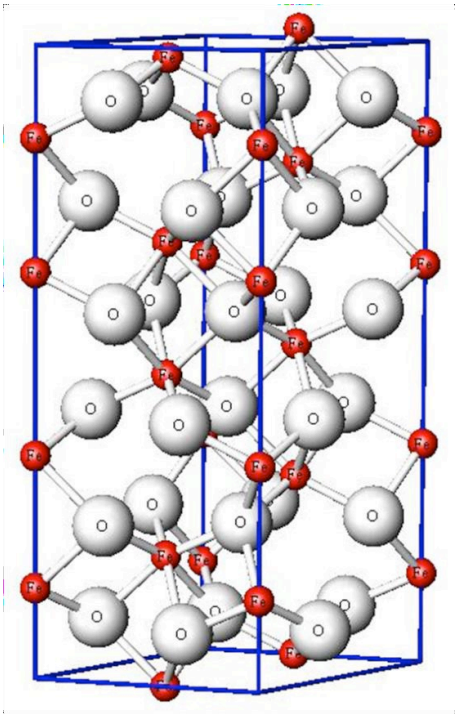

Figure II.10 : Représentation schématique de la structure de l'hématite α-Fe_2O_3.[24]

L'hématite est isostructurale au corindon (Al_2O_3). Sa structure est constituée de distorsionhexagonale (hcp) à proximité des plans (001) constitués d'atomes d'oxygène avec des ions Fe (III)occupant 2/3 des interstices octaédriques (Figure 10)[25]. Par conséquent,

chaque atome d'oxygène est entouré par quatre atomes de Fe et chaque atome de Fe a six voisins d'oxygène. Cet arrangement conduit à la formation de paires d'octaèdres $Fe(O)_6$ dont chacun partage des bords avec troisvoisins octaédriques dans le même plan et un bord et une face avec l'octaèdre situé sur le plan adjacent[26].L'hématite est habituellement indexée en symétrie hexagonale, c'est-à-dire (hkil), où h + k= -i et i est généralement omis.

II.4.3 Structure électronique et électrique

Comprendre la configuration électronique et les propriétés électriques des oxydes de fer,en particulier l'hématite, est cruciale dans l'application réussie de α-Fe_2O_3 en tant que photoélectrode de fractionnement de l'eau. Fe^{3+} a la configuration électronique $1s^2 2s^2 2p^6 3s^2 3p^6 3d^5$ tandis que Fe^{2+} a la configuration$1s^2 2s^2 2p^6 3s^2 3p^6 3d^6$. Par conséquent, les électrons dans l'orbitale***d*** et leurs caractéristiques sont ceux qui définissent les propriétés électriques des oxydes de fer.

Une orbitale est une région de l'espace occupée par un seul électron ou une paire d'électrons. Si deux électrons occupent une orbitale, ils auront des spins opposés. Il y a cinq différentes orbitales d orientées selon 5 orientations différentes dans l'espace. Les régions au sein des orbitales où la densité électronique est maximale sont appelées lobes de l'orbitale. Les cinq orbitales sont classées en deux séries d'orbitales selon la direction de leurs lobes. Trois orbitales (t_{2g}), à savoir d_{xy}, d_{yz}, d_{xz}, ont chacun quatre lobes qui sont dirigés autour des coordonnées des axes du noyau. Le deuxième ensemble d'orbitales (e_g), dx^2-y^2 et dz^2, ont leurs lobes orientés tout au long des axes [31]. Dans les oxydes et les hydroxydes de fer, les ions Fe sont coordonnés aux ions chargés négativementO^{2-} / OH^- . Par conséquent, en raison du champ électrostatique de la coordination, les orbitaux d de Fe ne montrent pas des énergies égales contrairement à leur état fondamental.

Les orbitaux d peuvent être remplis de différentes manières. La règle générale montrant le remplissage des orbitales d est décrit comme $(t2_g)^n(e_g)^m$ où m et n représentent le nombre d'électrons situés à chaque ensemble d'orbitales. Par exemple, la configuration de l'état fondamental de la coordination tétraédrique pour Fe^{3+} est $(eg)^2(t2g)^3$. Cela signifie que les deux premiers électrons entrent dans les orbitaux e_g et les trois autres entrent $t2_g$. Les diagrammes de Tanabe-Sugano (Figure 11) représentent les énergies de différents états multiélectroniques (multiplets), formés comme les résultats de la division du champ électrostatique causée par les ligands, en fonction de l'énergie de stabilisation du champ cristallin. Ce diagramme est utile pour le l'interprétation du comportement optique des oxydes

de fer et fournit un outil utile pour prédire les transitions électroniques entre différents états [34].

La structure électronique de l'oxyde de fer peut être simplifiée par de plus petites entités structurelles qui ressemblent à des propriétés similaires à celles des oxydes réels. Par exemple, FeO_6^{9-} représente Fe^{3+} en coordination octaédrique, c'est-à-dire hématite, et FeO_4^{5-} est utilisé pour la coordination tétraédrique de Fe^{3+} dans la magnétite (Fe_3O_4). Les diagrammes orbitaux moléculaires de ces deux types sont représentés à la Figure 12. L'hématite est un semi-conducteur extrinsèque avec une bande interdite de ~ 2.1-2.3 eV[27].Le comportement de type n et de type p peut être induit dans la structure de l'hématite; cependant, c'est plus difficile d'induire une conductivité de type p. Dans l'hématite de type n, la bande de conduction comprend les orbitales Fe^{3+} d vides tandis que la bande de valence est composée d'orbitales Fe 3d $2t_{2g}$ complètement remplis et quelques orbitales 2p antiliants de l'oxygène.

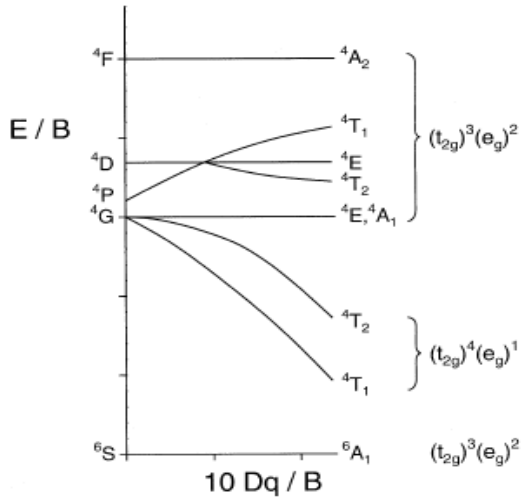

Figure II.11 Diagramme de Tanabe-SuganoduFe(III).[34]

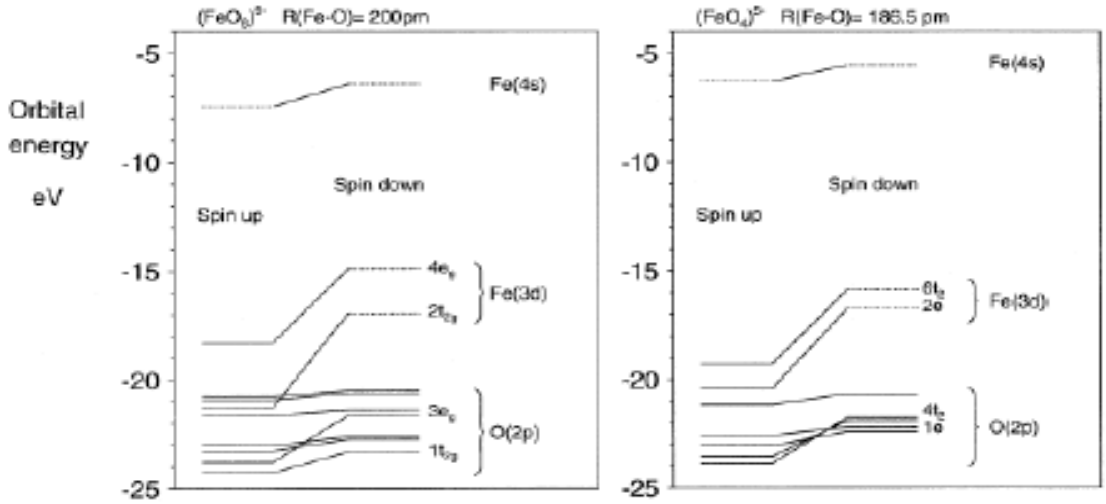

Figure II.12 Les diagrammes orbitaux moléculaires de FeO_6^{9-} and $FeO4^{5-}$ [34]

II.5 Méthodes d'élaboration du Fe_2O_3

Une variété de méthodes de fabrication telles que sol-gel [28] ont déjà été utilisée pourla préparation de photoélectrodes d'hématite. Deux types différents de photoélectrodes ont également été fabriqués ; granules et films. Dans ce qui suit, les principales techniques de fabrication pour la préparation des deux types de photoélectrodes d'hématite sont brièvement discutées.

II.5.1 Procédés de préparation en poudre

La préparation d'électrodes d'hématite en utilisant les techniques de traitement des poudres conventionnelles était l'une des premières méthodes utilisées [29]. Des poudres de α-Fe_2O_3 de différentes puretés sont utilisées comme matières de départ. Ces poudres sont ensuite mélangées, pressées et frittées pour former les photoélectrodes désirées.

Des échantillons d'hématite dopée peuvent également être préparés si les poudres d'hématites de départ sont mélangées avec les poudres d'agents dopants avant le frittage. Il y a des inconvénients associés avec cette méthode. Par exemple, les électrodes sont constituées de grosses particules d'hématite qui résultent entraînent des électrodes avec de petites surfaces. Les échantillons produits sont très épais et le taux de recombinaison est généralement très élevé. En outre, le procédé comprend également des procédures de mélanges et de frittages énergivores. En raison de ces inconvénients, le procédé de traitement des poudres n'a été utilisé que dans les premiers stades du développement des photoélectrodes d'hématite et n'est plus considéré comme une méthode appropriée pour la fabrication de photoélectrodes.

II.5.2 Pyrolyse par pulvérisation

La pyrolyse par pulvérisation est un procédé courant pour la préparation de photoélectrodes d'hématite qui a été largement utilisé par des groupes de recherche à travers le monde. Dans cette méthode, une solution contenant du fer est utilisée comme précurseur. Le précurseur est ensuite converti en petites gouttelettes à l'aide d'un atomiseur et transféré sur un substrat chauffé. Lorsque le précurseur se trouve sur le substrat, il subit des réactions chimiques qui conduisent à sa décomposition et un film est formé.

Une large gamme de précurseurs de fer peut être utilisée dans cette méthode. Différentes concentrations d'agents dopants peuvent également être ajoutées au précurseur de départ ou utilisées comme précurseurs. Les films produits par cette méthode ont relativement une bonne microstructure et fournissent une haute surface interne permettant la pénétration de l'électrolyte dans la photoélectrode d'hématite poreuse.

Comme le dépôt est effectué à des températures d'environ 450 °C, il n'y a pas besoin d'une étape supplémentaire de recuit. La pyrolyse par pulvérisation est une technique très rapide et polyvalente et permet le dépôt de films translucides sur différents substrats. Cependant, l'un des problèmes communs de cette méthode est le colmatage du jet atomiseur qui augmente les coûts de maintenances de l'appareil de dépôt.

II.5.3 Dépôt chimique en phase vapeur (CVD)

Le dépôt chimique en phase vapeur a été la première méthode utilisée dans la préparation de photoélectrodesd'hématite par Hardee et Bard [22,23] en 1976 et 1977. Il est très similaire à la pulvérisation par pyrolyse sur plusieurs aspects, mais leur différence fondamentale est que les réactions dans CVD prennent placer dans la phase gazeuse ; le précurseur subit unedécomposition avant d'atteindre le substrat et les particules du matériau de film souhaité sont déposées sur le substrat.La pyrolyse par pulvérisation a été la méthode de dépôt préférée pour la production d'hématiteen raison de la simplicité de l'appareil de dépôt et de la disponibilité des matériaux de démarrages.

Cependant, les résultats sans précédent rapportés par Cesar et al.[30] ont renouvelé l'intérêt pour la fabrication de photoélectrodes à hématite en utilisant la CVD à pression atmosphérique (APCVD). L'une des raisons de l'amélioration récente de la performance PEC est considérée à cause de la nanostructure dendritique unique des films d'hématite préparés par cette technique. Le principal avantage de cette méthode est que l'appareil est encore plus simple que la technique de pyrolyse par pulvérisation.

Un inconvénient majeur de l'APCVD des films d'hématite est le nombre limité de précurseurs de fer adapté à cette technique, car il nécessite un matériau avec une pression de vapeur suffisamment élevée à la température ambiante. Toutefois, d'autres types de CVD comme la CVD assisté par les aérosols (AACVD) présentent un grand degré de flexibilité dans la sélection de matériaux de départ tout en préservant l'avantage de simplicité de l'APCVD.

II.6. Technique de préparation à haute température

II.6.1 APCVD

Les procédés CVD réalisés à pression atmosphérique sont généralement connus sous le nom de APCVD. Dans cette méthode, le matériau de départ doit posséder une pression de vapeur suffisamment élevée à la pression atmosphérique afin de fournir un taux de dépôt satisfaisant. Certains précurseurs de l'APCVD sont chauffés à des températures supérieures à la température ambiante afin d'atteindre pression de vapeur adéquate pour le dépôt. Certains réactifs dans les réacteurs à pression atmosphérique doivent être fortement dilués avec des gaz inertes pour empêcher la précipitation en phase vapeur. Les réacteurs sous pression atmosphérique sont raisonnablement simples et peu coûteux.

II.6.2 AACVD

AACVD offre une meilleure capacité et flexibilité que le procédé CVD classique,en particulier pour la fabrication de composés multi composants avec une stœchiométrie bien contrôlée. Des produits chimiques peu coûteux et respectueux de l'environnement peuvent être utilisés comme précurseurs, ce qui est important pour la production à grande échelle ou en série. En outre, l'AACVD a généralement un taux de dépôt plus élevé et un coût global inférieur à celui de la méthode CVD classique.

Comparée aux méthodes CVD classiques, la technique AACVD présente les principaux avantages suivants[31, 32]:

i. Un plus large choix et la disponibilité de précurseurs pour les produits CVD de haute qualité à faible coût, qui sont un problème critique pour la production de masse.

ii. Simplification de la livraison et de la vaporisation des précurseurs via la génération d'un aérosol précurseur.

iii. Taux de dépôt élevé, qui peut être obtenu à partir d'un taux de transport de masse élevédu précurseur et l'amélioration possible de la sélection des précurseurs.

iv. Un environnement de réaction plus flexible (AACVD peut être utilisé sous basse pression, pression atmosphérique, ou même dans une atmosphère ouverte).

v. Simplification de la synthèse de produits multicomposants avec contrôle précis de la stœchiométrie.

La génération d'aérosols à ultrasons est la méthode la plus courante dans le procédé AACVD. Un générateur d'aérosol à ultrasons a un transducteur piézoélectrique placé sous la solution précurseur. Lorsqu'un champ électrique à haute fréquence est appliqué, le transducteur vibre et provoque la formation de fines gouttelettes[33]. La taille moyenne des particules atomisées ou nébulisées (d_h) est liée à la tension superficielle (T), la densité (σ) et la fréquence (f). Laformule suivante est utilisée pour déterminer la taille des gouttelettes [34]:

$$\boldsymbol{d_h = 0.73 \frac{\sqrt{T}}{\infty f^2}} \dots\dots\dots\dots\dots\dots\dots\dots\dots\dots \mathbf{17}$$

L'équation 17 suggère que lorsque les caractéristiques physiques d'un liquide précurseur sont connues, le diamètre des gouttelettes d'aérosol est seulement une fonction inverse de la fréquence ultrasons. Une fréquence ultrasonique plus élevée sera nécessaire pour obtenir des gouttelettes plus fines. La génération ultrasonique offre des avantages en termes de fourniture d'une taille de gouttelette appropriée pour le processus AACVD[35].

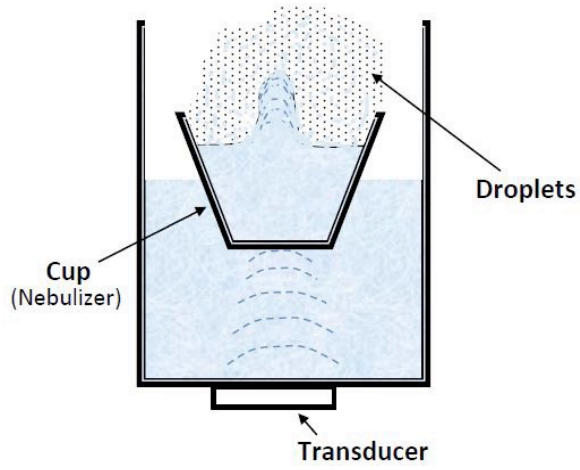

Figure II.13 Schéma du générateur ultrasonique d'aérosol [36]

Les gaz vecteurs sont utilisés pour aider à la délivrance de l'aérosol généré et son transport deà la zone de réaction. L'argon et l'azote sont les vecteurs inertes les plus couramment utilisésgaz, tandis que l'air comprimé est également utilisé pour le dépôt de produits d'oxydes. Des gaz réactifs comme H_2 peuvent également être introduits à ce stade avec d'autres gaz vecteurs primaires pour aider la réaction CVD ultérieure [37].

II.7 Technique de préparation à basse température :

Une approche de préparation d'électrode hématite nanostructurée est de fabriquer des films amorphes à basse température, puis les recuire à des températures plus élevées pour obtenir des électrodescristallines. Le principal avantage des méthodologies à basse température est le meilleur contrôle de la formation du film en raison des basses températures des procédés. Ces méthodes de fabrications sont facilement transposables à l'échelle industrielle. La perspective intéressante de cette approche est le potentiel de réduire la consommation d'énergie à l'étape post recuit par l'introduction de l'irradiation par micro-ondes. L'objectif principal de cette approche est de conserver la nanostructure du film amorphe tout en augmentant la cristallinité des électrodes d'hématite.

II.7.1. Méthode et principe de l'électrodéposition

Le but de l'électrodéposition est d'appliquer une couche superficielle sur un métal pour conférer à cette surface les différentes propriétés désirées. L'électrodéposition est une réaction d'oxydoréduction qui est déclenchée par une source de courant. Le bain d'électrolyse contient le sel métallique approprié, le substrat (électrode de travail) sur lequel doit s'effectuer le dépôt et l'électrolyte dans lequel il baigne les ions métalliquesM^{n+} de charge positive. La polarisation des électrodes va provoquer une migration de ces ions vers la cathode où l'ion métallique est neutralisé par les électrons fournis par la cathode et se dépose sur celle-ci sous forme de métal M suivant la réaction :

$$M^{n+} + ne^- \leftrightarrow M \quad \ldots\ldots\ldots\ldots\ldots\ldots\ldots 18$$

La réduction de l'ion M^{n+} et l'oxydation de l'atome métallique *M* se produisent simultanément. L'équation susmentionnée est associée un potentiel d'équilibre qui suit la loi de Nernst, à savoir :

$$E_{eq} = E_0 + \frac{RT}{nF} \times ln\left(\frac{a_{ox}}{a_{red}}\right) \quad \ldots\ldots\ldots\ldots\ldots\ldots 19$$

Où

E: le potentiel standard du couple ox/red (*V*),

R: la constante des gaz parfaits (8.314 $J.K^{-1}.mol^{-1}$),

T: la température à laquelle s'effectue la réaction (*K*),

n: le nombre d'électrons mis en jeu,

F: la constante de Faraday (96485,338 *C / mole d'électrons*),

a: l'activité du réactif ou du produit (a=γ *concentration [mol.l^{-1}], où γ n'est que très rarement égal à un.

On confond cependant très souvent activité et concentration).

Lorsque l'on soumet l'électrode métallique à un potentiel *E* différent du potentiel *Eeq*, on favorise la réactionsoit dans le sens 1 de la réduction, soit dans le sens 2 de l'oxydation. En particulier, lorsque le potentiel appliqué est inférieur à *Eeq*, il y a réduction de l'ion métallique en solution et dépôt du métal sur l'électrode. La différence de potentiel entre le potentiel de l'électrode et le potentiel d'équilibre est appelée la surtension. Elle s'exprime de la manière suivante :

$$\boldsymbol{\eta = E_1 - E_{eq}} \quad \ldots\ldots\ldots\ldots\ldots\ldots\ldots\ldots\ldots\ldots \mathbf{20}$$

Où E : le potentiel appliqué (*V*), i: le courant d'électrolyse, considéré négatif par convention dans le cas d'une réduction (*A*).

II.7.2 Autres méthodes

La synthèse à basse température de nanostructures d'hématite à partir de solutions chimiques est largement étudiée et, par conséquent, des méthodes viablespour la fabrication d'une large gamme de nanostructures d'hématites ont été développées, comprenant des nanoparticules [38], des nanocubes [39 ,40], des nanobattonnets [41] et des nanostructures en trois dimensions [42]. La synthèse hydrothermale comme méthode principale à basse température est une technique attrayante, car elle permet d'adapter la taille et la morphologie, un degré d'agglomération contrôlé, une incorporation réduite d'impuretés et une température de traitement relativement basse. Récemment, Tang et. al.[43] ont rapporté la fabrication de tiges d'hématites creuses et des microsphères en utilisant une solution de $FeCl_3$. Yang et. al.[44] ont produit avec succès plusieurs formes tridimensionnelles nanostructurées telles que des nanocubes d'hématites en utilisant un processus hydrothermal assisté par des anions avec recuit ultérieur. De plus, Almeida et. al.[45] ont présenté une méthode simple de production de nanostructures d'hématites avec des formes contrôlables en contrôlant la concentration de PO_4^{3-} dans les conditions hydrothermales.

Malgré tous ces succès, la fabrication de films minces directement à partir de solutions chimiques estrestée un défi jusqu'à présent. L'hématite, en particulier, est un matériau difficile à fabriqueren couches minces à partir de solutions chimiques puisque la formation

d'hydroxyde de fer en particulier FeOOH est favorisée dans de tels systèmes. En 2000, Pejova et. al.[46] a rapporté la préparation d'hématite en film mince en utilisant une méthode CBD (Chemical Bath Deposition). Le dépôt de film était essentiellement à la suite du traitement thermique d'une solution aqueuse de chlorure de fer (II) contenant de l'urée. Le produit chimique de la réaction globale du processus de dépôt a été suggéré pour conduire à la formation de $Fe_2O_3.H_2O$ selon les réactions suivantes:

$$\boldsymbol{2Fe^{3+} + NH_2CONH_2 + 5H_2O \rightarrow Fe_2O_3.H_2O + 2NH^{4+} + CO_2 + 4H^{+}} \ldots\ldots\ldots\ldots\ldots\ldots \boldsymbol{21}$$

Le dépôt a été effectué à 90-100 °C et donc l'urée a été décomposée en CO_2 et NH_3. À la suite de ce traitement de vieillissement en milieu aqueux, $Fe_2O_3.H_2O$ a été converti en FeOOH. Afin d'obtenir l'hématite, les films ont subi un recuit à 300-400 °C.

Références chapitre 2

[1] Honda Kenichi, J. Photochem. Photobiol., A: Chem. 166 (2004) 63–68.
[2] ZhangShanqing,WenWilliam,JiangDianlu,ZhaoHuijun,JohnRichard,Wilson Gregory J., Will Geoffrey D., J. Photochem. Photobiol., A: Chem. 179 (3) (2006) 305-313.
[3] K.Rajeshwar, N.R. De Tacconi, C.R. Chenthamarakshan, Curr. Opin. Solid State Mater. Sci. 8 (2004) 173–182.
[4] Viseur, Mathieu, Mémoire de Fin d'Etudes, « Etude de faisabilité de l'utilisation de l'hydrogène comme vecteur alternatif d'énergie », Université Libre de Bruxelles, (2007).
[5] B. Chavillon, Thèse de Doctorat, « Synthèse et caractérisation d'oxydes transparents conducteurs de type p pour application en cellules solaires à colorant ». Material chemistry. Université de Nantes, (2011).
[6] Bolton, J. R.; Sol. Energy 1996, 57, 37-50.
[7] Murphy, A. B.; Barnes, P. R. F.; Randeniya, L. K.; Plumb, I. C.; Grey, I. E.; Horne, M. D.; Glasscock, J. A.; Int. J. of Hydrogen Energy 2006, 31, 1999-2017.
[8] Bak, T.; Nowotny, J.; Rekas, M.; Sorell, C. C.; Int. J. of Hydrogen Energy 2002, 27, 991-1022
[9] Anderman, M.; Kennedy, J. H.; Semiconductor electrodes: Iron oxide (Fe2O3)," In Studies in Physical and Theoretical Chemistry, Finklea, H. O., Ed.; Elsevier Science: Amsterdam, Netherlands, 1988, pp 147-202
[10] Domen, K.; Naito, S.; Onishi, T.; Tamaru, K.; Chem. Phys. Lett. 1982, 92, 433-438
[11] Kamat, P. V.; Dimitrijevic, N. M.; Sol. Energy 1990, 44, 83-98.
[12] Kamat, P. V.; J. Phys. Chem. C 2007, 111, 2834-2860.
[13] Reber, J. F.; Rusek, M.; J. Phys. Chem. 1986, 90, 824-834.
[14] Hardee, K. H.; Bard, A. J.; J. Electrochem. Soc. 1976, 123, 1024-1026
[15] Hardee, K. H.; Bard, A. J.; J. Electrochem. Soc. 1977, 124, 215-224.
[16]Quinn, R. K.; Nasby, R. D.; Baugham, R. J.; Mater. Res. Bull. 1976, 11, 1011-1017
[17]Almeida, T. P.; Fay, M.; Zhu, Y. Q.; Brown, P. D.; J. Phys. Chem. C 2009, 113, 18689–18698.
[18] Kennedy, J. H., Frese, Jr., K. W.; J. Electrochem. Soc. 1978, 125, 709-714.
[19]Shinar, R.; Kennedy, J. H.; Sol. Energy Mater. 1982, 6, 323-335.
[20] Merchant, P.; Collins, R.; Kershaw, R.; Dwight, K.; Wold, A.; J. Solid State Chem. 1979, 27, 307-315.
[21] Beermann, N.; Vayssieres, L.; Lindquist, S. –E.; Hagfeldt, A.; J. Electrochem. Soc. 2000, 147, 2456-2461.
[22]Khan, S. U. M.; Akikusa, J.; J. Phys. Chem. B 1999, 103, 7184-7189.
Fujimori, A.; Saeki, M.; Kimizuka, N.; Taniguchi, M.; Suga, S.; Phys. Rev. B 1986, 34, 7318-7328.
[23] Lindgren, T.; Wang, H.; Beermann, N.; Vayssieres, L.; hagfeldt, A.; Lindquist, S. –E.; Sol. Energy Mater. Sol. Cells 2002, 71, 231-243
[24] http://www.geocities.jp/ohba_lab_ob_page/Structure/Hematite_bond.JPG (Accès le 20 Novembre 2016).
[25] Catti, M.; Valerio, G.; Dovesi, R.; Phys. Rev. B 1995, 51, 7441-7450.

[26] Cornell, R. M.; Schwertmann, U.; The Iron Oxides: Structure, Properties, Reactions, Occurrences and Uses, Wiley VCH Verlog GmbH & Co.: KGaA Weinheim, Germany, 2003
[27] Anderman, M.; Kennedy, J. H.; Semiconductor electrodes: Iron oxide (Fe2O3),” In Studies in Physical and Theoretical Chemistry, Finklea, H. O., Ed.; Elsevier Science: Amsterdam, Netherlands, 1988, pp 147-202.
[28] Satsangi, V. R.; Kumari, S.; Singh, A. P.; Shrivastav, R.; Dass, S.; Int. J. Hydrogen Energy 2008, 33, 312-318.
[29] Leygraf, C.; Hendewerk, M.; Somorjai, G. A.; J. Solid State Chem. 1983, 48, 357-367.
[30] Cesar, I.; Kay, A.; Gonzalez Martinez, J. A., Grätzel, M.; J. Am. Chem. Soc. 2006, 128, 4582–4583.
[31]Xu, C. Y.; Hampden-Smith, M. J.; Kodas, T. T.; Chem. Mater. 1995, 7, 1539-1546.
[32] Palgrave, R. G.; Parkin, I. P.; J. Am. Chem. Soc. 2006, 128, 1587-1597.
[33] Choy, K.-L.; In Handbook of Nanostructured Materials and Nanotechnology, Vol. 1: Synthesis and Processing, Nalwa, H. S., Ed.; Academic Press: San Diego, CA, 2000, pp 533–577.
[34] Lang, R. J.; J. Acoust. Soc. Am. 1962, 34, 6-8.
[35] Rodes, C.; Smith, T.; Crouse, R.; Ramachandran, G.; Aerosol Sci. Technol. 1990, 13, 220-229
[36] Renault, O.; Labeau, M.; J. Electrochem. Soc. 1999, 146, 3731-3735.
[37] Glerup, M.; Kanzow, H.; Almairac, R.; Castignolles, M.; Bernier, P.; Chem. Phys. Lett. 2003, 377, 293-298.
[38] Dong, W. T.; Zhu, C. S.; J. Mater. Chem. 2002, 12, 1676– 1683.
[39] Ma, J.; Lian, J.; Duan, X.; Liu, X.; Zheng, W.; J. Phys. Chem. C 2010, 114, 10671-10676.
[40] Hamada, S.; Matijivic, E.; J. Colloid Interface Sci. 1981, 84, 274–277.
[41] Wang, X.; Chen, X. Y.; Gao, L. S.; Zheng, H. G.; Ji, M. R.; Tang, C. M.; Shen, T.; Zhang, Z. D.; J. Mater. Chem. 2004, 14, 905– 907.
[42] An, Z. G.; Zhang, J. J.; Pan, S. L.; Yu, F.; J. Phys. Chem. C 2009, 113, 8092–8096.
[43] Zeng, S. Y.; Tang, K. B.; Li, T. W.; Liang, Z. H.; Wang, D.; Wang, Y. K.; Zhou, W. W.; J. Phys. Chem. C 2007, 111, 10217– 10225.
[44] Zhang, F. H.; Yang, H. Q.; Xie, X. L.; Li, L.; Zhang, L. H.; Yu, J.; Zhao, H.; Liu, B.; Sens. Actuators B 2009, 141, 381–389.
[45] Almeida, T. P.; Fay, M.; Zhu, Y. Q.; Brown, P. D.; J. Phys. Chem. C 2009, 113, 18689–18698.
[46] Pejova, B.; Najdoski, M.; Grozdanov, I.; Isahi, A.; J. Mater. Sci. Mater. Elect. 2000, 11, 405-409.

Chapitre III

Techniques d'élaboration et Caractérisations Utilisées

A. Élaboration d'une couche d'oxyde de Fer

1. La voie électrochimique « Électrodeposition »

Lors de l'électrodéposition, un revêtement métallique est électrodéposé sur la cathode d'une cellule électrolytique constituée d'une électrode positive (anode), d'une électrode négative (cathode) et d'un électrolyte solution (contenant les ions métalliques) à travers laquelle circule le courant électrique. En contrôlant avec soin le flux d'électrons, le poids du matériau déposé peut être mesuré selon la loi d'électrolyse de Faraday [1].Les principales variables d'électrodéposition comprennent la densité de courant, la distribution du courant, le pH, la température, l'agitation et la composition de la solution. Un procédé typique de galvanoplastie consiste entrois types d'électrodes et d'électrolytes (Fig.III-1) :

- L'électrode auxiliaire (compteur): c'est une électrode qui aide à faire passer le courant àtravers la cellule; le courant passe de WE et de CE; généralement aucun processus d'intérêt ne se produit à la surface de la CE; exemple: fil de Pt.
- L'électrode de référence (ER): c'est une électrode qui peut maintenir un potentiel constant en changeant les conditions expérimentales; le potentiel WE est référencé par rapport au potentiel ER; les ER sont typiquement des anodes dans des cellules électrochimiques; exemple: NHE.
- L'électrode de travail (WE) / Indicateur Électrode: c'est typiquement unecathode; exemple: électrode sélective aux ions ou métal noble.
- L'électrolyte de support: c'est une substance ionique (généralement un sel) qui assure la conduction; exemple: KCl. L'électrolyte de support réduit la migration; il ne subit pas de chimie redox, et donc ses ions sont appelés ions spectateurs. Parfois, l'électrolyte de support est appelé simplement l'électrolyte.

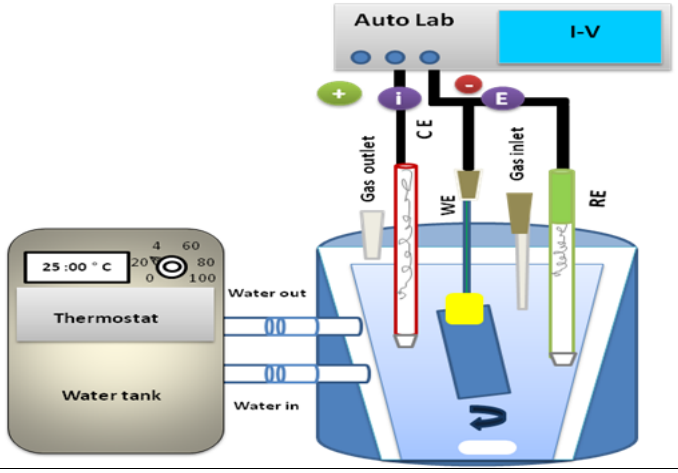

FigureIII-1. Représentation schématique de cellules électrochimiques à trois électrodes.

2. La voie hydrothermale

Le processus hydrothermal (Fig. III-2) met en jeu une réaction hétérogène qui requiert la présence de solvantsaqueuxsoushautepressionetàhautetempératurepourladissolutionetla recristallisationdematériauxquisontrelativementinsolublesdanslesconditionsordinaires.Il s'agit d'un procédé régulièrement utilisé lors de la synthèse de couches avec une composition de phasesparticulières.La voie hydrothermalepeutégalementêtreutiliséepourlasynthèsedenanocristaux,oupourla conception de matériaux destinés à une application spécifique.

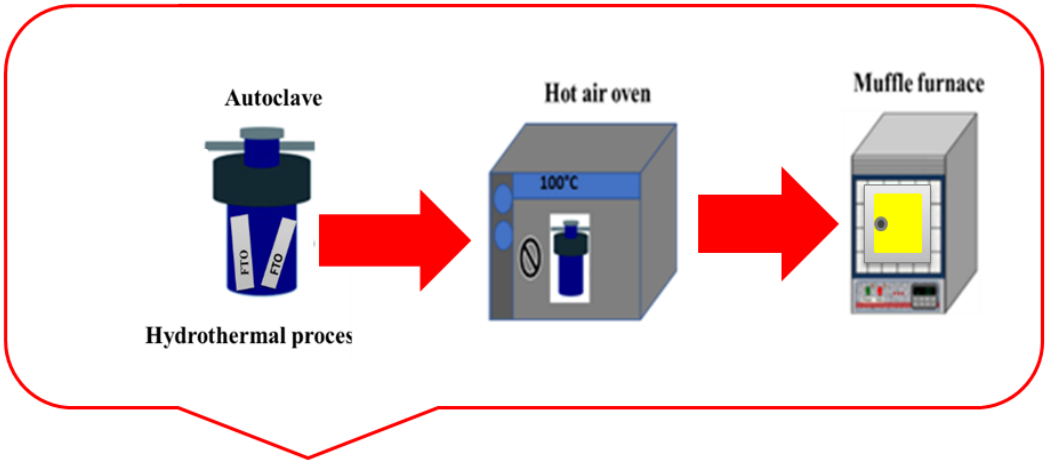

Figure 2. Représentation schématique de processus hydrothermal.

Lesnanoparticulesobtenuesau cours du processushydrothermalpeuventsubiruntraitement supplémentairedemanièreàmodifierlataille,la morphologieetlastructurecristallinedesnanoparticules.Lasynthèsehydrothermalemetenjeu différents mécanismes :

- Un phénomène de dissolution-cristallisation qui assure le transport de matière via la solution: c'est le cas de la ''maturation'' d'Ostwald qui entraîne unecroissance secondaire desparticules.Danslecasoùleprécipitéinitialn'estpaslaphasethermodynamiquement stable, un nouveau régime de nucléation (le plus souvent hétérogène) et de croissance se met en place et conduit à la nouvelle phase.
- Unréarrangementàl'étatsolidequientraînelaréorganisationlocaledela structureinitiale,parexemple,commelacristallisationd'unephaseamorpheoula déshydratation d'un hydroxyde.

- Une agrégation de particules primaires qui peut contribuer à abaisser l'énergie interfaciale et à accroître fortement la taille des particules finales. Ce dernier mécanisme est actuellementl'objetd'unecontroversepoursavoirs'ilpermetd'obtenirunedispersion.
- l'agrégationpeutêtreparfoisordonnéeetconduireàlaformationdemonocristauxpar éliminationdesjointsdegrains(liaisonchimiqueentrelessurfacesourecristallisationdes zones de joints).

3. Le recuit

Le recuit a un effet important surles propriétés physiques des couches minces.L'effet du recuit à l'air à des températures comprises entre450 et700°C a été étudié.Une température optimale de 550 °C a été obtenue (voir figure III-3). La figure 3 montre le profildu recuit ; on observe deux lignes (rouge et noire), larouge correspond àla température maximale et la noire à la température requise, t_2 représente le temps pendant lequel nous devons atteindre la température requise (550 °C), t_3 le temps où la température reste constante pendant 4 heures et $t_4$au le temps de chute de la température. Les films tels que déposés ont été recuits à 550 °C à l'air. Après le recuit le film apparait uniformément rouge.

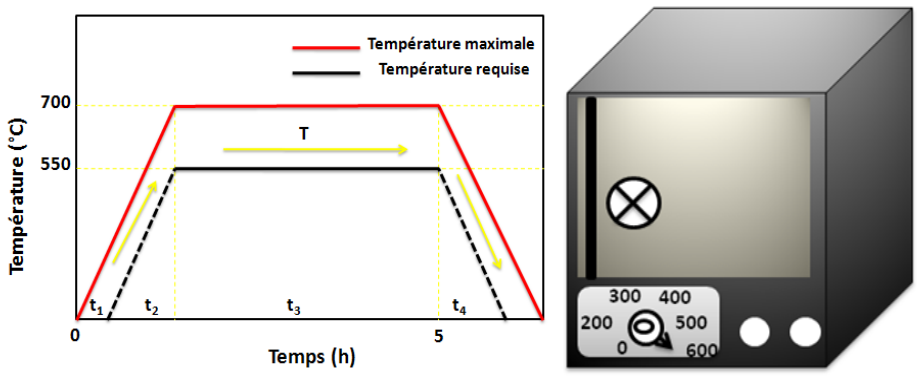

Figure 3. Schéma de principe du processus de recuit.

B. Méthode d'analyse

1 Spectroscopie UV-visible

La spectroscopie optique UV-visible (UV-vis) permet de mesurer l'absorption des photons par le matériau. Dans ce travail, les spectres UV-vis ont été enregistrés en utilisant un

spectrophotomètre haute résolution (HR 4000-vis-NIR). La lampe est utilisée comme source d'excitation. Un détecteur mesure ensuite la transmission et l'absorbance de l'échantillon. La lumière transmise traverse l'échantillon avant d'être détectée, tandis que l'absorbance est une mesure de la lumière absorbée par l'échantillon.

2 . Analysepardiffraction des rayons X (DRX)

La diffraction des rayons X est largement utilisée pour caractériser les matériaux cristallins. C'est un outil qui permet d'identifier les différentes phases cristallines présentes dans les matériaux solides ou en poudre. L'interférence constructive de deux ondes X donne le diagramme de diffraction des RX (Fig.III-4)

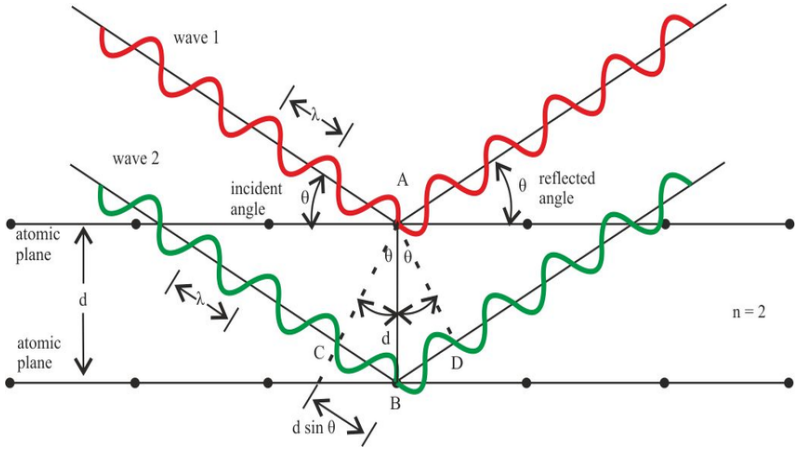

Figure III-4 : Représentation schématique de la diffraction des rayons X par un cristal (loi de Bragg)

La relation générale entre la longueur d'onde des rayons X incidents, l'angle d'incidence et l'espacement entre les plans cristallins des atomes est connue sous le nom de loi de Bragg et s'exprime comme suit:

$$\mathbf{n\lambda = 2d\ sin\theta} \qquad (\mathbf{1})$$

où $\boldsymbol{n}$ est l'ordre de diffraction, $\boldsymbol{\lambda}$ est la longueur d'onde des rayons X incidents, $\boldsymbol{d}$ est l'espacement interplanaire du cristal et $\boldsymbol{\theta}$ est l'angle d'incidence. Étant donné que dans un cristal les atomes sont disposés de façon périodique, les ondes diffractées seront constituées de maxima d'interférence (pics) avec la même symétrie que dans la distribution des atomes. Le diagramme de diffraction des RX permet donc de déterminer la distribution des atomes dans un cristal. La diffraction des RX peut non seulement être utilisée pour identifier la phase cristalline d'un matériau par comparaison aux données provenant de structures connues, mais aussi dequantifier les changements dans les paramètres cellulaires, l'orientation cristalline, la taille des cristallites et d'autres paramètres structuraux. La taille moyenne des cristallites peut

être estimée à partir du diagramme de diffraction des RX en utilisant l'équation de Scherrer [2,3] :

$$D = \frac{K\lambda}{\beta cos\theta} \ldots\ldots\ldots\ldots\ldots\ldots\ldots\ldots\ldots\ldots (2)$$

Où β est l'élargissement de la ligne à mi-hauteur (FWHM, après prise en compte de l'élargissement de l'instrument), K est la constante de Scherrer qui est d'environ 0.9, λ est la longueur d'onde incidente et D est taille de la cristallite.

3 .Microscopie électronique à balayage à émission de champ (FESEM)

FESEM est une technique utilisée pour obtenir des informations topographiques et morphologiques sur un échantillon (voir figure III-5). Dans la mesure MEB, l'échantillon à étudierest bombardé par un faisceau d'électrons. L'électron d'un faisceau incident excite un électron du matériau qui quitte l'échantillon s'il a une énergie suffisante (appelée électron secondaire) ou est dispersé (appelé électron rétrodiffusé). Les électrons secondaires et rétrodiffusés sont détectés par deuxdétecteurs différents. Les électrons secondaires proviennent généralement de la surface de l'échantillon.

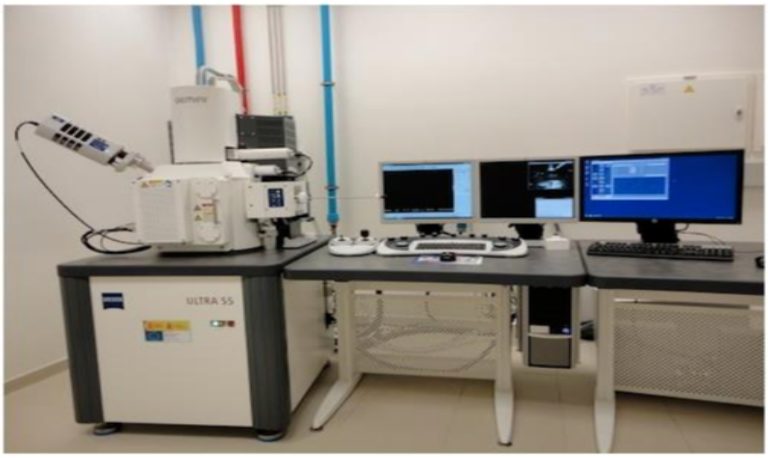

Figure III-5. Image de la microscopie électronique à balayage (FESEM), un Zeiss ULTRA 55

S'ils proviennent profondément del'intérieur de l'échantillon, les électronsperdront suffisamment d'énergie en transit vers la surface etne pourront quitter l'échantillon. Le nombre d'électrons détectés change en fonction de l'orientation de la surface. En raison de la variation du nombre d'électrons détectés, la luminosité du moniteur change, ce qui donne une image tridimensionnelle. En revanche, les électrons diffusés en arrière possèdent des énergies

différentes selon qu'ils sont dispersés à partir d'un noyau plus lourd ou plus léger. Les électrons dispersés à partir d'un noyau plus lourd ont une énergie plus élevée que ceux dispersés à partir d'un noyau plus léger, et ainsi l'image de l'élément noyau plus lourd apparaît plus brillante [4]. Dans notre étude,la MEB a été réalisée sur des couches minces déposées sur substrat de FTO, à l'aide de Zeiss ULTRA 55 Excel équipé d'un canon à émission de champ de 30 kV.

4. Spectroscopie à dispersion d'énergie (EDS)

La spectroscopie à dispersion d'énergie (EDS) permet une mesure quantitative de la composition élémentaire d'un échantillon. Spécifiquement, lorsqu'un électron incident entre en collision avec un électron atomique interne, l'électron du noyau est éjecté, laissant un vide. Un électron de la coque externe remplit le vide laissé par l'électron de base et un photon X est émis.Les tensions de fonctionnement typiques dépendent de la profondeur de l'échantillonà sonder. Cette profondeur peut être estimée en utilisant un logiciel utilisant des simulations de Monte-Carlo. Des tensions de fonctionnement plus élevées permettent également d'inclure des pics d'énergie plus élevés, ce qui augmente la précision de la caractérisation. La précision de la caractérisation est augmentée par des temps d'acquisition plus longs, des détecteurs de résolution plus élevée.

5. Microscopie à force atomique (AFM)

Un microscope à force atomique est capable de fournir une image tridimensionnelle de la surface et est donc très utile pour caractériser la topographie de surface (voir figure III-6). Dans un AFM, on utilise un porte-à-faux avec un bout pointu (quelques centaines de nanomètres de diamètre) composé de Si ou de SiO_2. En raison de la variation topographique, le porte-à-faux dévie et la déviation est mesurée en utilisant un faisceau laser réfléchi par le porte-à-faux. Si le laser change de position en raison de la force sur le cantilever, une tension est appliquée à la piézoélectrique pour faire revenir le laser à son origine. La force sur le porte-à-faux dépend des caractéristiques de surface del'échantillon. La pointe est maintenue en contact continu ou alterné avec la surface de l'échantillon et le porte-à-faux se déplacesur l'échantillon à l'aide d'un contrôleur piézoélectrique. La hauteur de la pointe change pendant le mouvement du porte-à-faux et l'amplitude de la déviation est tracée en fonction de la position de la pointe sur la surface qui crée une carte topographique de la surface. [5]

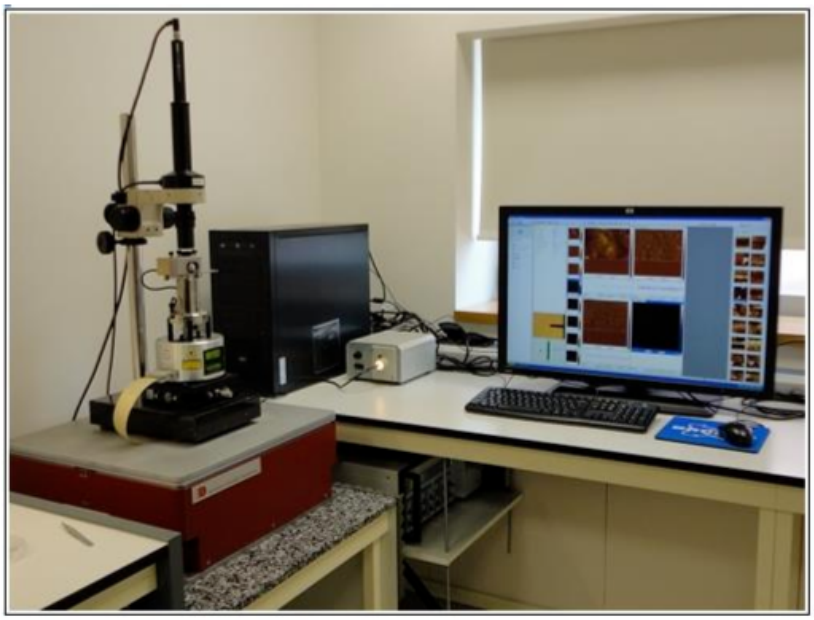

Figure III-6. Images de la microscopie à force atomique multimode 8 de Bruker (AFM)

6. Analyse par microscopie électronique à transmission (TEM)

Le TEM est une technique de microscopie dans laquelle un faisceau d'électrons est transmis sous vide à travers un échantillon mince. Il est capable de se concentrer sur une seule nanoparticule pour identifier directement sa morphologie, sa structure cristalline et sa composition chimique. Le principe du TEM est similaire à celui d'un projecteur de diapositives: lorsque le faisceau d'électrons traverse l'échantillon, seules certaines parties sont transmises, formant une image de contraste qui passe à travers une lentille grossissante puis est projetée sur un écran fluorescent ou est détectée par une caméra à dispositif de couplage chargé (CCD). La figure III-7 montre une photographie et un diagramme schématique d'une installation de TEM. La cathode du canon à électrons, qui est souvent faite à partir de filament de tungstène, est chauffée par un courant élevé pour produire un flux d'électrons. Ceux-ci sont accélérés par un champ de 100-300 keV et, lorsqu'ils voyagent dans la colonne, la tension croissante augmente leur énergie cinétique et diminue la longueur d'onde effective. Les lentilles du condenseur sont responsables de la formation du faisceau primaire et de la focalisation du faisceau sur un petit cylindre, tandis que l'ouverture du condenseur élimine les électrons diffusés aux grands-angles. Le faisceau frappe l'échantillon sur le porte-échantillon et une grande partie de celui-ci est transmise, agrandie et focalisée par l'objectif et ensuite par les lentilles du projecteur. Enfin, un écran fluorescent ou CCD est utilisé pour former une image.

Le TEM est capable de créer des motifs de diffraction à partir d'une zone minuscule, appelée Diffraction de zone sélectionnée (SAD); en agissant surles réglages de la lentille ducondenseur, la SAD peut aller de quelques centaines de nanomètresnm à un nanomètre de diamètre.

Figure III-7. Image de la microscopie électronique à transmission (TEM) JEOL JEM 2100F

La microanalyse aux rayons X par dispersion d'énergie (EDX) est utilisée pour mesurer les rayons X émis lors d'un bombardement électronique dans un MET afin de définir la composition chimique des matériaux sur les nano et micro-échelles. Les éléments présents dans l'échantillon sont déterminés à partir des énergies de rayons X émis par la zone excitée par le faisceau d'électrons. La proportion de détection des rayons X caractéristiques donne une mesure des quantités des éléments présents dans l'échantillon. Les pourcentages de poids sont calculés en utilisant des énergies de crête spécifiques relatives aux coques d'énergie individuelles des atomes de chaque élément et les zones de pic sont déterminées en utilisant un étalon calibré interne, habituellement du cobalt. Les mesures MET des films minces rapportés dans ce travail ont été faites à l'aide d'un JEOL JEM2100F fonctionnant à 200 keV.

7. Analyse photoélectrochimique

7.1. Cellule, électrolyte et montage

Le composant principal de la cellule PEC est le semi-conducteur, qui convertit les photons incidents en paires électron-trou. Ces électrons et ces trous sont spatialement séparés l'un de l'autre en raison de la présence d'un champ électrique à l'intérieur du semi-conducteur, la figure III-8 montre un diagramme d'énergie simplifié qui constitue l'anode et une contre-électrode. Les deux électrodes sont interconnectées via une source de circuit externe. Lesunitésdebasedel'analyseurélectrochimiqueetphotoélectrochimiqueutilisé sont :

- Unecelluleenverred'unecontenancede100mletpossédantunhublotenquartz(qui contrairement au verre, laisse passer la lumière UV). Elle est positionnée perpendiculairement aufaisceauconformémentàlafigureIII-8.Elleestbaséesurunsystèmeàtroisélectrodes immergées dans la solution à analyser. Les trois électrodes sont :
    - Une électrode de travail: électrode de Fe_2O_3 de surface active égal à 1 cm^2.
    - Uneélectrodederéférence : électrodeAg/AgCl (3M KCl)
    - Une électrode auxiliaire (parfois aussi, appelée contre électrode) : électrode de Pt, elle assure le passage du courant dans le circuit électrique et sa mesure.
- Unpotentiostat/galvanostat Autolab detypePGSTAT302N (Metrohm, Netherlands) pilotéparunlogicielNova 10.
- Unelampeà Xe est utilisée pour l'illumination de films semi-conducteurs, d'intensité150Watts (PLSSXE 300/300UV) émettantprincipalementdansl'UV-A(domaine d'absorption du Fe_2O_3) et illumine la totalité de la surface de l'électrode.Divers filtres passe-bande à ondes longues sont situés entre la source de lumière et l'électrode échantillon [6],couplé par un chopper. L'ensemble du système estcontrôlé par un logiciel fait maison.
- La solution de l'électrolyte est composée de NaOH 0.1M (le volume de la solution est égal à 0.1L).

Lorsque des semi-conducteurs dopés ***n*** sont mis en contact avec un électrolyte, le courant circule jusqu'à ce que leurs potentiels électrochimiques soient équilibrés et que l'équilibre soit atteint. L'absorption de photons avec une énergie dépassant la bande interdite génère des paires électrons-trous proches de l'interface semi-conducteur/électrolyte. Dans le cas où le niveau de Fermi (E_F) se situe au-dessus du potentiel redox standard (Vo redox), les électrons seront retirés du semi-conducteur vers l'électrolyte, laissant derrière eux des charges positives. Une séparation de charge se produit lorsque les trous atteignent la surface et réagissent avec l'électrolyte. Le champ électrique est important en ce qui concerne le processus de séparation

des pairs électrons/trou photogénérés. L'ordre de charge dans l'électrolyte est souvent décrit dans les termes des couches de Helmholtz et Gouy-Chapman [7].

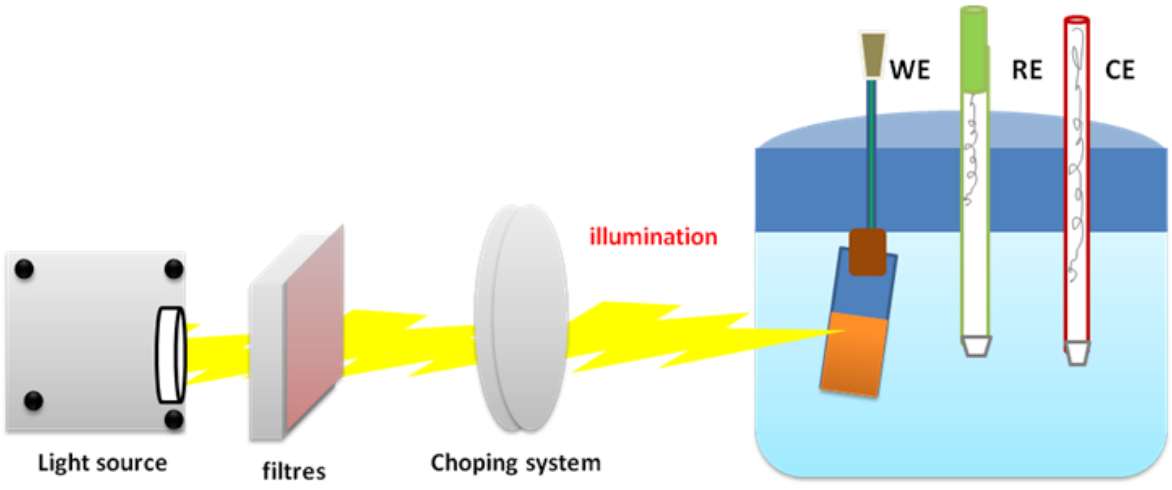

Figure III- 8. Diagramme schématique d'une cellule photoélectrochimique (PEC).

7.2. Techniques électrochimiques

Les méthodes électrochimiques peuvent être classées selon deux groupes distincts : les méthodes stationnaires et les méthodes nonstationnaires dites transitoires, dans notre cas on n'utilise que les méthodestransitoires.

- Techniques transitoires

Les différentes techniques transitoires se différencient les unes des autres par la forme du signal respectif appliqué : une impulsion, un balayage ou une modulation.

7.2.1. La chronoampérométrie

Lachronoampérométrieconsisteàimposeràl'électrodedetravailunpotentieletàenregistrer, en fonction du temps, le courant qui traverse l'interface électrode /électrolyte. Le choix de la tension d'excitation est dicté généralement par les courbes de polarisation I-E.

7.2.2.La méthode à balayage en potentiels: Voltamétrie cyclique

Les mesures de Voltamétrie cyclique reviennent à effectuer des balayages linéaires en potentielsautourd'unepositiondonnéeetd'observerleséventuellesapparitionset/ou disparitiondesphénomènesélectrochimiques(oxydationet/ouréduction).Lebalayagede–0.2 à 0 V avec une vitesse de50 mV/s^{-1}.

7.2.3. Voltampérométrie cyclique (CV) à un potentiel de bande plate et une densité de donneur déterminés

Comme décrit par Boschloo et Fitzmaurice, la voltamétrie cyclique peut être utilisée pour calculer les potentiels de bandes plates des électrodes dans l'électrolyte aqueux. Pour ce faire, il faut veiller à ce que la plage de potentiel soit telle que le film électrode soit toujours dans des conditions d'appauvrissement ; c'est-à-dire que le potentiel appliqué est plus positif que le potentiel debande plate (Vfb). Ils ont montré que le courant estune fonction approximativement linéaire du potentiel appliqué, dans les directions des balayages avant et inverse. De plus, le courant à un potentiel donné dépend linéairement de la vitesse de balayage. S'il n'y a pas de pics dus à des réactions électrochimiques, on peut supposer qu'il n'y a pas de courant faradique et que l'origine de ce courant doit donc être capacitive. La capacité différentielle (C) est donnée par

$$C = \frac{dQ}{dV} = I\frac{dt}{dV} = \frac{I}{v} \qquad (3)$$

Avec Qla charge, V le potentiel, I le courant et v(Vs^{-1}) la fréquence de balayage utilisée pour l'enregistrement de laC-V. Par conséquent, si la densité de courant est tracée en fonction de la vitesse de balayage à différents potentiels, la pente de ces diagrammes peut être considérée comme la capacité de la couche de charge spatiale à un potentiel donné (la capacité de l'électrode nanostructurée peut être calculée en utilisant l'équation ci-dessus).

Les données provenant des balayages avant des C-V sont utilisées pour calculer la capacité. Les relations linéaires sont obtenuesà des potentiels proches de Vfb. À partir des diagrammes de Mott-Schottky, la densité des donneurs $N_D$et le potentiel debandes plates peuvent être calculés en utilisant l'équation ci-dessous :

$$\frac{1}{{C_{SC}}^2} = \frac{2}{e\varepsilon\varepsilon_0 N_D {A_S}^2}\left(E - E_{fb} - \frac{KT}{e}\right) \text{Poursemi} - \text{conducteur de typen} \qquad (4)$$

$$\frac{1}{{C_{SC}}^2} = -\frac{2}{e\varepsilon\varepsilon_0 N_D {A_S}^2}\left(E - E_{fb} + \frac{KT}{e}\right) \text{Pour semi} - \text{conducteur de type p} \qquad (5)$$

Avec $e$la charge de l'électron,ε la constante diélectrique dusemi-conducteur, ε_o la permittivité duvide, A_S la surface de l'électrode de travail, $k$la constante deBoltzmann et Tla température.

7.2.4. IPCE

L'efficacité de conversion du photon incident (IPCE) est obtenue en mesurant le flux de photons incident provenant d'un monochromateur (TMc300, Bentham Instruments Ltd., Berkshire, Royaume-Uni) où on utilise une lampe àxénon de 300W. La lumière est calibrée en utilisant une photodiode au silicium. Les spectres de photocourant sont mesurés à un potentiel constant par rapport à Ag / AgCl en combinant un amplificateur à verrouillage (Bentham 485, Bentham Instruments Ltd., Berkshire, Royaume-Uni) avec un potentiostat intégré. Les lectures sont recueillies à des intervalles de 20 nm tandis que la lumière monochrome balaie l'intervalle spectral 360-680 nm.

$$\mathbf{IPCE}(\%) = \frac{\mathbf{1240}\cdot i_{photocurrent}\,(\mu A/cm^2)}{\lambda(\mathrm{nm})\cdot j_{photons}(\mu W/cm^2)} * \mathbf{100}\% \qquad \mathbf{(6)}$$

où$i_{photocurrent}$est la densité de photocourant, $\lambda(nm)$la longeureu d'onde de la lumière incidente, et$j_{photons}$ l'énergie des photons incidents par seconde et par cm^2.

8. Mesures de la caractéristique courant-tension (J-V)

L'efficacité d'une cellule solaire est évaluée à travers sa caractéristique courant-tension (J-V) qui fournit des informations quantitatives sur la qualité globale du dispositif et aide à identifier les problèmes au sein de la cellule solaire et ceux associés à ses contacts électriques. Une cellule solaire, lorsqu'elle n'est pas éclairée (c'est-à-dire dans l'obscurité), le courant dans une diode peut en outre être décrit par l'équation de la diode de Schokley [8], qui est donnée par

$$\boldsymbol{I_d = I_0(\exp\left(\frac{qV_d}{nKT}\right) - 1)} \qquad \mathbf{(7)}$$

Où$\boldsymbol{I_d}$ est le courant net circulant dans la cellule, $\boldsymbol{I_0}$ est le courant de saturation sombre (ou courant de fuite), $\boldsymbol{V_d}$ est la tension appliquée, $\boldsymbol{q}$ est la charge de l'électron, $\boldsymbol{n}$ est le facteur d'idéalité de la diode, $\boldsymbol{k}$ est la constante de Boltzmann et $\boldsymbol{T}$ est la température absolue. En revanche, lorsque la lumière est incidente sur la cellule solaire, le courant total est une superposition à la fois du courant d'obscurité et du courant généré par la lumière (I_L) [9].

$$\boldsymbol{I = I_d - I_L = I_0(\exp\left(\frac{qV}{nKT}\right) - 1) - I_L} \qquad \mathbf{(8)}$$

Les deux courants circulentdans des directions opposées dans la cellule solaire. Les électrons et les trous générés par la lumièrese déplacent à travers le circuit externe.Si au cours d'une mesure J-V unetension directe suffisamment grandeest appliquée, elle polarise la diode avant, puis les électrons et les trous surmontent la barrière de potentiel donnant naissance au courant de diode $\boldsymbol{I_d}$. Les équations (7) et (8) peuvent être utilisées pour tracerdes courbes J-V comme le montre la figure 9.La qualité d'une cellule solaire est mesurée en fonction de quatre paramètres de performance différents. Le premier paramètre est le courant de court-circuit J_{SC}, qui est équivalent à I_L dans l'équation (8). C'est le courant lorsque la cellule solaire est court-circuitée. Le courant de court-circuit résulte de la génération de porteurs de charge par la lumière et de la séparation de ces porteurs de charge par le champ électrique intégré. J_{SC}dépend de certains facteurs tels que le spectre et l'éclairement énergétique de la lumière, les propriétés optiques des matériaux formant la cellule solaire, son épaisseur, ainsi que la durée de vie des porteurs minoritaires dans la couche absorbante.Le second paramètre est la tension développée à travers la cellule solaire lorsqu'elle est en circuit ouvert, de sorte qu'aucun courant ne peut circuler. Cette tension est connue sous le nom de tension decircuit ouvert, V_{CO}. La tension en circuit ouvert dépend de plusieurs facteurs tels que la bande interdite de la couche active, le comportement de la diode dans l'obscurité, la densité de défauts à la jonction et les pertes parrecombinaison.

Le troisième paramètre de performance fourni par la mesure J-V est le facteur de remplissage, FF, c'estlerapport de la puissance de sortie maximale de la cellule solaire au produit de I_{SC}et V_{CO}, donné par :

$$\boldsymbol{FF = \frac{P_{max}}{I_{SC} \times V_{oc}} = \frac{V_{max} \times I_{max}}{I_{SC} \times V_{oc}} \ldots\ldots\ldots\ldots (9)}$$

Où I_{max} et V_{max} sont respectivement les valeurs de la tension et du courant au point de puissance maximale, comme illustré sur la Figure III-9. Le facteur de remplissage dépend également de la densité des défauts dans la masse du semi-conducteur et de la jonction, ainsi que des résistances shunt et série, présentes dans la cellule solaire. Le quatrième paramètre est l'efficacité de la cellule solaire, qui est le rapport de la puissance de sortie de la cellule solaire à la puissance incidente. L'efficacité d'une cellule solaire est donnée par:

$$\boldsymbol{\eta = \frac{P_{max}}{P_{in}} = \frac{V_{max} \times I_{max}}{incident\ solar\ radiation \times Area\ of\ solar\ cell} \ldots\ldots\ldots\ldots\ldots (10)}$$

Où ***FF*** est le facteur de remplissage (équation9) et P_{in} est la puissance incidente (provenant du soleil ou d'un simulateur solaire). Il est à noter que ces quatre paramètres peuvent dépendre du spectre utilisé pour la mesure ainsi que de la température. Les cellules solaires sont généralement mesurées à température ambiante et avec un spectre solaire AM 1.5.

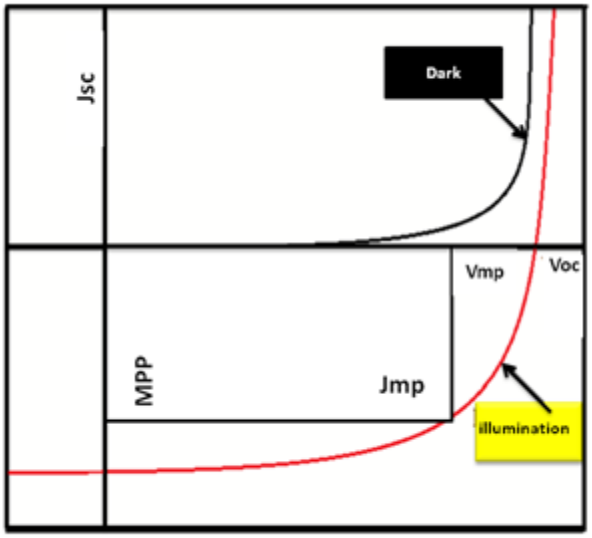

Figure III- 9. Exemple de courbes J-V pour une cellule solaire dans l'obscurité et pour la même cellule solaire sous éclairage.

Références chapitre 3

[1] Z.S. Pillai, P.V. Kamat: J. Phys. Chem. 2003, B107, 945.

[2] A. L. Patterson, Phys. Rev., 1939, 56, 978-982.

[3] J. I. Langford and A. J. C. Wilson, J. Appl. Crystallogr., 1978, 11, 102-113.

[4] Leamy, H. J. Charge collection scanning electron microscopy. Journal of Applied Physics, 53(6), R51-R80. (1982).

[5]Eaton, P., & West, P. Atomic force microscopy. Oxford University Press. (2010).

[6] Bak, A., Choi, W., & Park, H. (2011). Enhancing the photoelectrochemical performance of hematite (α-Fe2 O3) electrodes by cadmium incorporation. Applied Catalysis B: Environmental, 110, 207-215.

[7] A. J. Bard, L. R. Faulkner, Electrochem. Methods: Fundamental and Application, VHC, New York, USA 1995.

[8] Nelson, Jenny. Physics of Solar Cells. Imperial College Press, UK, 2008.

[9] Honsberg, C., & Bowden, S. (2010). Pvcdrom. Internet: http://pveducation. org/pvcdrom,[Jun 5, 2013].

Chapitre IV

Article 1:

Hydrothermal synthesis of Nanostructured Cr-doped hematite with enhanced Photoelectrochemical activity

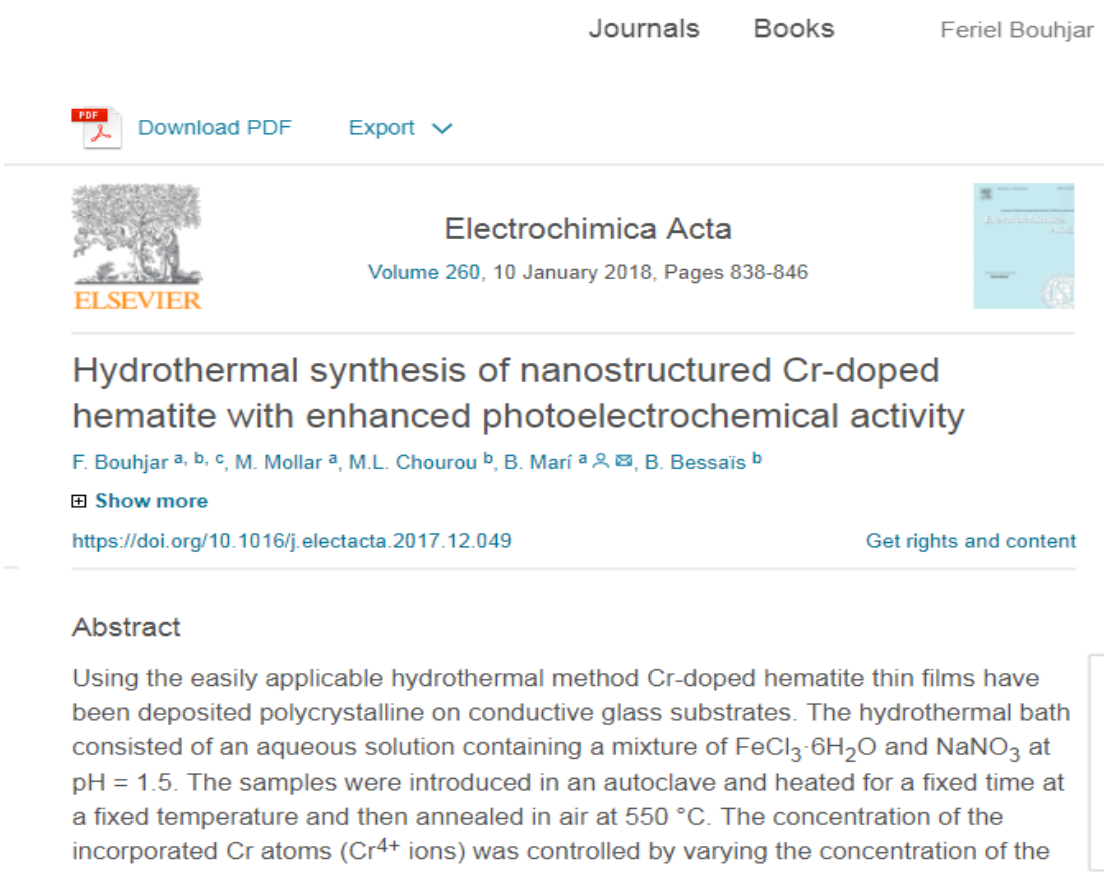

Hydrothermal synthesis of Nanostructured Cr-doped hematite with enhanced photoelectrochemical activity

Feriel Bouhjar[a, b,c,d], M.L. Chourou[b], M.Mollar[a], B. Marí[a] and B. Bessaïs[b]

a. *Institut de Disseny i Fabricació (IDF) - Departament de Física Aplicada, UniversitatPolitècnica de València, Camí de Vera s/n, 46022 València, Spain.*
b. *Photovoltaic Laboratory, Research and Technology Centre of Energy, Borj-Cedria Science and Technology Park, BP 95, 2050 Hammam-Lif, Tunisia*
c. *Ecole Nationale Supérieure d'ingénieurs de Tunis-ENSIT*
d. *University of Tunis*

Abstract

Using the easily applicable hydrothermal method Cr-doped hematite thin films have been deposited polycrystalline on conductive glass substrates. The hydrothermal bath consisted of an aqueous solution containing a mixture of $FeCl_3.6H_2O$ and $NaNO_3$ at pH = 1.5. The samples were introduced in an autoclave and heated for a fixed time at a fixed temperature and then annealed in air at 550ºC. The concentration of the incorporated Cr atoms (Cr^{4+} ions) was controlled by varying the concentration of the $Cr(ClO_4)_3$precursor solution, varied from 0 % to 20 %. All samples followed morphological and structural studies using field-emission scanning electron microscopy, high-resolution transmission electron microscopy and X-ray diffraction. Chronoamperometry measurements showed that Cr-doped hematite films exhibited higher photoelectrochemical activity than the undoped films. The maximum photocurrent density and incident photon conversion efficiencies (IPCE) were obtained for 16 at.% Cr-doped films. This high photoactivity can be attributed to both the large active surface area and increased donor density caused by Cr-doping in the **α**-Fe_2O_3films. All samples reached their best IPCE at 400 nm. IPCE values for 16 at.% Cr-doped hematite films were thirty times higher than that of undoped samples. This high photoelectrochemical performance of Cr-doped hematite films is mainly attributed to an improvement in charge carrier properties.

Keywords:*Thin films; Hematite; Chromium; XRD analysis; FESEM analysis; TEM analysis; Optical properties;Photoelectrochemicalproperties.*

1. Introduction

For the last twenty years, hematite (α-Fe_2O_3) is considered as the most promising material in view of cost, abundance and photocatalytic properties. Hematite has emerged as an efficient photocatalyst used in solar water splitting as well as hydrogen production due to its appropriate optical band gap (2.1-2.2 eV). According to theoretical predictions, solar-to-hydrogen efficiency of hematite can reach 16.8% and water splitting photocurrent can extent 12.6 mA/cm^2 [1,2,3]. Moreover, hematite exhibits an extraordinary chemical stability in an oxidative environment. However, the applied performance of hematite for solar water splitting is far from the ideal case which has been limited by several factors such as poor conductivity, short lifetime of the excited state carrier (10 ps), poor oxygen evolution reaction (OER) kinetics, short hole diffusion length, and improper band position for an unbiased Photoelectrochemical method [4].

So far, the photoelectrochemical activity (PECA) of hematite has remained quite low because of two main drawbacks. First, the conduction band edge energy of **α-**Fe_2O_3system lies below the reversible hydrogen potential, thus hindering the charge-transfer process of photogenerated carriers (electrons and holes) at the hematite/electrolyte. Second, undoped hematite exhibits a rapid non-radiative electron–hole recombination due to its high density of intrinsic defects. As a result, the defects induce a short diffusion length almost 4 nm compared to the light penetration depth. Therefore, hematite has a relatively poor conductivity, severely limiting the overall photocurrent. However, incorporating foreign metallic atoms into the α-Fe_2O_3 structure has been considered an effective approach to inhibit the above-mentioned drawbacks and consequently enhance the PECA of hematite.

A large range of elements, mostly belonging to transition metals such as Sn [5], Cu [6], Pt [7], Si [8,9,10,11], Ti [12,13,14], V[7], Al [7,15], Cd [16], Mo [17], Nb [18], Mg [7], Rh [19], Ce [20], Co [21], Cu [7,22], Zn [7,23], Cr [7,17], Pt [11], and Ta [24] have been used to dope hematite.Table I shows a review of the achievements in some typically doped **α-**Fe_2O_3that can be found in the literature. Data in Table I includes the kind of the doping agents and the performance of the hematite water splitting photoelectrodes. These data are compared with the Cr-doped hematite obtained from the hydrothermal method described in this work. To dope **α-**Fe_2O_3, diverse methods have been attempted, using a range of synthesizing methods including sol–gel [25,26,27], hydrothermal [28,29], magnetron sputtering [30,31], atomic layer deposition [32], spray pyrolysis *Diagramme de Tanabe-Sugano du Fe(III)* [8,33,34,35],atmospheric pressure chemical vapor deposition (APCVD) [11,36,37], and electrodeposition [38,39,40,41]. These dopants influence the conductivity of the hematite as

well as band gap width, the Fermi level, and charge-transfer- processes. However, based on the literature, some researchers reported contradictory effects of doping on photoelectrochemical performances. This apparent discrepancy in the results has mainly been attributed to the doping concentration and processing methods. Undoped and doped hematites have been grown by various methods that can roughly be categorized in two groups. The first group involves physical deposition using gas as precursors and necessitates expensive and sophisticated devices as is the case in atomic layer deposition, chemical vapor deposition and magnetron sputtering. The second group includes wet chemical synthesizing methods requiring solution precursors and relatively low cost, simple utensils or set ups as in the case of electrochemical deposition, spray pyrolysis, sol–gel coating and hydrothermal growth. Compared to the methods, the hydrothermal method has several advantages. First, it is a reproducible, facile and inexpensive method since it consists of sealed "one pot" reactions requiring an operating temperature as low as 100°C. Second, it allows crystalline growth of versatile nanostructured doped hematite with precise control of the microstructure morphologies. Recently, McFarland and co-workers [38] were able to fabricate Pt, Mo and Cr doped and undoped hematite films as PEC electrodes for water splitting.They found that the photoactivity of the iron oxide was improved by co-deposition with Mo or Cr. The best performing samples were 5% Cr and 15% Mo doped, which had IPCEs at 400 nm of 6% and 12%, respectively, with an applied potential of 0.4V vs Ag/AgCl. These IPCE values were 2.2 and 4 times higher than the undoped sample for the 5% Cr and 15% Mo samples, respectively. No evidence was found that the improved performance was due to the electrocatalytic effects of the dopant at the surface of the hematite thin film. The major effect of the Mo and Cr dopants is to improve the charge transport properties of the hematite so that a greater fraction of the photon generated electron/hole pairs is available for surface redox chemistry.

Furthermore, under factual operating conditions, high over potentials are desirable not only because of non-idealities but also due to the complexity of water splitting reactions. Current progress in nanostructured hematite synthesis including nanoparticles [42,43], nanowires [44] and nanonets [45] opens opportunities in tackling the drawbacks mentioned above. As a matter of fact, nanostructured photoanode offers an increased semiconductor/electrolyte interfacial area for water oxidation, as well as a substantial reduction of the diffusion length for minority carriers [46,47,48]. In this way, hole recombination can be decreased if the surface feature dimensions are tuned to be close to the hole diffusion length of **α-**Fe_2O_3 (2 – 4 nm [49] or 20 nm [50]). Nanostructures increase light absorption by increasing light scattering

and trapping. As a result, nanostructured hematite photoelectrodes greatly facilitate the collection of charge carriers better than if they were simply bulky and smooth[51]. An additional doping of hematite photoanodes has been extensively studied to perform a further enhancement of the photoactivity of these photoanodes [51, 52,53]. Numerous studies have shown that PEC water splitting is advantageous combining nanostructure and doping effects [54,55]. Therefore, a more straightforward and up scaling fabrication method of nanostructured doped hematite electrodes is needed to compare the doping effects in terms of PECA before addressing their stability under real operating conditions. To date, no significant data have been published on optical, structural and electrical properties as well as PECA of chrome doped **α**-Fe_2O_3films when synthesized by the hydrothermal method. In this study, we prepared Cr-doped **α**-Fe_2O_3 thin films by a hydrothermal process. The photoelectrochemical response shows that the samples are effective for the photo splitting of water and the doping level affects the photocatalytic of the thin films. The optimum sample is **α**-Fe_2O_3 doped with 16at.% Cr. It is believed that this result could bebeneficial for the applications of Cr-doped **α**-Fe_2O_3 in the fields of photocatalysis and photoelectrical devices.

Table I: Summary of the results obtained for doped hematite photoelectrodes, fabrication methods and photoelectrochemical characteristics

Dopant	**Preparation Method**	**Potential (V)**	**Electrolyte**	**Light Intensity ($mW \cdot cm^{-2}$)**	**IPCE (%)**	**Photocurrent Density ($mA \cdot cm^{-2}$)**	**Ref.**
undoped Mo Cr	Electrodeposition	0.4 vs. Ag/AgCl	1 M NaOH	410	3 12 6	0.690 2,00 1,2	[17]
Undoped Si Ti	Sputtering	0.5 vs. SCE	1 M NaOH	100	U.A. 3 15	Negligible 0.100 0.620	[53]
Undoped Ti Ti-Al Ta Ti-Pt Ni	Spray Pyrolysis	0.45 vs. NHE	0.1M NaOH	U.A.	U.A.	0.800 4.000 4.000 1.000 0.800 Negligible	[52]
Undoped Pt	Electrodeposition	0.4vs. Ag/AgCl	1 M NaOH	410	3 12	0.690 1.340	[38]
Undoped Al	Electrodeposition	0.4 vs. Ag/AgCl	1 M NaOH	410	3 8	0.690 ~1.000	[39]
Undoped Ti	Spray Pyrolysis	0.5 vs. SCE	1 M NaOH	150	U.A.	Negligible 1.980	[56]
Undoped Mg	Spray Pyrolysis	0.2 vs. SCE	0.5 M H_2SO_4	U.A.	U.A.	U.A. 0.22	[57]
Undoped Zn	Spray Pyrolysis	0 vs. SCE	0.5 M H_2SO_4	40	U.A. 20	U.A. U.A.	[58]
Undoped Cr	Hydrothermal	0.1vs. Ag/AgCl	1M NaOH	100	Negligible 6	1.77 2.68	our work

U.A. = Unavailable

2. Experimental

2.1. Material and methods

The flowchart illustrating the synthesis of nanostructured **α-**Fe_2O_3 thin films by the hydrothermal method is displayed in Figure 1. Initially, a fluorine-doped tin oxide (FTO) coated glass plate purchased from Pilkington glass company (USA), was cut into small rectangular pieces having a surface of 3x1 cm^2 to serve as a starting substrate. These pieces were ultrasonically pre-cleaned by sequential rinses with acetone, distilled water, and ethanol. The hydrothermal bath was an aqueous solution containing a solution 0.15M$FeCl_3$, 1M$NaNO_3$ and 1M $Cr(ClO_4)_3$ [59,60,61]. Some drops of hydrochloric acid (HCl) were added to adjust the pH of the mixture to 1.5. $Cr(ClO_4)_3$solutionswere added to the bath intended for Cr-doped films. The additional amount of Cr was calculated so that the molar ratio Cr/(Cr+ Fe) remained in the range of 0-20 at. %. All chemicals were purchased from Sigma Aldrich and used as received without any additional purification. Double deionized water, exhibiting a resistivity close to 15 MΩ·cm was generated by a Milli-Q academic ultra-pure water purification system (Millipore, Bedford, MA, USA). Once the solution was prepared, some FTO glass substrates were placed at the bottom of a Teflon recipient. Only 20 ml were transferred to the recipient so that the substrates were partially immersed in the solution. Then, the recipient was inserted in a stainless-steel autoclave. The filled autoclave was tightly sealed before being heated at 100 °C for 6h in an oven. Finally, the system (autoclave with the samples) was naturally cooled down to room temperature. Under hydrothermal conditions, the aqueous solution enables the Fe^{3+}hydrolysis ions with OH^-, producing iron oxide nuclei, as described by the following reaction (1):

$$\mathbf{Fe^{3+}_{(aq)} + 3OH^-_{(aq)} \rightarrow \beta\text{-}FeOOH_{(s)} + H_2O} \qquad \mathbf{(1)}$$

Finally, a uniform yellowish layer of akageneite β-FeOOH covered the FTO/glass substrates uniformly. The akageneite-coated substrates were then washed with deionized water and subsequently introduced in a muffle furnace to be sintered in air at 550°C for 4 hours. At theend of this calcination step, the β-FeOOH was converted into α-Fe_2O_3. Correspondingly, as illustrated in Figure 1, the color of the substrate turned from yellow to red-brown indicating a phase transition from β-FeOOH to **α-**Fe_2O_3 [57].The chemical reaction expected to occur during this phase transition is represented by the reaction displayed below (2):

$$\mathbf{2\beta\text{-}FeOOH_{(s)} \rightarrow Fe_2O_{3(s)} + H_2O_{(L\ or\ G)}} \qquad \mathbf{(2)}$$

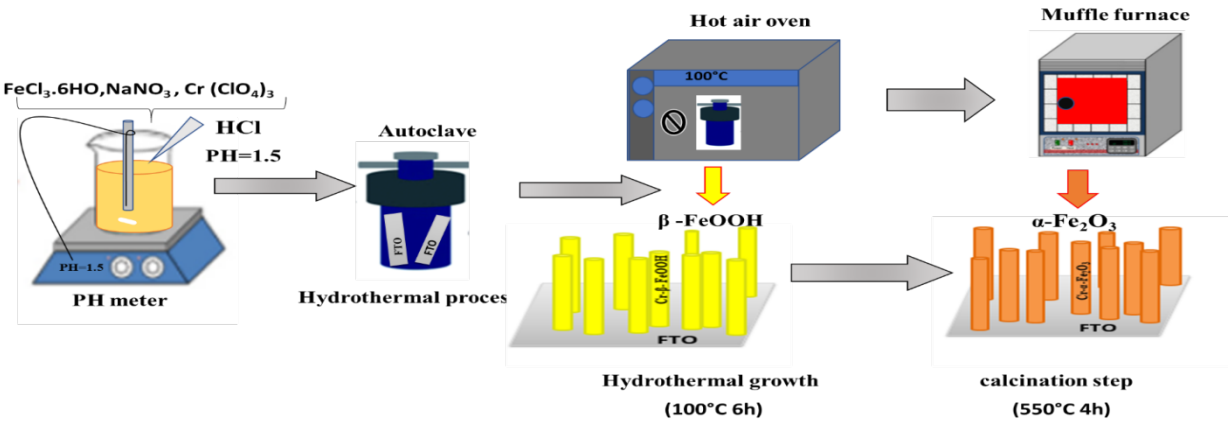

Fig. 1: Schematic illustration of Cr-doped hematite photoanodes synthesized by the hydrothermal method.

2.2. Characterization setup

Microstructural properties of various hematite films were obtained at room temperature using a RigakuUltima IV X-ray diffractometer (XRD) in the Bragg-Bentano configuration using CuKα radiation (λ = 1.54060 Å). Chemical composition, surface morphology, and topography were characterized using energy dispersive spectroscopy (EDX) coupled to a field emission scanning electron microscope (FESEM) Zeiss ULTRA 55, equipped with an In-Lens SE detector. The selected electron diffraction and high-resolution transmission electron microscopy (HRTEM) images were obtained by a JEOL-2010 TEM set at an acceleration voltage of 200 kV.Optical absorption was recorded with a UV-visible spectrophotometer HR4000 provided by Ocean Optics. The spectrophotometer was coupled to an integrating sphere to collect both specular and diffuse transmittance.

The photoelectrochemical measurements of the samples were performed in a quartz cell to facilitate light reaching the photoelectrode surfaces.The surface area of the working electrode was 0.2 cm^2.The electrolyte consisted of 1 M solution of NaOH (pH = 13.6) with a pure nitrogen stream bubbling before and during the test to remove the dissolved oxygen. The chronoamperometric curves of the hematite thin films were also obtained at + 0.1 V (vs. Ag/AgCl) both in dark and under illumination performed by a 300 W Xenon lamp (PLSSXE300/300UV). The luminous intensity of the Xenon lamp was fixed at 100 $mWcm^{-2}$. The set-up was completed with an automatic shutter and a filter box. The whole system was controlled by homemade software.

For wavelength-dependent photocurrent measurements a monochromator giving a ~20 nm band-pass from 360 to 680 nm was used together with cut off filters to eliminate secondary -

harmonics. To be able to detect low photocurrent intensity, the set-up was completed with a photo-chopper and a lock-in amplifier (signal recovery). The absolute intensity of the incident excitation light was measured with a radiometer/photometer (international light). The incident photon to electron conversion efficiency (IPCE) of the samples was calculated as follows:

$$\mathbf{IPCE}(\%) = \frac{\mathbf{1240}\cdot i_{photocurrent}\,(\mu\mathrm{A}/cm^2)}{\lambda(\mathrm{nm})\cdot j_{photons}(\mu W/cm^2)} * \mathbf{100}\% \quad \mathbf{(3)}$$

Were $i_{photocurrent}$ is the photocurrent densities, $\lambda(nm)$is wavelength of the incident light and $j_{photons}$ is the measured irradiance.

3. Results and discussion

3.1. Morphological characterization

3.1.1. FESEM analysis

The morphology of undoped and Cr-doped **α-**Fe_2O_3 samples obtained under hydrothermal conditions was monitored by FESEM images (Figure 2). Figure 2 shows a typical morphology of hematite nanorod (NR) arrays grown on the FTO substrates by the hydrothermal process. Top view images show clearly that hematite NRs are uniformly distributed on the substrate and oriented upward with respect to the substrate. While others are detached from the substrate, being free standing and horizontal. Each hematite NR looks like a grain of rice as can be seen in Fig. 2 (a,b,c,d, and e (200nm)) of the as-prepared sample, enabling the identification of a typical nanoparticle formation. On the other hand, top-view analysis of Cr-doped **α-**Fe_2O_3 electrodes synthesized during hydrothermal treatment 550 °C for 4h showed that this substrate is formed by rods. The effect of different Cr-doped **α-**Fe_2O_3 did not affect the morphology of the iron oxide nanoparticles.

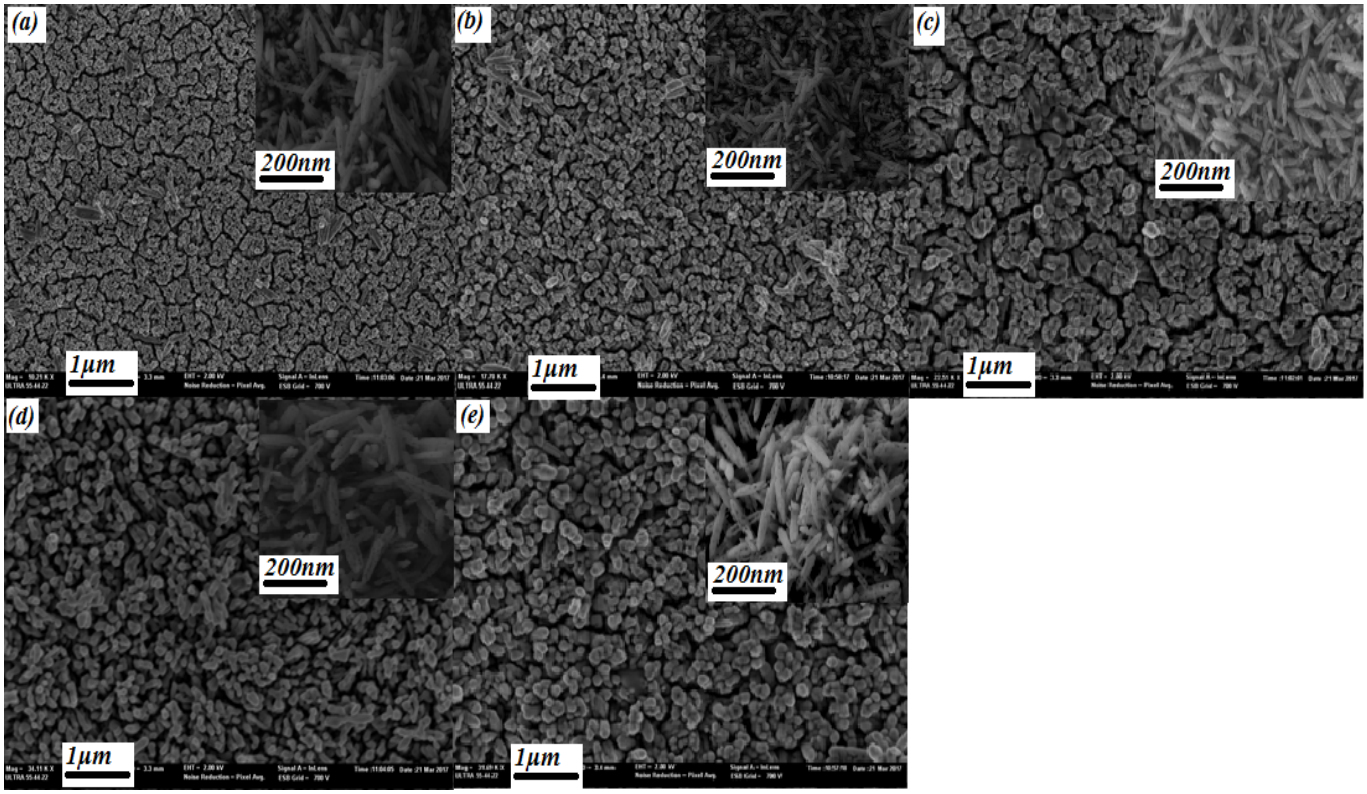

Fig. 2: FESEM of hydrothermal deposited α-Fe_2O_3 (a) undoped, (b) 4at.% Cr, (c) 8at.% Cr, (d) 16 at.% Cr, and (e) 20 at.% Cr (1µm and 200nm).

3.1.2. HRTEM analysis

The morphology of α-Fe_2O_3nanostructure films was characterized by TEM and HRTEM. Figure 3 (a, b) shows a low magnification TEM image of the α-Fe_2O_3nanostructures analyzed shows that the as-synthesized NRs exhibit a smooth surface and a relatively uniform diameter along the axial direction, using the high-resolution transmission electron microscopy (HRTEM) technique Figure 3 (c, d, e, f) shows a clear interplanar distance of 2.24 nm, matching the d_{110} spacing of pure hexagonal hematite. The NRs tend to have a parallel alignment, owing to weak Van der Waals attraction. The inset displays the electron diffraction (ED) pattern, which was taken of the entire area. The diffraction ring indicates the polycrystalline nature of α-$Fe_2O_3$and is highly consistent with the XRD results (Figure 4).Furthermore, the elemental mapping images (Figure 3 B) of the Fe (Kα), O (Kα), Cr(Kα) nanorod reveal that the Cr dopants are distributed over all the nanostructures without any segregation on the surface or inside the crystals.

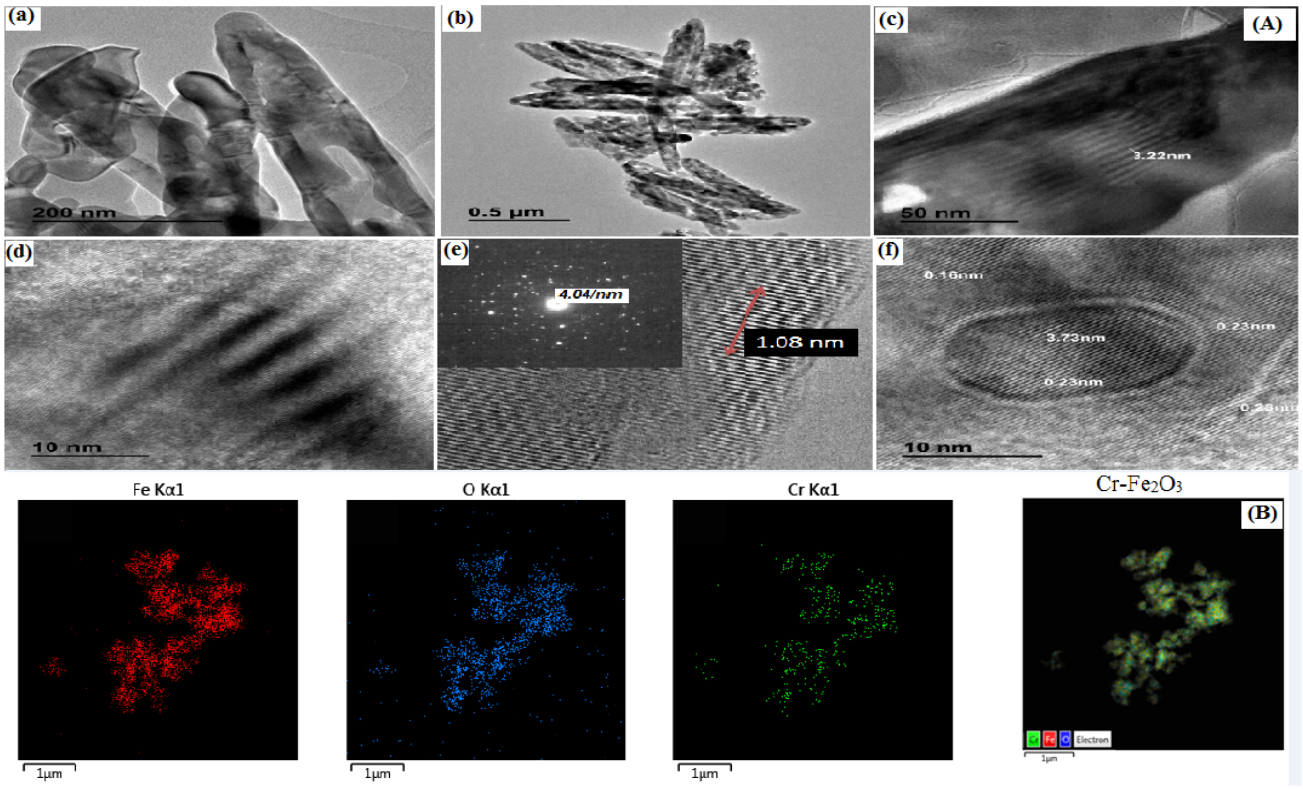

Fig.3 :(A) HRTEM of hydrothermally deposited undoped α-Fe_2O_3, (B) Element Mapping images of the Cr-Fe_2O_3 photoanode.

3.2. Structural characterization

Figure 4 shows the XRD patterns of doped and undoped hematite films. The diffraction peaks match the JCPDS Card No. 33–0664.Diffraction peaks located at 2θ = 24.2°, 33.1°, 35.6°, 40.9°, 49.5°, 54.1° and 64°correspond to (012), (104), (110), (113), (024), (116) and (300) diffraction planes,respectively. No peak corresponding to mixed oxides or impurities was detected in any of the samples. Hematite (**α**-Fe_2O_3) belongs to the space group R-3c (167) with the lattice parameters a= 5.036 Å, b= 5.036 Å, and c = 13.74 Å. This result proves that after being heated in air at 550°C for 4 h, the precursor was completely converted from FeOOH to a pure α-Fe_2O_3rhombohedral phase.Hence, undoped and Cr-doped hematite films havethe same crystal structure as **α**-Fe_2O_3.

The crystallite size of the samples was calculated using the Debye–Scherer formula:

$$D = \frac{(K\lambda)}{(\beta \cos \theta)} \qquad (4)$$

where λ = 1.5405 Å is the wavelength of Cu Kα radiation, β, the full width at half maximum (FWHM) of the main diffraction peak in radian, θ, the Bragg angle and k, the Scherrer's constant equal to 0.90.

Table 1 displays the calculated crystallite sizes for hematite samples doped at different Cr concentrations for the most intense peaks that correspond to (012) and (110) diffraction planes. The average crystallite size was found to decrease from44 nm to 11.7 nm for (012) and 40.6 nm to 4.8 nm for (110) as Cr doping varied from 0% to 20%, leading to a gradual decline of the intensity of the (012) and (110) XRD lines (See Fig. 4). The shift to higher angles observed for XRD peaks as Cr content increases (Table 1) confirms the replacement of Fe^{2+} ions (ion radius = 0.74 Å) by the smaller Cr $^{3+}$ ions (ion radius = 0.69 Å). This replacement results in a contraction of the**α**-Fe_2O_3lattice.It is also worth noting that EDX and optical analysis confirmed Cr-doping.

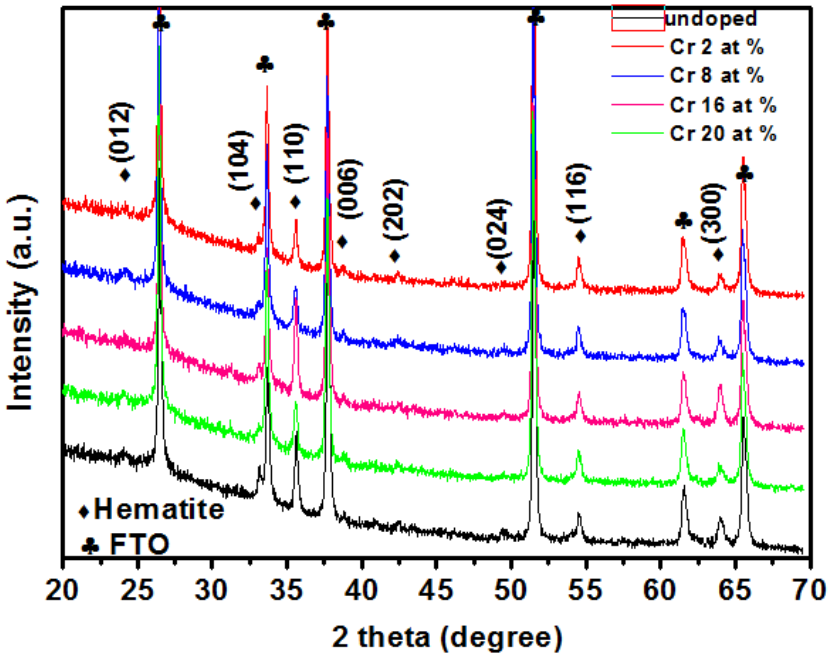

Fig.4: XRD patterns of α-$Fe_2O_3$and Cr-doped α-Fe_2O_3films at different Cr concentrations.

Table1: Variation of the crystallite size of undoped and Cr-doped α-Fe_2O_3vs Cr content.

Sample ID	2θ (°) Peak (012)	Crystallite Size [nm]	2θ (°) Peak (110)	Crystallite Size [nm]
Fe_2O_3	24.13	44.0	33.14	40.6
Fe_2O_3: Cr 4%	24.21	31.6	33.24	31.5
Fe_2O_3: Cr 8%	24.28	23.2	33.26	23.1
Fe_2O_3 : Cr 16%	24.30	17.7	33.28	18.6
Fe_2O_3 : Cr 20%	24.32	11.7	33.33	4.8

3.3. EDX analysis

Elemental analysis of the **α**-Fe_2O_3thin films was done by Energy Dispersive X-ray analysis (EDX) spectra (Fig. 5). The L line of the Fe element peaks at 0.6398 keV, while the K-line of oxygen peaks at 0.525 keV. The atomic percentages of Fe, Cr, and O in undoped and Cr-doped **α**-Fe_2O_3 are shown in Fig. 5. The excess of oxygen (detected by EDX) could have arisen from SnO_2, as all Cr-doped films keep the hematite structure, it can be assumed that the films do not deviate excessively from the stoichiometric composition. The calculated atomic ratio of Fe and O is approximately equal to 2:3, which agrees with the stoichiometric composition of α-Fe_2O_3, indicating that the films are rather thick so that only oxygen coming from the hematite is detected. On the other hand, the Cr concentration in the films is different from that existing in the precursor solution.

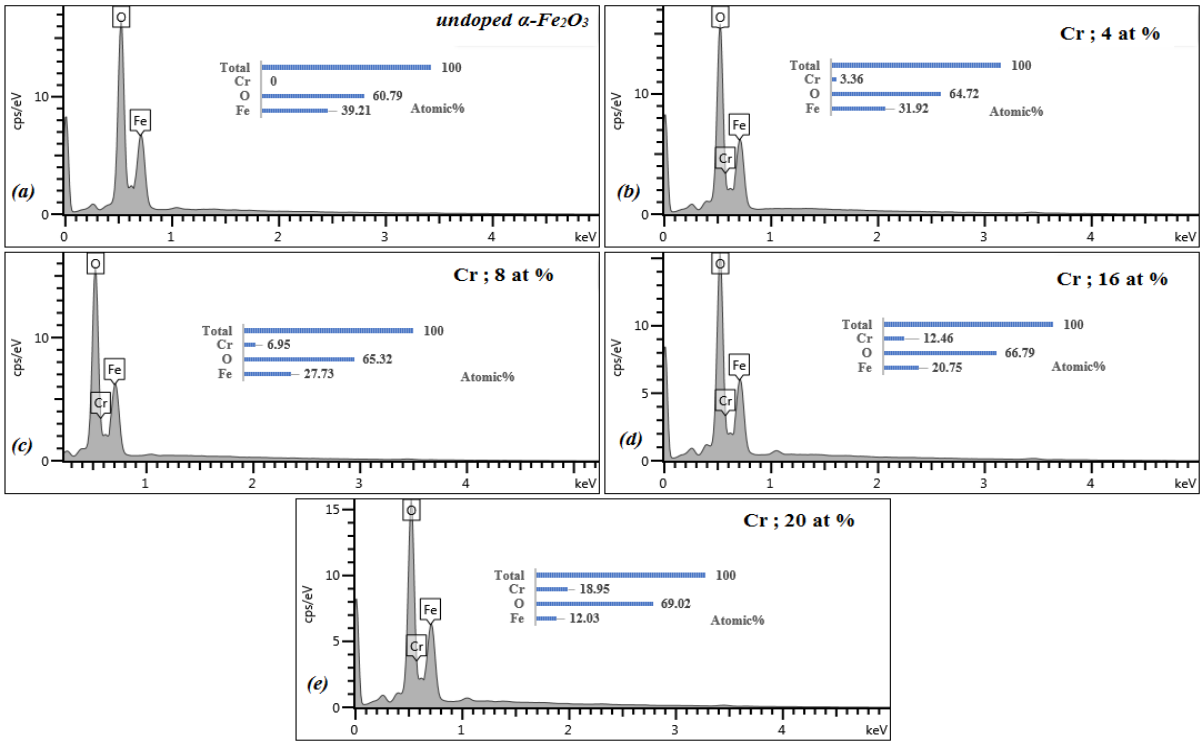

Fig.5: EDX spectrum of (a) undoped α-Fe_2O_3, (b) 4at.%Cr-doped α-Fe_2O_3, (c) 8at.%Cr-doped α-Fe_2O_3 (d) 16at.% Cr-doped α-Fe_2O_3 and (e) 20 at.% Cr-doped α-Fe_2O_3.

3.5 Optical characterization of Cr-doped Fe_2O_3 thin films

Figure 6 shows the optical transmission spectra in the wavelength range of 450 to 800 nm. The films displayed a transparency above 65% with an excitation wavelength above 600 nm. With increasing Cr content, the absorption edge (550–700 nm) shifted towards the longer wavelength region. It appears that **α**-Fe_2O_3has a high absorbance in the blue region, indicating its applicability as an absorbing material in this wavelength range (Figure 7). The effect of Cr-doping on the band-gap energy of the synthesized films was determined from the Tauc plot.

The band-gap energy (E_g) is estimated from the optical transmission spectra by calculating the absorption coefficient as follows [30]:

$$\alpha = \frac{1}{d} ln \left(\frac{1}{T}\right) \qquad (5)$$

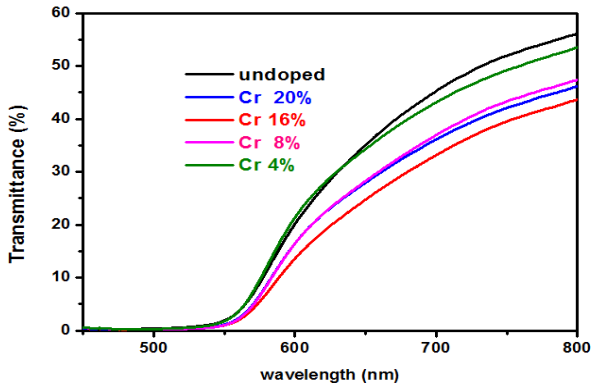

Fig. 6: Transmittance spectra of undoped and Cr doped α-Fe_2O_3

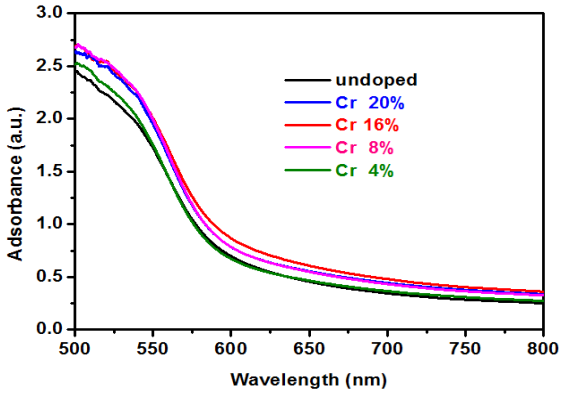

Fig.7. Absorbance spectra of undoped and Cr doped α-Fe_2O_3

The relation between the absorption coefficient and the incident light energy hν is approximated as [62]:

$$\alpha h\nu = A\,(h\nu - Eg)^{n} \qquad (6)$$

where α is the absorption coefficient, A is a constant, h is the Planck's constant, ν is the photon frequency, E_g is the optical bandgap, and n is equal to 1/2 for direct bandgap transitions and 2 for indirect ones. Figure 8 shows the Tauc plot for direct bandgap transitions for undoped and Cr-doped **α**-Fe_2O_3 films. The optical band-gap energy of undoped**α**-Fe_2O_3filmswas estimated to be 2.154 eV, slightly lower than that of bulk **α**-Fe_2O_3 (2.3 eV). It can be observed that the optical band-gap of Cr-doped **α**-Fe_2O_3remainsin the range of 2.05 eV - 2.1eV (Table 2).

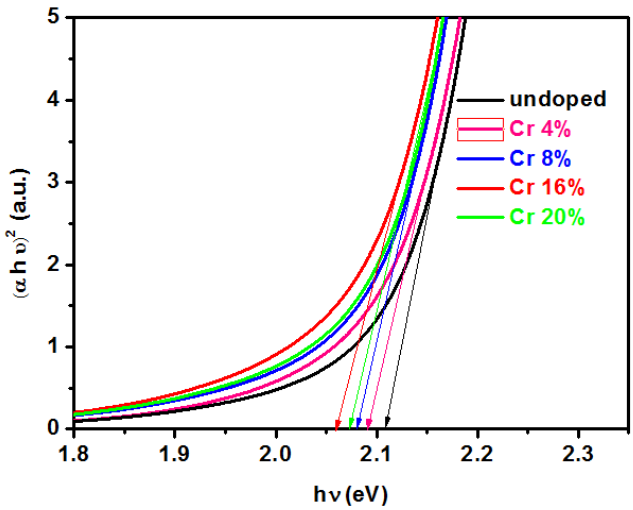

Fig.8: Tauc plot of undoped and Cr-doped α-Fe_2O_3

Table 2. Optical band-gap for α-Fe_2O_3 thin films having different Cr-doping

α-Fe_2O_3: Cr-doping	Cr 0 %	Cr 4%	Cr 8%	Cr 16%	Cr 20%
Bandgap energy (Eg) (eV)	2.15	2.09	2.08	2.05	2.07

3.6 Photoelectrochemical properties of the Cr-doped α-Fe_2O_3electrode.

The photocurrent response was measured under visible light irradiation. To improve the photocurrent response of **α-**Fe_2O_3 films the charge carrier transport must be enhanced in bulk and on the surface to reduce carrier recombination at both sites. All measurements were made in 1M NaOH [63,64] electrolyte and under a potential bias of 0.4 V.

Furthermore, we conducted chronoamperometric measurements under repeated light-on and light-off conditions for all hematite films with and without Cr doping. As shown in Fig. 9, the photocurrent of hematite is low and all Cr-doped hematite films exhibit higher photocurrents than undoped ones. Hematite films with 16 at. % of Cr displays the highest photocurrent, which is consistent with the UV-vis.

The results clearly demonstrate that the photocurrent density generated from the Cr-doped α-Fe_2O_3electrode is significantly higher than that of undoped electrodes due to the presence of an easier electron transport mechanism. In fact, structural studies showed that XRD peaks exhibited a slight shift towards higher diffraction angles as Cr doping increases, which indicates that Fe^{3+} ions were replaced by smaller Cr^{4+}ions. Accordingly, Cr (Cr^{4+}) acts as an electron donor in the **α-**Fe_2O_3matrix, thus confirming the substitution of Fe^{3+} by Cr^{4+}ions.

In fact, Cr doping increases the donor concentration and enhances thechargecarrier transportation by increasing the electric field across the space charge layer. The growth of the donor concentration would reduce the width of the space charge layer; hence, the charge carriers within the region should be efficiently separated before recombination. On the other hand, a higher concentration of dopant would provide more efficient defect-scattering/recombination inhibiting the increased separation efficiency,which might also explain the variation of the photocurrent density with the doping levels.

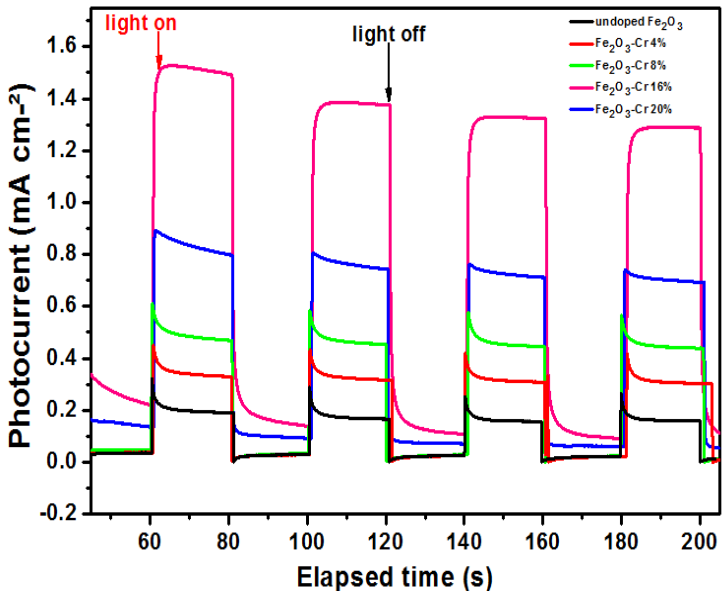

Figure 9: Photocurrent intensity for Cr-doped Fe_2O_3 electrodes under on/off illumination, measured in 1M NaOH electrolyte with a bias potential of +0.4 V, under successive illumination cycles.

Figure 10 shows the performance of doped samples as compared to undoped sample. Significant performance enhancements were observed upon doping throughout the illumination wavelengths. The performance of the 4 at.% Cr-doped films is 4 times higher than that of the undoped sample. The IPCE of 16 at.% Cr-doped films measured at 400 nm with an applied bias of +0.4 V (vs. Ag/AgCl) is 6%, which corresponds to a thirty-fold improvement over the undoped hematite. The higher photon energy was absorbed in the outmost layers of hematite and therefore, the photogenerated holes have a shorter diffusion path to reach the surface where they will contribute in H_2O oxidation reaction. An anodic applied bias will increase the collection efficiency of the electrons, and an IPCE improvement can be seen in Figure 10. Furthermore, the applied bias will enable H_2O reduction at the Pt counter-electrode by overcoming the mismatch (0.4 V (vs. Ag/AgCl)) between the hematite conduction band edge level and the reversible hydrogen potential (see Figure 11). The improved IPCE performance is implausible to be related to an increase in the absorption of the doped samples since no significant change was obtained in the absorption spectra of the different Cr-doped samples (see Figure 7).

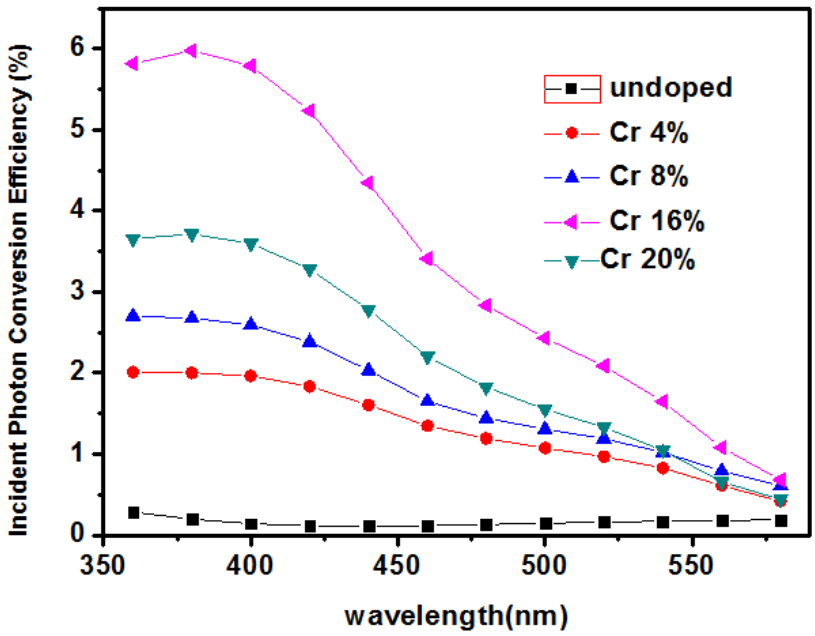

Figure 10: IPCE for undoped and Cr-doped α-Fe_2O_3 films at an applied potential of +0.4 V (vs. Ag/AgCl) in1 M NaOH.

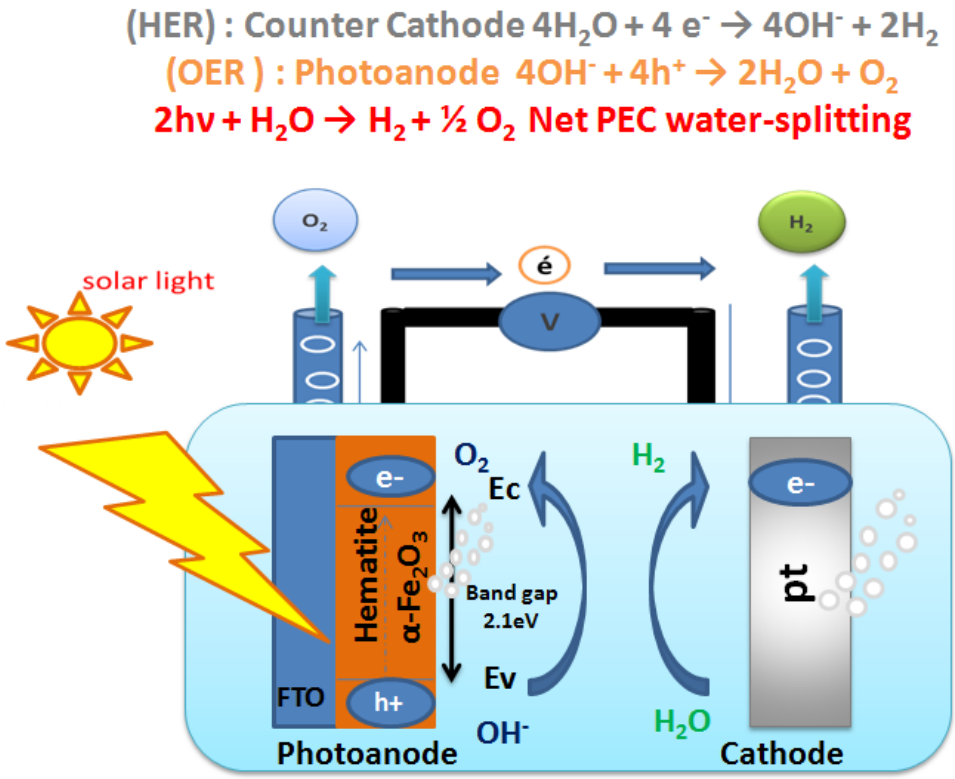

Figure 11: Energy diagram of the n-type hematite photoanode and schematic illustration of the photoelectrochemical water splitting on photoanode and cathode.

4. Conclusions

Cr-doped **α**-Fe_2O_3 films were successfully deposited on FTO-coated glass substrates using the hydrothermal method and an annealing process. The concentration of the incorporated Cr atoms (Cr^{4+} ions) was controlled by varying the concentration of the $Cr(ClO_4)_3$precursor solution, (i.e., the concentration of the dopant in the sample can be controlled by adjusting the electrolyte composition). The Cr dopant served as an ionized donor and was found to increase the carrier density of the **α**-Fe_2O_3films. The major effect of Cr atoms is the improvement of the conductivity and the charge transport properties of the **α**-Fe_2O_3films. The photoactivity of the iron oxide was improved by co-deposition with Cr. The best performing samples have a doping rate of 16 at% Cr, which in turn has anIPCE of 6% at 400 nm, with an applied potential of +0.4V (vs Ag/AgCl). These IPCE values were thirty times higher than that of the undoped sample. Hence, a greater fraction of the photon-generating electron–hole pairs is available for surface redox chemistry. The apparent optimum at 16 at.% Cr doping may balance these competing effects most effectively and yield the best PCE performance. The Cr-doped **α**-Fe_2O_3 films provide potential applications in photocatalysis for water splitting or in photoelectrical devices.

Références article 1

[1] A. B.Murphy, P. R. F.Barnes, L. K. Randeniya, I. C. Plumb, Grey, M. D. Horne, & J. A lasscock, International Journal of Hydrogen Energy, 31(14) (2006), 1999-2017.
[2] Z.B. Chen, T. F. Jaramillo, T. G. Deutsch, A. Kleiman-Shwarsctein, A. J. Forman, N. Gaillard, R. Garland, K. Takanabe, C. Heske, M. Sunkara, E. W. McFarland, K. Domen, E. L. Miller, J. A. Turner and H. N. Dinh, J. Mater. Res., (2010), 25, 3.
[3] K. Sivula, F. L. Formal, M. Grätzel, ChemSusChem, 4, (2011), 432−449.
[4] T.W. Hamann, Dalton Trans., 41, (2012) 7830−7834.
[5] V. M. Aroutiounian, V. M. Arakelyan, G. E. Shahnazaryan, H. R. Hovhannisyan, H. L. Wang, J. A. Turner, Sol. Energy 2007, 81, 1369.
[6] J. S. Jang, J. Lee, H. Ye, F. R. F. Fan, A. J. Bard, J. Phys. Chem. C 2009, 113, 6719
[7] Y. S. Hu, A. Kleiman-Shwarsctein, A. J. Forman, D. Hazen, J. N.Park, E. W. McFarland, Chem. Mater. 2008, 20, 3803.
[8]I. Cesar, A. Kay, J. A. G. Martinez, M. Gratzel, J. Am. Chem. Soc. 2006, 128, 4582.
[9]S. Saremi-Yarahmadi, K. G. U. Wijayantha, A. A. Tahir, B. Vaidhyanathan, J. Phys. Chem. C 2009, 113, 4768.
[10] Y.Q.Liang, C.S. Enache, R. van de Krol, Int. J. Photoenergy 2008 (2008) 1.
[11]I. Cesar, K. Sivula, A. Kay, R. Zboril, M. Gratzel, J. Phys. Chem. C 113 (2009) 772.
[12] Y. S. Hu, A. Kleiman-Shwarsctein, G. D. Stucky, E. W. McFarland, Chem. Commun. 2009, 2652.
[13] F. Morin, J. Phys. Rev. 1951, 83, 1005.
[14] J.S. Jang, J. Lee, H. Ye, F.R.F. Fan, A.J. Bard, J. Phys. Chem. C 113 (2009) 6719.
[15] A. Kleiman-Shwarsctein, M. N. Huda, A. Walsh, Y. F. Yan, G. D. Stucky, Y. S. Hu, M. M. Al Jassim, E. W. McFarland, hem. Mater. 2010, 22, 510.
[16] A. Bak, W. Choi, H. Park, Appl. Catal. B 2011, 110, 207.
[17]A. Kleiman-Shwarsctein, Y. S. Hu, A. J. Forman, G. D. Stucky, E. W. McFarland, J. Phys. Chem. C 2008, 112, 15900.
[18] V. M. Aroutiounian, V. M. Arakelyan, G. E. Shahnazaryan,G. M. Stepanyan, E. A. Khachaturyan, H. Wang, J. A. Turner,Sol. Energy 2006, 80, 1098.
[19] K. Gurunathan, P. Maruthamuthu, Int. J. Hydrogen Energy 20 (1995) 287.
[20] G.K. Reddy, K. Gunasekara, P. Boolchand, P.G. Smirniotis, J. Phys. Chem. C 115 (2011) 920.
[21] R. Schrebler, L. Ballesteros, A. Burgos, E.A. Dalchiele, J. Electrochem. Soc. 158 (2011) D500.
[22] C.L. Chun, D.R. Baer, D.W. Matson, J.E. Amonette, R.L. Penn, Environ. Sci Technol. 44 (2010) 5079.
[23] J. Velev, A. Bandyopadhyay, W. H. Butler, S. Sarker, Phys.Rev. B 2005, 71, 205208.
[24] A.A. Akl, Appl.Surf.Sci.233(2004)307.
[25] C.D. Park, J. Walker, R. Tannenbaum, A.E. Stiegman, J. Frydrych, L. Machala, ACS Appl.Mater.Int.1(2009)1843.
[26] A. Watanabe, H. Kozuka, J. Phys. Chem. B 107 (2003) 12713.
[27] A. Memar, W. R. W. Daud, S. Hosseini, E. Eftekhari, L. J. Minggu,Sol. Energy 2010, 84, 1538.

[28] C.J. Jia, L.D. Sun, Z.G. Yan, L.P. You, F. Luo, X.D. Han, Y.C. Pang, Z. Zhang, C.H. Yan, Angew.Chem. Int.Ed.44(2005)4328.
[29]K.Sue, T. Sato, S. Kawasaki, Y. Takebayashi, S. Yoda, T. Furuya, T. Hiaki, Ind. Eng. Chem.Res. 49 (2010) 8841.
[30]E.L. Miller,D.Paluselli, B.Marsen,R.E. Rocheleau, Thin Solid Films 466 (2004) 307.
[31] Z.H. Zhang, M.F. Hossain, T. Miyazaki, T. Takahashi, Environ. Sci. Technol. 44 (2010)4741.
[32] M.Aronniemi, J. Saino, J. Lahtinen, ThinSolidFilms516(2008)6110.
[33]W. Widiyastuti, R. Balgis, F. Iskandar, K. Okuyama, Chem. Eng. Sci. 65 (2010) 1846.
[34] A. Duret, M. Gratzel, J. Phys. Chem. B 2005, 109, 17184.
[35]C. J. Sartoretti, B. D.Alexander, R. Solarska, W. A. Rutkowska, J. Augustynski, R. Cerny, J. Phys.Chem. B 2005, 109,13685.
[36] S. Saremi-Yarahmadi, K. G. U. Wijayantha, A. A. Tahir,B.Vaidhyanathan, J. Phys. Chem. C 2009, 113, 4768.
[37] A. Kay, I. Cesar, M. Gratzel, J. Am. Chem. Soc. 2006,128, 15714.
[38]Y.S. Hu, A. Kleiman-Shwarsctein, A.J. Forman, D. Hazen, J.N. Park, E.W. McFar-land, Chem.Mater.20 (2008) 3803.
[39] A. Kleiman-Shwarsctein, M.N. Huda, A. Walsh, Y.F. Yan, G.D. Stucky, Y.S. Hu, M.M. Al-Jassim, E.W. McFarland, Chem.Mater.22(2010)510.
[40] R. L. Spray, K. S. Choi, Chem. Mater. 2009, 21, 3701.
[41]A. Bak, W. Choi, H. Park, Appl. Catal. B 2011, 110, 207.
[42]U.Bjorksten, J.Moser, M. Gratzel,Chem Mater 1994, 6, (6), 858-863.
[43]H. L. Wang, J.A. Turner, J.Electrochem. Soc. 2010, 157, (11), F173-F178.
[44]L. Vayssieres, J.H. Guo, J. Nordgren, J. Nanosci.Nanotechno.2001, 1, (4),385-388.
[45] L. Li, Y. Yu, F. Meng, Y. Tan, R.J. Hamers, S. Jin, Nano Lett. 2012, 12, (2), 724-731.
[46]M. Grätzel, Photoelectrochemical cells, NATURE VOL 414 15 NOVEMBER 2001
[47] A. Boudjemaa, S. Boumaza, M. Trari, R. Bouarab, A. Bougueliac, Physical and photoelectrochemical characterizations of a-Fe_2O_3.Application for hydrogen production, International Journal of Hydrogen Energy 34 (2009) 4268–4274
[48]A. Boudjemaa, M. Trari, Photo-catalytic hydrogen production over Fe2O3 based catalysts international journal of hydrogen energy 35 (2010) 7684 -7689.
[49]J. H. Kennedy and K. W. Frese, Jr, J. Electrochem. Soc., 1978, 125(5), 709–714
[50]M.P. Dare-Edwards, J.B. Goodenough, A.Hamnett, P.R. Travelling, J. Chem. Soc. Faraday Trans. I 1983,79, 2027-2041
[51] A. Mao, G.Y. Han, J.H. Park, Journal of Materials Chemistry 20 (2010) 2247–2250.
[52] C. J. Sartoretti, B.D. Alexander, R. Solarska, W.A.Rutkowska, J.Augustynski, R. Cerny, J Phys Chem B 2005, 109, (28), 13685-13692.
[53]J.A.Glasscock,P. R. F. Barnes, I.C. Plumb, N.Savvides, Journal ofPhysical Chemistry C 2007, 111, (44), 16477-16488.
[54]Yichuan Ling, Gongming Wang, Damon A. Wheeler, Jin Z. Zhang, and Yat Li, Nano Lett., 2011, 11 (5), 2119–2125

[55]Yanming Fu, Chung-Li Dong, Zhaohui Zhou, Wan-Yi Lee, Jie Chen, PenghuiGuo, Liang Zhao and ShaohuaShen Phys. Chem. Chem. Phys., 2016,18, 3846-3853
[56] S.Kumari, A.P. Singh, Sonal, D. Deva, R. Shrivastav, S. Dass, V.R. Satsangi, Int. J. Hydrogen Energy 2010, 35, 3985-3990.
[57] W.B.Ingler Jr, S.U.M. Khan; Thin Solid Films 2004, 461, 301–308.
[58]W.B.Ingler, Jr., J.P.Baltrus, S.U.M. Khan; J. Am. Chem. Soc. 2004, 126, 10238-10239.
[59] L. Vayssieres, N. Beermann, S.E. Lindquist, A. Hagfeldt, Controlled aqueous chemical growth of oriented three-dimensional crystalline nanorod arrays: application to iron(III) oxides, Chem. Mater. 13 (2001) 233–235.
[60] A. Annamalai, P.S. Shinde, A. Subramanian, J.Y. Kim, J.H. Kim, S.H. Choi, J.S. Lee, J.S. Jang, J. Mater. Chem. A 3 (2015) 5007–5013.
[61]MingyangLi,ZiyangZhang,FeiyiLyu,Xinjun He, Zhihao Liang, Muhammad-SadeeqBalogun, XihongLu,Ping-PingFang,YexiangTong, Electrochim. Acta, 186 (2015) 95-100.
[62] M.R. Belkhedkar, A.U. Ubale, International Journal of Materials and Chemistry, 4 (2014) 109-116.
[63] S.S. Shinde, R. A. Bansode, C. H. Bhosale, and K.Y.Rajpure, Journal of Semiconductors 32 (2011) 013001.
[64] Flavio L. Souza, Kirian P. Lopes, Pedro A.P. Nascente, Edson R. Leite, Solar Energy Materials & Solar Cells 93(2009) 362–368.

Article 2:

Electrochemical fabrication and characterization of p-CuSCN/n-Fe_2O_3heterojunction devices for hydrogen production

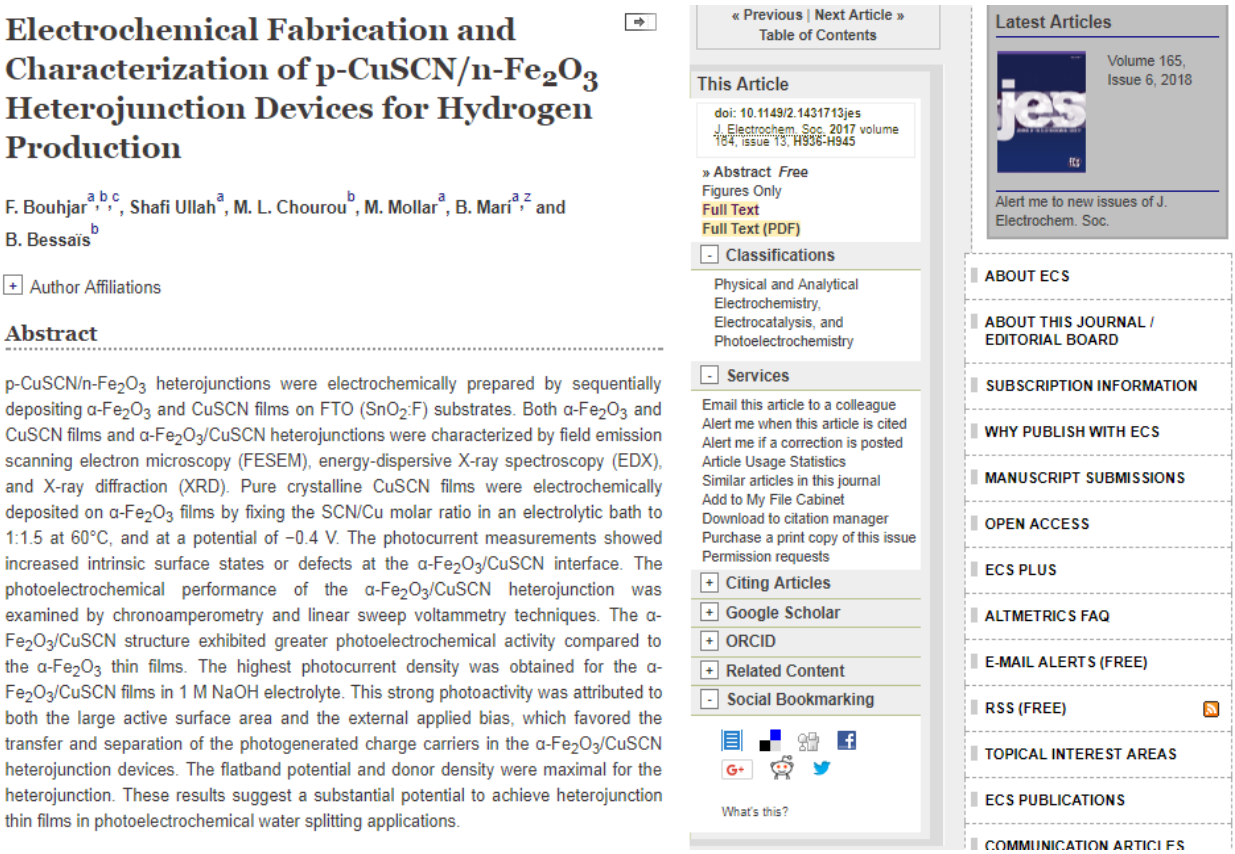

Electrochemical Fabrication and Characterization of p-CuSCN/n-Fe_2O_3 Heterojunction Devices for Hydrogen Production

F. Bouhjar[a,b,c], Shafi Ullah[a], M. L. Chourou[b], M. Mollar[a], B. Marí[a,z] and B. Bessaïs[b]

Author Affiliations

Abstract

p-CuSCN/n-Fe_2O_3 heterojunctions were electrochemically prepared by sequentially depositing α-Fe_2O_3 and CuSCN films on FTO (SnO_2:F) substrates. Both α-Fe_2O_3 and CuSCN films and α-Fe_2O_3/CuSCN heterojunctions were characterized by field emission scanning electron microscopy (FESEM), energy-dispersive X-ray spectroscopy (EDX), and X-ray diffraction (XRD). Pure crystalline CuSCN films were electrochemically deposited on α-Fe_2O_3 films by fixing the SCN/Cu molar ratio in an electrolytic bath to 1:1.5 at 60°C, and at a potential of −0.4 V. The photocurrent measurements showed increased intrinsic surface states or defects at the α-Fe_2O_3/CuSCN interface. The photoelectrochemical performance of the α-Fe_2O_3/CuSCN heterojunction was examined by chronoamperometry and linear sweep voltammetry techniques. The α-Fe_2O_3/CuSCN structure exhibited greater photoelectrochemical activity compared to the α-Fe_2O_3 thin films. The highest photocurrent density was obtained for the α-Fe_2O_3/CuSCN films in 1 M NaOH electrolyte. This strong photoactivity was attributed to both the large active surface area and the external applied bias, which favored the transfer and separation of the photogenerated charge carriers in the α-Fe_2O_3/CuSCN heterojunction devices. The flatband potential and donor density were maximal for the heterojunction. These results suggest a substantial potential to achieve heterojunction thin films in photoelectrochemical water splitting applications.

Electrochemical fabrication and characterization of p-CuSCN/n-Fe_2O_3 heterojunction devices for hydrogen production

F. Bouhjar [a, b, c],Shafi Ullah[a],M.L. Chourou[b], M. Mollar [a],B.Marí [a] and B. Bessaïs [b]

a. Institut de Disseny i Fabricació, Universitat Politècnica de València. Camí de Vera s/n 46022 València (Spain)

b. Laboratoire Photovoltaïque, Centre de Recherches et des Technologies de l'Energie Technopole de Borj – Cedria, Hammam-Lif 2050(Tunisia)

c. University of Tunis

Abstract

p-CuSCN/n-Fe_2O_3 heterojunctions were electrochemically prepared by sequentially depositing α-Fe_2O_3 and CuSCN films on FTO (SnO_2:F) substrates. The α-Fe_2O_3 and CuSCN films and the α-Fe_2O_3/CuSCN heterojunctions were characterized by Field Emission Scanning Electron Microscopy (FESEM), Energy-Dispersive X-ray spectroscopy (EDX), and X-Ray Diffraction (XRD). Pure crystalline CuSCN films were electrochemically deposited on α-Fe_2O_3 films by fixing the SCN/Cu molar ratio in the electrolytic bath to 1:1.5 at 60 °C and at a potential of -0.4 V. The photocurrent measurements showed an increase of the intrinsic surface states or defects at the α-Fe_2O_3/CuSCN interface. The photoelectrochemical performance of the α-Fe_2O_3/CuSCN heterojunction was examined by chronoamperometry and linear sweep voltammetry techniques. It was found that the α-Fe_2O_3/CuSCN structure exhibits a higher photoelectrochemical activity when compared to α-Fe_2O_3 thin films. The highest photocurrent density was obtained for α-Fe_2O_3/CuSCN films in 1 M NaOH electrolyte. This high photoactivity was attributed to the high active surface area and to the external applied bias; which favors the transfer and the separation of the photogenerated charge carriers in α-Fe_2O_3/CuSCN heterojunction devices. The flat band potential and the donor density were found to be maximal for the heterojunction. These results suggest a substantial potential to achieve heterojunction thin films in photoelectrochemical water splitting applications.

Keywords:α-Fe_2O_3/CuSCN; Interface; Electrochemical deposition; Heterojunction; photocurrent; Mott-Schottky.

Introduction

In recent years, a great deal of attention has been paid to heterogeneous thin film deposition on highly structured semiconductor substrates such as Fe_2O_3, ZnO, TiO_2, and GaN to form heterojunction; the latter semiconductor are essential in many electrical, photoelectrical, and catalytic applications generally requiring an enlargement of the interface area. Thermodynamically, the water splitting reaction is an uphill process that requires a minimum energy of 1.23 eV as the Gibbs free energy change is $\Delta G° = 237.2$ kJ mol^{-1} or 2.46 eV per H_2O molecule [1].However, a high overpotential is needed due to non-idealities in real operations taking into account the water splitting reaction complexity. The water splitting process requires two steps as it is not quite as straightforward as ripping apart the three atoms in H_2O. The full reaction requires the participation of two H_2O molecules, which are then separated according to the following reduction and oxidation half-reaction[2].

Reduction reaction:

$$2H^+ + 2e^- \rightarrow H_2 \ (E^0_{red} = 0.00\text{V/RHE}) \quad \textbf{(1)}$$

Oxidation reaction:

$$2H_2O + 4h^+ \rightarrow O_2 + 4H^+ \ (E^0_{ox} = -1.23\ \text{V/RHE}) \quad \textbf{(2)}$$

Overall reaction:

$$2H_2O \rightarrow 2H_2 + O_2 \ (\Delta E = -1.23\ \text{V/RHE}) \quad \textbf{(3)}$$

where RHE indicates a reversible hydrogen electrode (RHE).

Given that four-electron water oxidation is the rate-limiting step in the overall water splitting reaction, the development of high-efficiency photoanodes for O_2 evolution capable of overcoming the high overpotential requiring to perform this reaction represents an important barrier that must be overcome [3].Hematite (α- Fe_2O_3) is one of the most promising photoanode candidates as it has a narrow bandgap of ~2.1-2.2 eV and allows a ~16.0% theoretical solar-to-hydrogen (STH) efficiency for photoelectrochemical (PEC) water splitting [4,5,6]. Moreover, compared to other narrow bandgap semiconductors, α- Fe_2O_3 offers many additional advantages, including excellent stability in alkaline solutions, earth abundance, and nontoxicity [3-7].However, α- Fe_2O_3 has extremely poor electrical conductivity with a hole diffusion length of 2–4 nm[8]and suffers from a high charge carriers recombination leading toa low PEC performance; the future success of α- Fe_2O_3 photoanodes in PEC water splitting

remains questionable, as α- Fe_2O_3 itself can hardly achieve rather high PEC efficiency for practical potentialuse and necessitates modification to improve the PEC performance.

Herein, an overview of the synthesis, modification, and characterization of nanostructured α-Fe_2O_3 thin film is provided with an emphasis on charge carrier dynamics and PEC properties[9]. In the past few years, an increasing number of studies focused on α-Fe_2O_3 heterostructures, which incorporate the second material to promote charge separation, chargecollection, and surface catalysis. Indeed, higher PEC activities have been achieved with such α-Fe_2O_3 heterostructure-based photoanodes than with their single-component counter-parts, such as WO_3/α-Fe_2O_3 [10], ZnO/α-Fe_2O_3[11], n-Si/α-Fe_2O_3[12], α-Fe_2O_3/NiO[13],α-Fe_2O_3:Ti/Cu_2O[14],p-Si/ α-Fe_2O_3 /Au[15],and α-Fe_2O_3 /Gr/$BiV_{1-x}Mo_xO_4$ [16].

Table I shows a review of the characteristics of some typical α-Fe_2O_3-based semiconducting heterojunctions that can be found in the literature. Data in Table I include the type of the heterostructure, the fabrication method, the suggested electrons and holes charge transfer and the main photoelectrical properties of these heterostructures. These data are compared with the electrochemically deposited Fe_2O_3/CuSCN heterojunction described in this work.

The CuSCN is a p-type hole-conducting material, transparent in the visible light spectrum range, having a reasonable hole conductivity ($\geq 5\times10^{-4} S\cdot cm^{-1}$) [17] and a good chemical stability [18].In this work, we describe the electrochemical deposition of Fe_2O_3/CuSCN heterojunction films. CuSCN films having various compositions were deposited on smooth Fe_2O_3 surfaces. The characterization of the films was carried out using FESEM and X-ray diffraction (XRD)techniques.

Table I: Hematite-based heterostructures including fabrication methods, suggested charge transfer and photoelectrochemical characteristics.

Heterostructure	**Fabrication method**	**Suggested charge transfer**		**Photoelectrochemistry**	**Ref**
		Electron	**Hole**		
WO_3/ α-Fe_2O_3	Sol–gel	WO_3→ α-Fe_2O_3	None	Photocurrent:22μAcm^{-2}at 0.8V vs. Ag/AgCl (500 W Xe lamp) lec-trolyte: 0.2 M Na_2SO_4 (pH = 7.5)	**[19]**

WO_3/ α-Fe_2O_3	spin coating and Spray pyrolysis	None	None	Photocurrent:22 mA cm^{-2}at 0.8V vs. Ag/AgCl; electrolyte: 0.05 M PBS (pH = 7)	**[20]**
ZnO/α-Fe_2O_3	Hydrothermal and spin coating	α-Fe_2O_3 →ZnO	ZnO → α-Fe_2O_3	Photocurrent:1.6mA cm^{-2} at 0.6V vs. Ag/AgCl; electrolyte:1 M NaOH	**[21]**
α-Fe_2O_3 /Gr/$BiV_{1-x}Mo_xO_4$	Hydrothermal and spin coating	$BiV_{1-x}Mo_xO_4$ → α-Fe_2O_3	α-Fe_2O_3 →$BiV_{1-x}Mo_xO_4$	Photocurrent: 0.39 mA cm^{-2} at 1.5 V vs. RHE (64 mW cm^{-2}λ > 420 nm); electrolyte: 0.01 M Na_2SO_4	**[22]**
α-Fe_2O_3/$ZnFe_2O_4$	Spin coating	$ZnFe_2O_4$ → α-Fe_2O_3	α-Fe_2O_3 → $ZnFe_2O_4$	Photocurrent: 0.44 mA cm^{-2} at 0.2 V vs. Ag/AgCl; electrolyte: 0.1 M glucose and 0.5 M NaOH (pH = 13.0)	**[23]**
α-Fe_2O_3: Ti/$ZnFe_2O_4$	Hydrothermal and surface treatment	$ZnFe_2O_4$ →α-Fe_2O_3: Ti	α-Fe_2O_3: Ti → $ZnFe_2O_4$	Photocurrent: 0.3 mA cm^{-2}at 1.4 V vs. RHE; electrolyte: 1 M KOH	**[24]**
α-Fe_2O_3: Co/$MgFe_2O_4$	Hydrothermal and wet impregnation	$MgFe_2O_4$ → α-Fe_2O_3 : Co	α-Fe_2O_3: Co →$MgFe_2O_4$	Photocurrent: 3.34 mA cm^{-2} at 1.4 V vs. RHE; electrolyte: 0.01 M Na_2SO_4	**[25]**
p-$CaFe_2O_4$/n-Fe_2O_3	Hydrothermal and two-step annealing	p-$CaFe_2O_4$ → n-Fe_2O_3	n-Fe_2O_3→ p-$CaFe_2O_4$	Photocurrent: 0.53 mA cm^{-2}at 1.23 V vs. RHE; electrolyte: 1.0 M KOH (pH = 13.9)	**[26]**
α-Fe_2O_3: Ti/Cu_2O	Spray pyrolysis	Cu_2O →α-Fe_2O_3: Ti	α-Fe_2O_3: Ti → Cu_2O	Photocurrent: 2.60 mA cm^{-2}at 0.95 V vs. SCE (Xe lamp, 150 mW cm^{-2}); electrolyte: 0.1 M NaOH	**[27,28]**
α-Fe_2O_3/CuSCN	electrodeposition	CuSCN→ α-Fe_2O_3	α-Fe_2O_3→ CuSCN	Photocurrent: 2.90 mA cm^{-2} at 0.59 V vs. Ag/AgCl. (Xe lamp: 150 W); electrolyte 0.1 M NaOH(pH = 13.9)	**our work**

2. Experimental details

2.1. Electrodeposition

The iron oxide films were deposited using an electrodeposition bath consisting of an aqueous solution containing ferric chloride ($FeCl_3$. $6H_2O$, purity (p)⩾98.0), hydrogen peroxide (H_2O_2⩾99.99%), Potassium fluoride (KF, p⩾99.97%) and Potassium chloride (KCl, p⩾99.0%). Potassium perchlorate ($KClO_4$, p⩾99.0%), Copper(II) perchlorate hexahydrate ($Cu(ClO_4)_2 \cdot 6H_2O$, p⩾98.0%), Ammonium thiocyanate (NH_4SCN , p⩾99.0%) and triethanolamine (TEA, $C_6H_{15}NO_3$, p⩾99.5%) were used as precursors for the electrodeposition of CuSCN.All chemicals were purchased from Aldrich chemicals and used as received.The experimental set-up used to prepare α-Fe_2O_3 films consisted of a computer-controlled potentiostat/galvanostat and a classical three-electrode electrochemical cell. The electrochemical cell was filled with an electrolyte solution containing deionized water + 5mM $FeCl_3$ +5mM KF+ 1M H_2O_2 + 0.1 M KCl. The working electrode (WE) is a fluorine-doped tin oxide (FTO) coated glass having a sheet resistance of 10 Ω/□;it was previously cleaned in an ultrasonic acetone bath for 15 min and then rinsed in distilled water and dried. Pt and Ag/AgCl electrodes were used as counter-electrode and reference electrode, respectively. The films were deposited by cathodic electrodeposition. In order to have a thickness of approximately 500 nm for all Fe_2O_3films, the deposition potential was fixed at - 0.1V and the debited charge was 1.2 C. The temperature of the solution was fixed at 298 K by a thermostat. After the deposition process, the films were rinsed with distilled water. To obtain the desired α-Fe_2O_3phase, the deposited films were annealed at 650°C for 2hin air. The electrodeposition of CuSCN was performed in the same way thanthe Fe_2O_3 films. The deposition potential was fixed at -0.4 V and the debited charge was 1C giving rise to a film thickness a of about 3µm. The temperature of the solution was fixed at 333 K by a thermostatic bath. The electrolytic bath was prepared from 0.1M $KClO_4$, 0.01 M $Cu(ClO_4)_2 \cdot 6H_2O$, 0.05 M NH_4SCN and 0.06 M TEA ($C_6H_{15}NO_3$). About 0.5-1.0 mL of 2 M NH_3 was added to the electrolyte to keep the pH of the solution around 9.

2.2. Materials characterization

The crystal structure of α-$Fe_2O_3$and α-Fe_2O_3/CuSCN heterojunction were investigated by XRD (Rigaku Ultima IV diffractometer in the Bragg-Bentano configuration) using the CuKα radiation (λ = 1.54060 Å). The microstructural and elemental analyses were characterized using a Zeiss ULTRA 55 model scanning electron microscope (SEM) equipped with an energy dispersive spectroscopy (EDS) system. To determine the band gap energy was estimated from the optical absorption, which was measured by recording the transmission

spectra using a UV-Visible spectrophotometer (Ocean Optics HR4000) coupled to an integrating sphere (in order to collect both specular and diffuse transmittance).

The photoluminescence (PL) was measured using a He-Cd laser (λ=325 nm) and a Jobin Yvon-Horiba spectrometer coupled to a Hamamatsu back-thinned Si-CCD detector.

2.3. Photoelectrochemical and electrochemical analyses

The PEC measurements were performed in a quartz cell to facilitate the light reaching the photoelectrode surface. The light exposed surface of the working electrode is 0.25 cm^2. The electrolyte used in all PEC measurements is 1.0M NaOH (pH = 13.6). The electrolyte was purged with nitrogen gas before the experiments in order to prevent any possible reaction with dissolved oxygen at the counter-electrode. A potentiostat/galvanostatAutolab PGSTAT302N (Metrohm, Netherlands) with a Pt rod counter-electrode and an Ag/AgCl saturated in 3 M KCl reference electrode was used.The films were illuminated with a 150 W Xenon lamp (PLSSXE300/300UV) coupled to a chopper and a selective blue filter (λ >400 nm).The set-up was completed with an automatic shutter and a filter box. The whole system was controlled by a homemade software. The J-V curves were monitored by linear sweep voltammetry (LSV) at 100 mV/s setting the potentiostat in the range of 0V to +0.8 V vs Ag/AgCl. The chronoamperometry curves of the films were also obtained at +0.1 V both in dark and under illumination with an intensity of about 1 SUN (100 mW cm^{-2}) at the film surface. Mott–Schottky measurements were performed using an electrochemical impedance analyzer in the three-electrode configurationin a 0.1 M NaOH electrolyte solution; theAC amplitude was 10mV and the frequency was in the 100 kHz - 0.1 Hzrange. The flat band potential (V_{fb}) and the donor density (N_D) were determined in the dark from the impedance measurements.

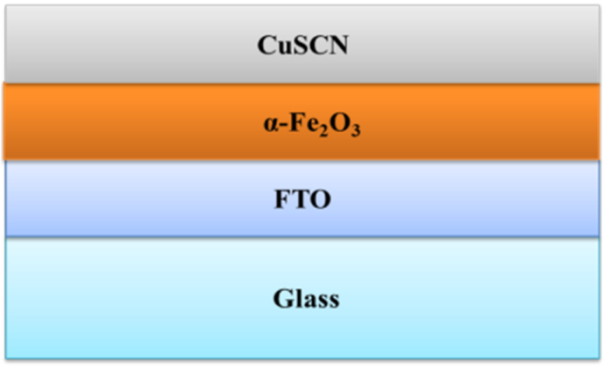

Schematic cross-sectional view of heterojunction: FTO glass, compact α-Fe_2O_3, and CuSCN (HTM).

3. Results and discussion

Figure 1 shows a schematic cross-sectional view of the α-Fe_2O_3/CuSCN heterojunction deposited on FTO glass substrates.

3.1. Potential variation

Figure 2.a shows the cyclic voltammogramof the Fe_2O_3films recorded at 50 mV/s.During the negative sweeps Fe^{3+} was reduced to Fe. In the reduction region, the film is deposited at apotential ranging between –0.2 and 0 V. These films showed negligible photo-activity and were not further characterized[29].Furthermore, in the positive sweep the films were deposited by an electrochemical oxidation of the Fe^{2+} ions to Fe^{3+} ions followed by precipitation of Fe^{3+} ions as ferric hydroxide (Fe $(OH)_3$). The anodic deposition of the Iron oxide is represented by the following equations [30].

$$Fe^{2+} \leftrightarrow Fe^{3+} + e^- \quad \textbf{(4)}$$

$$Fe^{3+} + 3OH^- \rightarrow Fe(OH)_3\downarrow \quad \textbf{(5)}$$

Figure 2.b shows a cyclic voltammogram performed at 200mV/s ontoaα-Fe_2O_3 electrode using the electrolytic solution described in the experimental section. The voltammetric scan was initiated at 0 V towards the negative direction of up to -0.8 V. The cathodic threshold potential for the reduction of Cu^{2+} to Cu^+ ions in the solution is about -0.20 V. The cathodic current increases slowly to -0.40 V, then steeply up to -0.60V, and then becomes almost constant. The initial slow increase of the current indicates the existence of Cu(II)-TEA complexes in the solution that results in slow diffusion leading to a shift of the reduction potential to more negative values as well as small cathodic reaction current density [31]. The electrodeposition of CuSCN is manifest when a white film appears on the electrodesurface at about -0.30Vand subsequently grows rapidly as the potential increases up to -0.60 V, which is referred to as the kinetically controlled region. In the potential range -0.60 to -0.80 V, the saturation current density indicates that the diffusion process reaches a limit accompanied with a minor co-deposition of copper. Small brown spots are observed in the film when the deposition potential was above -0.60 V. The voltammetric scan from -0.80 to 0.40V shows a sharp peak at about -0.20 V, which means that the CuSCN layer acts as a passivating layer for the α-Fe_2O_3 electrode. Another maximum around 0.30 to 0.40 V is related to the oxidation of

Cu^{+} to Cu^{2+} ions. Hence, the growth process of the CuSCN film from the TEA chelated aqueous solution suggests that the cupric ions related to the Cu(II)-TEA complexes and stabilized in the electrolyte solution, were first reduced to cuprous ions ($Cu^{2+}+e^{-}\rightarrow Cu^{+}$), and then the CuSCN film forms from the reaction between cuprous ions and thiocyanate ions ($Cu^{+}+SCN^{-}\rightarrow CuSCN$). Such a deposition takes place in a potential ranging between -200 and -550 mV. Thereafter, Cu codeposition would occur. Hence, one may conclude that the appropriate deposition potentials in the sole deposition of CuSCN in the TEA-chelated aqueous solution should be selected in the potential range of -200 to -550 mV. To further study the influence of the composition of the electrolytic bath on the nucleation and growth of the CuSCN films electrodeposited on the α-Fe_2O_3surface, chronoamperometry measurements based on current transient recorded during the electrodeposition process at -0.40 V were performed. Figure 3 shows the chronoamperometry for a CuSCN film depositesd from an electrolyte containing Cu and SCN in the molarproportion of 1:1.5. The rapid surge in the current density observed at the onset of the applied potential is due to the double layer charging, and then, the current density decayed gradually due to an increase in the electric resistance of the electrochemical system related to nucleation and growth of CuSCN crystals having semiconductor characteristics[32]. After an interval of about 200 s, there is a gradual increase of the current density for a period of time and then the current density becomes constant.

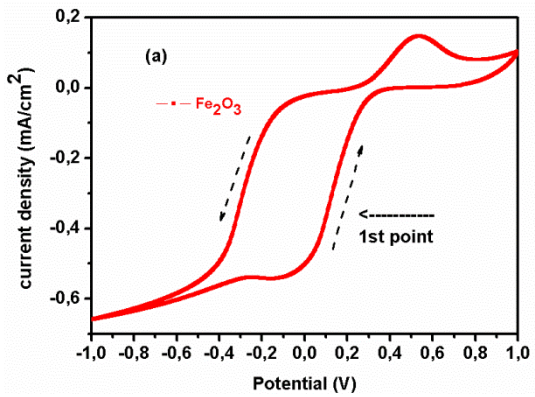

Figure 2.a: Linear sweep voltammetry of Fe_2O_3 precursor solution in the range of -1V to 1V on the indium fluoride oxide electrode at a rate 50mVs^{-1}.

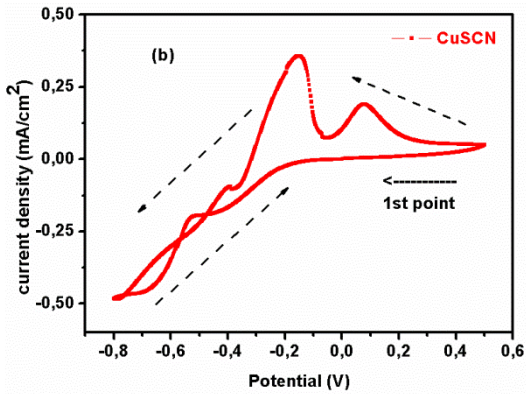

Figure 2.b: Linear sweep voltammetry of CuSCN precursor solution in the range of -0.8V to 0.6V at a rateof 200 mVs^{-1}.

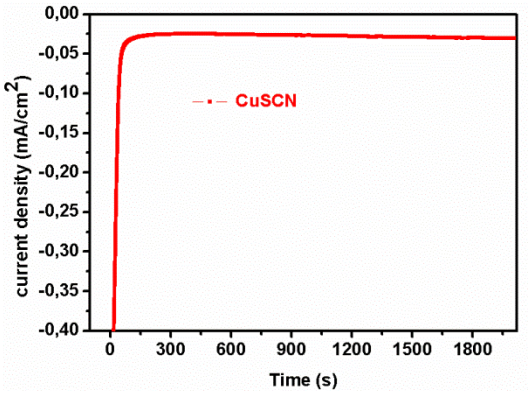

Figure 3: Chronoamperometry of CuSCN with a Cu: SCN ratio of 1:1.5.

3.2. Morphological, chemical composition and structural characterizations

Figures 4a and 4b display the FESEM images of the CuSCN and the α-Fe_2O_3 films deposited on FTO substrates, respectively.FESEM image of CuSCN(Figure 4a) shows a mixture of leafy and intrinsic trigonal pyramid shapes with some dispersion in the grain sizes. Figure 4b shows the morphology of the α-Fe_2O_3films, revealing nanostructured grains having a size dimension of about 20 nm. Figures4 c and 4d show the CuSCN films deposited on α-Fe_2O_3 covered substrates at different magnifications. For CuSCN films deposited on α-Fe_2O_3only trigonal pyramid shapes with bigger grain sizes of approximately 3 μm are observed. On the other hand, one may notice that the grainsize of CuSCN films deposited on α-Fe_2O_3 are greater than those deposited on FTO.

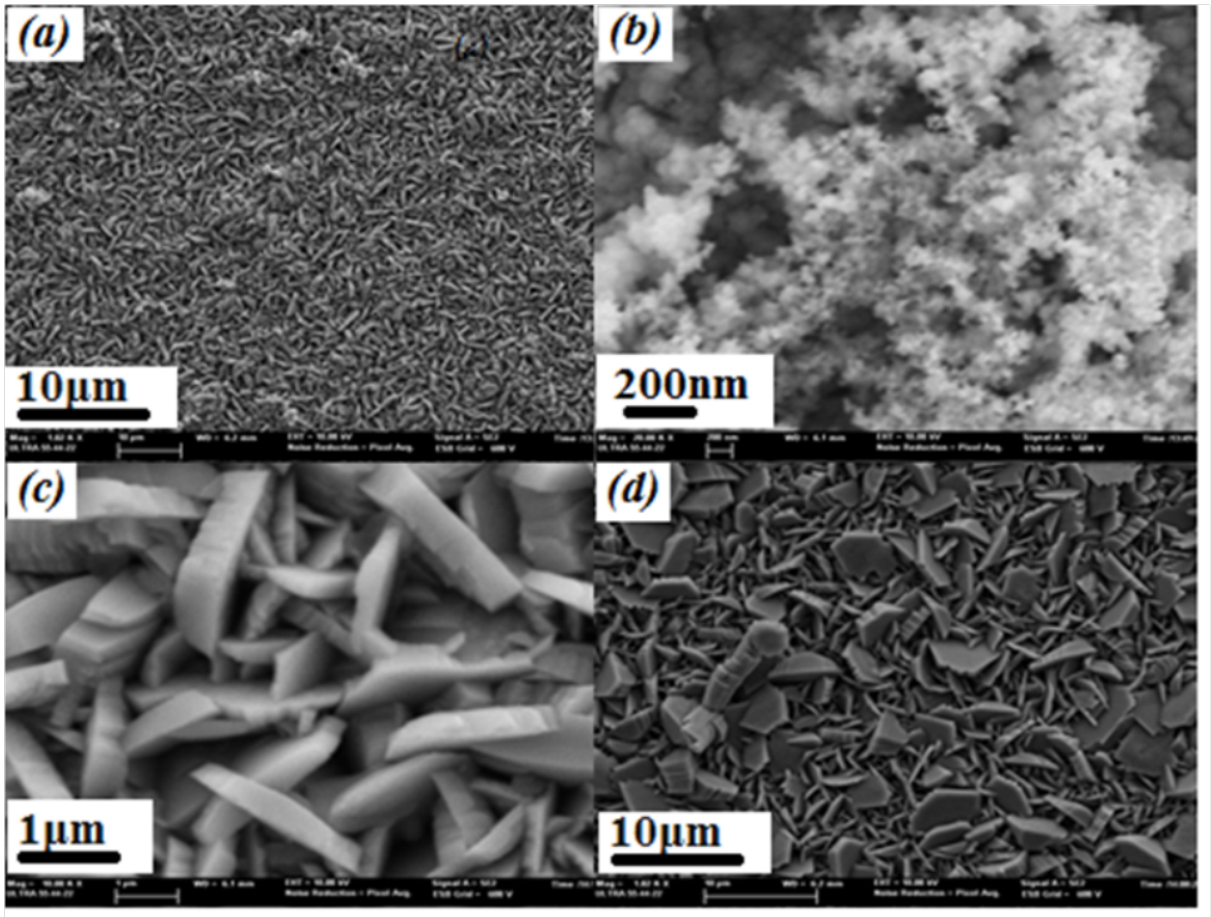

Figure 4: FESEM images for (a) CuSCN (b) α-Fe_2O_3(c) α-Fe_2O_3/CuSCN (1µm) (d) α-Fe_2O_3/CuSCN (10µm).

Figure 5 shows vertical cross section images of α-Fe_2O_3 (Figures 5 a-b), CuSCN (Figure 5c) and α-Fe_2O_3/CuSCN (Figure 5d) thin films deposited on FTO glass. The thickness of theα-Fe_2O_3films is about 500nm and that of the CuSCN layer is about 3.7 µm. Figure 5d shows a cross-sectional FESEM image of the complete device (FTO/α-Fe_2O_3/CuSCN). The overall thickness between the border of the FTO layer and the top of the CuSCN layer corresponding to the α-Fe_2O_3/CuSCNheterojunction is about 4. 2µm.The stoichiometric proportions of the CuSCN films prepared in an electrolyte solution having a molar ratio [Cu^{2+}]/[SCN^-] of 1:1.5 at a static potential of -400 mV and a temperature of 333 K were estimated by EDX analyses.

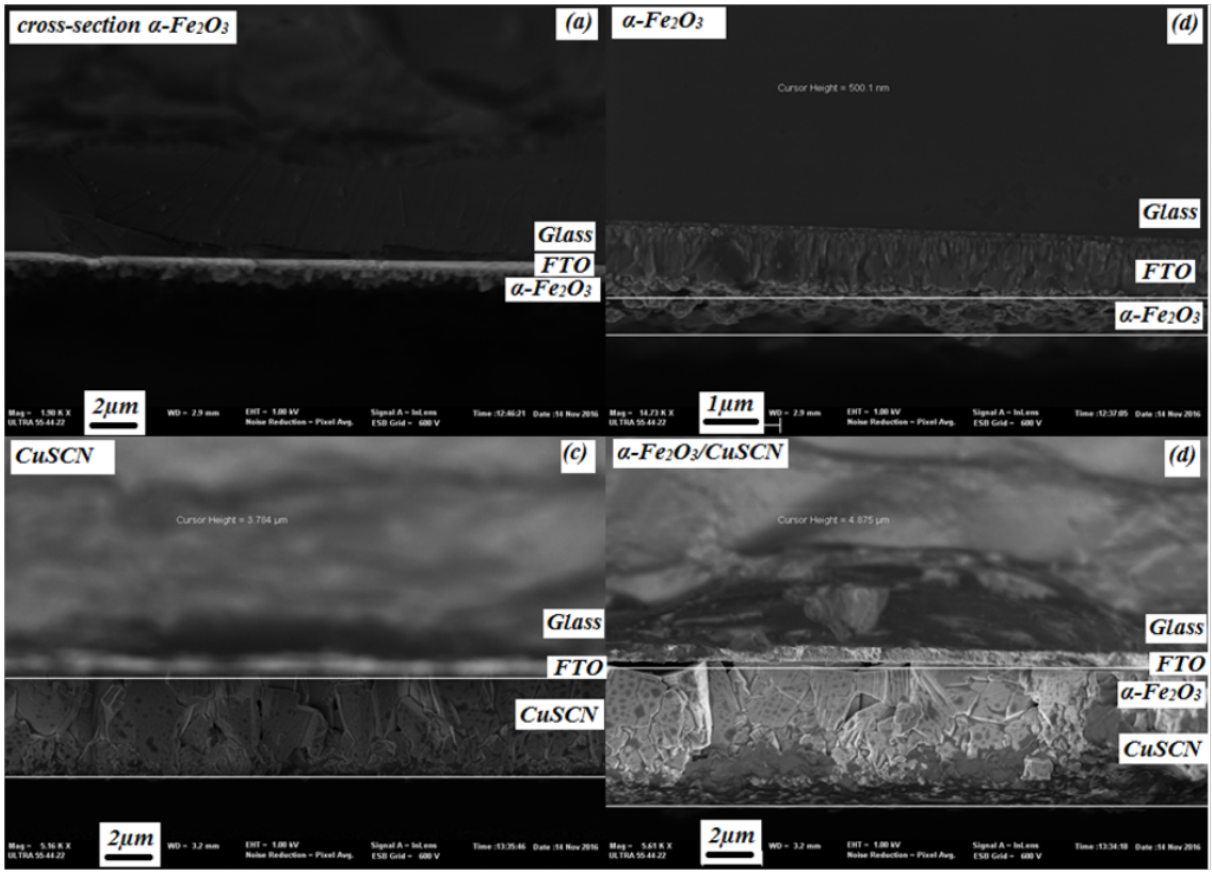

Figure 5: Vertical cross section of (a-b)α-Fe_2O_3, (c) CuSCN and (d) heterojunction thin films.

Figures 6a and 6b show EDXelemental analyses of the electrodeposited α-$Fe_2O_3$and CuSCN, respectively. The line observed at 0.72 keV corresponds to the L line of Fe, while the oxygen K line is peaking at 0.525 keV. The calculated atomic ratio of Fe and O is approximately equal to 2:3, which well agrees with the stoichiometric composition of α-Fe_2O_3. The percentages of the elements calculated from the EDX spectra are shown in the inset of figure 6a. Figure 6b shows the EDX spectrum of the electrodeposited CuSCN film; only lines corresponding to Cu, S, C and N are observed. The inset in Figure 6b displays the calculated percentages for the elements of the CuSCN film. The content of S in CuSCN film represents the SCN content in the film, as S is not provided from environmental impurities. It is reported in the literature that when SCN is in stoichiometric excess, $Cu(SCN)_{(1+x)}$ would show p-type semiconductor characteristics [33]. It may be pointed out that the composition of the films in the above reference [32,34] is determinedfrom the X-ray photoelectron spectroscopy (XPS) technique. In the XPS technique, only the composition of the surface is determined, which is released from the excess of SCN ions during the growth of the film, and it is very likely that some SCN ions might have been adsorbed on the surface, and consequently XPS analysis

would show a stoichiometric excess of SCN.However, in the work of Zang et al. [35], the composition of the film determined by EDX analysis showed a stoichiometric excess of copper and still the films behaved like a p-type semiconductor like of that prepared herein. These results are confirmed by Mott–Schottky measurements performed on these samples, which reveal the p-type behavior of the electrodeposited CuSCN films (See Figure 14 b).

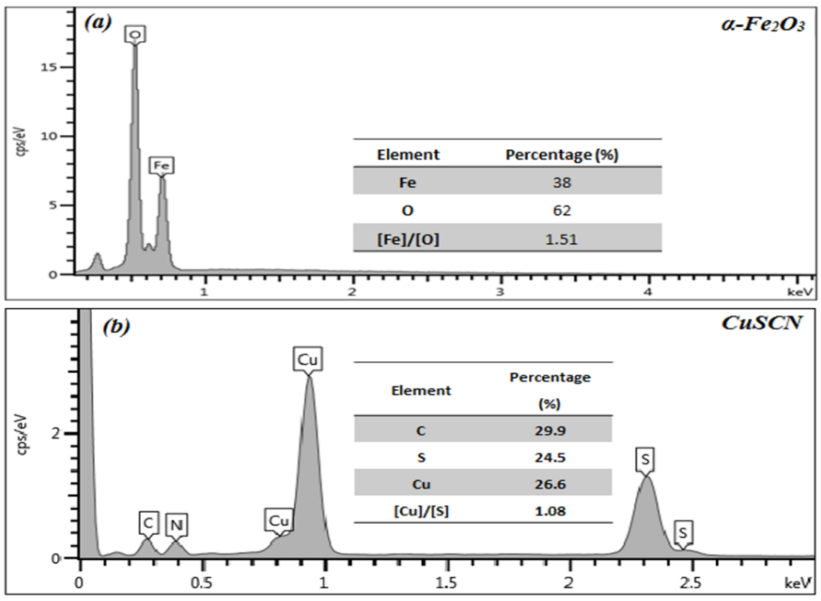

Figure 6: (a) EDX spectrum for α-Fe_2O_3,(b)EDX spectrum for CuSCN thin films

Figure 7 shows the XRD patterns of the Fe_2O_3 and CuSCN layers deposited on FTO substrates. The XRD patterns of the Fe_2O_3/CuSCN bilayer and the FTO substrates are also shown. The XRD peaks of the α-Fe_2O_3films are observed at 2θ = 24.1°, 33.1°, 35.6°, 40.9°, 49.4°, 54.0° and 64°, which correspond to the (012), (104), (110), (113), (024), (116) and (300) planes of the hematite phase, respectively. The dominant peaks are associated to the (104) and (110) planes. The diffraction peaks of the trigonal structure of the α-Fe_2O_3matches well with the reference pattern JCPDS card file n°33-0664, which corresponds to the space group R3c (167) with lattice parameters a = b = 5.03 nm and c = 13.74 nm.

It is well known that CuSCN exists in two polymorphic forms, α and β, where the β form is commonly available and more stable [36,37]. β-CuSCN has a hexagonal crystal structure where layers of SCN ions separate Cu cation planes and strong three-dimensionally Cu–S bonds interconnect these layers. For the CuSCN films, all diffraction peaks can be well indexed to the trigonal-phase β-CuSCN (space group R3m, n° 160). Compared with the standard diffraction pattern of CuSCN (JCPDS card file no. 29-0581), no specific peaks related to other phases of CuSCN or impurities can be observed, indicating a high purity and

crystallinity of the final products. For the Fe_2O_3/CuSCN bilayer, all peaks match the Fe_2O_3 and CuSCN patterns except those marked with asterisks that come from the FTO substrate.

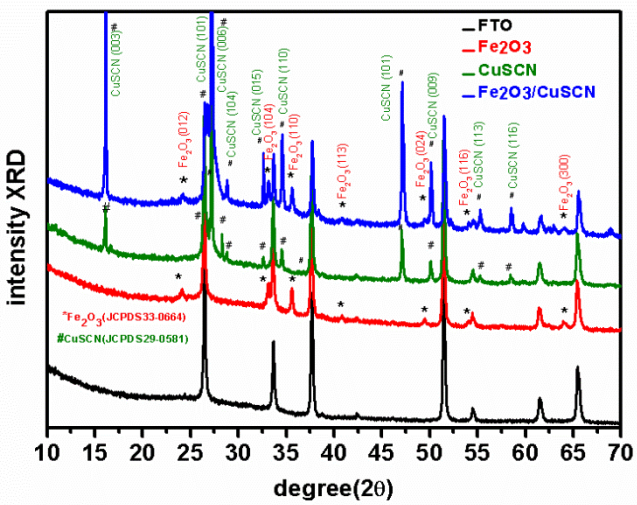

Figure 7: XRD spectra of FTO,α-Fe_2O_3, CuSCN and the Fe_2O_3/CuSCN bilayer.

3.3. Optical properties of CuSCN

Figure 8a and 8b show the transmission and absorption spectra of the CuSCN film and the α-Fe_2O_3, respectively. The energies of the optical bandgaps can be determined from the the transmission spectra [38].The transmittance spectrum of CuSCN (Figure 8a) shows a high optical transmission value above 60% in the visible range.A significant increase in the absorption below 320 nm can be assigned to the intrinsic band gap absorption of CuSCN.It appears that α-Fe_2O_3 films have a high absorbance in the visible region, indicating their applicability as an absorbing material [39](Figure 8b).

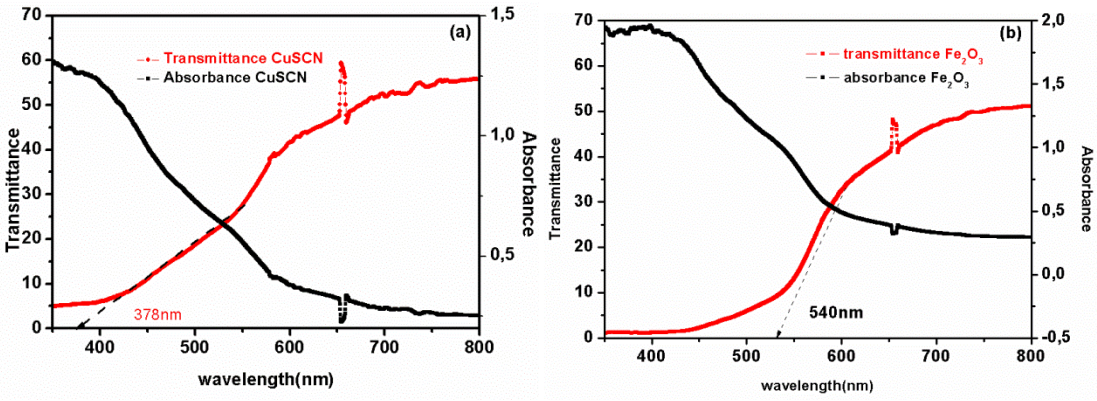

Figure 8: Transmittance and absorbance spectra of CuSCN(a) and α-Fe_2O_3 (b).

To calculate the optical band-gap energy (E_g) of the films, the absorption coefficient can be estimated as follows**:**

$$\alpha = \frac{1}{d} \ln\left(\frac{1}{T}\right) \qquad (6)$$

The relation between the absorption coefficient **α** and the energy of the incident light ***hv*** is given by [40]: $\alpha h\nu = A\,(h\nu - Eg)^n$ **(7)**

where ***α*** is the absorption coefficient, ***A*** is a constant, ***h*** is the Planck's constant, ***v*** is the photon frequency, ***Eg*** is the optical band gap, and***n*** is equal to 2 for direct transition, and to 1/2 for indirect transition. According to the Tauc plot(($\alpha h\nu)^2$vs.***hv*)** (Fig. 9), the optical band gap ***Eg*** of the typical CuSCN film is about 3.3 eV. Jaffe et al.[41]predicted the existence of an indirect bandgap of 3.5 eV from an electronic band structure model calculated using the density functional theory, although absorption measurements performed on CuSCN samples indicated the presence of an indirect bandgap of 3.9 eV.Figure 9 depicts the Tauc plot of α-Fe_2O_3 films. One may point out direct band gap energy of about 2.1 eV, which is smaller than that of bulk α-Fe_2O_3 (2.3 eV) [42].

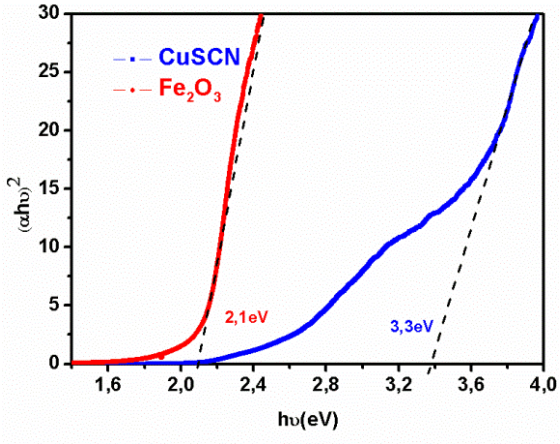

Figure 9: Tauc plot of CuSCN and α-Fe_2O_3

Figure 10 shows the normalized photoluminescence (PL) spectra for α-Fe_2O_3 and CuSCN films and for the α-Fe_2O_3/CuSCN bilayer, the excitation wavelength is the 325 nm of a He-Cd laser. The PL spectrum of the α-Fe_2O_3 shows a wide PL peak centered around 623 nm with a Full Width at Half Maximum (FWHM) of about 100 nm. The PL spectrum of CuSCN exhibits a broad band centered at 590 nm and slightly shifted to higher energy as compared to α-Fe_2O_3. Radiative transitions in CuSCN would involve deep levels (located near the middle of the gap) because the energy of the emitted photons is approximately half of the band gap energy. The PL spectrum of the Fe_2O_3/CuSCN bilayer is indistinguishable of the PL spectrum of α-Fe_2O_3. Fig 11a depicts a scheme of the energy band diagram corresponding to α-Fe_2O_3 and CuSCN before and after the formation of the heterojunction. This scheme is useful to explain the PL behaviors. Radiative recombination mainly takes place in the Fe_2O_3 layer, which means that instead of recombining through CuSCN deep levels the photoelectrons generated in the CuSCN layer move to Fe_2O_3 where they recombine radiatively. As a result, the PL spectrum of the Fe_2O_3/CuSCN heterojunction does not show any recombination in the CuSCN layer.

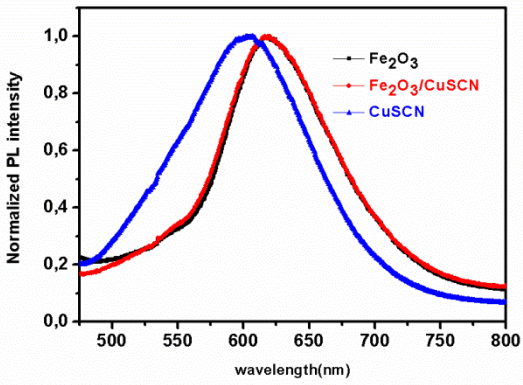

Figure 10:PL spectraof α-Fe_2O_3, CuSCN and Fe_2O_3/CuSCN.

3.4. Photoelectrochemical measurements

3.4.1. Current voltage characteristics

The nanostructured α-Fe_2O_3 and CuSCN films, and the α-Fe_2O_3/CuSCNheterojunction, were used as photoelectrodes in a photoelectrochemical cell, and current-voltage characteristics were recorded under dark and illumination. The externally applied bias was varied from 0V vs Ag/AgCl (cathodic bias) to 0.8 V vs Ag/AgCl (anodic bias).

Figure 12 shows the photocurrent density versus applied potential for all films. For the CuSCN films, the photocurrent slightly increases for potentials over 0.4 V and then remains constant up to 0.8V. For α-Fe_2O_3,the photocurrent continuously increases for potentials above 0.55 V. In the case of the α-Fe_2O_3/CuSCN heterojunction (Fig.12) the current density in the dark is negligible in all the potential range, while under illumination the photocurrent starts increasing continuously with the applied potential from 0.2 V; it is always higher than that observed for Fe_2O_3 and CuSCN independently. Both α-Fe_2O_3 and the α-Fe_2O_3/CuSCN heterojunctions behave like photoanodes under illumination. The photocurrent density exhibited by the α-Fe_2O_3/CuSCN heterojunction may be due to improved visible light absorption and to an efficient separation of the photogenerated charge carriers (Fig.11a).

A proposed mechanism for the enhanced photocurrent density heterojunction α-Fe_2O_3/ CuSCN sample can be described as follows: under visible light irradiation, both α-Fe_2O_3 and CuSCN could be excited; in that case an electron transfer occurs from the CuSCN conduction band to that of the α-Fe_2O_3, which in turn may lead to hydrogenproduction at the counter-electrode. This transfer process is thermodynamically favorable since the valence and conduction bands in CuSCNbecome more negative than thatof the α-Fe_2O_3band levels, which in turn enhances the separation of the photogenerated charge carriers.After an initial decay in the photocurrent observed in the first illumination cycle the photocurrent tends to keep constant under long-term illumination that means an effective charge separation inside the α-Fe_2O_3/CuSCN heterojunction.A similar type of band positioning and charge carrier movement has also been reported earlier in case of TiO_2/Si [43], CuO/ ZnO [44], $CuFe_2O_4$/TiO_2[45], Bi_2O_3/$BiVO_4$[46], and MoS_2/CdS [47].

The measurements of the photocurrent under pulsed light were achieved using a chronoamperometry technique (Fig. 13.a). In the steady state, the α-Fe_2O_3/FTO electrode shows aphotocurrent density f about 5μA/cm^2.However, the α-Fe_2O_3/CuSCN/FTOheterojunction shows a photocurrent densityof about 15μA/cm^2, which is3 times bigger than that of the α-Fe_2O_3/FTO electrode. Figure 13b showsthe variation of the photocurrent density versus elapsed time during switch on/offof light for both α-Fe_2O_3/FTO and α-Fe_2O_3/CuSCN/FTO electrodes. The photocurrent density drops in the first two cycles and then was steady and quasi-reproducible after several on–off cycles of light, with no overshoot at the beginning or the end of the on–off cycle, indicating that the direction of the electron diffusion isfree from grain boundaries, which can create traps to hinder electron movement and slow down the photocurrent generation[48].

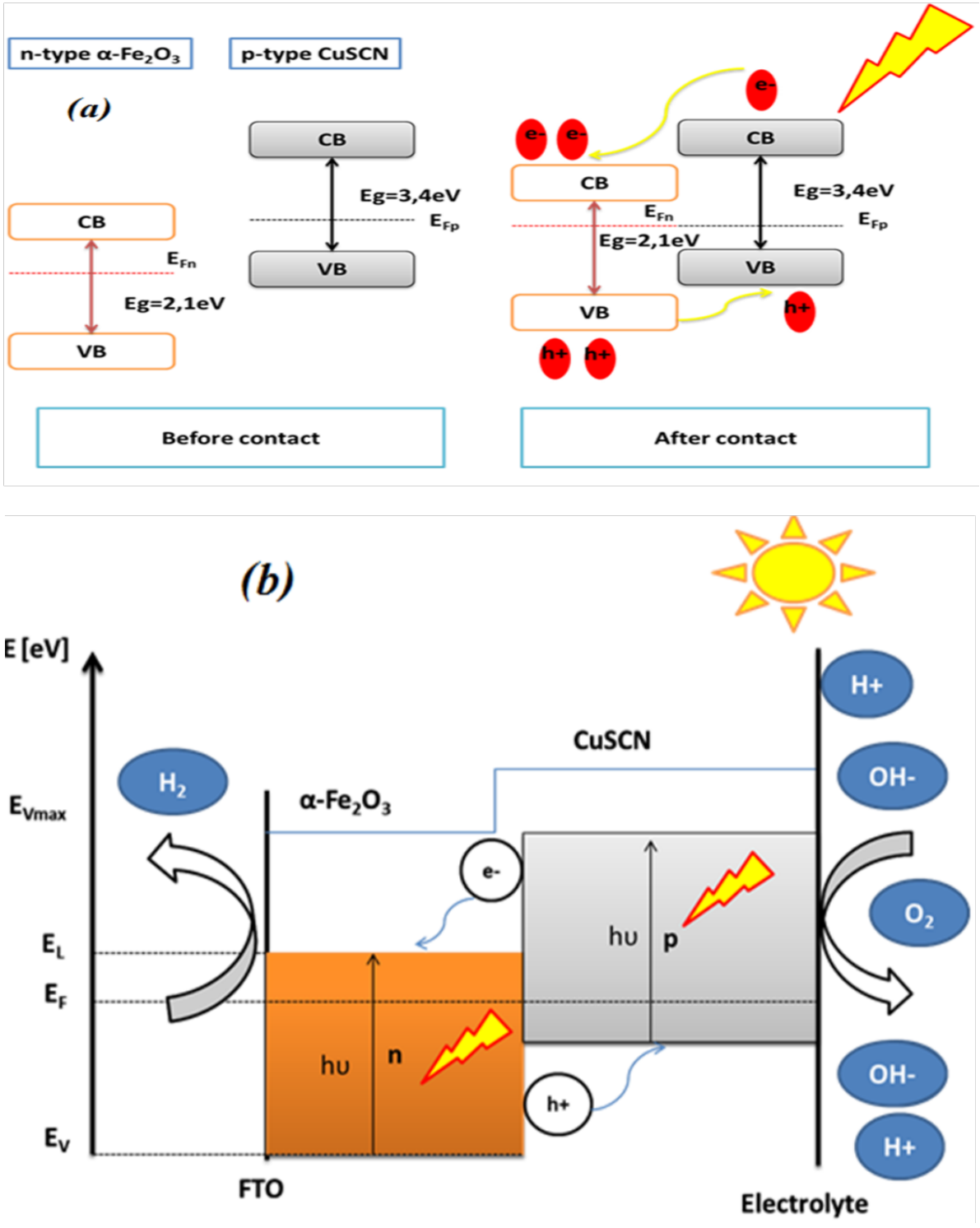

Figure 11: (a) Energy band diagram of α-Fe_2O_3 and CuSCN before and after the formation p-n junction (b) schematic energy band diagram of the α-Fe_2O_3 and CuSCN heterojunction with the band bending and alignment due to the solution.

It is believed that deposition of CuSCN on α-Fe_2O_3 enhanced the photoactivity of the photoanode in two aspects: (i) the p–n junction can effectively extract holes and separate charge carriers, leading to enhanced photocurrent, and (ii) The loading of the heterojunction

photoanode with CuSCN further facilitates the electron transfer at the electrode/electrolyte interface and thus enhances the photoelectrochemical water oxidation.

To validate the energy band diagram suggested in Figure 11, we have made additional measurements of the photocurrent generated by the heterostructure under illumination with a wavelength that excites only the hematite (λ >400 nm).Figure 13c shows the photocurrent generated by the α-Fe_2O_3/CuSCN heterostructure under white light illumination and under light illumination with λ >400nm. When using white light both α-Fe_2O_3 and CuSCN are exited and the charge transfer is that shown in Figure 11 (b); holes generated in the hematite are transferred to the valence band of the CuSCN and photogenerated electrons in the CuSCN are transferred to α-Fe_2O_3. When illuminating at wavelengths higher than 400 nm (λ >400 nm) only the hematite part is excited and the measured photocurrent is due to the charge transfer from α-Fe_2O_3 to CuSCN. As expected the photocurrent is lower in this case because the charge transfer from CuSCN to α-Fe_2O_3 has not been activated.

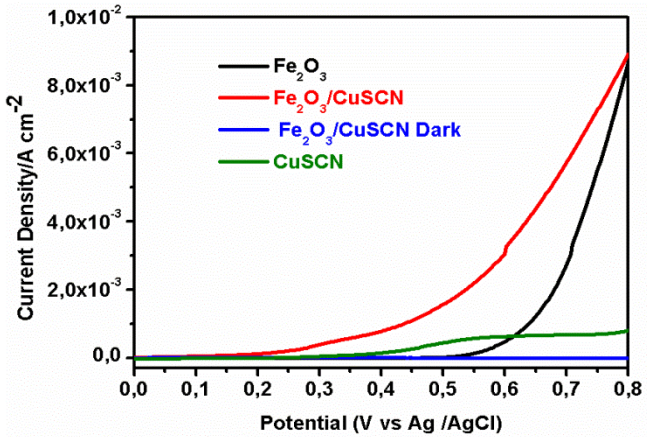

Figure 12:I-V characteristics of the α-Fe_2O_3, CuSCN and Fe_2O_3/CuSCN electrodesinthe dark and under illumination.

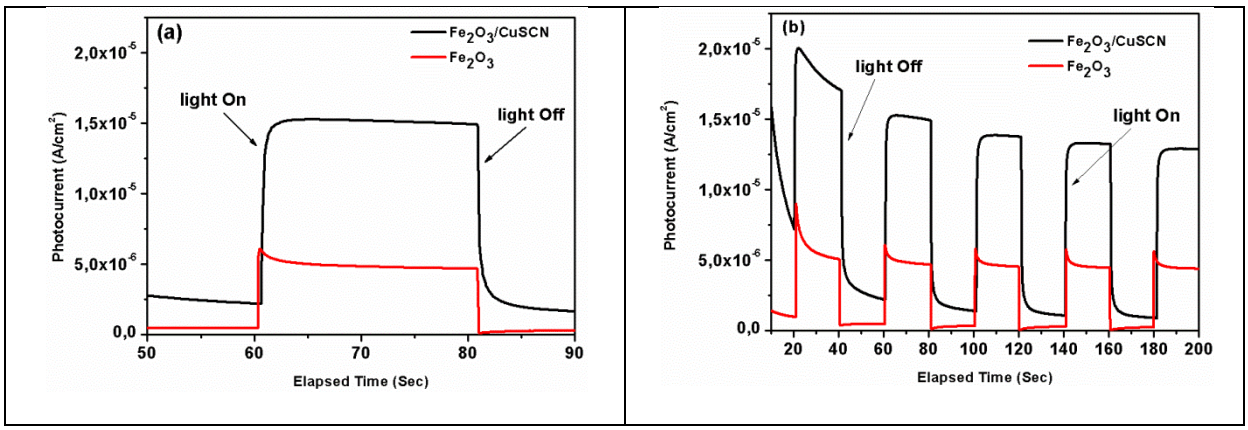

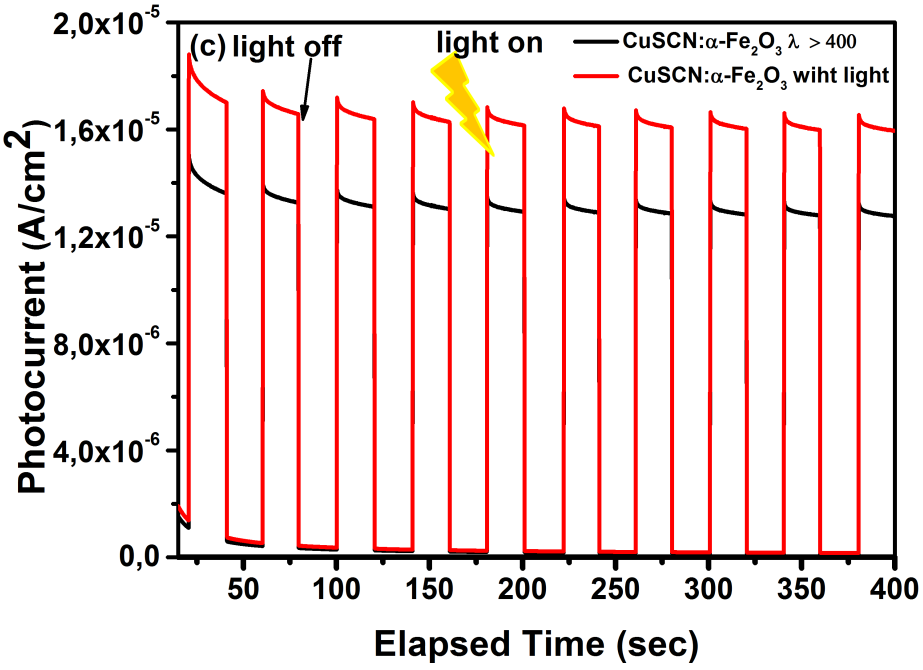

Figure 13:(a) Photocurrent intensity for α-Fe_2O_3 and α-Fe_2O_3/CuSCN electrodes under on/off illumination, measured in 1M NaOH electrolyte under a bias potential of +0.1 V, (b) Time dependence of the photocurrent intensities forα-Fe_2O_3 and α-Fe_2O_3/CuSCN electrodesunder successive illumination cyclesand (c) Time dependence of the photocurrent intensities for α-Fe_2O_3/CuSCN electrode under on/off illumination cycles (white light and λ>400 nm).

3.4.2. Mott–Schottky analysis

The Mott–Schottky plot ($1/C^2$vs applied potential) was obtained and analyzedfor all the samples. The flat band potential is an important physical property as regard tothe performance of the material in photoelectrochemicalwater splitting. Both N_D and E_{fb} were estimated from the Mott-Schottky equations (Eqs. 8and 9) [49]:

$$\frac{1}{{C_{SC}}^2} = \frac{2}{e\,\varepsilon\,\varepsilon_0 N_D {A_S}^2}\left(E - E_{fb} - \frac{KT}{e}\right) \text{for n-type semiconductor} \qquad \textbf{(8)}$$

$$\frac{1}{{C_{SC}}^2} = -\frac{2}{e\,\varepsilon\,\varepsilon_0 N_D {A_S}^2}\left(E - E_{fb} + \frac{KT}{e}\right) \text{forp-type semiconductor} \qquad \textbf{(9)}$$

where, e is the electron charge, ε is the dielectric constant of the semiconductor, ε_o is the vacuum permittivity, A_S is the surface area of the working electrode, k is the Boltzmann's constant, and T the temperature.The positive slopes confirm that α-$Fe_2O_3$is a n-type semi-conducting material, and the negative slopes indicate that the CuSCN is a p-type semi-conductingmaterial. The calculated donor density increases from $1.6\cdot10^{21}$ cm^{-3}forthe α-Fe_2O_3 photoanodeto $2.8\cdot10^{21}$ $cm^{-3}$for α-Fe_2O_3/CuSCN. By taking the x-axis intercept of the linear fit to the Mott-Schottky plots, the flat band potential was estimated to be -0.14 V vs Ag/AgCl for

the α-Fe_2O_3photoanode, and to -0.64V vs Ag/AgCl for the α-Fe_2O_3/CuSCN heterojunction (Fig. 14a and 14c).

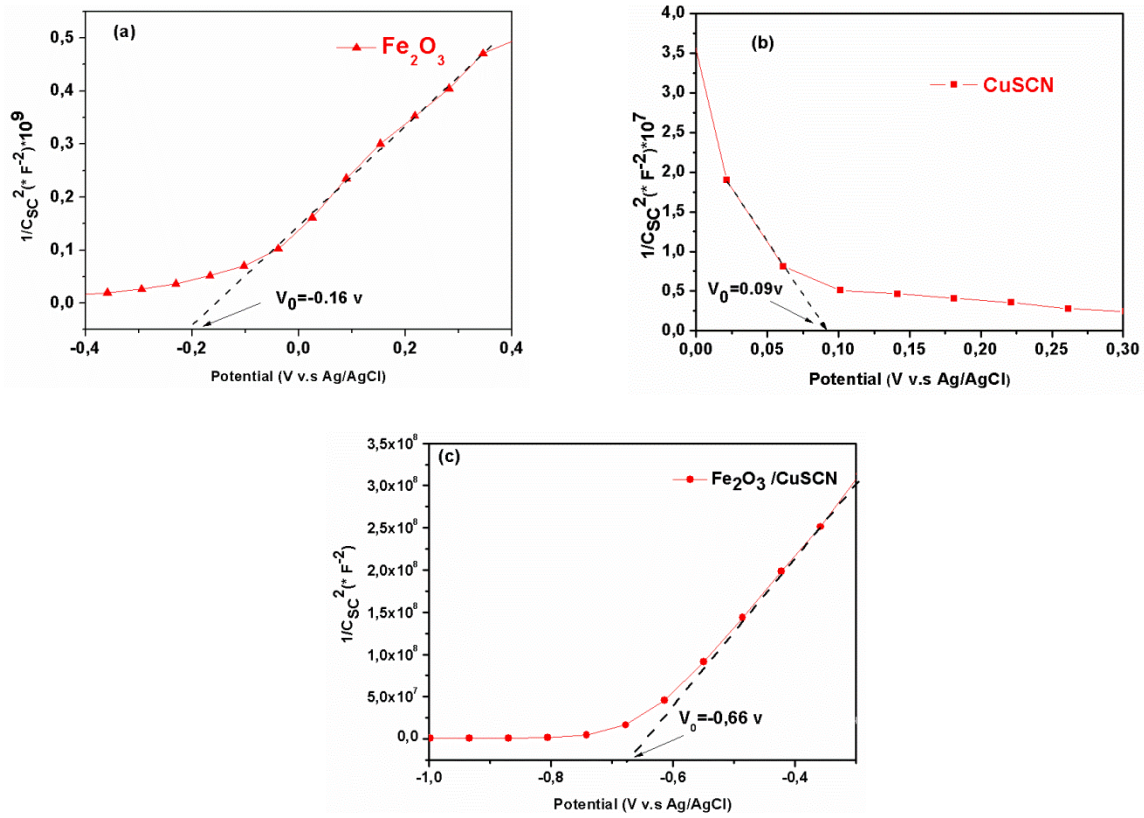

Figure 14:Mott–Schottky plot for (a) α-Fe_2O_3, (b) CuSCN, (c) α-Fe_2O_3/CuSCN.

4. Conclusions

Semiconducting materials such as n-Fe_2O_3 and p-CuSCN were successfully electrodeposited on FTO substrates. Chelating agents and a weak basic electrolyte solution of NH_3were used to avoid acidic etching of the α-Fe_2O_3. This enables us to study the energetic behavior of both semiconductors and the n-Fe_2O_3/p-CuSCN heterojunction performances as regard to photoelectrochemical applications.FESEM shows that CuSCN can easily grow thicker to cover the α-Fe_2O_3substrate. EDX analyses revealed that CuSCN films have a slight excess of copper. The photoelectrochemical performance of the nanostructured α-Fe_2O_3/CuSCN heterojunction is higher than that of FTO/α-Fe_2O_3 and FTO/CuSCN.A maximum photocurrent density of 2.9 mA/cm^2 at 0.59 V versus Ag/AgCl was exhibited for the α-Fe_2O_3/CuSCN photoelectrode. The improvement of the photocurrent density is attributed of two major combined factors: (i) generation of anelectric field inthe heterojunction that suppresses the recombination of photogenerated charge carriers and (ii) application of an adequate external bias favoring the transfer and separation of the photogenerated charge

carriers in the α-Fe_2O_3/CuSCN heterojunction. Enhancement in the photocurrent density has also been attributed to an appropriate band edge alignment of the semiconductors that enhances lightabsorption inboth semiconductors.

Références article 2

[1]R. Brimblecombe, G. Charles Dismukes, Gerhard F. Swiegers and Leone Spiccia, Molecular water-oxidation catalysts for photoelectrochemical cells, Journal Homepage, Dalton Transactions, (43), 9374-9384,(2009).

[2]M. S. Prévot and K. Sivula, Photoelectrochemical Tandem Cells for Solar Water Splitting J. Phys. Chem. C 117 17879–17893(2013).

[3]A. Valdés, J. Brillet, M. Grätzel et al., Solar hydrogen production with semiconductor metal oxides: new directions in experiment and theory Phys. Chem. C hem. Phys , 14 , 49–70,(2012).

[4]A. B.Murphy, P. R. F.Barnes, L. K. Randeniya, I. C. Plumb, Grey, M. D. Horne, &J. A Glasscock, Efficiency of solar water splitting using semiconductor electrodes. International Journal of Hydrogen Energy, 31(14), 1999-2017, (2006).

[5]Z.B. Chen, T. F. Jaramillo, T. G. Deutsch, A. Kleiman-Shwarsctein, A. J. Forman, N. Gaillard, R. Garland, K. Takanabe, C. Heske, M. Sunkara, E. W. McFarland, K. Domen, E. L. Miller, J. A. Turner and H. N. Dinh, J. Mater. Res, 25, 3, (2010).

[6]K. Sivula, F. L. Formal, M. Grätzel, Solar water splitting: progress using hematite (α-Fe_2O_3)photoelectrodes.ChemSusChem, 4, 432−449,(2011).

[7]T.W. Hamann, Splitting water with rust: hematite photoelectrochemistry, Dalton Trans., 41,7830−7834,(2012).

[8]J.H.Kennedy, & K. W. Frese, Photooxidation of water at α-Fe2O3 electrodes. Journal of the Electrochemical Society,125(5) 709-714, (1978).

[9] A.W. Damon, W.Gongming,L.Yichuan,L.YatandZ. Z.Jin, Nanostructured hematite: synthesis, characterization, charge carrier dynamics, and photoelectrochemical properties Energy Environ. Sci. 5,6682−6702,(2012).

[10] K. Sivula, F. L. Formal and M. Gra¨tzel, Chem. Mater., 2009, 21, 2862–2867.

[11] Y.-K. Hsu, Y.-C. Chen and Y.-G. Lin, ACS Appl. Mater. Interfaces, 2015, 7, 14157–14162.

[12] M. T. Mayer, C. Du and D. Wang, J. Am. Chem. Soc., 2012, 134, 12406–12409.

[13]J. Li, F.Meng, S. Suri, W. Ding, F.Huang and N. Wu, Chem.Commun.,2012,48, 8213–8215.

[14] D. Sharma, S. Upadhyay, A. Verma, V. R. Satsangi, R. Shrivastav and S. Dass, Thin Solid Films, 2015, 574, 125–131.

[15] X. Wang, K.-Q. Peng, Y. Hu, F.-Q. Zhang, B. Hu, L. Li, M. Wang, X.-M. Meng and S.-T. Lee, Nano Lett., 2014, 14,
18–23.

[16] Y. Hou, F. Zuo, A. Dagg and P. Feng, Nano Lett., 2012, 12, 6464–6473.

[17]B.O'Regan, & D.T. Schwartz Efficient Photo-Hole Injection from Adsorbed Cyanine Dyes into Electrodeposited Copper(I) Thiocyanate Thin Films Chem Mater 7,1349–1354,(1995).
[18]L.B.Wang, B.L. Kang, P. Wang,Y. Qiu, Review of recent progress in solid-state dye-sensitized solar cells Sol Energ Mater SolCell 90,549–573,(2006).
[19] W. Luo, T. Yu, Y. Wang, Z. Li, J. Ye and Z. Zou, J. Phys. D: Appl. Phys., 2007, 40, 1091–1096.
[20] F. Boudoire, R. Toth, J. Heier, A. Brauna and E. C. Constable, Energy Environ. Sci., 2014, 7, 2680–2688.
[21] Y.-K. Hsu, Y.-C. Chen and Y.-G. Lin, ACS Appl. Mater. Interfaces, 2015, 7, 14157–14162.
[22]Y. Hou, F. Zuo, A. Dagg and P. Feng, Nano Lett., 2012, 12, 6464–6473.
[23] Y. Guo, Y. Fu, Y. Liu and S. Shen, RSC Adv., 2014, 4, 36967–36972.
[24] C. Miao, S. Ji, G. Xu, G. Liu, L. Zhang and C. Ye, ACS Appl. Mater. Interfaces, 2012, 4, 4428–4433.
[25] Y. Hou, F. Zuo, A. Dagg and P. Feng, Angew. Chem., Int. Ed., 2013, 52, 1248–1252.
[26] M. G. Ahmed, T. A. Kandiel, A. Y. Ahmed, I. Kretschmer, F. Rashwan and D. Bahnemann, J. Phys. Chem. C, 2015, 119, 5864–5871
27
[28] D. Sharma, S. Upadhyay, A. Verma, V. R. Satsangi, R. Shrivastav and S. Dass, Thin Solid Films, 2015, 574, 125–131.
[29]L. P. Wen, Y. J.Guo,S.H.I Zhi-qiang, H. Hua, L. Lang, Z. Yong-Nan, L. Guo-Dong and Z. Yong-cun, Preparation and Supercapacitive Properties of Fe2O3/Active Carbon Nanocomposite,s chem. res. chinese universities 28(5) ,780-783,(2012).
[30]W. Mao-Sung, and L. Rung-Hau, Electrochemical Growth of Iron Oxide Thin Films with Nanorods and Nanosheets for Capacitors, J. Electrochem. Soc. 156, A737,(2009).
[31]N.Yong, J. Zhengguo, Y. F. wand J. Am. Ceram. Soc., 90 [9], 2966–2973,(2007).
[32]B. Debasis,C.K. Suresh, M.C. Matthew, and SudiptaSeala, In situ synthesis of carbon nanotubes decorated with palladium nanoparticles using arc-discharge in solution method J. Phys. Chem. B 108, 556,(2004).
[33] K. Tennakone,A. H. Jayatissa SAN Fernando,S. Wickramanayake,S. Punchihewa,L. K. Weerasena,W. D. R. Premasiri,Semiconducting and Photoelectrochemical Properties of n- and p-Type β-CuCNS, Phys Stat Sol (a) 103,491–497,(1987).
[34]Ni, Yong, Zhengguo Jin et Yanan Fu ."Electrodeposition of p-type CuSCN thin films by a new aqueous electrolyte with triethanolamine chelation." Journal of the American Ceramic Society 90.9 (2007): 2966-2973.
[35]Q. Zang, H.Guo, Z. Feng, L. Lin, J. Zhou, Z .Lin, ElectrochimActa, 55(2010) 4889–4894.
[36]D. L .Smith, V.J .Saunders,ActaCrystallogr B 37,1807–1814,(1981).
[37]J.E.Jaffe, T.C. Kaspar, T.C. Droubay, T.Varga, M.E. Bowden, G.J. Exarhos, J Phys Chem C 114,9111–9117(2010).
[38] P. Pattanasattayavong, N.Yaacobi-Gross, K. Zhao, G. O. N. Ndjawa, Li J, F. Yan, B. C. O'Regan, A. Amassian and T. D.Anthopoulos, Hole-transporting transistors and circuits

based on the transparent inorganic semiconductor copper(I) thiocyanate (CuSCN) processed from solution at room temperature. Adv. Mater. 25,1504–9,(2013).
[39]A. A. AKl Applied science 233, 307-319,(2004).
[40]L. Dghoughi, B. Elidrissi,C. Bernède, M. Addou, M. Alaouilamrani,M. Regragui,H. Erguig, Applied surface sciences 253 ,1823-1829,(2006).
[41] J. E.Jaffe, T. C.Kaspar, T .C. Droubay, T. Varga, M. E. Bowden and G. J. Exarhos, Electronic and defect structures of CuSCN J. Phys. Chem. C 114,9111–7,(2010).
[42]M.R.Belkhedkar, A.U.Ubale; International journal of Materials and chemistry,4(5) ,109-116,(2014).
[43]D.Sharma,S.Upadhyay,V.R.Satsangi,R.Shrivastav,S. Dass, Improvedphotoelectrochemical water splitting performance of Cu2O/SrTiO3 heterojunction photoelectrode, J. Phys. Chem. C 118,25320,(2014).
[44]K.K. Baek, H.L. Tuller, Atmosphere sensitive CuO/ZnO junctions, Solid State Ionics 75, 179,(1995).
[45]A. Kezzim, N. Nasrallah, A. Abdi, M. Trari, Visible light induced hydrogen on the novel hetero-system CuFe2O4/TiO2, Energy Convers. Manag. 52, 2785,(2011).
[46]L. Chen, Q. Zhang, R. Huang, S.F. Yin, S.L. Luo, C.T. Au, Porous peanut-like Bi2O3-BiVO4 composites with heterojunctions: one-step synthesis and their photocatalytic properties, Dalton Trans. 41, 9513,(2012).
[47]L.Ying, X. Y.Yu, W.D. Zhang, MoS2/CdS heterojunction with high photoelectrochemical activity for H2 evolution under visible light: the role of MoS2, J. Phys. Chem. C 117,12949, (2013).
[48] M. Sookhakian, Y.M. Amin, S. Baradaran, M.T. Tajabadi,A. MoradiGolsheikh,W.J. Basirun, Thin Solid Films 552,204–211,(2014).
[49] G. Rahman, O.S. Joo, Electrodeposited nanostructured a-Fe2O3 thin films for solar water splitting: Influence of Pt doping on photoelectrochemical performance; Materials Chemistry and Physics 140, 316-322,(2013).

Article 3:

Influence of a compact α-Fe_2O_3 layer on the photovoltaic performance of perovskite-based solar cells

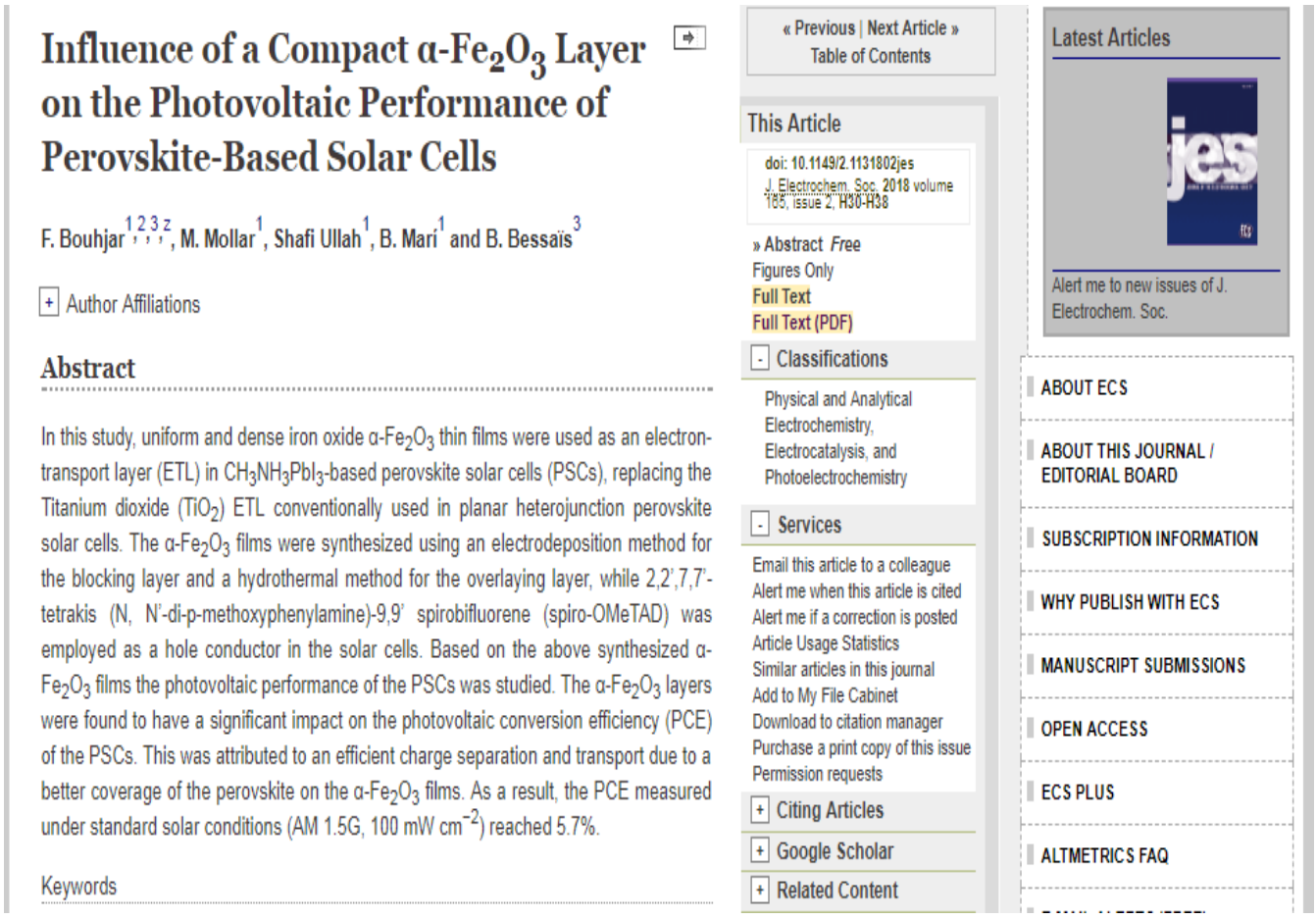

Influence of a Compact α-Fe_2O_3 Layer on the Photovoltaic Performance of Perovskite-Based Solar Cells

F. Bouhjar[1,2,3,z], M. Mollar[1], Shafi Ullah[1], B. Mari[1] and B. Bessaïs[3]

Author Affiliations

Abstract

In this study, uniform and dense iron oxide α-Fe_2O_3 thin films were used as an electron-transport layer (ETL) in $CH_3NH_3PbI_3$-based perovskite solar cells (PSCs), replacing the Titanium dioxide (TiO_2) ETL conventionally used in planar heterojunction perovskite solar cells. The α-Fe_2O_3 films were synthesized using an electrodeposition method for the blocking layer and a hydrothermal method for the overlaying layer, while 2,2',7,7'-tetrakis (N, N'-di-p-methoxyphenylamine)-9,9' spirobifluorene (spiro-OMeTAD) was employed as a hole conductor in the solar cells. Based on the above synthesized α-Fe_2O_3 films the photovoltaic performance of the PSCs was studied. The α-Fe_2O_3 layers were found to have a significant impact on the photovoltaic conversion efficiency (PCE) of the PSCs. This was attributed to an efficient charge separation and transport due to a better coverage of the perovskite on the α-Fe_2O_3 films. As a result, the PCE measured under standard solar conditions (AM 1.5G, 100 mW cm^{-2}) reached 5.7%.

Keywords

Influence of a compact α-Fe_2O_3 layer on the photovoltaic performance of perovskite-based solar cells

F. Bouhjar[a, b,c],M. Mollar[a],Shafi Ullah[a],B. Marí[a] and B. Bessaïs[b]

[a].*Institut de Disseny i Fabricació (IDF) - Departament de Física Aplicada, Universitat Politècnica de València, Camí de Vera s/n, 46022 València, Spain.*
[b].*Photovoltaic Laboratory, Research and Technology Centre of Energy, Borj-Cedria Science and Technology Park, BP 95, 2050 Hammam-Lif, Tunisia*
[C].*University of Tunis*

Abstract

In this study, uniform and dense iron oxide α-Fe_2O_3thin films are used as an electron-transport layer (ETL) in $CH_3NH_3PbI_3$-based perovskite solar cells (PSCs), in substituting the Titanium dioxide (TiO_2) ETL conventionally used in planar heterojunction perovskite solar cells. The α-Fe_2O_3 films were synthesized using an electrodeposition method for the blocking layer and a hydrothermal method for the overlaying layer, while 2,2',7,7'-tetrakis (N, N'-di-p-methoxyphenylamine)-9,9' spirobifluorene (spiro-OMeTAD) was employed as a hole conductor in solar cells. Based on the above synthesized α-Fe_2O_3 films the photovoltaic performances of the PSCs were studied. The α-Fe_2O_3 layers were found to have a significant impact on the photovoltaic conversion efficiency (PCE) of the PSCs. This was attributed to an efficient charge separation and transport due to a better coverage of the perovskite on the α-Fe_2O_3 films.As a result, the PCE measured under standard solar conditions (AM 1.5G, 100mW cm^{-2}) reaches 5.7%.

Keywords:*α-Fe_2O_3; Electrochemical deposition; hydrothermal deposition; XRD analysis; FESEM analysis; Optical properties; photoelectrochemical properties; $CH_3NH_3PbI_3$; perovskite solar cells.*

1. Introduction:

Up until now, organ metallictrihalide perovskites $CH_3NH_3PbX_3$ (X is iodine or a mixture of iodine, chlorine and bromine) have been considered as the most promising light absorption materials for solar energy conversion because of their wide absorption range [1], high extinction coefficient[2], ambipolar charge transport[3], and long electron–hole diffusion length[4]. However, recently, Perovskite-based solar cells (PSCs) have attracted increasing attention due to their superior performance and ease of fabrication. Indeed, spectacular progress in improving the photovoltaic performance has been achieved in this field, and the power conversion efficiency (PCE) of PSCs has been greatly increased surpassing 20% [5,6,7 ,8 ,9 ,10].

To further understand the material properties and the mechanisms of the functioning device, simplified planar heterojunction structured devices have become the focus of many research endeavours[11]. PSCs are usually composed of a fluorine doped tin oxide (FTO) conductive substrate, a compact electron-selective layer (ESL), a mesoporous scaffold layer (optional), an organic–inorganic hybrid perovskite layer, a hole-transporting material (HTM), and a metallic electrode [12].

The quality of the ESL and perovskite layers is indispensable to get efficient PSCs [13],and plays an important role in reducing thestructural and electronic defects in the films, which in turn can significantly affect the device performance. In the case of PSCs, a lot of emphasis has been placed on perovskite film processing and alternative hole transport materials, due to the high cost of 2,2’,7,7’-tetrakis-(N,N-di-p-methoxyphenamine)-9,9’-spiro-bifluorene (spiro-OMeTAD)[14].On the other hand, less attention has been paid to processing ESLs. Frequently integrated in PSCs as a promising ESL material, TiO_2 is a semiconductor with a wide band gap[15]. However, TiO_2 has low electron mobility, which might create unbalanced charge transport in the perovskite[16]**.** Besides, this compact layer often requires high temperature sintering at 450–500°C prior to use[17,18,19]making it incompatible with flexible substrates and easy fabrication. Indeed,Snaith et al[14]suggested that oxygen vacancies in the TiO_2 electrode are activated by UV light, which increase charge traps causing the degradation of the PCEs of the PSCs. Therefore, many efforts have been done to use other n-type inorganic nanocrystals as alternative electron conductors in PSCs.

Several n-type inorganic nanocrystals such as ZnO[20], SnO,CdSe[21], CdS and α-Fe_2O_3 have been considered as possible substitute of TiO_2, and have displayed considerable power conversion efficiency[22,23]**.** Among all the alternative materials, α-Fe_2O_3 has been widely

used as an anode material for super capacitors[24]. Itis one of the most common n-type materials, and the most stable iron oxide with n-type semiconducting properties under ambient conditions. It has been used as photoanode in dye-sensitized solar cells to enhance the electron transfer rate[25]**,** however its use as an electron transporting replacing TiO_2 has not yet been reported. Thus, we employed low cost α-Fe_2O_3 for the first time as the ETL material instead of TiO_2 in planar perovskite cells. The charge accumulation at the perovskite/α-Fe_2O_3 interface is significantly reduced and hence is prominently effective in reducing the hysteresis[26]. Furthermore, the fabricated solar cells show a good stability upon exposure to ambient air without any encapsulation.The studied materials for perovskite solar cells are $CH_3NH_3PbI_3$,$CH_3NH_3PbI_{3-x}Cl_x$,$CH_3NH_3PbBr_3$,$CH_3NH_3Pb(I_{1-X}Br_x)_3$, $HC(NH_2)_2PbI_3$,$HC(NH_2)_2Pb(I_{1-X}Br_x)_3$, and $CH_3NH_3SnI_3$. In Table 1, the reported performances are summarized in terms of material $CH_3NH_3PbI_3$ and cell configuration.HTM materials are also important for high efficiency perovskite solar cells, where the most studied HTM is spiroMeOTAD,but polymertic HTMs such as the thiophene derivative P3HT and tryarylamine-based PTAA have also been tested. In addition, inorganic HTMs such as NiO, CuI, and CuSCN are confirmed to be suitable for perovskite solar cells.

Materials	Cell configuration	J_{sc} [mA/cm^2]	V_{oc} [V]	FF	PCE (%)	Ref
$MAPbI_3$	mesoporous-TiO_2/$MAPbI_3$/spiro-MeOTAD	17.6	0.888	0.62	9.7	[27]
	$MAPbI_3$/PCBM	10.32	0.60	0.63	3.9	[28]
	mesoporous-TiO_2/$MAPbI_3$/P3HT-MWNT	14.8	0.76	0.57	6.45	[29]
	rutile TiO_2 nanorod/$MAPbI_3$/spiro-MeOTAD	15.6	0.955	0.63	9.4	[30]
	mesoporous-ZrO_2/$MAPbI_3$/spiro-MeOTAD	17.3	1.07	0.59	10.8	[31]
	NiO/$MAPbI_3$/PCBM	13.24	1.040	0.69	9.51	[32]
	mesoporous-TiO_2/$MAPbI_3$/CuI	17.8	0.55	0.62	6.0	[33]
	Fe_2O_3/$MAPbI_3$/ spiro-MeOTAD	11.27	1.55	0.33	5.7	our work

Table 1. Photovoltaic performance of perovskite ($MAPbI_3$) solar cells. J_{sc}, V_{oc} and FF stand for short-circuit current density, open-circuit voltage, and fill factorrespectively.

The present report mainly focuses on the deposition of a compact α-Fe_2O_3 film, and its impact on the growth of the perovskite layer, providing a comprehensive understanding of the properties of the α-Fe_2O_3/perovskite interface. The α-Fe_2O_3 films are fabricated using an electrodeposition method for the blocking layer and a hydrothermal method for the overlying layer. Then the as-synthesized α-Fe_2O_3 films are used for PSCs. The impact of the growth of the α-Fe_2O_3 film on the properties of the α-Fe_2O_3/perovskite interface and on the performance of PSCs is investigated. Morphologically uniform α-Fe_2O_3 film let's achieve a PCE of 5.7%.These results show the application possibility of α-Fe_2O_3 in PSCs, and provide the principle for the choice of the electron transport layer for efficient PSCs.

2. Experimental details

2.1. Synthesis of α-Fe_2O_3 thin films

2.1.1. Under layer fabrication (α-Fe_2O_3 (A))

The experimental set-up used to prepare α-Fe_2O_3thin films consists of a computer-controlled potentiostat/galvanostat and a classic threeelectrodes electrochemical cell. The electrochemical cell was filled with a solution containing 5mM $FeCl_3$ +5mM KF+ 1M H_2O_2 +0.1M KCl as supporting electrolyte in deionized water. The working electrode is a substrate composed of fluorine-doped tin oxide (FTO) coated glass having a sheet resistance of 10 Ω;the previous substrate is cleaned in an ultrasonic acetone bath for 10 min, then rinsed in distilled water and dried. Pt and Ag/AgCl electrodes were used as a counter electrode and a reference electrode, respectively. The films were deposited by cathodic electrodeposition. The deposition potential was fixed at - 0.15 V and the deposited charge was 1.2 C for all samples in order to have a thickness of approximately 40-60 nm for all Fe_2O_3films. A thermostat fixed the solution temperature at 298K. After deposition, the films were rinsed with distilled water. To obtain the desired α-Fe_2O_3phase, the deposited films were annealed in air at 650°C for 2h. The transition between phases, from β-FeOOH (yellow) to **α**-Fe_2O_3 (red–brown) is shown in figure 1.

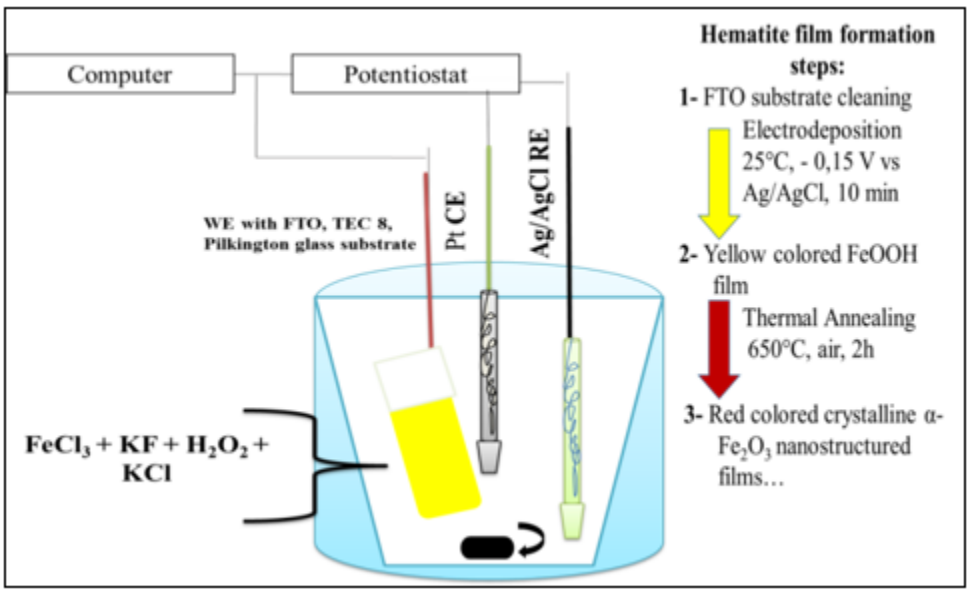

Figure 1: Schematic representations of a typical three-electrode electrochemical cell

2.1.2. On layer fabrication (α-Fe_2O_3 (B))

Nanostructured **α**-Fe_2O_3 (B) thin films were obtained after annealing hydrothermally deposited iron films on a smooth α-Fe_2O_3 surface (A). The bath was done by filling a 30-mL recipient, with a 20-mL aqueous solution containing 0.15 M of $FeCl_3.6H_2O$ and 1 M $NaNO_3$ at pH 1.5 (adjusted by HCl), leading to the deposition of iron hydroxides (FeOOH). Iron films were deposited on the **α**-Fe_2O_3 (A) substrate from an iron precursor solution ($FeCl_3.6H_2O$). [34,35,36].A piece of FTO/**α**-Fe_2O_3 (A) was put into the autoclave, then heated at 100°C for 6h and naturally cooled down to ambient temperature. Under hydrothermal conditions, this solution enables the interaction of Fe^{3+} ions with OH^-, producing iron oxide nuclei, as described by Eq. (1):

$$\mathbf{Fe^{3+}_{(aq)} + 3OH^-_{(aq)} \rightarrow \beta\text{-}FeOOH_{(s)} + H_2O_{(l)} \quad (1)}$$

As a result, a uniform layer of β-FeOOH grows on the FTO substrate. The akageneite-coated substrate was then washed with deionized water and subsequently sintered in air at 550°C for 4 hours. During the annealing process, the β-FeOOHconverts into α-Fe_2O_3.The phase transition from β-FeOOH (yellow) to **α**-Fe_2O_3 (red–brown) is shown in figure 2. During the phase transition, the occurring chemical reaction is due to the thermal treatment, it can be represented by Eq. (2):

$$2\beta\text{-}FeOOH_{(s)} \rightarrow Fe_2O_{3(s)} + H_2O_{(L\ or\ G)} \quad (2)$$

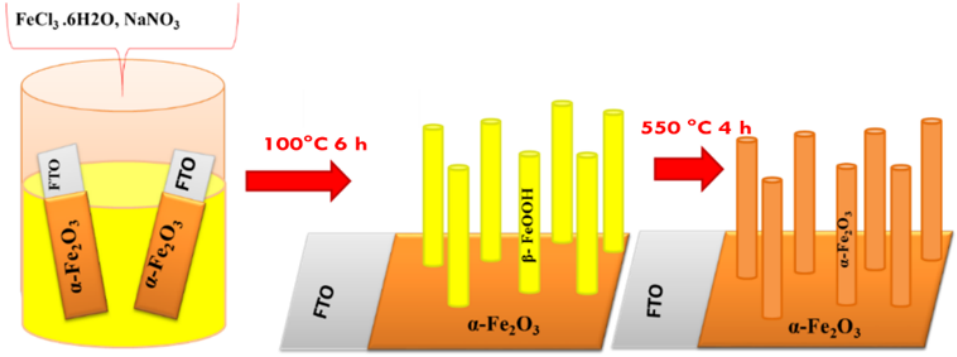

Figure 2: Schematic representations of the syntheses methods adopted for α-Fe_2O_3 hematite photoanode film electrodeposited on α-Fe_2O_3(A) substrate.

2.2. fabrication of the perovskite-based Solar cell ($CH_3NH_3PbI_3$ or $MAPbI_3$)

The $MAPbI_3$ perovskite precursor solution was prepared from an equimolar of Methylammonium iodide (CH_3NH_3I or MAI)/Lead (II) iodide(PbI_2), in a 40%dimethylformamide (DMF) solution with ratios 1:1 (1:1 mol %) for MAI: PbI_2 and then stirred for 2h at 70 °C. The mixture was deposited onto (FTO) covered glass by spin-coating at 3500 rpm for 11 s. A drop of toluene was added after 2-4 s before the end then dried at 5000 rpm for 30s.The resulting perovskite layers were then annealed at 100°C for 1h. Before the deposition process, the FTO glass substrates were cleaned with ethanol, isopropanol, and water for 15 min, and then dried with clean dry air. The reaction results in the formation of a compact and flat crystalline MAI-DMFPbI_2 intermediate phase film.

$$PbI_2\text{-}MAI\text{-}DMF \rightarrow MAPbI_3 + DMF\uparrow \quad (3)$$

The intermediate phase film is successfully converted into a crystalline perovskite film by annealing at 100 °C, as shown in Eq. (3). The DMF is removed in the intermediate phase film, leaving a compact and flat morphology (Fig. 3).

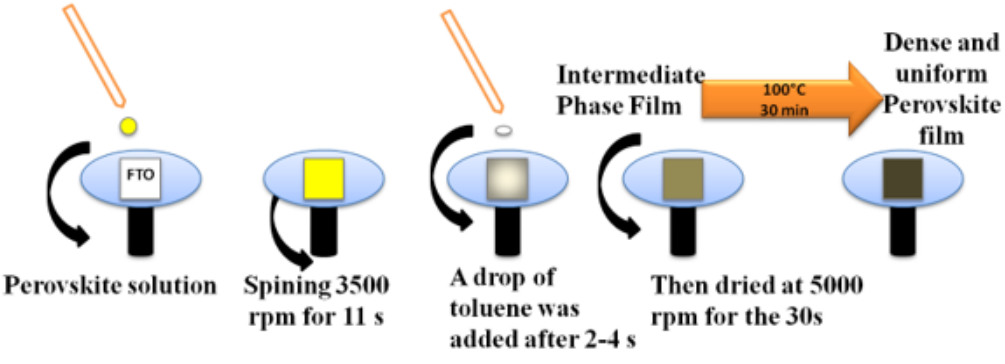

Figure 3: Solvent engineering procedure for preparing the uniform and dense perovskite film

The hole-transporting layer (HTM) was then deposited via spin-coating using a 0.788M solution of 2,2',7,7'-tetrakis-(N, N-di-p-methoxyphenylamine)9,9'-spirobifluorene (spiro-OMeTAD) in chlorobenzene, with additives of 0.0184M lithium bis (trifluoromethanesulfonyl) imide (added in 0.61M acetonitrile solution) and 0.0659M 4-tert-butylpyridine. The HTM was spin coated at 4500 rpm for 30 s inside adrybox. Finally,the top anode (a 50 nm-thick gold (Au) film)contact was deposited by thermal evaporation under a vacuum of ~10-6Torr, yielding an active area of 0.2 cm^2, to complete the creation of the device (inset in Fig. 4).

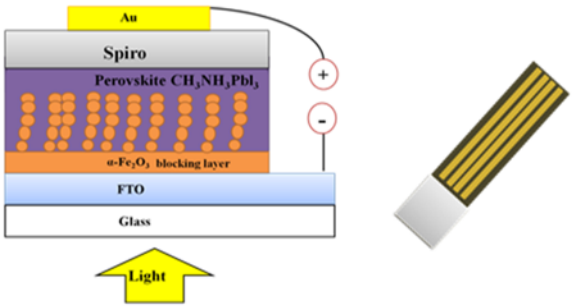

Figure 4 A: Scheme of the perovskite solar cell

Figure. 4 B shows the energy level diagram for the different solar cell components, depicting the conduction band of α-Fe_2O_3, conduction and valence bands of $CH_3NH_3PbI_3$ perovskite, and position of the highest occupied molecular orbital (HOMO) of Spiro-OMeTAD as HTM. In this scheme,the electrons and holes generated in $CH_3NH_3PbI_3$ can be energetically injected into the α-Fe_2O_3 and HTM phases respectively.[37,38]

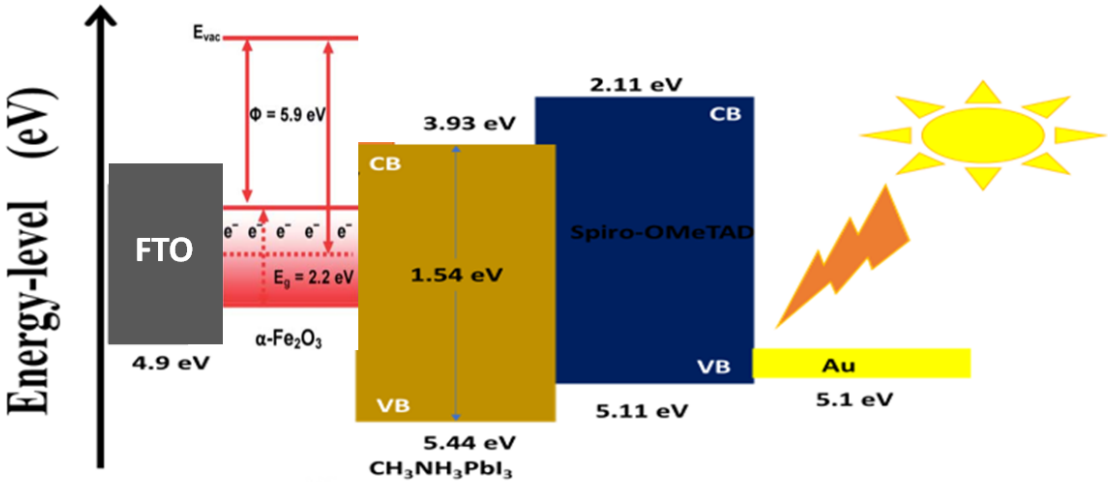

Figure 4 B: Energy-level diagram for each component of the device

3. Results and discussion

3.1. Structural characterization

The crystal structure of α-Fe_2O_3 and α-Fe_2O_3/perovskite thin films wasinvestigated by X-ray diffraction (XRD) using a Rigaku Ultima IV diffractometer in the Bragg-Brentano configuration (the X-ray radiation is $\lambda_{CuK\alpha}$= 1.54060 Å). Figure 5 (a) shows the XRD patterns of α-Fe_2O_3(A), α-Fe_2O_3(B) and a α-Fe_2O_3/α-Fe_2O_3bilayer deposited on FTO substrates. The diffractograms of the α-Fe_2O_3/α-$Fe_2O_3$and the FTO substrates are also shown.The XRD lines of the α-Fe_2O_3films are observed at 2θ = 24.1°, 33.1°, 35.6°, 40.9°, 49.4°, 54.0° and 64°, corresponding to the (012), (104), (110), (113), (024), (116) and (300) planes of the hematite phase, respectively. The dominant lines correspond to the (104) and (110) planes. The diffraction lines of the trigonal structure of α-Fe_2O_3matches well with the reference pattern of the JCPDS card file n°33-0664, which corresponds to the space group R3c (167) with lattice parameters a=b=5.03 nm and c= 13.74 nm.

Figure 5 (b) shows the X-Ray diffractograms for the $MAPbI_3$ and α-Fe_2O_3 (A)/α-Fe_2O_3 (B)/ $MAPbI_3$/FTO thin films. XRD lines are located at 15°, 20°, 24.4°, 28.4°, 31.8°, 40.6° and 43°. $MAPbI_3$ thin films crystallize and stabilize into the same cubic structure (Fig. 5 (c)). The most intense diffraction line located below 15° corresponds to the (100) diffraction plane and the lines located at about 20°, 30° and 34° are related to the (110), (200) and (210) orientation planes, respectively. One may also observe two diffraction lines located at 26.5° and 33.7°corresponding to the FTO substrates. For the α-Fe_2O_3 (A)/α-Fe_2O_3 (B)/$MAPbI_3$/FTO layers, all lines match the α-Fe_2O_3 (A), α-Fe_2O_3 (B), and $MAPbI_3$ patterns except those marked with a solid dark point that come from the FTO substrate.

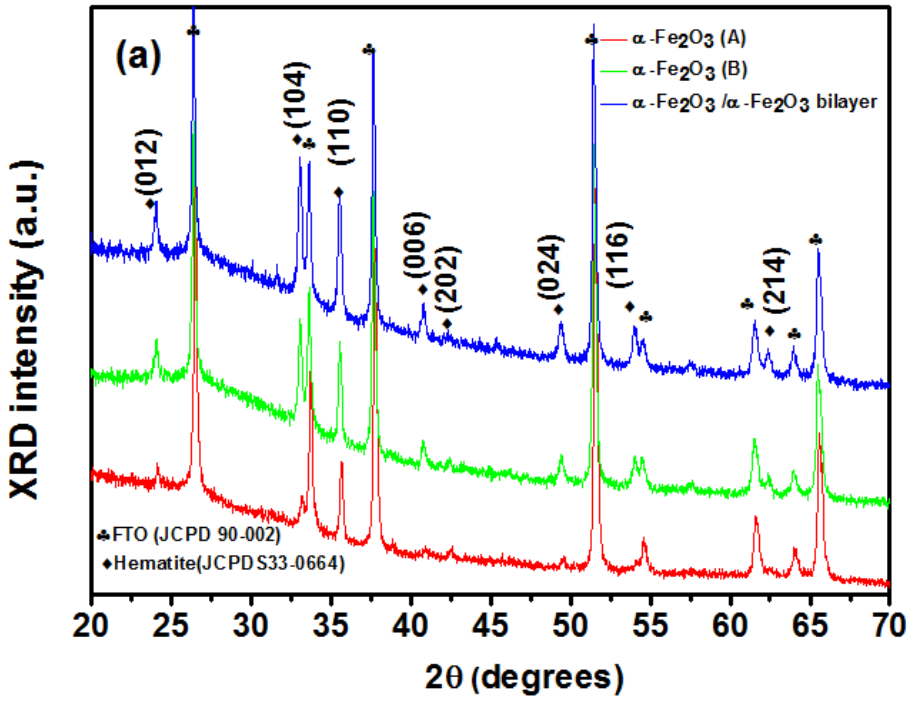

Figure 5 (a) XRD spectra of α-Fe_2O_3(A), α-Fe_2O_3(B) and α-Fe_2O_3/α-Fe_2O_3bilayer.

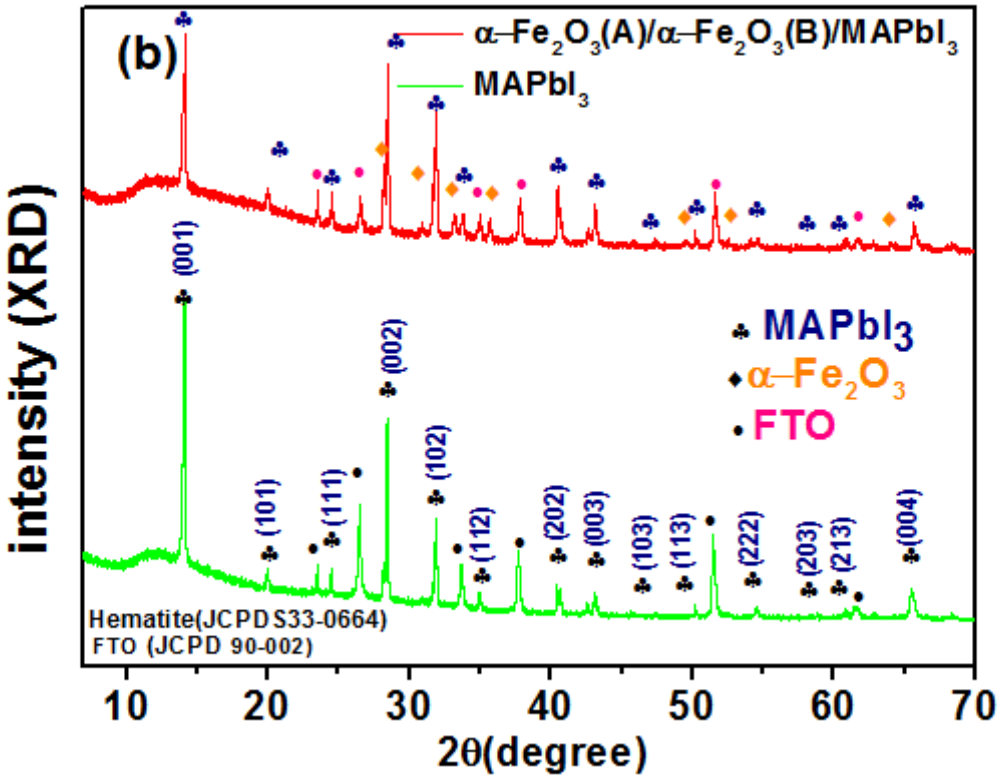

Figure 5 (b). XRD patterns of $MAPbI_3$ and α-Fe_2O_3(A)/α-Fe_2O_3(B)/$MAPbI_3$/FTO.

3.2. Morphological characterization

The microstructural and elemental analyses were characterized using a Zeiss ULTRA 55 model scanning electron microscope (FESEM) equipped with an energy dispersive spectroscopy (EDS) system. Figure 6 displays the FESEM images of (a) α-Fe_2O_3 (A), (b) α-Fe_2O_3 (B), (c) α-Fe_2O_3(A)/α-Fe_2O_3(B), (d) $MAPbI_3$, (e) α-Fe_2O_3 (A)/α-Fe_2O_3(B)/$MAPbI_3$ and (f) the solar cell deposited on FTO substrates, respectively. Figure 6 (a) shows vertically grown segregated nanostructured islands made up of small Fe_2O_3(A) nanoparticles, showing some grain size dispersion. Figure 6 (b)shows the microstructure of the as-prepared sample. The later allows us to point out the formation of typical anisotropic-like nanoparticles, mainly composed of nanostructured rods, which is a characteristic of the mesoporous film. Figure 6 (c) depicts the morphology of α-Fe_2O_3/α-Fe_2O_3bilayer that reveals nanostructured aggregates having a grain size of approximately 20 nm. The α-Fe_2O_3(B) grains deposited on α-Fe_2O_3(A)are larger than those deposited on FTO.Figure 6 (d) shows that the $MAPbI_3$ film is composed of dense and homogenous fibre-like crystals with the presence of voids due to solvent evaporation.Figure 6 (e) shows that the fibre-like $MAPbI_3$ films deposited on α-Fe_2O_3(A)/α-Fe_2O_3(B) have dissimilar shapes and sizes.Figure 6 (f) shows the α-Fe_2O_3(A)/α-Fe_2O_3(B)/$MAPbI_3$/spiro-OMeTAD/Au, where the $MAPbI_3$ film becomes uniform with a denser morphology.

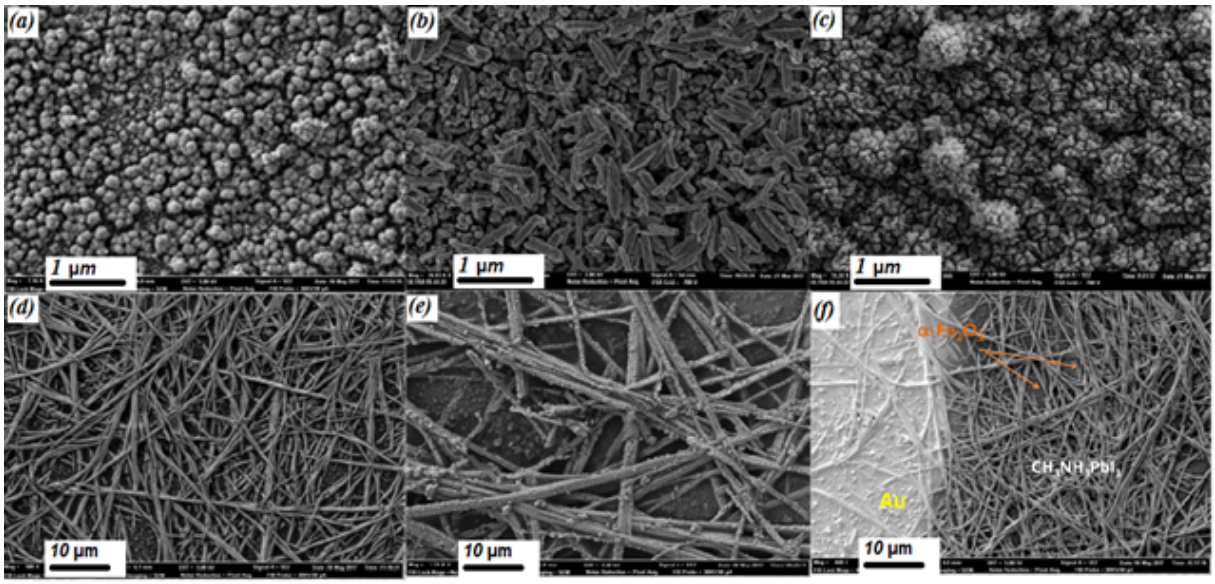

Figure 6: FESEM images of (a) α- Fe_2O_3(A), (b) α-Fe_2O_3(B), (c) α- Fe_2O_3(A)/α-Fe_2O_3(B), (d)$MAPbI_3$, (e) α-Fe_2O_3(A)/α-Fe_2O_3(B)/$MAPbI_3$ and (f) solar cell.

Figure 7 shows the vertical cross section of the FESEM image of the entire structure (α-Fe_2O_3 (A)/ α-Fe_2O_3 (B)/ $MAPbI_3$/spiro-OMeTAD/Au) deposited on FTO. The thickness of the cell is about 4.8µm.

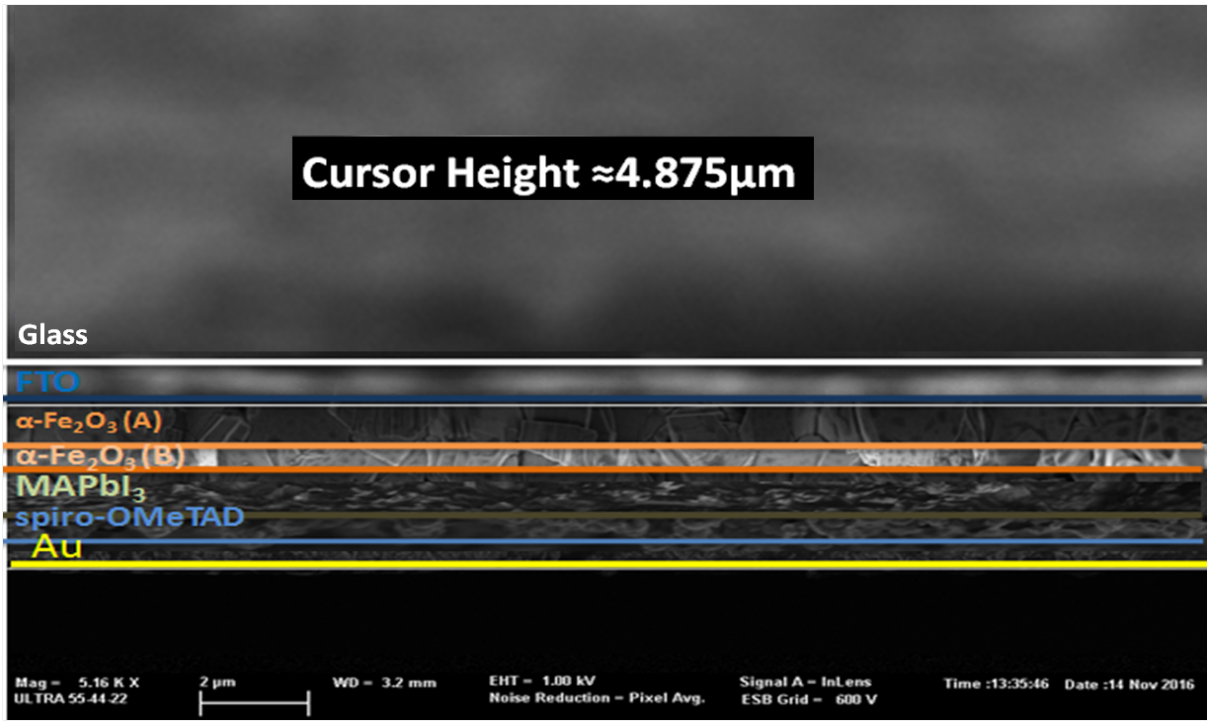

Figure 7: Vertical cross section of (a) α-Fe_2O_3(A), (b) α-Fe_2O_3/α-Fe_2O_3 thin films.

3.3. EDX analyses

Figure 8.A shows a EDX elemental analysis of the deposited $MAPbI_3$, α-Fe_2O_3(A)/α-Fe_2O_3(B), α-Fe_2O_3(A)/α-Fe_2O_3(B)/$MAPbI_3$. The line observed at 0.72 keV corresponds to the L line of Fe, and the oxygen K line is peaking at 0.525 keV. The calculated atomic ratio of Fe and O is approximately equal to 2:3, whichwell agrees with the stoichiometric composition of α-Fe_2O_3. The percentage of each element was calculated from EDX analyses (Fig. 8).The element ratio of the $MAPbI_3$ film is shown in Figure 8.A (a);two featured lines peaking at 2.48 and 3.98 keV are assigned to the Pb and I elements, respectively.The EDXpresented in Fig.8.A (a) shows that Pb and I are well distributed on a large energy scale. Figures 8.A (c-d) show the elemental composition of the solar cell and confirm the presence of each element formingthe cell. The line observed at 2.3 keV corresponds to the M line of the gold (Au) contacts.

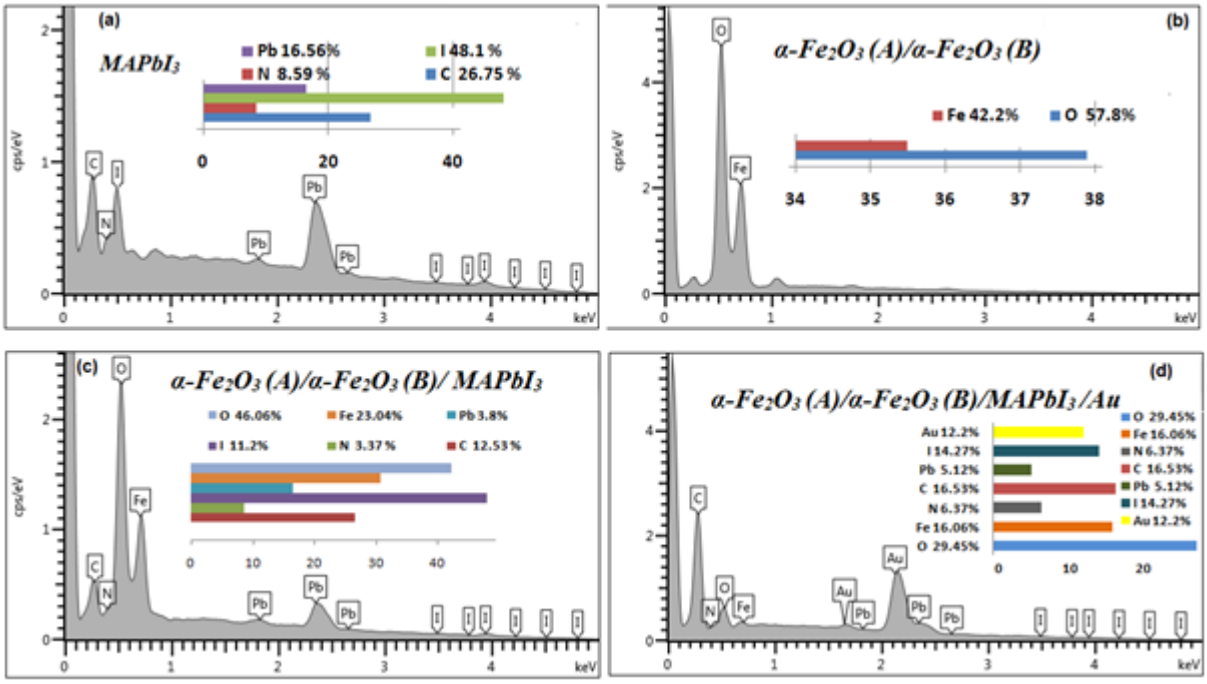

Figure 8.A: EDX spectrum for (a) $MAPbI_3$, (b) α-Fe_2O_3(A)/α-Fe_2O_3(B), (c) α-Fe_2O_3(A)/α-Fe_2O_3(B)/$MAPbI_3$, and (d) solar cell.

Figure 8.B showsthe spatial distribution ofα-Fe_2O_3+$MAPbI_3$, wherePb and I are three-dimensionally well-distributed in the α-Fe_2O_3 film. The atomic percentage calculated from the EDX analyses indicates that the Pb to I ratio is 1:3. Compared to the Fe atomic ratio, Pb has a relatively lower atomic percentage indicating that the perovskite sensitizer does not densely cover theα-Fe_2O_3 surface.It can be concluded that the α-Fe_2O_3composites can uniformly encapsulate the $CH_3NH_3PbI_3$ crystals.

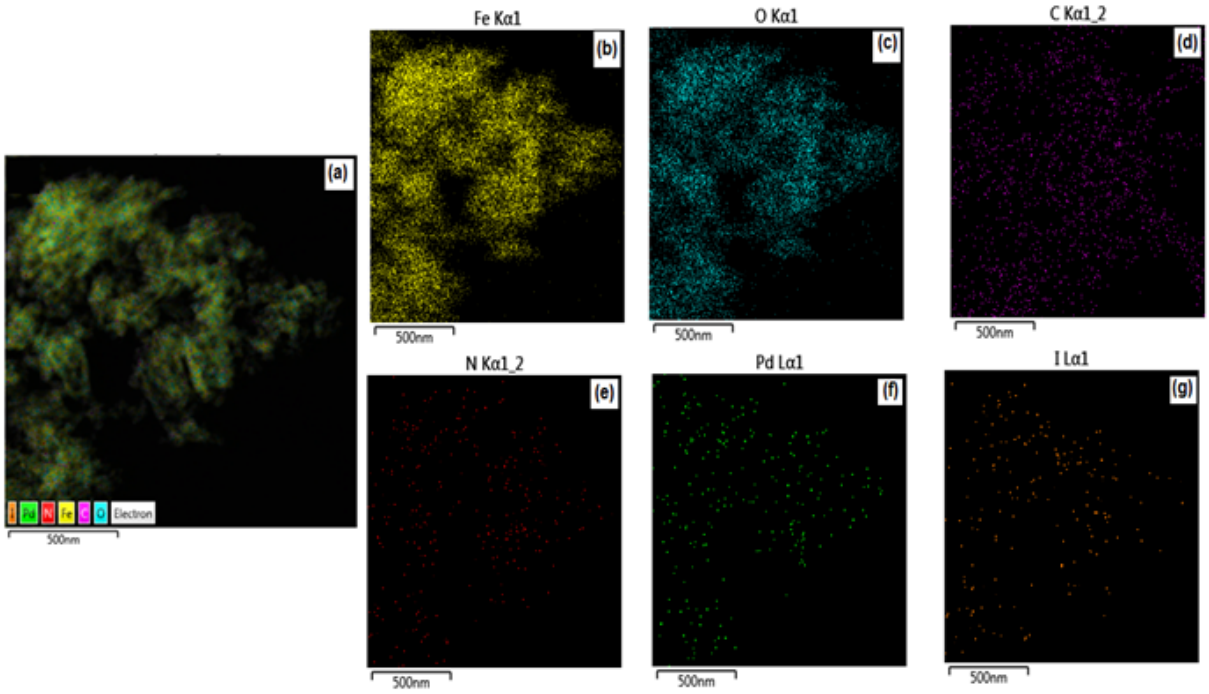

Figure 8 B: EDX mapping for(a) α-Fe_2O_3(A)/α-Fe_2O_3(B)/$MAPbI_3$, (b) Fe map, (c) O map, (d) C map, (e) N map, (f) Pb map and (g) I map.

3.4. Optical characterization of α-Fe_2O_3 thin films

The band gap energy was determined from the optical absorption by recording the transmission spectra using a UV-Visible spectrophotometer (Ocean Optics HR4000) coupled with an integrating sphere (to collect both specular and diffuse transmittance). Figure 9 shows the transmission spectra of the α-Fe_2O_3/α-Fe_2O_3 bilayer, from which the optical band gap energies can be determined. The transmittance spectrum of the α-Fe_2O_3/α-Fe_2O_3 bilayer shows a high optical transmission ratio: above 30% in the visible range. A significant increase in absorption below 533 nm can be assigned to the intrinsic band gap absorption of the α-Fe_2O_3/α-Fe_2O_3 bilayer.

According to the solid band theory, the relation between the absorption coefficient $\boldsymbol{\alpha}$ and the energy of the incident light $\boldsymbol{h\nu}$ is given by[39]:

$$\alpha h\nu = A\,(h\nu - Eg)^{n} \qquad (4)$$

Where $\boldsymbol{\alpha}$ is the absorption coefficient, $\boldsymbol{A}$ is a constant, $\boldsymbol{h}$ is the Planck's constant, $\boldsymbol{\nu}$ is the incident photon frequency, $\boldsymbol{Eg}$ is the optical band gap, and $\boldsymbol{n}$ is equal to 2 for a direct transition, and to 1/2 for an indirect transition. Figure 9 depicts the Tauc plot of α-Fe_2O_3/α-

Fe_2O_3 bilayer. One may point out a direct band gap energy of about 2.3 eV, smaller than that of bulk α-Fe_2O_3 (2.3 eV).

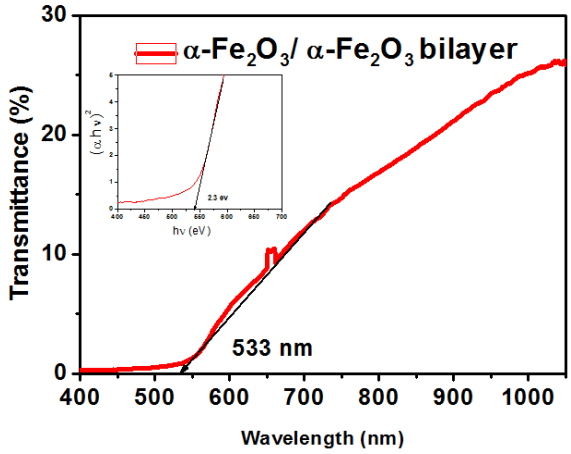

Figure 9: Transmission and Tauc plot (inset) of α-Fe_2O_3/α-Fe_2O_3bilayer

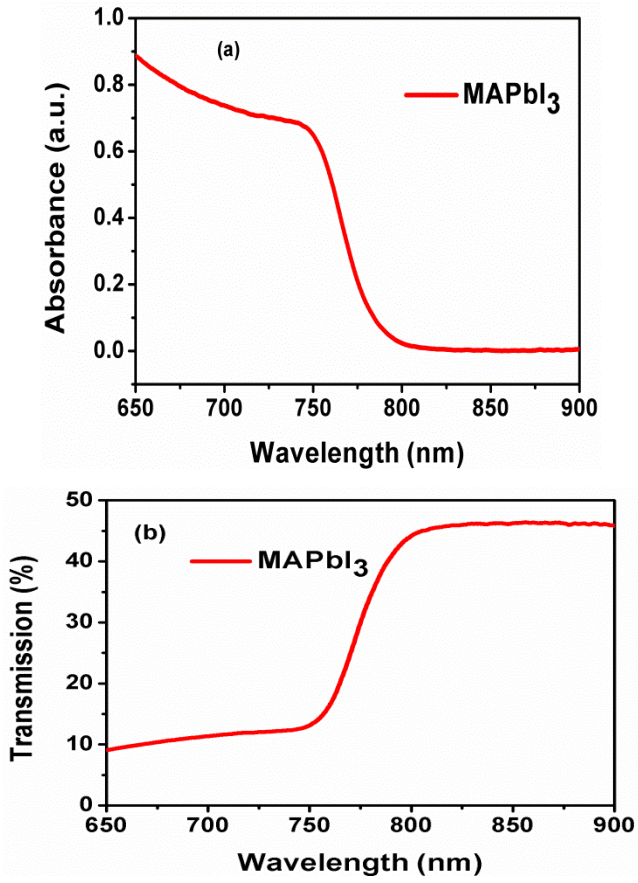

Figure 10: Absorbance (a) and Transmission (b) plots of perovskite thin films.

Figure 10 shows the transmission and the absorbance of the$MAPbI_3$ perovskite thin film. The main features of the transmission spectra arethe existence of a sub-band gap absorption tail

followed by astrong rise of the absorption, which corresponds to excitonicabsorption, and then a transition from the valence band to theconduction band. When excitonic absorption dominates theabsorption spectrum, the classical relationship between the coefficients (α) and the band gap energy (Eg) is commonly used for calculating the direct band gap of a semiconductor:

$$(\alpha.h\nu)^2=A(E-Eg) \qquad (5)$$

Where E is the incident photon energy and A is a constant [40].One may point out a direct band gap energy of about 1.58eV.

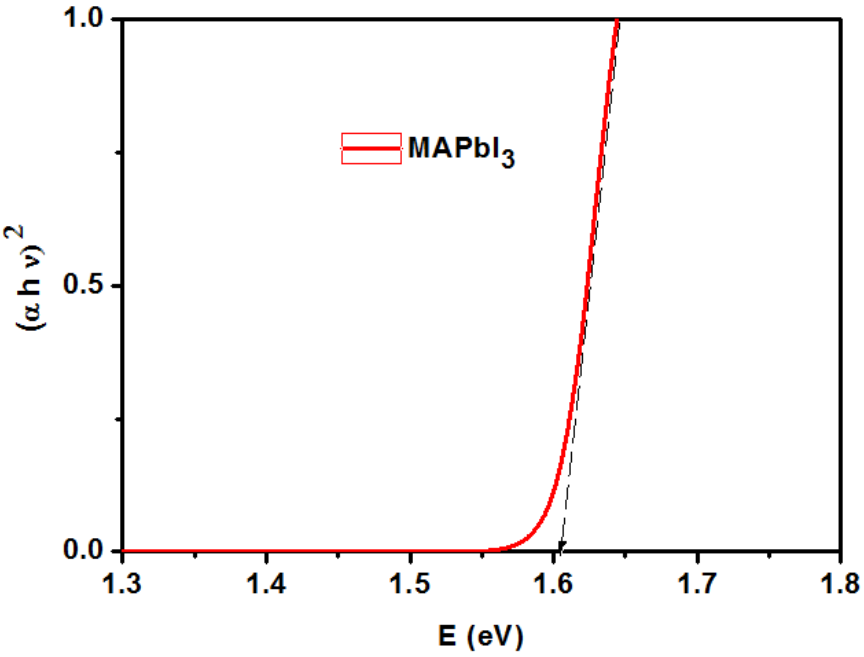

Figure 11: Taucplot of the perovskite thin films.

3.5.Photoelectrochemical properties of α-Fe_2O_3 electrodes.

The PEC measurements were performed in a quartz cell to enable light reaching the photoelectrode surface. The surface area of the light-exposed working electrode was about 0.25 cm^2. The electrolyte used in all PEC measurements is 1M NaOH (pH = 13.6). The electrolyte is purged with nitrogen gas prior to experiments to prevent any possible reaction with dissolved oxygen at the counter-electrode. A potentiostat/galvanostatAutolab PGSTAT302N (Metrohm, Netherlands) with a Pt rod counter electrode and an Ag/AgCl saturated in 3 M KCl reference electrode was used. The films are illuminated with a 300 W Xenon lamp (PLSSXE300/300UV) equipped with a UV cut-off filter (λ> 420 nm). The set-up

was completed with an automatic shutter and a filter box. The whole system was controlled by homemade software. The chronoamperometry curves of the films were also obtained at +0.1 V, both in the dark and under illumination with a light intensity of about 1 SUN (100 mW cm^{-2}) at the sample surface**.**

For wavelength-dependent photocurrent measurements a monochromator giving a ~20 nm bandpass from 360 to 680 nm was used together with cut off filters to eliminate secondary - harmonics.The incident photon to electron conversion efficiency (IPCE) of the samples was calculated as follows:

$$\mathbf{IPCE}(\%) = \frac{\mathbf{1240}\cdot i_{photocurrent}\,(\mu\mathbf{A}/cm^2)}{\boldsymbol{\lambda}(\mathbf{nm})\cdot j_{photons}\,(\mu W/cm^2)} * \mathbf{100}\% \quad \mathbf{(6)}$$

The photocurrent density–voltage (J–V) characteristics of theα-Fe_2O_3(A)/α-Fe_2O_3(B)/$MAPbI_3$ solar cell were registered using a potentiostat/galvanostatAutolab PGSTAT302 under AM 1.5G illumination (50mW cm^{-2}) provided by a calibrated solar simulator (using a standard silicon solar cell before measurement).

The photocurrent intensities under pulsed light were measured using a chronoamperometric technique (Fig. 12). All measurements were made in 1M NaOH[41,42] electrolyte and under a potential bias of 0.1 V. Figure 12 shows the variation of the photocurrent density according to the elapsed time during on/off cycles. In the steady state, the α-Fe_2O_3(A)/FTO electrode shows a photocurrent density of about 3mA/cm^2. However, the α-Fe_2O_3/α-Fe_2O_3/FTO bilayer shows a photocurrent density of about 12mA/cm^2, which is 4and 2 times greater than that of the α-Fe_2O_3(A)/FTO and α-Fe_2O_3(B)/FTO electrodes, respectively. The photocurrent density dropped in the first two cycles and then was steady and quasi-reproducible after several on–off cycles of light illumination. There was no overshoot at the beginning or at the end of the on–off cycle, meaning that the direction of the electron diffusion is free from grain boundaries, which can create traps to hinder electron movement and slow down the photocurrent generation[43]**.**

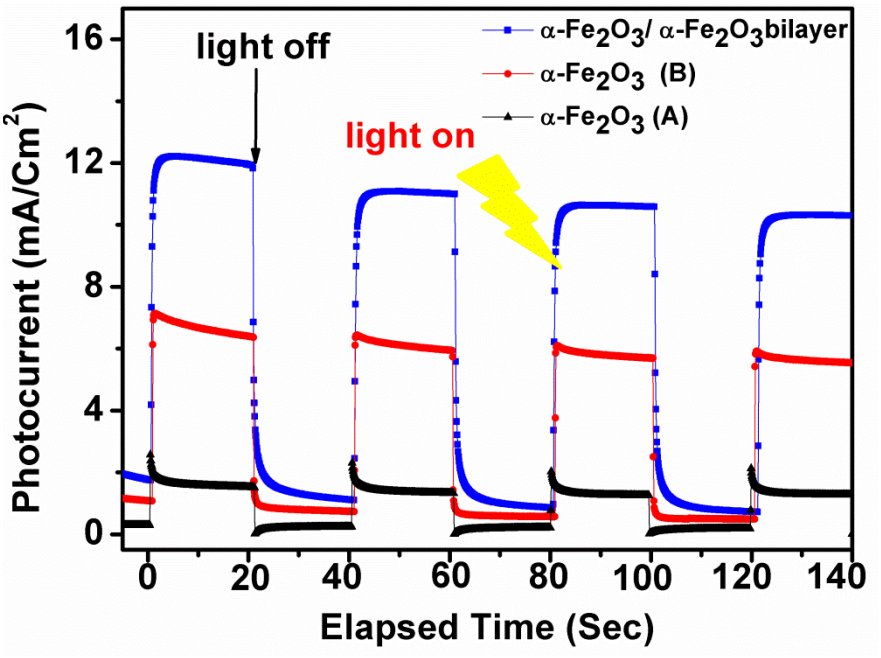

Figure 12: Photocurrent intensity for α-Fe_2O_3(A), α-Fe_2O_3(B) and α-Fe_2O_3/α-Fe_2O_3 (bilayer) electrodes under successive on/off illumination cycles, measured in 1 M NaOH electrolyte under a bias potential of +0.1 V.

Figure 13 shows the action spectra for the best performing α-Fe_2O_3/α-Fe_2O_3/FTO bilayer samples compared to the α-Fe_2O_3(A), α-Fe_2O_3(B) films. Significant performance gains were observed upon all throughout the illumination wavelengths. The best performing samples were α-Fe_2O_3/ α-Fe_2O_3/FTO bilayer, which had IPCEs at 400 nm of 9%, with an applied potential of 0.4V v.s Ag/AgCl. These IPCE values were 3 times higher than the α-Fe_2O_3 (A) and α-Fe_2O_3 (B) samples for the α-Fe_2O_3/ α-Fe_2O_3/FTO bilayer samples.The high energy photons are absorbed in the outermost layers of hematite and therefore, the photogenerated holes have a shorter diffusion path to reach the surface where they will participate in oxidative chemical reaction. A positively applied potential will increase the collection efficiency of the electrons and the IPCE increases, as shown in Figure 13. Furthermore, the applied bias will facilitate hydrogen production at the Pt counter electrode by shifting its negative potential to overcome the approximately 0.4 V (vs. Ag/AgCl) difference between the hematite flat band potential and the hydrogen redox level.

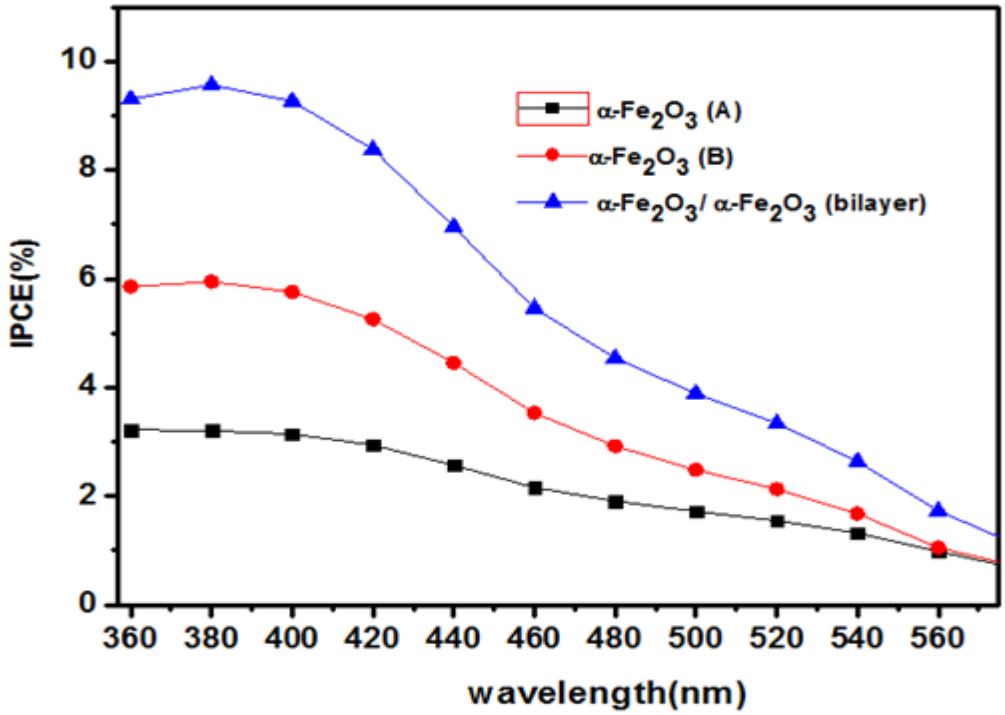

Figure 13: IPCE for α-Fe_2O_3(A), α-Fe_2O_3(B) and α-Fe_2O_3/α-Fe_2O_3(bilayer) at 0.4 V (vs. Ag/AgCl) applied potential in N_2 degassed 1 M NaOH.

3.6. Photocurrent density–voltage (J-V) of the solar cell device.

Figure 14 depicts the dark and under illumination (J–V) characteristicsof the α -Fe_2O_3(A)/α-Fe_2O_3(B)/$MAPbI_3$/Au solar cell. From the J–V curves, we can deduce open-circuit voltage (V_{oc}) and short-circuit current density (J_{sc}). These parameters are summarized in Table 2. The power conversion efficiency (η (%)) and Fill factor (FF (%)) are calculated from the following equations:

$$\mathbf{FF} = \frac{\mathbf{I_{max}V_{max}}}{\mathbf{I_{sc}V_{oc}}} \mathbf{(7)}$$

$$\boldsymbol{\eta(\%)} = \frac{\mathbf{I_{sc}V_{oc}FF}}{\mathbf{P_{input}}} \mathbf{*100\ (8)}$$

where, P_{input} is the power of the incident light, I_{max} and $V_{max}$are the current andvoltage corresponding to the maximum power point (Mpp),I_{sc} is the short circuit current, and V_{oc} is the open circuit potential, both can be extracted from the (J-V) curves.However, under illumination, the current magnitude of the cell increases up promptly. The current becomes stronger and increases more rapidly. This is sincethe conductivity of α-Fe_2O_3 is improved with the incorporation of perovskite. It should be emphasized that proper perovskite can greatly enhance the separation of electron-hole pairs.The device exhibited an encouraging

solar conversion efficiency of 5.76%, with its open circuit voltage (Voc) of 1.55 V, short-circuit current density (Jsc) of 11.27 mA/cm2, and fill factor (FF) of 33%.

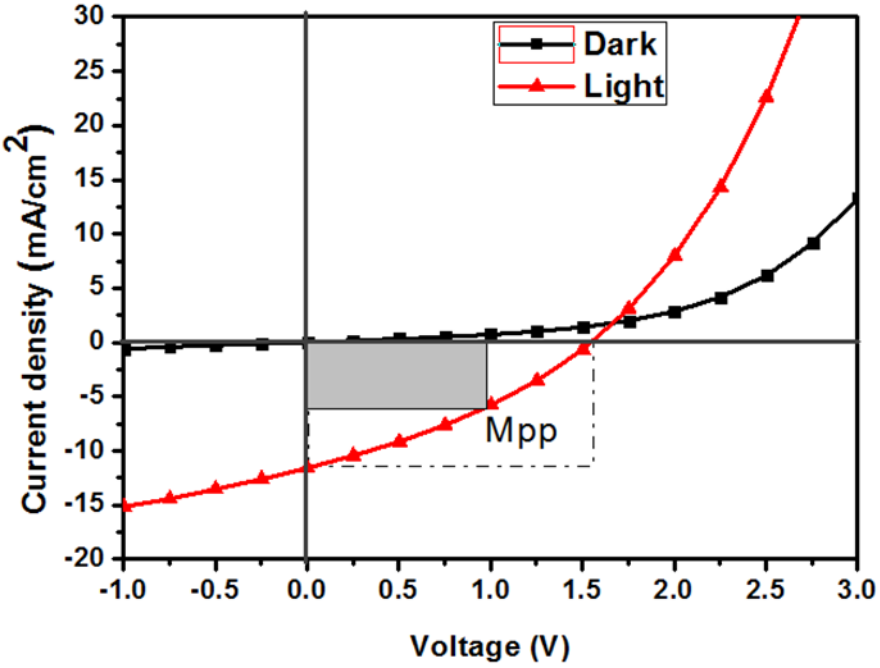

Figure 14: J-V curve solar cell devices in the dark and illumination.

Sample	V_{oc}***[V]***	J_{sc} ***[mA cm^{-2}]***	V_{max}***[V]***	J_{max} ***[mA cm^{-2}]***	***Fill factor [%]***	**η** ***[%]***
Perovskite solar cells	**1.55**	**11.27**	**0.99**	**5.7**	**33%**	**5.76%**

Table 2: Photovoltaic parameters of Perovskite solarcells

4. Conclusion

In this study, we the performance of PSCs based on α-Fe_2O_3as the electron transport material, perovskite as the light harvester, and spiroMeOTAD as the hole transporting material. The α-Fe_2O_3 thin film was prepared by the electrodeposition and the hydrothermal processes. The perovskite layer is synthesized on the surface of the α-Fe_2O_3 thin film using the spin coating method. It was found that the growth of the α-Fe_2O_3 thin film has a clear influence on the uniform formation of the perovskite layer. Dense α-Fe_2O_3 thin films with appropriate grain sizes can ensure uniform coverage of the perovskite film, forming a better contact between the α-Fe_2O_3 film and the perovskite layer, which is able to not only facilitate the charge transport, but also to reduce charge recombination of the α-Fe_2O_3/perovskite interface.The photoelectrochemical performance of the nanostructured α-Fe_2O_3/ α-Fe_2O_3bilayer is higher than that of FTO/ α-Fe_2O_3 (A) and FTO/ α-Fe_2O_3 (B). Water splitting performance was evaluated and the highest photocurrent density of 12 mA/cm^2v.s Ag/AgCl was exhibited for the α-Fe_2O_3/ α-Fe_2O_3bilayer photoelectrode, which had IPCEs at 400 nm of 9%, with an applied potential of 0.4V v.s Ag/AgCl.The dependence of the photovoltaic properties of PSCs on α-Fe_2O_3 is carefully examined. The stability of PSCs is also studied. The best-performing device with a PCE of 5.76%, a V_{oc} of 1.55V, a J_{sc} of 11.27 mA cm^{-2}, and a FF of 33% is demonstrated. This effect can be ascribed to the dense perovskite films that lead to full coverage of the α-Fe_2O_3 film, forming a better contact with the α-Fe_2O_3 thin film. In addition, the best performing device is also the most stable among all the devices presented. Therefore, we can state that the contact between α-Fe_2O_3 and the perovskite layer is the critical factor that determines the photovoltaic performance of PSCs. Moreover, the results indicate the great potential of α-Fe_2O_3 as an electron transport material, which provides high variety for perovskite-based solar cell design.

Références article 3

[1] Y. Ogomi, A. Morita, S. Tsukamoto, T. Saitho, N. Fujikawa, Q. Shen, T. Toyoda, K. Yoshino, S. S. Pandey, T. Ma and S. Hayase, J. Phys. Chem. Lett., 2014, 5, 1004.

[2]S. Kazim, M. K. Nazeeruddin, M. Gr¨atzel and S. Ahmad, Angew. Chem., Int. Ed., 2014, 53, 2812.

[3] J. M. Ball, M. M. Lee, A. Hey and H. J. Snaith, Energy Environ. Sci., 2013, 6, 1739.

[4] Q. Dong, Y. Fang, Y. Shao, P. Mulligan, J. Qiu, L. Cao andJ. Huang, Science, 2015, 347, 967.

[5]A. Kojima, K. Teshima, Y. Shirai and T. Miyasaka, J. A.Chem. Soc., 2009, 131, 6050–6051

[6]M. M. Lee, J. Teuscher, T. Miyasaka, T. N. Murakami and H. J. Snaith, Science, 2012, 338, 643–647

[7]M. Liu, M. B. Johnston and H. J. Snaith, Nature, 2013, 501, 395–398.

[8] H. Zhou, Q. Chen, G. Li, S. Luo, T.-B. Song, H.-S. Duan,Z. Hong, J. You, Y. Liu and Y. Yang, Science, 2014, 345, 542–546.

[9]W. S. Yang, J. H. Noh, N. J. Jeon, Y. C. Kim, S. Ryu, J. Seo and. I. Seok, Science, 2015, 348, 1234–1237.

[10]N.-G. Park, J. Phys. Chem. Lett., 2013, 4, 2423–2429.

[11] H. T. Peng, W. H. Sun, Y. L. Li, W. B. Yan, P. R. Yu, H. P. Zhou, Z. Q. Bian and C. H. Huang, J. Photonics Energy, 2016, 6, 022002.

[12]Q. S. Dong, Y. T. Shi, K. Wang, Y. Li, S. F. Wang, H. Zhang, Y. J. Xing, Y. Du, X. G. Bai and T. L. Ma, J. Phys. Chem. C, 2015, 119, 10212–10217.

[13] Q. Wu, W. Zhou and Q. Liu, ACS Appl. Mater. Interfaces, 2016, 8, 34464–34473.

[14]H. J. Snaith, J. Phys. Chem. Lett., 2013, 4, 3623–3630.

[15] J. H. Noh, H. I. Sang and H. H. Jin, Nano Lett., 2013, 13, 1764–1769.

[16] A. Dymshits, L. Iagher and L. Etgar, Materials, 2016, 9, 60.

[17] J. T. W. Wang, J. M. Ball and E. M. Barea, Nano lett, 2013, 14,24–730.

[18] J. M. Ball, M. M. Lee, A. Hey and H. J. Snaith, Energy Environ.Sci., 2013, 6, 1739–1743.

[19] M. J. Carnie, C. Charbonneau, M. L. Davies, J. Troughton,T. M. Watson, K. Wojciechowski, H. Snaith and D. A. Worsley, Chem. Commun., 2013, 49, 7893–7895.

[20] Q. Zhang, C. S. Dandeneau, X. Zhou and C. Cao, Adv. Mater. 2009, 21, 4087–4108

[21] L. Wang, W. F. Fu, Z. W. Gu, C. C. Fan, X. Yang, H. Y. Li and H. Z. Chen, J. Mater. Chem. C, 2014, 2, 9087–9090.

[22] D. –Y. Son, J. –H. Im, H. –S. Kim and N. –G. Park, J. Phys.Chem. C, 2014, 118, 16567–16573.

[23] M. H. Kumar, N. Yantara and S. Dharani, Chem. Commun,2013,49, 11089–11091.

[24] H. Wang, Z. Xu, H. Yi, H. Wei, Z. Guo and X. Wang, Nano Energy, 2014, 7, 86.

[25]H. Niu, S. Zhang, Q. Ma, S. Qin, L. Wan, J. Xu and S. Miao, RSC Adv., 2013, 3, 17228.

[26]D. H. Song, M. H. Jang, M. H.Lee, J. H.Heo,J. K. Park, S. J. Sung, D.H. Kim, K.H. Hong andS. H.Im,A discussion on the origin and solutions of hysteresis in perovskite hybrid solar cells. J. Phys. D: Appl. Phys. 49 (2016) 473001 (11pp).

[27] H.-S.Kim,C.R.Lee, J.H. Im,K.B.Lee,T.Moehl,A.Marchioro, S.J.Moon, R.H. Baker,J. H. Yum,J. E. Moser, M.Grätzel, N.G.Park,Sci. Rep.2012 , 2 , 591.
[28]J.Y.Jeng,Y.F.Chiang,M.H. Lee, S. R. Peng, T. F.Guo, P.Chen, T.C.Wen, Adv. Mater. 2013, 25, 3727.
[29] M. H. Kumar, N. Yantara, S. Dharani, M. Graetzel, S. Mhaisalk, P. P. Boix, N.Mathews,Chem.Commun.201,49, 11089.
[30] H.S. Kim, J.WLee, N.Yantar, P. P.Boi, S. A.Kulkarni, S.Mhaisalkar, M.Gratzel, N.-G.Park, Nano Lett. 2013, 13, 2412.
[31]D.Bi,S.J.Moon, L.Häggman, G.Boschloo, LYang, E. M. JJohansson, M. K.Nazeeruddin, M. Grätzel, A. Hagfeldt,RSC Adv. 2013, 3, 18762.
[32] K.C.Wang, J.Y.Jeng, P.S. Shen, Y.C.Chang, E. W.G. Diau, C.H.Tsai, T.Y. Chao, H.C.Hsu, P.Y.Lin, P. Chen, T.-F. Guo T.C. Wen, Sci. Rep.2014, 4, 4756.
[33] J. A. Christians, R. C. M. Fung, P. V. Kamat, J. Am. Chem.Soc. 2014, 136, 758.
[34]L. Vayssieres, N. Beermann, S.E. Lindquist, A. Hagfeldt, Controlled aqueous chemical growth of oriented three-dimensional crystalline nanorod arrays: application to iron(III) oxides, Chem. Mater. 13 (2001) 233–235.
[35] A. Annamalai, P.S. Shinde, A. Subramanian, J.Y. Kim, J.H. Kim, S.H. Choi, J.S. Lee, J.S. Jang, Bifunctional TiO2 underlayer for α-Fe2O3nanorod based photoelectrochemical cells: enhanced interface and Ti4þ doping, J. Mater. Chem. A 3 (2015) 5007–5013.
[36] M. Li,Z. Zhang,F.Lyu,X. He,Z.Liang, M. S. Balogun, X. Lu, P. P. Fang, Y. Tong, Facile Hydrothermal Synthesis of Three Dimensional Hematite Nanostructures with Enhanced Water Splitting Performance, ElectrochimicaActa, 20 December 2015 Volume 186, 20 December 2015, Pages 95-100.
[37] J. Cui, H. Yuan, J. Li, X. Xu, Y. Shen, H Lin and M. Wang, Recent progress in efficient hybrid leadhalide perovskite solar cells, Sci. Technol. Adv. Mater. 16 (2015) 036004 (14pp)
[38] Y. V. Kaneti, Q. M. D. Zakaria, Z. Zhang, C. Chen,J Yue, M. Liu, X. Jiang and A.YuaSolvothermal synthesis of ZnO-decorated a-Fe2O3 nanorods with highly enhanced gas-sensing performance toward n-butanol, Cite this: J. Mater. Chem. A, 2014, 2, 13283
[39] M.R. Belkhedkar, A.U. Ubale, International Journal of Materials and chemistry,4(2014) 109-116.
[40] R. J. Elliott, Phys. Rev. 108, 1384 (1957)
[41] S.S. Shinde, R. A. Bansode, C. H. Bhosale, and K.Y.Rajpure, Journal of Semiconductors32 (2011) 013001.
[42] F. L. Souza, K. P. Lopes, P. A. P. Nascente, E. R. Leite, Solar Energy Materials & SolarCells 93(2009) 362–368.
[43]M. Sookhakian, Y.M. Amin, S. Baradaran, M.T. Tajabadi, A. MoradiGolsheikh, W.J.Basirun, Thin Solid Films (2014) 204–211.

Chapitre V

Discussion générale

Dans ce chapitre, nous discutons les principaux résultats de la présente thèse, fruits de trois années de recherche et des publications présentées dans le chapitre précédent.

Les résultatsobtenusont montréque les dispositifs fabriqués ont des performances supérieuresaux dispositifsphotoélectrochimiquesàbasede l'oxyde de fer seul. Plusieurs idées ont été avancées afind'améliorerles rendements de conversion.

Des films de α-Fe_2O_3dopés au chrome ont été déposés avec succès sur des substrats de verre revêtus de FTO en utilisant le procédé hydrothermique et un procédé de recuit. La concentration des atomes de Cr incorporés (ionsCr^{4+}) a été contrôlée en faisant varier la concentration de la solution duprécurseur Cr $(ClO_4)_3$ (à savoir, la concentration du dopant dans l'échantillon est contrôlée en ajustant la composition électrolytique). L'effet majeur des atomes de Cr est l'amélioration de la conductivité et des propriétés de transport de charge des films de α-Fe_2O_3. La photoactivité de l'oxyde de fer a été améliorée par dopageauCr. Les échantillons les plus performants ont un taux de dopage de 16 at.% Cr, qui à son tour a un IPCE de 6% à 400 nm, avec un potentiel appliqué de + 0,4V (vs Ag/AgCl). Les valeurs de l'IPCE du matériau dopé étaient trente fois plus élevées que celles du matériau non dopé. Par conséquent, une fraction plus grande de paires électron-trou est disponible pour la chimie redox de surface. L'optimum apparent avec un dopage de 16 at.% de Cr peut équilibrer ces effets concurrents de la manière la plus efficace et donner les meilleures performances de PCE. Les films α-Fe_2O_3 dopés au Cr fournissent des applications potentielles dans des dispositifs photoélectriques ou dans la photocatalyse appliquée au craquage de l'eau.

Le n-Fe_2O_3 et p-CuSCN ont été électrodéposés avec succès sur des substrats FTO formant ainsi une hétérojonction. Une solution électrolytiquede base faible (NH_3) est utiliséepour éviter l'attaque acide de α-Fe_2O_3. Cela nous a permisd'étudier le comportement énergétique des deux semi-conducteurs et les performances photoélectrochimiques de l'hétérojonction n-Fe_2O_3/p-CuSCN. La FESEM montre qu'on peut facilement fabriquer du CuSCN épais pour recouvrir le substrat α-Fe_2O_3. Lesanalyses EDX ont révélé que les films de CuSCN ont un léger excès encuivre. Les performances photoélectrochimiques de l'hétérojonction nanostructurée α-Fe_2O_3/CuSCN sont supérieures à celle de FTO/α-Fe_2O_3 et FTO/CuSCN. La photoélectrode α-Fe_2O_3 / CuSCN exhibe un maximum de densité de photocourant de 2.9 mA/cm^2 à 0.59 V (vs Ag / AgCl). L'amélioration de la densité de photocourant est attribuée à deux facteurs principaux combinés: (i) génération d'un champ électrique dans l'hétérojonction qui supprime la recombinaison des porteurs de charge photogénérés et (ii) l'application d'une polarisation externe adéquate favorisant le transfert et la séparation des porteurs de charge photogénérés dans l'hétérojonctionα-Fe_2O_3/CuSCN. L'amélioration de la densité de

photocourant a également été attribuée à un alignement approprié des bords de bande des semi-conducteurs améliorant ainsi l'absorption de la lumière dans les deux semi-conducteurs. Finalement dansl'étudebasée sur le α-Fe_2O_3 comme matériau de transport d'électrons, nous avons utilisé les perovskites comme absorbeur de lumière de lumière, et le spiroMeOTAD comme matériau de transport de trous. Le film mince d'α-Fe_2O_3 a été préparé par électrodéposition et les processus hydrothermaux. La couche de pérovskite a étésynthétisée sur la surface du film mince d'α-Fe_2O_3 en utilisant la méthode de revêtement par centrifugation. Il a été constaté que la croissance du film mince d'α-Fe_2O_3 a une influence évidente sur la formation uniforme de la couche de pérovskite. Des couches minces denses de α-Fe_2O_3 avec des granulométries appropriées peuvent assurer une couverture uniforme du film de pérovskite, formant un meilleur contact entre le film d'α-Fe_2O_3 et la couche de pérovskite, ce qui facilite non seulement le transport de charge, mais aussi réduit la recombinaison des charges à l'interface α-Fe_2O_3/perovskite. Pour le craquage de l'eau la densité de photocourant maximale observée pour la photoélectrode α-Fe_2O_3/α-Fe_2O_3 est de 12mA/cm^2 vs Ag/AgCl, l'IPCE évaluée à 400 nm est de 9% avec un potentiel appliqué de 0.4V vs Ag/AgCl. La dépendance des propriétés photovoltaïques des PSC sur α-Fe_2O_3a étésoigneusement examinée. La stabilité des PSC a étéégalement étudiée. Le dispositif le plus performant aun PCE de 5.76 %, un Voc de 1.55 V, un Jsc de 11.27 $mAcm^{-2}$ et un FF de 33 %. Cet effet peut être attribué aux films de pérovskite dense qui conduisent à une couverture complète du film mince d'α-Fe_2O_3et un meilleur contact. De plus, le dispositif le plus performant est également le plus stable parmi tous les dispositifs présentés. Par conséquent, nous pouvons affirmer que le contact entre α-Fe_2O_3 et la couche de pérovskite est le facteur critique qui détermine lesperformances photovoltaïques des PSC. En outre, les résultats indiquent ungrand potentiel de l'α-Fe_2O_3 en tant que matériau de transport d'électrons, pour la conception de cellules solaires à base de perovskite.

Chapitre VI

Conclusion et perspectives

Conclusions

Dans cette partie nous analysons le niveau de conformité des objectifs énoncés dans l'introduction aux résultats obtenus. Les principales conclusions sont également compilées, les contributions les plus pertinentes de ce travail sont exposées et plusieurs lignes de travail futures sont proposées.

Comme nous l'avons vu tout au long de ce document, nous avons réussi à élaborer l'oxyde de fer par voie hydrothermale et voie électrochimique. Afin d'améliorer les performances de cette photoanode nous avons dopé l'oxyde de fer, et l'avons utilisé dans une cellule photovoltaïquecomme matériau de transport d'électrons.

Atteindre les objectifs

Le premier objectif consiste en l'élaboration et la caractérisation de l'oxyde de fer (hématite)dopé au chromeparla voie hydrothermale (article 1).

Le deuxième objectif consiste utiliser l'oxyde de fer dans deshétérostructures et l'utiliser comme matériau de transport d'électrons dans une cellule photovoltaïque (articles 2 et 3).

Futures lignes de recherche

Enfin, il y a plusieurs façons de continuer les travaux entamés dans cette thèse. D'une part, outre le chrome on peut étendre le dopage à plusieurs éléments. D'autre part, il est prévu d'étendre l'étude à d'autres hétérostructures en utilisnat l'hématite.

Il serait également intéressant de combiner plusieurs couches et même plusieurs cellules (tandem cell).

Les couches minces d'oxyde de fer peuvent présenter un grand potentiel pour une recherche de pointe visant à améliorer pour leurs caractéristiques électriques et optiques et les rendre rentables dans plusieurs applications.

Les procédés de fabrication tels que l'électrodéposition et l'hydrothermal, etc. sont des techniques très appropriées et peu coûteuses pour améliorer l'efficacité et réduire le coût de fabrication des films minces.

Remerciements

Ce travail a été soutenu par :

- le Ministère de l'Enseignement Supérieur et de la Recherche scientifique **Tunisie**
- Université de **Tunis**
- Laboratoire de Photovoltaïque (LPV), Centre de Recherches et des Technologies de l'Energie, Technopole de Borj Cédria **Tunisie**
- Ministerio de Economía y Competitividad (ENE2013-46624-C4-4-R) et Generalitat **Valenciana** (Prometeus 2014/044).
- Group d'optoelectronica i semiconductors. Departament de Física Aplicada – Institut de Disseny i Fabricació (IDF).
- l'Université Polytechnique de **Valence** (UPV).

➢ Annexe

Articles publiés

- **F. Bouhjar**, M.L. Chourou, Shafi Ullah, B. Marí and B. Bessaïs; **Electrochemical fabrication and characterization of p-CuSCN/n-Fe_2O_3 heterojunction devices for hydrogen production**, Journal of the Electrochemical Society, 164 (13) H1-H10 (2017). Published on line 29-oct-2017. DOI:10.1149/2.1431713jes

- Shafi Ullah, **Feriel Bouhjar**, Hanif Ullah, Miguel Mollar, Bernabé Marí **Synthesis of in-gap band $CuGaS_2$:Cr absorbers and numerical assessment of their performance in solar cells** Solar in Article Energy Materials and Solar Cells · July 2017 DOI: 10.1016/j.solmat.2017.06.062

- **F. Bouhjar**, M. Mollar, M.L. Chourou, B. Marí and B. Bessaïs, **Hydrothermal synthesis of Nanostructured Cr-doped hematite with enhanced photoelectrochemical activity**, Electrochimica Acta 260, p.838-846 (2018) doi: 10.1016/j.electacta.2017.12.049

- **F. Bouhjar**, M. Mollar, Shafi Ullah, B. Marí and B. Bessaïs, **Influence of a compact α-Fe_2O_3 layer on the photovoltaic performance of perovskite-based solar cells.** Journal of The Electrochemical Society. 165 (2) H1-H9 (2018)Section: Physical and Analytical Electrochemistry, Electrocatalysis, and Photoelectrochemistry.DOI:10.1149/2.1131802jes

- **F. Bouhjar**, B. Bessaïs and B. Marí Ultrathin-Layer α-Fe_2O_3 Deposited Under Hematite for Solar Water **Splitting Journal of Solid State Electrochemistry doi.org/10.1007/s10008-018-3946-7.**

- Suzan Saber, **Feriel Bouhjar**, Miguel Mollar, Amany El Nahrawy, Nagwa Khattab, Ali Eid, Mohamed AboAly, Bernabé Marí Single Step Electrodeposited Kesterite Cu_2ZnSnS_4 (CZTS) thin films at low annealing temperatures **Journal of Insights in Analytical Electrochemistry DOI: 10.21767/2470-9867.100028. Vol.4 No.1:8. 2018.**

➢ Articles Soumis

- **F. Bouhjar**, B. Bessaïs and B. Marí, Electrodeposited chrome-doped α-Fe2O3 thin film for solar water splitting, **Journal of Applied Electrochemistry JACH-D-18-00179.**

- **F. Bouhjar**, B. Bessaïs and B. Marí, Photo-deposition of Cobalt-Phosphate Group-modified hematite for efficient water splitting, **Journal of RSC Advances, published by the Royal Society of Chemistry RA-ART-03-2018-002584.**

- Shafi Ullah, **Feriel Bouhjar**, Hanif Ullah, Miguel Mollar, Bernabé Marí, Fabrication of Cd1-xZnxS Buffer Layers Deposited by Chemical Bath Deposition for Photovoltaic Applications, **Journal of Renewable Energy RENE-D-17-02488.**

- **F. Bouhjar**, B. Bessaïs and B. Marí, Efficient perovskite flexible solar cells with low cost and low-temperature-processed ZnO electron transport layer. **Energy & Environmental Science - EE-ART-04-2018-001240**

- **F. Bouhjar**, B. Bessaïs and B. Marí Hydrothermal fabrication and characterization of ZnO/Fe_2O_3 heterojunction devices for hydrogen production **Journal of Energy Chemistry JECHEM_2018_330.**

Journal of The Electrochemical Society, **164** (13) H936-H945 (2017)
0013-4651/2017/164(13)/H936/10/$37.00 © The Electrochemical Society

Electrochemical Fabrication and Characterization of p-CuSCN/n-Fe_2O_3 Heterojunction Devices for Hydrogen Production

F. Bouhjar,[a,b,c] Shafi Ullah,[a] M. L. Chourou,[b] M. Mollar,[a] B. Marí,[a,z] and B. Bessaïs[b]

[a]*Institut de Disseny i Fabricació, Universitat Politècnica de València, 46022 València, Spain*
[b]*Laboratoire Photovoltaïque, Centre de Recherches et des Technologies de l'Energie Technopole de Borj - Cedria, Hammam-Lif 2050, Tunisia*
[c]*University of Tunis, Tunis, Tunisia*

p-CuSCN/n-Fe_2O_3 heterojunctions were electrochemically prepared by sequentially depositing α-Fe_2O_3 and CuSCN films on FTO (SnO_2:F) substrates. Both α-Fe_2O_3 and CuSCN films and α-Fe_2O_3/CuSCN heterojunctions were characterized by field emission scanning electron microscopy (FESEM), energy-dispersive X-ray spectroscopy (EDX), and X-ray diffraction (XRD). Pure crystalline CuSCN films were electrochemically deposited on α-Fe_2O_3 films by fixing the SCN/Cu molar ratio in an electrolytic bath to 1:1.5 at 60°C, and at a potential of −0.4 V. The photocurrent measurements showed increased intrinsic surface states or defects at the α-Fe_2O_3/CuSCN interface. The photoelectrochemical performance of the α-Fe_2O_3/CuSCN heterojunction was examined by chronoamperometry and linear sweep voltammetry techniques. The α-Fe_2O_3/CuSCN structure exhibited greater photoelectrochemical activity compared to the α-Fe_2O_3 thin films. The highest photocurrent density was obtained for the α-Fe_2O_3/CuSCN films in 1 M NaOH electrolyte. This strong photoactivity was attributed to both the large active surface area and the external applied bias, which favored the transfer and separation of the photogenerated charge carriers in the α-Fe_2O_3/CuSCN heterojunction devices. The flatband potential and donor density were maximal for the heterojunction. These results suggest a substantial potential to achieve heterojunction thin films in photoelectrochemical water splitting applications.
 [DOI: 10.1149/2.1431713jes]

Manuscript submitted April 28, 2017; revised manuscript received September 5, 2017. Published October 28, 2017.

In recent years, a great deal of attention has been paid to heterogeneous thin film deposition on highly structured semiconductor substrates, such as Fe_2O_3, ZnO, TiO_2, and GaN, to form heterojunctions. The last semiconductors are essential in many electrical, photoelectrical and catalytic applications, and generally require an enlarged interface area. In thermodynamic terms, the water splitting reaction is an uphill process that requires a minimum energy of 1.23 eV as the Gibbs free energy change is $\Delta G^{\circ} = 237.2$ kJ mol^{-1} or 2.46 eV per H_2O molecule.[1] However, a high overpotential is necessary due to non idealities in real operations by taking into account water splitting reaction complexity. The water splitting process requires two steps as it is not quite as straightforward as ripping apart the three atoms in H_2O. The full reaction requires the participation of two H_2O molecules, which are then separated according to the following reduction and oxidation half-reaction.[2]

Reduction reaction:

$$2H^+ + 2e^- \rightarrow H_2 = \left(E^0_{red} = 0.00\,\text{V/RHE}\right) \quad [1]$$

Oxidation reaction:

$$2H_2O + 4h^+ \rightarrow O_2 + 4H^+ \left(E^0_{ox} = -1.23\,\text{V/RHE}\right) \quad [2]$$

Overall reaction:

$$2H_2O \rightarrow 2H_2 + O_2\,(\Delta E = -1.23\,\text{V/RHE}) \quad [3]$$

where RHE indicates a reversible hydrogen electrode (RHE).

Given that four-electron water oxidation is the rate-limiting step in the overall water splitting reaction, one major barrier that must be overcome is to develop high-efficiency photoanodes for O_2 evolution to be capable of overcoming the high overpotential, which implies having to perform this reaction.[3] Hematite (α- Fe_2O_3) is one of the most promising photoanode candidates as it has a narrow bandgap of ∼ 2.1–2.2 eV and allows ∼ 16.0% theoretical solar-to-hydrogen (STH) efficiency for photoelectrochemical (PEC) water splitting.[4–6] Compared to other narrow bandgap semiconductors, α- Fe_2O_3 also offers many additional advantages, including excellent stability in alkaline solutions, earth abundance and nontoxicity.[3–7] However, α-Fe_2O_3 has extremely poor electrical conductivity with a hole diffusion length of 2–4 nm,[8] and it undergoes a high charge carriers recombination that leads to poor PEC performance. The future success of α-Fe_2O_3 photoanodes in PEC water splitting remains questionable as α- Fe_2O_3 itself can hardly achieve relatively good PEC efficiency for practical potential uses, and requires modifications to improve PEC performance.

An overview of the synthesis, modification, and characterization of nanostructured an α-Fe_2O_3 thin film is provided herein, and emphasis is placed on charge carrier dynamics and PEC properties.[9] Increasingly more studies has focused on α-Fe_2O_3 heterostructures in recent years, which incorporate the second material to promote charge separation, charge collection and surface catalysis. Indeed greater PEC activities have been achieved with such α-Fe_2O_3 heterostructure-based photoanodes than with their single-component counterparts; e.g., WO_3/α-Fe_2O_3,[10] ZnO/ α-Fe_2O_3,[11] n-Si/ α-Fe_2O_3,[12] α-Fe_2O_3 /NiO,[13] α-Fe_2O_3:Ti/Cu_2O,[14] p-Si/ α-Fe_2O_3 /Au,[15] and α-Fe_2O_3 /Gr/$BiV_{1-x}Mo_xO_4$.[16]

Table I shows a review done of the characteristics of some typical α-Fe_2O_3-based semiconducting heterojunctions that can be found in the literature. The data in Table I include heterostructure type, fabrication method, suggested electrons and holes charge transfer, as well as the main photoelectrical properties of these heterostructures. These data are compared with the electrochemically deposited Fe_2O_3/CuSCN heterojunction described in this work.

CuSCN is a p-type hole-conducting material that is transparent within the visible light spectrum range, which possesses reasonable hole conductivity ($\geq 5 \times 10^{-4}\,\text{S}\cdot\text{cm}^{-1}$)[17] and good chemical stability.[18] In this work, we describe the electrochemical deposition of Fe_2O_3/CuSCN heterojunction films. CuSCN films with several compositions were deposited on smooth Fe_2O_3 surfaces. Characterization of films was carried out by FESEM and X-ray diffraction (XRD) techniques.

Experimental

Electrodeposition.—Iron oxide films were deposited using an electrodeposition bath that consists of an aqueous solution containing ferric chloride ($FeCl_3 . 6H_2O$, purity (p)≥98.0), hydrogen peroxide (H_2O_2, ≥99.99%), potassium fluoride (KF, p≥99.97%) and potassium chloride (KCl, p≥99.0%). Potassium perchlorate ($KClO_4$, p≥99.0%), copper(II) perchlorate hexahydrate ($Cu(ClO_4)_2 \cdot 6H_2O$, p≥98.0%), ammonium thiocyanate (NH_4SCN, p≥99.0%) and triethanolamine (TEA, $C_6H_{15}NO_3$, p≥99.5%) were used as precursors for the electrodeposition of CuSCN. All the chemicals were purchased from

[z]E-mail: bmari@fis.upv.es

Table I. Hematite-based heterostructures, including fabrication methods, suggested charge transfer and photoelectrochemical characteristics.

Heterostructure	Fabrication method	Suggested charge transfer		Photoelectrochemistry	Ref.
		Electron	Hole		
WO_3/ α-Fe_2O_3	Sol–gel	WO_3→ α-Fe_2O_3	None	Photocurrent: 22 μAcm^{-2} at 0.8 V vs. Ag/AgCl (500 W Xe lamp) elec- trolyte: 0.2 M Na_2SO_4 (pH = 7.5)	19
WO_3/ α-Fe_2O_3	spin coating and Spray pyrolysis	None	None	Photocurrent: 22 mAcm^{-2} at 0.8 V vs. Ag/AgCl; electrolyte: 0.05 M PBS (pH = 7)	20
ZnO/α-Fe_2O_3	Hydrothermal and spin coating	α-Fe_2O_3 →ZnO	ZnO → α-Fe_2O_3	Photocurrent: 1.6 mA cm^{-2} at 0.6 V vs. Ag/AgCl; electrolyte: 1 M NaOH	21
α-Fe_2O_3 /Gr/BiV_{1-x} Mo_xO_4	Hydrothermal and spin coating	BiV_{1-x} Mo_xO_4 → α-Fe_2O_3	α-Fe_2O_3 →BiV_{1-x} Mo_xO_4	Photocurrent: 0.39 mA cm^{-2} at 1.5 V vs. RHE (64 mW cm^{-2} λ > 420 nm); electrolyte: 0.01 M Na_2SO_4	22
α-Fe_2O_3/$ZnFe_2O_4$	Spin coating	$ZnFe_2O_4$ → α-Fe_2O_3	α-Fe_2O_3 → $ZnFe_2O_4$	Photocurrent: 0.44 mA cm^{-2} at 0.2 V vs. Ag/AgCl; electrolyte: 0.1 M glucose and 0.5 M NaOH (pH = 13.0)	23
α-Fe_2O_3: Ti/$ZnFe_2O_4$	Hydrothermal and surface treatment	$ZnFe_2O_4$ →α-Fe_2O_3: Ti	α-Fe_2O_3: Ti → $ZnFe_2O_4$	Photocurrent: 0.3 mA cm^{-2} at 1.4 V vs. RHE; electrolyte: 1 M KOH	24
α-Fe_2O_3: Co/$MgFe_2O_4$	Hydrothermal and wet impregnation	$MgFe_2O_4$ → α-Fe_2O_3: Co	α-Fe_2O_3: Co →$MgFe_2O_4$	Photocurrent: 3.34 mA cm^{-2} at 1.4 V vs. RHE; electrolyte: 0.01 M Na_2SO_4	25
p-$CaFe_2O_4$/n-Fe_2O_3	Hydrothermal and two-step annealing	p-$CaFe_2O_4$ → n-Fe_2O_3	n-Fe_2O_3 → p-$CaFe_2O_4$	Photocurrent: 0.53 mA cm^{-2} at 1.23 V vs. RHE; electrolyte: 1.0 M KOH (pH = 13.9)	26
α-Fe_2O_3: Ti/Cu_2O	Spray pyrolysis	Cu_2O →α-Fe_2O_3: Ti	α-Fe_2O_3: Ti → Cu_2O	Photocurrent: 2.60 mA cm^{-2} at 0.95 V vs. SCE (Xe lamp, 150 mW cm^{-2}); electrolyte: 0.1 M NaOH	27
α-Fe_2O_3/CuSCN	electrodeposition	CuSCN→ α-Fe_2O_3	α-Fe_2O_3 → CuSCN	Photocurrent: 2.90 mA cm^{-2} at 0.59 V vs. Ag/AgCl. (Xe lamp: 150 W); electrolyte 0.1 M NaOH(pH = 13.9)	our work

Aldrich chemicals and were used as received. The experimental setup followed to prepare α-Fe_2O_3 films consisted of a computer-controlled potentiostat/galvanostat and a classical three-electrode electrochemical cell. The electrochemical cell was filled with an electrolyte solution that contained deionized water + 5 mM $FeCl_3$ + 5 mM KF + 1 M H_2O_2 + 0.1 M KCl. The working electrode (WE) is a fluorine-doped tin oxide- (FTO) coated glass with a sheet resistance of 10 Ω/□. It was previously cleaned for 15 min in an ultrasonic acetone bath and then rinsed in distilled water and dried. The Pt and Ag/AgCl electrodes were used as a counter-electrode and a reference electrode, respectively. Films were deposited by cathodic electrodeposition. To obtain a thickness of approximately 500 nm for all the Fe_2O_3films, the deposition potential was fixed at −0.1 V and the debited charge was 1.2 C. The temperature of the solution was fixed at 298 K by a thermostat. After the deposition process, films were rinsed with distilled water. To obtain the desired α-Fe_2O_3 phase, the deposited films were annealed at 650°C for 2 h in air. The electrodeposition of CuSCN was performed in the same way as with the Fe_2O_3 films. The deposition potential was fixed at −0.4 V and the debited charge was 1 C, which gave rise to a film thickness of about 3 μm. The solution temperature was fixed at 333 K by a thermostatic bath. The electrolytic bath was prepared from 0.1 M $KClO_4$, 0.01 M Cu $(ClO_4)_2 \cdot 6H_2O$, 0.05 M NH_4SCN and 0.06 M TEA ($C_6H_{15}NO_3$). About 0.5–1.0 mL of 2 M NH_3 was added to the electrolyte to keep the pH of the solution at around 9.

Materials characterization.—The crystal structures of the α-Fe_2O_3 and α-Fe_2O_3/CuSCN heterojunction were investigated by XRD (Rigaku Ultima IV diffractometer in the Bragg-Bentano configuration) using CuKα radiation (λ = 1.54060 Å). The microstructural and elemental analyses were characterized with scanning electron microscope (SEM) (model Zeiss ULTRA 55), equipped with an energy dispersive spectroscopy (EDS) system. To determine the bandgap, energy was estimated from the optical absorption, which was measured by recording the transmission spectra in a UV-Visible spectrophotometer (Ocean Optics HR4000) coupled to an integrating sphere to collect both specular and diffuse transmittances.

Photoluminescence (PL) was measured by an He-Cd laser (λ = 325 nm) and a Jobin Yvon-Horiba spectrometer coupled to a Hamamatsu back-thinned Si-CCD detector.

Photoelectrochemical and electrochemical analyses.—The PEC measurements were taken in a quartz cell to help the light reach the photoelectrode surface. The light-exposed surface of the working electrode was 0.25 cm^2. The electrolyte used in all PEC measurements was 1.0 M NaOH (pH = 13.6). The electrolyte was purged with nitrogen gas before the experiments to prevent any possible reaction with dissolved oxygen at the counter-electrode. A potentiostat/galvanostat Autolab PGSTAT302N (Metrohm, the Netherlands), with a Pt rod counter-electrode and an Ag/AgCl saturated in 3 M KCl reference electrode, was used. Films were illuminated by a 150 W Xenon lamp (PLSSXE300/300UV) coupled to a chopper and a selective blue filter (λ > 400 nm). The setup was completed with an automatic shutter and a filter box. The whole system was controlled by homemade software. The J-V curves were monitored by linear sweep voltammetry (LSV) at 100 mV/s by setting the potentiostat within the range of 0 V to +0.8 V vs. Ag/AgCl. The chronoamperometry curves of the

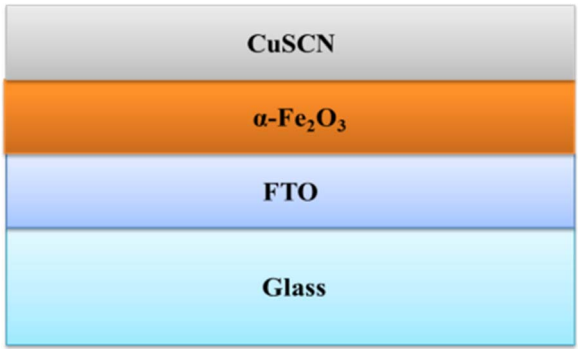

Figure 1. Schematic cross-sectional view of FTO/glass, compact α-Fe_2O_3, and CuSCN (HTM).

films were also obtained at +0.1 V in the dark and with illumination at an intensity of about 1 SUN (100 mW cm^{-2}) on the film surface. Mott–Schottky measurements were taken using an electrochemical impedance analyzer with the three-electrode configuration in a 0.1 M NaOH electrolyte solution; the AC amplitude was 10 mV and frequency fell within the 100 kHz–0.1 Hz range. The flatband potential (V_{FB}) and donor density (N_D) were determined in the dark from the impedance measurements.

Results and Discussion

Figure 1 shows a schematic cross-sectional view of the α-Fe_2O_3/CuSCN heterojunction deposited on the FTO glass substrates.

Potential variation.—Figure 2a shows the cyclic voltammogram of the Fe_2O_3 films recorded at 50 mV/s. During negative sweeps, Fe^{3+} reduced to Fe. In the reduction region, the film was deposited at a potential that ranged between –0.2 and 0 V. These films showed negligible photo-activity and were not further characterized.[28] Furthermore in positive sweeps, films were deposited by the electrochemical oxidation of Fe^{2+} ions to Fe^{3+} ions, followed by the precipitation of Fe^{3+} ions as ferric hydroxide ($Fe(OH)_3$). The anodic deposition of the iron oxide is represented by the following equations[29]

$$Fe^{2+} \leftrightarrow Fe^{3+} + e^- \quad [4]$$

$$Fe^{3+} + 3OH^- \rightarrow Fe(OH)_3 \downarrow \quad [5]$$

Figure 2b shows a cyclic voltammogram performed at 200 mV/s onto an α-Fe_2O_3 electrode using the electrolytic solution described in the experimental section. The voltammetric scan was initiated at 0 V toward the negative direction of up to −0.8 V. The cathodic threshold potential for the reduction of Cu^{2+} to Cu^+ ions in the solution was about −0.20 V. The cathodic current increased slowly to −0.40 V, then steeply to −0.60 V to become almost constant. The initial slow increase in the current indicated the existence of Cu(II)-TEA complexes in the solution, which resulted in slow diffusion and led to a shift of the reduction potential to more negative values, as well as to small cathodic reaction current density. [21] The electrodeposition of CuSCN is manifest when a white film appears on the electrode surface at about −0.30 V, and subsequently grows rapidly as the potential increases up to −0.60 V, which is referred to as a kinetically controlled region. Within the potential range −0.60 to −0.80 V, the saturation current density indicated that the diffusion process reached a limit, accompanied by a minor co-deposition of copper. Small brown spots are observed on the film when the deposition potential goes above −0.60 V. The voltammetric scan from −0.80 to 0.40 V showed a sharp peak at about −0.20 V, which meant that the CuSCN layer acted as a passivating layer for the α-Fe_2O_3 electrode. Another maximum around from 0.30 to 0.40 V is related to the oxidation of Cu^+ to Cu^{2+} ions. Hence the growth process of the CuSCN film from the TEA chelated aqueous

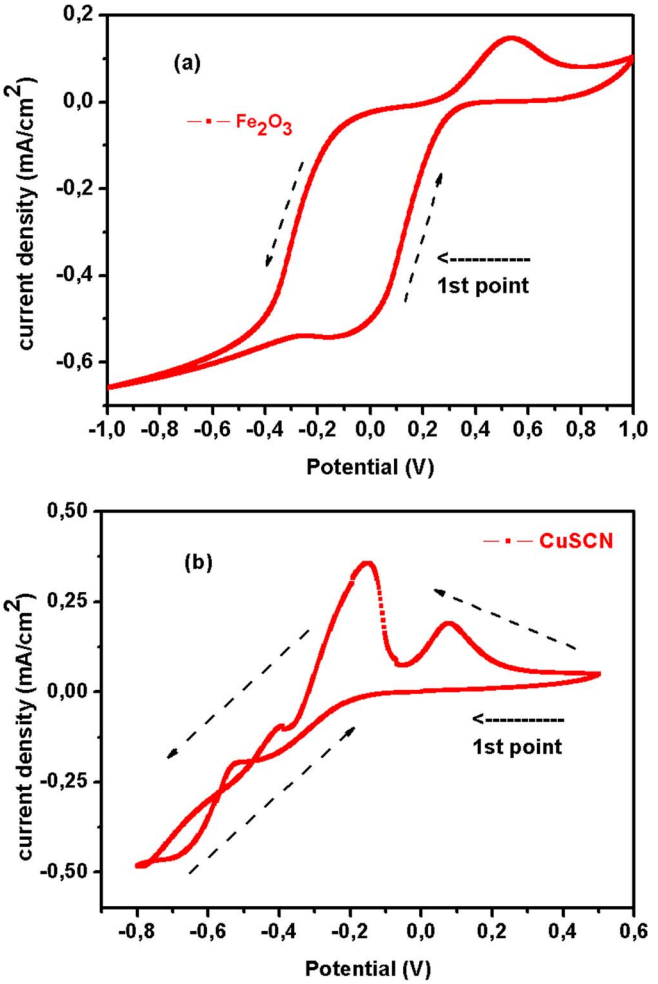

Figure 2. (a) Linear sweep voltammetry of the Fe_2O_3 precursor solution within the range of −1 V to 1 V on the fluoride doped Tin oxide electrode at a rate of 50 mVs^{-1}. (b) Linear sweep voltammetry of the CuSCN precursor solution within the range of −0.8 V to 0.6 V at a rate of 200 mVs^{-1}.

solution suggested that cupric ions, which were related to the Cu(II)-TEA complexes and stabilized in the electrolyte solution, first reduced to cuprous ions ($Cu^{2+}+e^- \rightarrow Cu^+$), and then the CuSCN film formed from the reaction between cuprous ions and thiocyanate ions ($Cu^+ + SCN^- \rightarrow$ CuSCN). Such a deposition took place within a potential range from −200 to −550 mV. Thereafter, Cu codeposition would occur. Hence we can conclude that the appropriate deposition potentials in the sole deposition of CuSCN in the TEA-chelated aqueous solution should be selected within the potential range from −200 to −550 mV. To further study the influence of the electrolytic bath composition on the nucleation and growth of the CuSCN films electrodeposited on the α-Fe_2O_3 surface, chronoamperometry measurements, based on the current transient recorded during the electrodeposition process at −0.40 V, were taken. Figure 3 shows the chronoamperometry for a CuSCN film deposited from an electrolyte that contained Cu and SCN in the molar proportion of 1:1.5. The rapid surge in current density observed upon the onset of the applied potential was due to double layer charging. Then the current density gradually decreased due to an increase in the electric resistance of the electrochemical system, which was related to the nucleation and growth of the CuSCN crystals with semiconductor characteristics.[22] After an interval of about 200 s, the current density gradual increased for a period of time and then the current density became constant.

Morphological, chemical composition and structural characterizations.—Figures 4a and 4b display the FESEM images of the

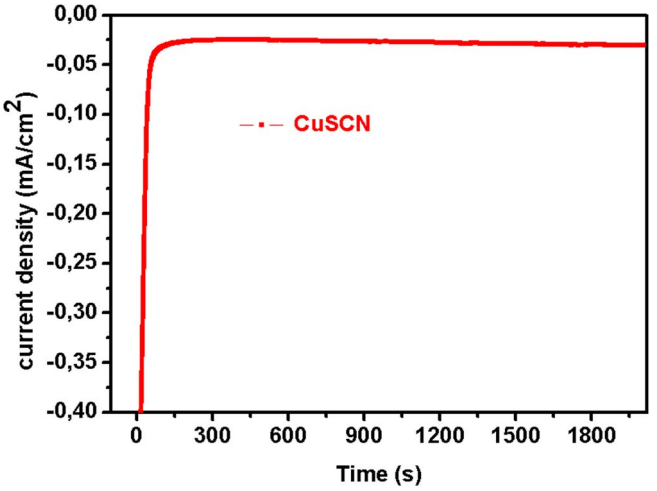

Figure 3. Chronoamperometry of CuSCN with a Cu: SCN ratio of 1:1.5.

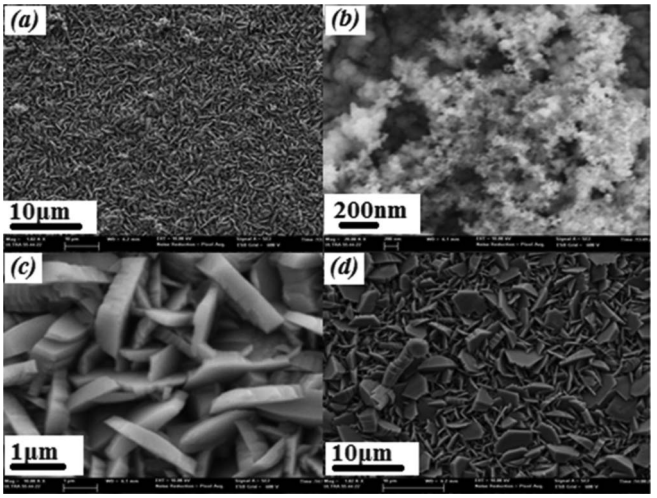

Figure 4. FESEM images of (a) CuSCN (b) α-Fe_2O_3 (c) α-Fe_2O_3/CuSCN (1 µm) (d) α-Fe_2O_3/CuSCN (10 µm).

CuSCN films and the α-Fe_2O_3 films deposited on FTO substrates, respectively. The FESEM image of CuSCN (Figure 4a) shows a mixture of leafy intrinsic trigonal pyramid shapes with some dispersion in grain sizes. Figure 4b depicts the morphology of the α-Fe_2O_3 films, and reveals nanostructured grains with a size dimension of about 20 nm. Figures 4c and 4d illustrate the CuSCN films deposited on the α-Fe_2O_3 covered substrates at different magnifications. For the CuSCN films deposited on α-Fe_2O_3, only the trigonal pyramid shapes with bigger grain sizes of approximately 3 µm are observed. We can see that the grain size of the CuSCN films deposited on α-Fe_2O_3 are bigger than those deposited on FTO.

Figure 5 shows the vertical cross-section images of the α-Fe_2O_3 (Figures 5a–5b), CuSCN (Figure 5c) and α-Fe_2O_3/CuSCN (Figure 5d) thin films deposited on FTO glass. The thickness of the α-Fe_2O_3 films and the CuSCN layer is about 500 nm and about 3.7 µm, respectively.

Figure 5d shows a cross-sectional FESEM image of the complete device (FTO/α-Fe_2O_3/CuSCN). The overall thickness between the FTO layer border and the top of the CuSCN layer that corresponded to the α-Fe_2O_3/CuSCN heterojunction is about 4.2 µm. The stoichiometric proportions of the CuSCN films prepared in an electrolyte solution with a molar ratio $[Cu^{2+}]/[SCN^{-}]$ of 1:1.5 at a static potential of −400 mV and a temperature of 333 K were estimated by EDX analyses. Figures 6a and 6b show the EDX emental analyses of the electrodeposited α-Fe_2O_3 and CuSCN, respectively. The line observed at 0.72 keV corresponds to the L line of Fe, while the oxygen K line peaks at 0.525 keV. The calculated atomic ratio of Fe and O approximately equals 2:3, which well agrees with the stoichiometric composition of α-Fe_2O_3. The percentages of the elements calculated from the EDX spectra are shown in the inset of Figure 6a. Figure 6b depicts the EDX spectrum

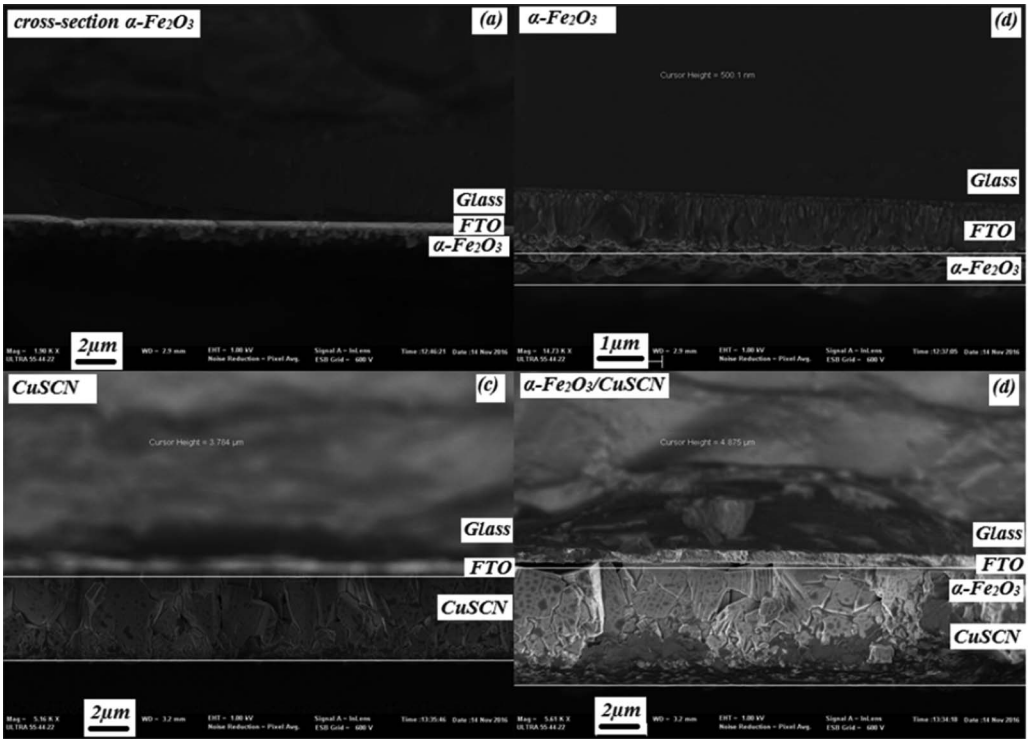

Figure 5. Vertical cross-section of (a-b) α-Fe_2O_3, (c) CuSCN and (d) heterojunction thin films.

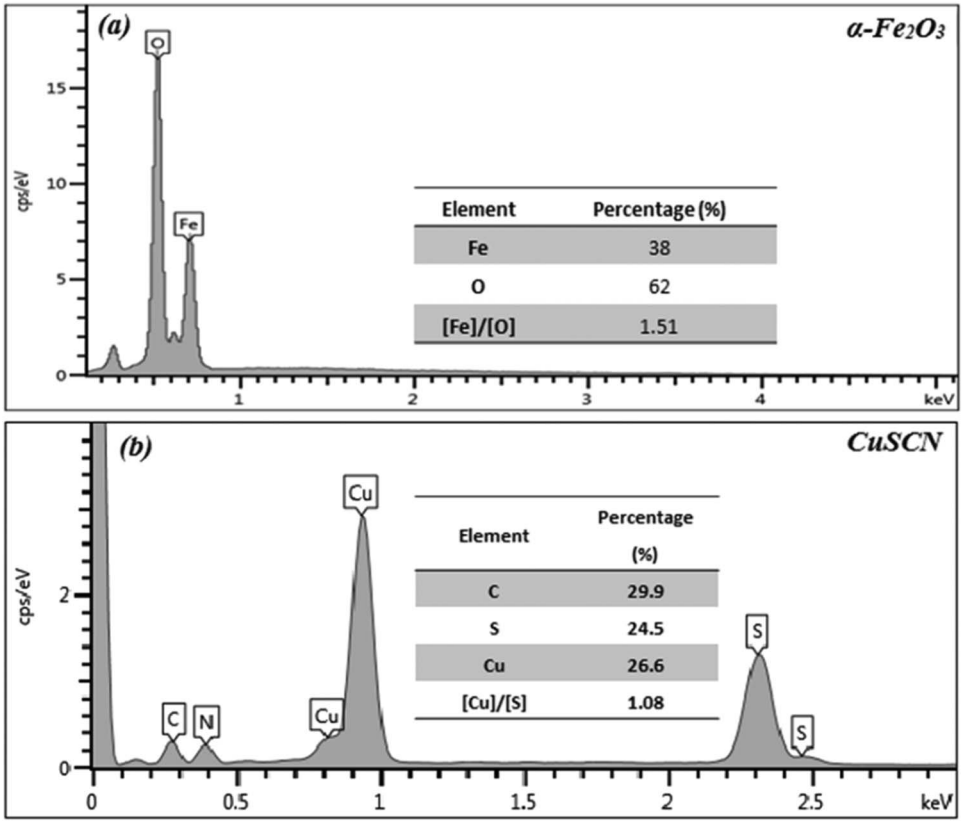

Figure 6. (a) EDX spectrum for α-Fe_2O_3, (b) EDX spectrum for the CuSCN thin films.

of the electrodeposited CuSCN film; only the lines that correspond to Cu, S, C and N are observed. The inset in Figure 6b displays the percentages calculated for the elements of the CuSCN film. The S content in the CuSCN film represents the SCN content in the film as S is not provided from environmental impurities. It has been reported in the literature that when SCN is in stoichiometric excess, $Cu(SCN)_{(1+x)}$ will show p-type semiconductor characteristics.[32] The composition of films in the above reference[32,33] was determined by the X-ray photoelectron spectroscopy (XPS) technique. In the XPS technique, only the surface composition was determined, which was released from the excess SCN ions during the film's growth. It is quite likely that some SCN ions might have been adsorbed on the surface, and consequently the XPS analysis would show a stoichiometric excess of SCN. However in the work of Zang et al.[34] the film composition determined by an EDX analysis revealed a stoichiometric excess of copper, and films still acted as a p-type semiconductor, similarly to that prepared herein. These results were confirmed by the Mott–Schottky measurements taken on these samples, which revealed the p-type behavior of the electrodeposited CuSCN films (See Figure 14b). Figure 7 shows the XRD patterns of the Fe_2O_3 and CuSCN layers deposited on the FTO substrates. The XRD patterns of the Fe_2O_3/CuSCN bilayer and the FTO substrates are also shown. The XRD peaks of the α-Fe_2O_3 films are observed at $2\theta = 24.1°$, 33.1°, 35.6°, 40.9°, 49.4°, 54.0° and 64°, which respectively correspond to the (012), (104), (110), (113), (024), (116) and (300) planes of the hematite phase. The dominant peaks are associated with planes (104) and (110). The diffraction peaks of the trigonal structure of the α-Fe_2O_3 well match the reference pattern JCPDS card file no. 33-0664, which corresponds to space group R3c (167) with lattice parameters a = b = 5.03 nm and c = 13.74 nm.

It is well-known that CuSCN exists in two polymorphic forms, α and β, where β is commonly available and more stable.[35,36] β-CuSCN has a hexagonal crystal structure in which layers of SCN ions separate Cu cation planes, and these layers asre interconnected by strong three-dimensionally Cu–S bonds. For the CuSCN films, all the diffraction peaks can be well indexed to the trigonal-phase β-CuSCN (space group R3m, no. 160). Compared to the standard diffraction pattern of CuSCN (JCPDS card file no. 29-0581), no specific peaks related to other phases of CuSCN or impurities were observed, which indicates the high purity and good crystallinity of the final products. For the Fe_2O_3/CuSCN bilayer, all the peaks matched the Fe_2O_3 and CuSCN patterns, except those marked with asterisks, which came from the FTO substrate.

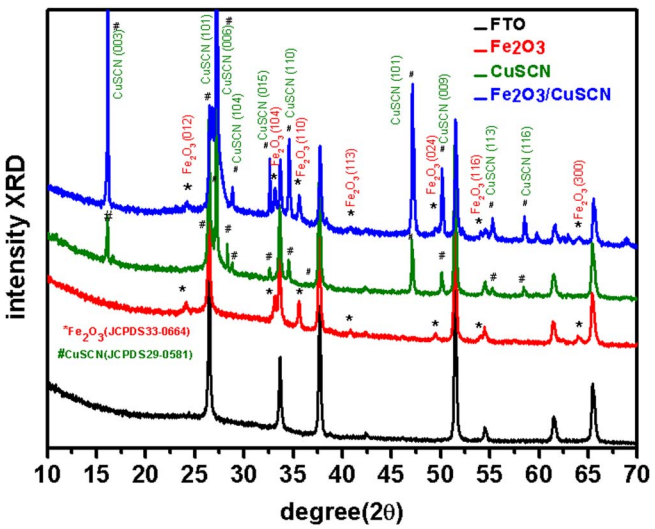

Figure 7. XRD spectra of FTO, α-Fe_2O_3, CuSCN and the Fe_2O_3/CuSCN bilayer.

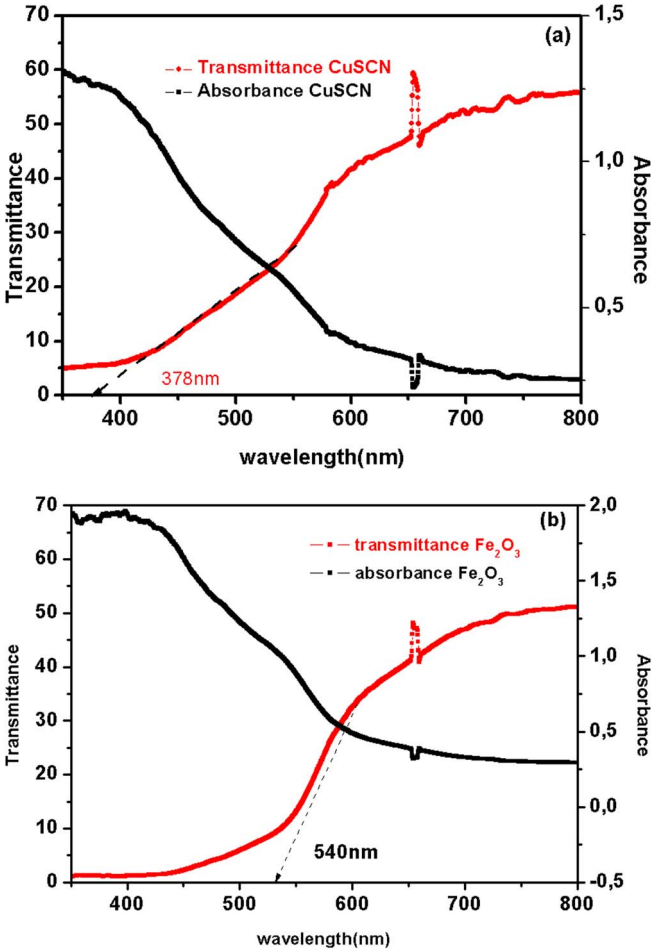

Figure 8. Transmittance and absorbance spectra of (a) CuSCN and (b) α-Fe_2O_3.

Optical Properties of CuSCN

Figures 8a and 8b respectively show the transmission and absorption spectra of the CuSCN film and α-Fe_2O_3. The energies of the optical bandgaps can be determined from the transmission spectra.[37] The transmittance spectrum of CuSCN (Figure 8a) reveals a high optical transmission value above 60% within the visible range. A significant increase in absorption below 320 nm can be assigned to the intrinsic bandgap absorption of CuSCN. It appears that the α-Fe_2O_3 films possess high absorbance in the visible region, which indicates their applicability as absorbing material[38] (Figure 8b). To calculate the optical band-gap energy (E_g) of films, the absorption coefficient can be estimated as follows:

$$\alpha = \frac{1}{d}\ln\left(\frac{1}{T}\right) \quad [6]$$

The relation between the absorption coefficient α and the energy of incident light $h\nu$ is given by:[30]

$$\alpha h\nu = A(h\nu - Eg)^n \quad [7]$$

where α is the absorption coefficient, A is a constant, h is Planck's constant, ν is photon frequency, Eg is the optical bandgap, and n equals 2 for the direct transition, and equals 1/2 for indirect transition. According to the Tauc plot (($\alpha h\nu$)^2 vs. $h\nu$) (Fig. 9), the optical bandgap Eg of the typical CuSCN film is about 3.3 eV. Jaffe et al.[40] predicted that an indirect bandgap of 3.5 eV existed from an electronic band structure model, which was calculated by the Density Functional Theory. However, the absorption measurements taken on the CuSCN samples indicated the presence of an indirect bandgap of 3.9 eV.

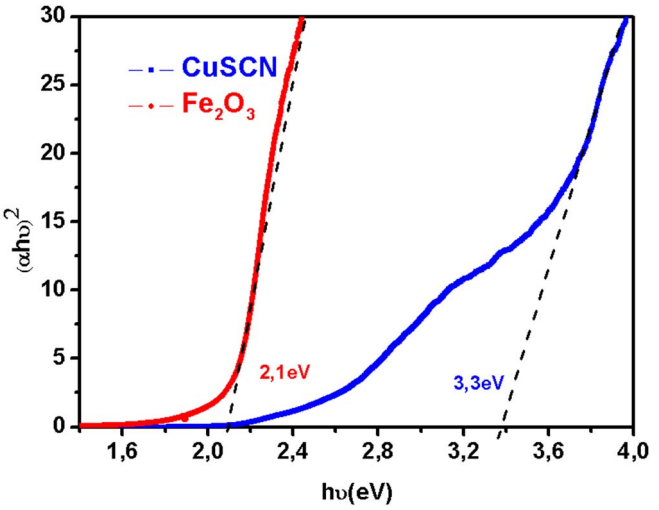

Figure 9. Tauc plot of CuSCN and α-Fe_2O_3.

Figure 9 depicts the Tauc plot of the α-Fe_2O_3 films, which might indicate a direct bandgap energy of about 2.1 eV, which is smaller than that of the bulk α-Fe_2O_3 (2.3 eV).[41]

Figure 10 shows the normalized photoluminescence (PL) spectra for the α-Fe_2O_3 and CuSCN films and for the α-Fe_2O_3/CuSCN bilayer, where the excitation wavelength is 325 nm of a He-Cd laser. The PL spectrum of α-Fe_2O_3 shows a wide PL peak that centers around 623 nm with a Full Width at Half Maximum (FWHM) of about 100 nm. The PL spectrum of CuSCN exhibits a broad band centered at 590 nm that slightly shifts to higher energy compared to α-Fe_2O_3. The radiative transitions in CuSCN would involve deep levels (located near the middle of the gap) because the energy of the emitted photons is approximately half the bandgap energy. The PL spectrum of the Fe_2O_3/CuSCN bilayer is indistinguishable of the PL spectrum of α-Fe_2O_3. Figure 11a depicts a scheme of the energy band diagram that corresponds to α-Fe_2O_3 and CuSCN before and after heterojunction formation. This scheme is useful for explaining PL behaviors. The radiative recombination takes place mainly on the Fe_2O_3 layer, which means that instead of recombining through the CuSCN deep levels, the photoelectrons generated on the CuSCN layer move to Fe_2O_3, where they radiatively recombine. As a result, the PL spectrum of the

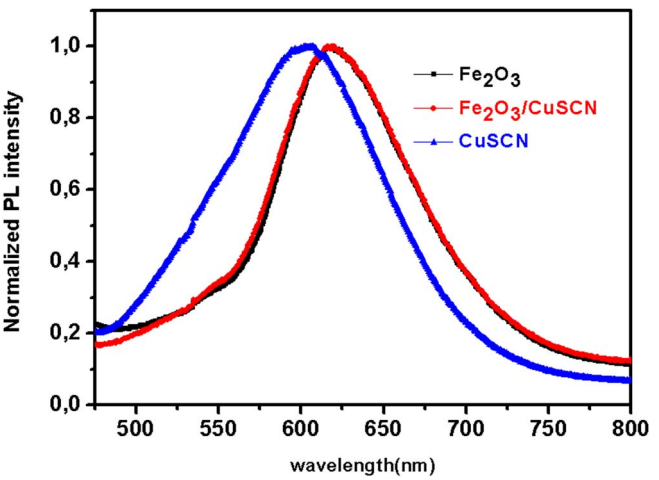

Figure 10. The PL spectrum of α-Fe_2O_3, CuSCN and Fe_2O_3/CuSCN.

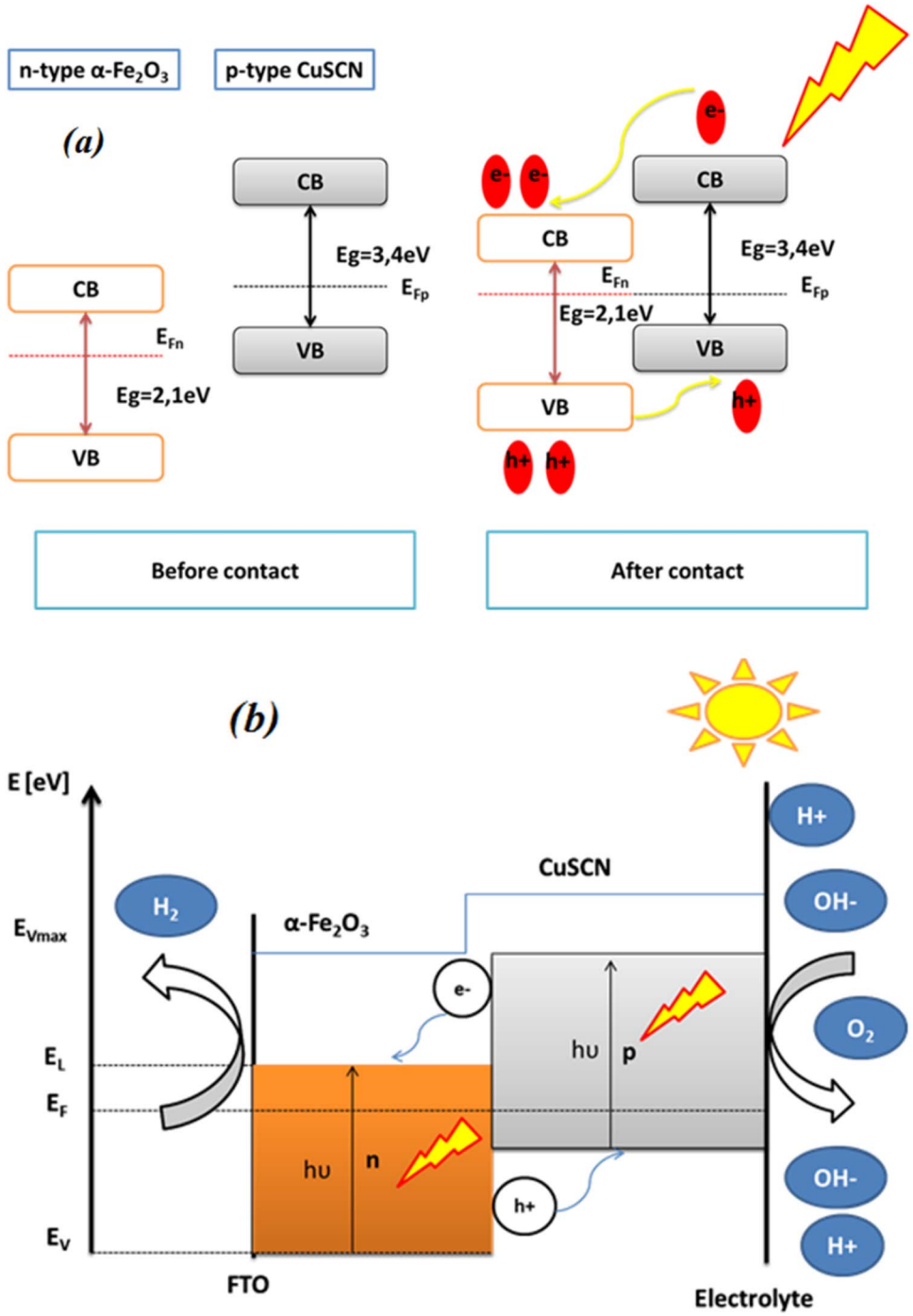

Figure 11. (a) Energy band diagram of α-Fe_2O_3 and CuSCN before and after p-n junction formation, (b) Schematic band energy diagram of the α-Fe_2O_3 and CuSCN heterojunction with the band bending and alignment due to the solution.

Fe_2O_3/CuSCN heterojunction shows no recombination on the CuSCN layer.

Photoelectrochemical measurements.—*Current voltage characteristics.*—The nanostructured α-Fe_2O_3 and CuSCN films, and the α-Fe_2O_3/CuSCN heterojunction, were used as photoelectrodes in a photoelectrochemical cell. Current-voltage characteristics were recorded in the dark and with illumination. The externally applied bias varied from 0 V vs. Ag/AgCl (cathodic bias) to 0.8 V vs. Ag/AgCl (anodic bias).

Figure 12 shows the photocurrent density versus the applied potential for all the films. The photocurrent for the CuSCN films slightly increases for those potentials over 0.4 V and then remains constant up to 0.8 V. For α-Fe_2O_3, the photocurrent continuously increases for those potentials above 0.55 V. For the α-Fe_2O_3/CuSCN heterojunction (Fig. 12), the current density in the dark is negligible within the whole potential range, but with illumination the photocurrent starts increasing continuously with the applied potential from 0.2 V; it is always higher than that observed for Fe_2O_3 and CuSCN independently. Both α-Fe_2O_3 and the α-Fe_2O_3/CuSCN heterojunctions behave like photoanodes with illumination. The photocurrent density exhibited by the α-Fe_2O_3/CuSCN heterojunction may be due to improved visible light absorption and to the efficient separation of the photogenerated charge carriers (Fig. 11a).

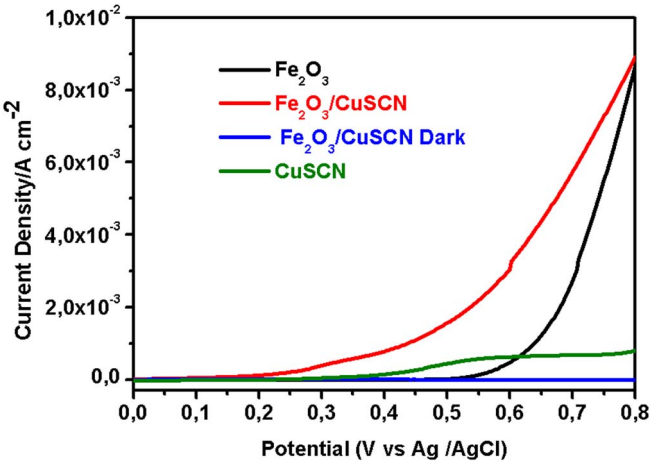

Figure 12. I-V characteristics of the α-Fe_2O_3 and CuSCN electrode in the dark and with illumination (0 V–0.8 V).

A mechanism proposed for the enhanced photocurrent density heterojunction α-Fe_2O_3/ CuSCN sample is described as follows: both α-Fe_2O_3 and CuSCN could be excited with visible light irradiation. In this case an electron transfer occurs from the CuSCN conduction band to that of the α-Fe_2O_3 which, in turn, may lead to hydrogen production at the counter-electrode. This transfer process is thermodynamically favorable since the valence and conduction bands in CuSCN become more negative than those of the α-Fe_2O_3 band levels which, in turn, enhances the separation of the photogenerated charge carriers. After an initial decay in the photocurrent in the first illumination cycle, the photocurrent tends to remain constant with long-term illumination, which means an effective charge separation inside the α-Fe_2O_3/CuSCN heterojunction. A similar type of band positioning and charge carrier movement has also been previously reported earlier for TiO_2/Si,[42] CuO/ZnO,[43] $CuFe_2O_4/TiO_2$,[44] $Bi_2O_3/BiVO_4$,[45] and MoS_2/CdS.[46]

Photocurrent measurements were taken under pulsed light by a chronoamperometry technique (Fig. 13a). In the steady state, the α-Fe_2O_3/FTO electrode gave a photocurrent density of about 5 μA/cm^2. However, the α-Fe_2O_3/CuSCN/FTO heterojunction showed a photocurrent density of about 15 μA/cm^2, which is 3 times bigger than that of the α-Fe_2O_3/FTO electrode. Figure 13b shows the variation of the photocurrent density versus the time elapsed during the switch on/off of light for both the α-Fe_2O_3/FTO and α-Fe_2O_3/CuSCN/FTO electrodes. Photocurrent density dropped in the first two cycles, and then became steady and quasi-reproducible after several on–off cycles of light with no overshoot at either the beginning or the end of the on–off cycle. This result indicates that the direction of the electron diffusion was free from grain boundaries, which could create traps that hinder electron movement and slow down photocurrent generation.[47]

It is believed that the deposition of CuSCN on α-Fe_2O_3 enhanced the photoactivity of the photoanode in two aspects: (i) the p–n junction could effectively extract holes and separate charge carriers to lead to an enhanced photocurrent; (ii) the loading of the heterojunction photoanode with CuSCN further facilitated the electron transfer at the electrode/electrolyte interface, and thus enhanced photoelectrochemical water oxidation.

To validate the energy band diagram suggested in Figure 11, we took further measurements of the photocurrent generated by the heterostructure with illumination and a wavelength that excited only the hematite (λ > 400 nm). Figure 13c shows the photocurrent generated by the α-Fe_2O_3/CuSCN heterostructure with white light illumination and light illumination with λ > 400 nm. Both α-Fe_2O_3 and CuSCN were exited with white light, and the charge transfer is that shown in Figure 11b; the holes generated in the hematite were transferred to the valence band of CuSCN and the photogenerated electrons in CuSCN were transferred to α-Fe_2O_3. When illuminating at wavelengths above 400 nm (λ > 400 nm) only the hematite part was excited and the measured photocurrent was due to the charge transfer from α-Fe_2O_3 to CuSCN. As expected the photocurrent was lower in this case because the charge transfer from CuSCN to α-Fe_2O_3 was not activated.

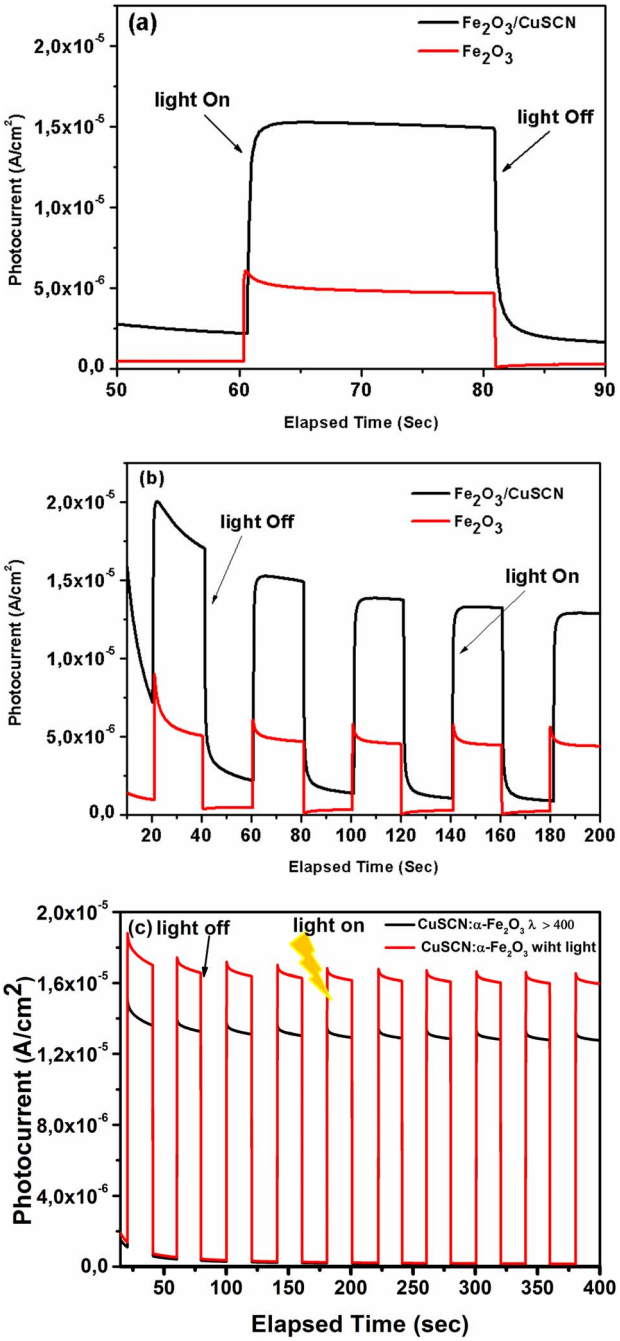

Figure 13. (a) Photocurrent intensity of the α-Fe_2O_3 and α-Fe_2O_3/CuSCN electrodes with on/off illumination, measured in 1 M NaOH electrolyte at a bias potential of +0.1 V. (b) Time dependence of the photocurrent intensities for the α-Fe_2O_3 and α-Fe_2O_3/CuSCN electrodes subjected to successive illumination cycles; (c) Time dependence of the photocurrent intensities for the α-Fe_2O_3/CuSCN electrode with on/off illumination cycles (white light and λ > 400 nm).

Mott–Schottky analysis.—The Mott–Schottky plot ($1/C^2$ vs. the applied potential) was obtained and analyzed for all the samples. The flatband potential is an important physical property as regards the material's performance during photoelectrochemical water splitting. Both N_D and E_{FB} were estimated from the Mott-Schottky equations

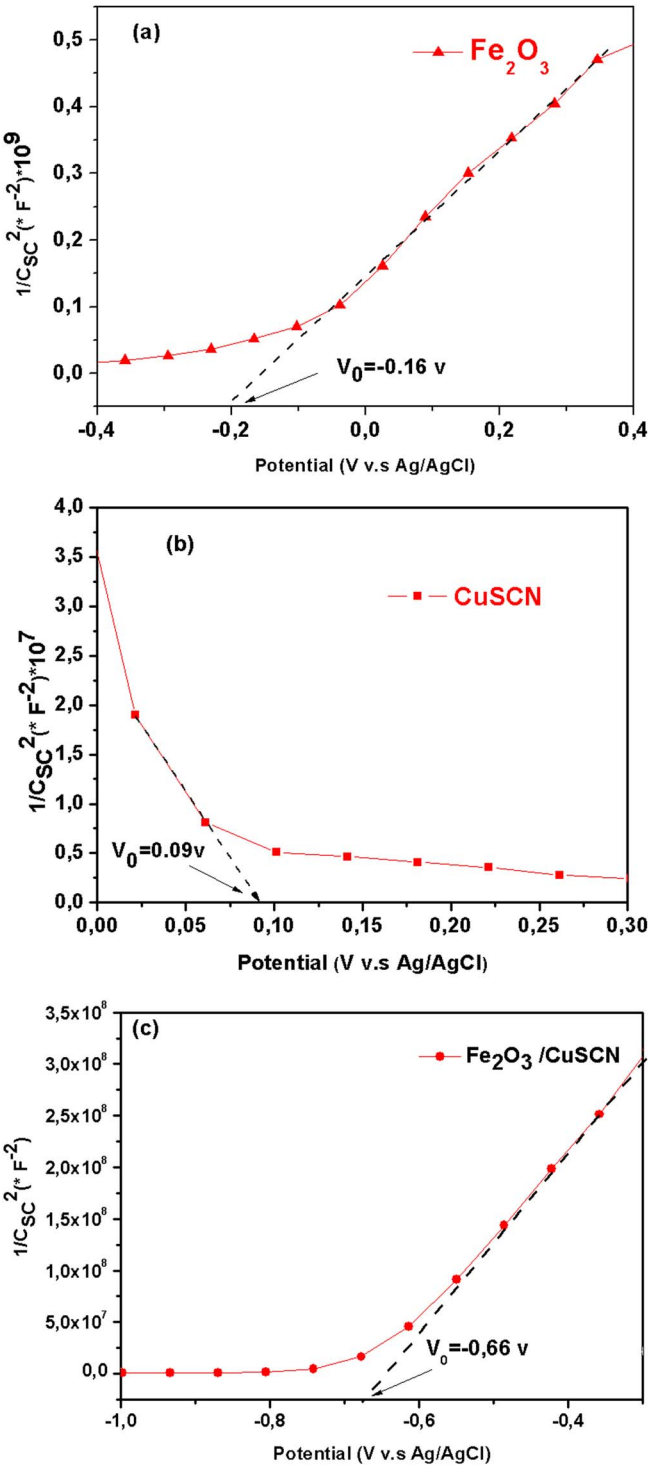

Figure 14. A Mott–Schottky plot for (a) α-Fe_2O_3 (b) CuSCN and (c) α-Fe_2O_3 /CuSCN.

(Eqs. 8 and 9):[48]

$$\frac{1}{C_{SC}{}^2} = \frac{2}{e\,\varepsilon\,\varepsilon_0 N_D A_S{}^2}\left(E - E_{fb} - \frac{KT}{e}\right)$$

for an n − type semiconductor [8]

$$\frac{1}{C_{SC}{}^2} = -\frac{2}{e\,\varepsilon\,\varepsilon_0 N_D A_S{}^2}\left(E - E_{fb} + \frac{KT}{e}\right)$$

for a p − type semiconductor [9]

where, e is the electron charge, ε is the dielectric constant of the semiconductor, ε_o is vacuum permittivity, A_S is the surface area of the working electrode, k is Boltzmann's constant, and T is temperature. The positive slopes confirmed that α-Fe_2O_3 was a n-type semi-conducting material, and the negative slopes indicated that CuSCN was a p-type semi-conducting material. The calculated donor density increased from $1.6 \cdot 10^{21}$ cm^{-3} for the α-Fe_2O_3 photoanode to $2.8 \cdot 10^{21}$ cm^{-3} for α-Fe_2O_3/CuSCN. By taking the x-axis intercept of the linear fit to the Mott-Schottky plots, the flatband potential was estimated to be −0.14 V vs. Ag/AgCl for the α-Fe_2O_3 photoanode, and to be −0.64 V vs. Ag/AgCl for the α-Fe_2O_3/CuSCN heterojunction (Figs. 14a and 14c).

Conclusions

Semiconducting materials, such as n-Fe_2O_3 and p-CuSCN, were successfully electrodeposited on FTO substrates. Chelating agents and a weak basic electrolyte solution of NH_3 were used to avoid the acidic etching of α-Fe_2O_3. This enabled us to study the energetic behavior of both semiconductors and the n-Fe_2O_3/p-CuSCN heterojunction performances for the photoelectrochemical applications. FESEM showed that CuSCN was able to easily grow thicker and cover the α-Fe_2O_3 substrate. The EDX analyses revealed that the CuSCN films had slightly excess copper. The photoelectrochemical performance of the nanostructured α-Fe_2O_3/CuSCN heterojunction was better than that of FTO/α-Fe_2O_3 and FTO/CuSCN. A maximum photocurrent density of 2.9 mA/cm^2 at 0.59 V versus Ag/AgCl was exhibited for the α-Fe_2O_3/CuSCN photoelectrode. The improved photocurrent density was attributed to two major combined factors: (i) generation of an electric field in the heterojunction, which suppressed the recombination of the photogenerated charge carriers; (ii) application of an adequate external bias that favored the transfer and separation of the photogenerated charge carriers in the α-Fe_2O_3/CuSCN heterojunction. Enhanced photocurrent density was also attributed to the appropriate band edge alignment of the semiconductors, which enhanced light absorption in both semiconductors.

Acknowledgments

This work was supported by the Ministry of High Education and Scientific Research (Tunisia), Ministerio de Economía y Competitividad (ENE2016-77798-C4-2-R) and Generalitat Valenciana (Prometeus 2014/044).

ORCID

B. Marí https://orcid.org/0000-0003-0001-419X

References

1. R. Brimblecombe, G. Charles Dismukes, Gerhard F. Swiegers, and Leone Spiccia, "Molecular water-oxidation catalysts for photoelectrochemical cells, Journal Homepage," *Dalton Transactions*, **43**, 9374 (2009).
2. M. S. Prévot and K. Sivula, "Photoelectrochemical Tandem Cells for Solar Water Splitting," *J. Phys. Chem. C*, **117**, 17879 (2013).
3. A. Valdés, J. Brillet, M. Grätzel et al., "Solar hydrogen production with semiconductor metal oxides: new directions in experiment and theory," *Phys. Chem. C hem. Phys*, **14**, 49 (2012).
4. A. B. Murphy, P. R. F. Barnes, L. K. Randeniya, I. C. Plumb, Grey, M. D. Horne, and J. A Glasscock, "Efficiency of solar water splitting using semiconductor electrodes," *International Journal of Hydrogen Energy*, **31**(14), 1999 (2006).
5. Z. B. Chen, T. F. Jaramillo, T. G. Deutsch, A. Kleiman-Shwarsctein, A. J. Forman, N. Gaillard, R. Garland, K. Takanabe, C. Heske, M. Sunkara, E. W. McFarland, K. Domen, E. L. Miller, J. A. Turner, and H. N. Dinh, *J. Mater. Res*, **25**, 3 (2010).
6. K. Sivula, F. L. Formal, and M. Grätzel, "Solar water splitting: progress using hematite (α-Fe_2O_3)photoelectrodes," *Chem Sus Chem*, **4**, 432 (2011).
7. T. W. Hamann, "Splitting water with rust: hematite photoelectrochemistry," *Dalton Trans.*, **41**, 7830 (2012).
8. J. H. Kennedy and K. W. Frese, "Photooxidation of water at α-Fe_2O_3 electrodes," *Journal of the Electrochemical Society*, **125**(5) 709 (1978).
9. A. W. Damon, W. Gongming, L. Yichuan, L. Yat, and Z. Z. Jin, "Nanostructured hematite: synthesis, characterization, charge carrier dynamics, and photoelectrochemical properties," *Energy Environ. Sci.*, **5**, 6682 (2012).

10. K. Sivula, F. L. Formal, and M. Gra¨tzel, *Chem. Mater.*, **21**, 2862 (2009).
11. Y.-K. Hsu, Y.-C. Chen, and Y.-G. Lin, *ACS Appl. Mater. Interfaces*, **7**, 14157 (2015).
12. M. T. Mayer, C. Du, and D. Wang, *J. Am. Chem. Soc.*, **134**, 12406 (2012).
13. J. Li, F. Meng, S. Suri, W. Ding, F. Huang, and N. Wu, *Chem. Commun.*, **48**, 8213 (2012).
14. D. Sharma, S. Upadhyay, A. Verma, V. R. Satsangi, R. Shrivastav, and S. Dass, *Thin Solid Films*, **574**, 125 (2015).
15. X. Wang, K.-Q. Peng, Y. Hu, F.-Q. Zhang, B. Hu, L. Li, M. Wang, X.-M. Meng, and S.-T. Lee, *Nano Lett.*, **14**, 18 (2014).
16. Y. Hou, F. Zuo, A. Dagg, and P. Feng, *Nano Lett.*, **12**, 6464 (2012).
17. B. O'Regan and D. T. Schwartz, "Efficient Photo-Hole Injection from Adsorbed Cyanine Dyes into Electrodeposited Copper(I) Thiocyanate," *Thin Films Chem Mater*, **7**, 1349 (1995).
18. L. B. Wang, B. L. Kang, P. Wang, and Y. Qiu, "Review of recent progress in solid-state dye-sensitized solar cells," *Sol Energ Mater SolCell*, **90**, 549 (2006).
19. W. Luo, T. Yu, Y. Wang, Z. Li, J. Ye, and Z. Zou, *J. Phys. D: Appl. Phys.*, **40**, 1091 (2007).
20. F. Boudoire, R. Toth, J. Heier, A. Brauna, and E. C. Constable, *Energy Environ. Sci.*, **7**, 2680 (2014).
21. Y.-K. Hsu, Y.-C. Chen, and Y.-G. Lin, *ACS Appl. Mater. Interfaces*, **7**, 14157 (2015).
22. Y. Hou, F. Zuo, A. Dagg, and P. Feng, *Nano Lett.*, **12**, 6464 (2012).
23. Y. Guo, Y. Fu, Y. Liu, and S. Shen, *RSC Adv.*, **4**, 36967 (2014).
24. C. Miao, S. Ji, G. Xu, G. Liu, L. Zhang, and C. Ye, *ACS Appl. Mater. Interfaces*, **4**, 4428 (2013).
25. Y. Hou, F. Zuo, A. Dagg, and P. Feng, *Angew. Chem., Int. Ed.*, **52**, 1248 (2013).
26. M. G. Ahmed, T. A. Kandiel, A. Y. Ahmed, I. Kretschmer, F. Rashwan, and D. Bahnemann, *J. Phys. Chem. C*, **119**, 5864 (2015).
27. D. Sharma, S. Upadhyay, A. Verma, V. R. Satsangi, R. Shrivastav, and S. Dass, *Thin Solid Films*, **574**, 125 (2015).
28. L. P. Wen, Y. J. Guo, S. H. I. Zhi-qiang, H. Hua, L. Lang, Z. Yong-Nan, L. Guo-Dong, and Z. Yong-cun, "Preparation and Supercapacitive Properties of Fe_2O_3/Active Carbon Nanocomposite,s," *chem. res. chinese universities*, **28**(5), 780 (2012).
29. W. Mao-Sung and L. Rung-Hau, "Electrochemical Growth of Iron Oxide Thin Films with Nanorods and Nanosheets for Capacitors," *J. Electrochem. Soc.*, **156**, A737 (2009).
30. N. Yong, J. Zhengguo, and Y. F. wand, *J. Am. Ceram. Soc.*, **90**(9), 2966 (2007).
31. B. Debasis, C. K. Suresh, M. C. Matthew, and SudiptaSeala, "In situ synthesis of carbon nanotubes decorated with palladium nanoparticles using arc-discharge in solution method," *J. Phys. Chem. B*, **108**, 556 (2004).
32. K. Tennakone, A. H. Jayatissa SAN Fernando, S. Wickramanayake, S. Punchihewa, L. K. Weerasena, and W. D. R. Premasiri, "Semiconducting and Photoelectrochemical Properties of n- and p-Type β-CuCNS," *Phys Stat Sol (a)*, **103**, 491 (1987).
33. Ni Yong and Zhengguo Jin et Yanan Fu, "Electrodeposition of p-type CuSCN thin films by a new aqueous electrolyte with triethanolamine chelation," *Journal of the American Ceramic Society*, **90**(9), 2966 (2007).
34. Q. Zang, H. Guo, Z. Feng, L. Lin, J. Zhou, and Z. Lin, *ElectrochimActa*, **55**, 4889 (2010).
35. D. L. Smith and V. J. Saunders, *Acta Crystallogr B*, **37**, 1807 (1981).
36. J. E. Jaffe, T. C. Kaspar, T. C. Droubay, T. Varga, M. E. Bowden, and G. J. Exarhos, *J Phys Chem C*, **114**, 9111 (2010).
37. P. Pattanasattayavong, N. Yaacobi-Gross, K. Zhao, and G. O. N. Ndjawa, Li J, F. Yan, B. C. O'Regan, A. Amassian, and T. D. Anthopoulos, "Hole-transporting transistors and circuits based on the transparent inorganic semiconductor copper(I) thiocyanate (CuSCN) processed from solution at room temperature," *Adv. Mater.*, **25**, 1504 (2013).
38. A. A. AKl, *Applied science*, **233**, 307 (2004).
39. L. Dghoughi, B. Elidrissi, C. Bernède, M. Addou, M. Alaouilamrani, M. Regragui, and H. Erguig, *Applied surface sciences*, **253**, 1823 (2006).
40. J. E. Jaffe, T. C. Kaspar, T. C. Droubay, T. Varga, M. E. Bowden, and G. J. Exarhos, "Electronic and defect structures of CuSCN," *J. Phys. Chem. C*, **114**,9111 (2010).
41. M. R. Belkhedkar and A. U. Ubale, *International journal of Materials and chemistry*, **4**(5), 109 (2014).
42. D. Sharma, S. Upadhyay, V. R. Satsangi, R. Shrivastav, and S. Dass, "Improved-photoelectrochemical water splitting performance of $Cu_2O/SrTiO_3$ heterojunction photoelectrode," *J. Phys. Chem. C*, **118**, 25320 (2014).
43. K. K. Baek and H. L. Tuller, "Atmosphere sensitive CuO/ZnO junctions," *Solid State Ionics*, **75**, 179 (1995).
44. A. Kezzim, N. Nasrallah, A. Abdi, and M. Trari, "Visible light induced hydrogen on the novel hetero-system $CuFe_2O_4/TiO_2$," *Energy Convers. Manag.*, **52**, 2785 (2011).
45. L. Chen, Q. Zhang, R. Huang, S. F. Yin, S. L. Luo, and C. T. Au, "Porous peanut-like Bi_2O_3-$BiVO_4$ composites with heterojunctions: one-step synthesis and their photocatalytic properties," *Dalton Trans*, **41**, 9513 (2012).
46. L. Ying, X. Y. Yu, and W. D. Zhang, "MoS_2/CdS heterojunction with high photoelectrochemical activity for H_2 evolution under visible light: the role of MoS_2," *J. Phys. Chem. C*, **117**, 12949 (2013).
47. M. Sookhakian, Y. M. Amin, S. Baradaran, M. T. Tajabadi, A. MoradiGolsheikh, and W. J. Basirun, *Thin Solid Films*, **552**, 204 (2014).
48. G. Rahman and O. S. Joo, "Electrodeposited nanostructured a-Fe_2O_3 thin films for solar water splitting: Influence of Pt doping on photoelectrochemical performance," *Materials Chemistry and Physics*, **140**, 316 (2013).

Hydrothermal synthesis of nanostructured Cr-doped hematite with enhanced photoelectrochemical activity

Article *in* Electrochimica Acta · December 2017

DOI: 10.1016/j.electacta.2017.12.049

CITATION
1

READS
59

5 authors, including:

Feriel Bouhjar
Universitat Politècnica de València
12 PUBLICATIONS **4** CITATIONS
SEE PROFILE

Bernabé Marí Soucase
Universitat Politècnica de València
189 PUBLICATIONS **1,789** CITATIONS
SEE PROFILE

Brahim Bessaïs
Centre des Recherches et des Technologies d…
148 PUBLICATIONS **1,454** CITATIONS
SEE PROFILE

Electrochimica Acta 260 (2018) 838–846

Contents lists available at ScienceDirect

Electrochimica Acta

journal homepage: www.elsevier.com/locate/electacta

Hydrothermal synthesis of nanostructured Cr-doped hematite with enhanced photoelectrochemical activity

F. Bouhjar [a, b, c], M. Mollar [a], M.L. Chourou [b], B. Marí [a, *], B. Bessaïs [b]

[a] Institut de Disseny i Fabricació (IDF) - Departament de Física Aplicada, Universitat Politècnica de València, Camí de Vera s/n, 46022 València, Spain
[b] Photovoltaic Laboratory, Research and Technology Centre of Energy, Borj-Cedria Science and Technology Park, BP 95, 2050 Hammam-Lif, Tunisia
[c] University of Tunis, Tunisia

ARTICLE INFO

Article history:
Received 13 August 2017
Received in revised form
2 December 2017
Accepted 7 December 2017
Available online 8 December 2017

Keywords:
Thin films
Hematite
Chromium
XRD analysis
FESEM analysis
TEM analysis
Optical properties
Photoelectrochemical properties

ABSTRACT

Using the easily applicable hydrothermal method Cr-doped hematite thin films have been deposited polycrystalline on conductive glass substrates. The hydrothermal bath consisted of an aqueous solution containing a mixture of $FeCl_3 \cdot 6H_2O$ and $NaNO_3$ at pH = 1.5. The samples were introduced in an autoclave and heated for a fixed time at a fixed temperature and then annealed in air at 550 °C. The concentration of the incorporated Cr atoms (Cr^{4+} ions) was controlled by varying the concentration of the $Cr(ClO_4)_3$ precursor solution, varied from 0% to 20%. All samples followed morphological and structural studies using field-emission scanning electron microscopy, high-resolution transmission electron microscopy and X-ray diffraction. Chronoamperometry measurements showed that Cr-doped hematite films exhibited higher photoelectrochemical activity than the undoped films. The maximum photocurrent density and incident photon conversion efficiencies (IPCE) were obtained for 16 at.% Cr-doped films. This high photoactivity can be attributed to both the large active surface area and increased donor density caused by Cr-doping in the α-Fe_2O_3 films. All samples reached their best IPCE at 400 nm. IPCE values for 16 at.% Cr-doped hematite films were thirty times higher than that of undoped samples. This high photoelectrochemical performance of Cr-doped hematite films is mainly attributed to an improvement in charge carrier properties.

1. Introduction

For the last twenty years, hematite (α-Fe_2O_3) is considered as the most promising material in view of cost, abundance and photocatalytic properties. Hematite has emerged as an efficient photocatalyst used in solar water splitting as well as hydrogen production due to its appropriate optical band gap (2.1–2.2 eV). According to theoretical predictions, solar-to-hydrogen efficiency of hematite can reach 16.8% and water splitting photocurrent can extent 12.6 mA/cm^2 [1–3]. Moreover, hematite exhibits an extraordinary chemical stability in an oxidative environment. However, the applied performance of hematite for solar water splitting is far from the ideal case which has been limited by several factors such as poor conductivity, short lifetime of the excited state carrier (10 ps), poor oxygen evolution reaction (OER) kinetics, short hole diffusion length, and improper band position for an unbiased Photoelectrochemical method [4].

So far, the photoelectrochemical activity (PECA) of hematite has remained quite low because of two main drawbacks. First, the conduction band edge energy of α-Fe_2O_3 system lies below the reversible hydrogen potential, thus hindering the charge-transfer process of photogenerated carriers (electrons and holes) at the hematite/electrolyte. Second, undoped hematite exhibits a rapid non-radiative electron–hole recombination due to its high density of intrinsic defects. As a result, the defects induce a short diffusion length almost 4 nm compared to the light penetration depth. Therefore, hematite has a relatively poor conductivity, severely limiting the overall photocurrent. However, incorporating foreign metallic atoms into the α-Fe_2O_3 structure has been considered an effective approach to inhibit the above-mentioned drawbacks and consequently enhance the PECA of hematite.

A large range of elements, mostly belonging to transition metals such as Sn [5], Cu [6], Pt [7], Si [8–11], Ti [12–14], V [7], Al [7,15], Cd [16], Mo [17], Nb [18], Mg [7], Rh [19], Ce [20], Co [21], Cu [7,22], Zn [7,23], Cr [7,17], Pt [11], and Ta [24] have been used to dope hematite. Table 1 shows a review of the achievements in some

* Corresponding author.
E-mail address: bmari@fis.upv.es (B. Marí).

https://doi.org/10.1016/j.electacta.2017.12.049
0013-4686/

Table 1
Summary of the results obtained for doped hematite photoelectrodes, fabrication methods and photoelectrochemical characteristics.

Dopant	Preparation Method	Potential (V)	Electrolyte	Light Intensity ($mW \cdot cm^{-2}$)	IPCE (%)	Photocurrent Density ($mA \cdot cm^{-2}$)	Ref.
undoped	Electrodeposition	0.4 vs. Ag/AgCl	1 M NaOH	410	3	0.690	[17]
Mo					12	2,00	
Cr					6	1,2	
Undoped	Sputtering	0.5 vs. SCE	1 M NaOH	100	U.A.	Negligible	[53]
Si					3	0.100	
Ti					15	0.620	
Undoped	Spray Pyrolysis	0.45 vs. NHE	0.1 M NaOH	U.A.	U.A.	0.800	[52]
Ti						4.000	
Ti-Al						4.000	
Ta						1.000	
Ti-Pt						0.800	
Ni						Negligible	
Undoped	Electrodeposition	0.4vs. Ag/AgCl	1 M NaOH	410	3	0.690	[38]
Pt					12	1.340	
Undoped	Electrodeposition	0.4 vs. Ag/AgCl	1 M NaOH	410	3	0.690	[39]
Al					8	~1.000	
Undoped	Spray Pyrolysis	0.5 vs. SCE	1 M NaOH	150	U.A.	Negligible	[56]
Ti						1.980	
Undoped	Spray Pyrolysis	0.2 vs. SCE	0.5 M H_2SO_4	U.A.	U.A.	U.A.	[57]
Mg						0.22	
Undoped	Spray Pyrolysis	0 vs. SCE	0.5 M H_2SO_4	40	U.A.	U.A.	[58]
Zn					20	U.A.	
Undoped	Hydrothermal	0.1vs. Ag/AgCl	1 M NaOH	100	Negligible	1.77	our work
Cr					6	2.68	

U.A. = Unavailable.

typically doped **α-**Fe_2O_3 that can be found in the literature. Data in Table 1 includes the kind of the doping agents and the performance of the hematite water splitting photoelectrodes. These data are compared with the Cr-doped hematite obtained from the hydrothermal method described in this work. To dope **α-**Fe_2O_3, diverse methods have been attempted, using a range of synthesizing methods including sol–gel [25–27], hydrothermal [28,29], magnetron sputtering [30,31], atomic layer deposition [32], spray pyrolysis [8,33–35], atmospheric pressure chemical vapor deposition (APCVD) [11,36,37], and electrodeposition [38–41]. These dopants influence the conductivity of the hematite as well as band gap width, the Fermi level, and charge-transfer- processes. However, based on the literature, some researchers reported contradictory effects of doping on photoelectrochemical performances. This apparent discrepancy in the results has mainly been attributed to the doping concentration and processing methods. Undoped and doped hematites have been grown by various methods that can roughly be categorized in two groups. The first group involves physical deposition using gas as precursors and necessitates expensive and sophisticated devices as is the case in atomic layer deposition, chemical vapor deposition and magnetron sputtering. The second group includes wet chemical synthesizing methods requiring solution precursors and relatively low cost, simple utensils or set ups as in the case of electrochemical deposition, spray pyrolysis, sol–gel coating and hydrothermal growth. Compared to the methods, the hydrothermal method has several advantages. First, it is a reproducible, facile and inexpensive method since it consists of sealed “one pot” reactions requiring an operating temperature as low as 100 °C. Second, it allows crystalline growth of versatile nanostructured doped hematite with precise control of the microstructure morphologies. Recently, McFarland and co-workers [38] were able to fabricate Pt, Mo and Cr doped and undoped hematite films as PEC electrodes for water splitting. They found that the photoactivity of the iron oxide was improved by co-deposition with Mo or Cr. The best performing samples were 5% Cr and 15% Mo doped, which had IPCEs at 400 nm of 6% and 12%, respectively, with an applied potential of 0.4 V vs Ag/AgCl. These IPCE values were 2.2 and 4 times higher than the undoped sample for the 5% Cr and 15% Mo samples, respectively. No evidence was found that the improved performance was due to the electrocatalytic effects of the dopant at the surface of the hematite thin film. The major effect of the Mo and Cr dopants is to improve the charge transport properties of the hematite so that a greater fraction of the photon generated electron/hole pairs is available for surface redox chemistry.

Furthermore, under factual operating conditions, high overpotentials are desirable not only because of non-idealities but also due to the complexity of water splitting reactions. Current progress in nanostructured hematite synthesis including nanoparticles [42,43], nanowires [44] and nanonets [45] opens opportunities in tackling the drawbacks mentioned above. As a matter of fact, nanostructured photoanode offers an increased semiconductor/electrolyte interfacial area for water oxidation, as well as a substantial reduction of the diffusion length for minority carriers [46–48].

In this way, hole recombination can be decreased if the surface feature dimensions are tuned to be close to the hole diffusion length of **α-**Fe_2O_3 (2–4 nm [49] or 20 nm [50]). Nanostructures increase light absorption by increasing light scattering and trapping. As a result, nanostructured hematite photoelectrodes greatly facilitate the collection of charge carriers better than if they were simply bulky and smooth [51]. An additional doping of hematite photoanodes has been extensively studied to perform a further enhancement of the photoactivity of these photoanodes [51–53]. Numerous studies have shown that PEC water splitting is advantageous combining nanostructure and doping effects [54,55].

Therefore, a more straightforward and up scaling fabrication method of nanostructured doped hematite electrodes is needed to compare the doping effects in terms of PECA before addressing their stability under real operating conditions.

To date, no significant data have been published on optical, structural and electrical properties as well as PECA of chrome doped **α-**Fe_2O_3 films when synthesized by the hydrothermal method. In this study, we prepared Cr-doped **α-**Fe_2O_3 thin films by a hydrothermal process. The photoelectrochemical response shows that the samples are effective for the photo splitting of water and

the doping level affects the photocatalytic of the thin films. The optimum sample is **α-**Fe_2O_3 doped with 16 at.% Cr. It is believed that this result could be beneficial for the applications of Cr-doped **α-**Fe_2O_3 in the fields of photocatalysis and photoelectrical devices.

2. Experimental

2.1. Material and methods

The flowchart illustrating the synthesis of nanostructured **α-**Fe_2O_3thin films by the hydrothermal method is displayed in Fig. 1. Initially, a fluorine-doped tin oxide (FTO) coated glass plate purchased from Pilkington glass company (USA), was cut into small rectangular pieces having a surface of 3 × 1 cm^2 to serve as a starting substrate. These pieces were ultrasonically pre-cleaned by sequential rinses with acetone, distilled water, and ethanol. The hydrothermal bath was an aqueous solution containing a solution 0.15 M $FeCl_3$, 1 M $NaNO_3$ and 1 M $Cr(ClO_4)_3$ [59–61]. Some drops of hydrochloric acid (HCl) were added to adjust the pH of the mixture to 1.5. $Cr(ClO_4)_3$ solutions were added to the bath intended for Cr-doped films. The additional amount of Cr was calculated so that the molar ratio Cr/(Cr + Fe) remained in the range of 0–20 at. %. All chemicals were purchased from Sigma Aldrich and used as received without any additional purification. Double deionized water, exhibiting a resistivity close to 15 MΩ cm was generated by a Milli-Q academic ultra-pure water purification system (Millipore, Bedford, MA, USA). Once the solution was prepared, some FTO glass substrates were placed at the bottom of a Teflon recipient. Only 20 ml were transferred to the recipient so that the substrates were partially immersed in the solution. Then, the recipient was inserted in a stainless-steel autoclave. The filled autoclave was tightly sealed before being heated at 100 °C for 6 h in an oven. Finally, the system (autoclave with the samples) was naturally cooled down to room temperature.

Under hydrothermal conditions, the aqueous solution enables the Fe^{3+} hydrolysis ions with OH^-, producing iron oxide nuclei, as described by the following reaction (1):

$$Fe^{3+}_{(aq)} + 3OH^-_{(aq)} \rightarrow \beta\text{-}FeOOH_{(s)} + H_2O \quad (1)$$

Finally, a uniform yellowish layer of akageneite β-FeOOH covered the FTO/glass substrates uniformly. The akageneite-coated substrates were then washed with deionized water and subsequently introduced in a muffle furnace to be sintered in air at 550 °C for 4 h. At the end of this calcination step, the β-FeOOH was converted into α-Fe_2O_3. Correspondingly, as illustrated in Fig. 1, the color of the substrate turned from yellow to red-brown indicating a phase transition from β-FeOOH to **α-**Fe_2O_3 [57]. The chemical reaction expected to occur during this phase transition is represented by the reaction displayed below (2):

$$2\beta\text{-}FeOOH(s) \rightarrow Fe_2O_3(s) + H_2O\ (L \text{ or } G) \quad (2)$$

2.2. Characterization setup

Microstructural properties of various hematite films were obtained at room temperature using a Rigaku Ultima IV X-ray diffractometer (XRD) in the Bragg-Bentano configuration using CuK_α radiation (λ = 1.54060 Å). Chemical composition, surface morphology, and topography were characterized using energy dispersive spectroscopy (EDX) coupled to a field emission scanning electron microscope (FESEM) Zeiss ULTRA 55, equipped with an In-Lens SE detector. The selected electron diffraction and high-resolution transmission electron microscopy (HRTEM) images were obtained by a JEOL-2010 TEM set at an acceleration voltage of 200 kV. Optical absorption was recorded with a UV–visible spectrophotometer HR4000 provided by Ocean Optics. The spectrophotometer was coupled to an integrating sphere to collect both specular and diffuse transmittance.

The photoelectrochemical measurements of the samples were performed in a quartz cell to facilitate light reaching the photoelectrode surfaces. The surface area of the working electrode was 0.2 cm^2. The electrolyte consisted of 1 M solution of NaOH (pH = 13.6) with a pure nitrogen stream bubbling before and during the test to remove the dissolved oxygen. The chronoamperometric curves of the hematite thin films were also obtained at + 0.1 V (vs. Ag/AgCl) both in dark and under illumination performed by a 300 W Xenon lamp (PLSSXE300/300UV). The luminous intensity of the Xenon lamp was fixed at 100 $mWcm^{-2}$. The set-up was completed with an automatic shutter and a filter box. The whole system was controlled by homemade software.

For wavelength-dependent photocurrent measurements a monochromator giving a ~20 nm bandpass from 360 to 680 nm was used together with cut off filters to eliminate secondary -harmonics. To be able to detect low photocurrent intensity, the set-up was completed with a photo-chopper and a lock-in amplifier (signal recovery). The absolute intensity of the incident excitation light was measured with a radiometer/photometer (international light). The incident photon to electron conversion efficiency (IPCE)

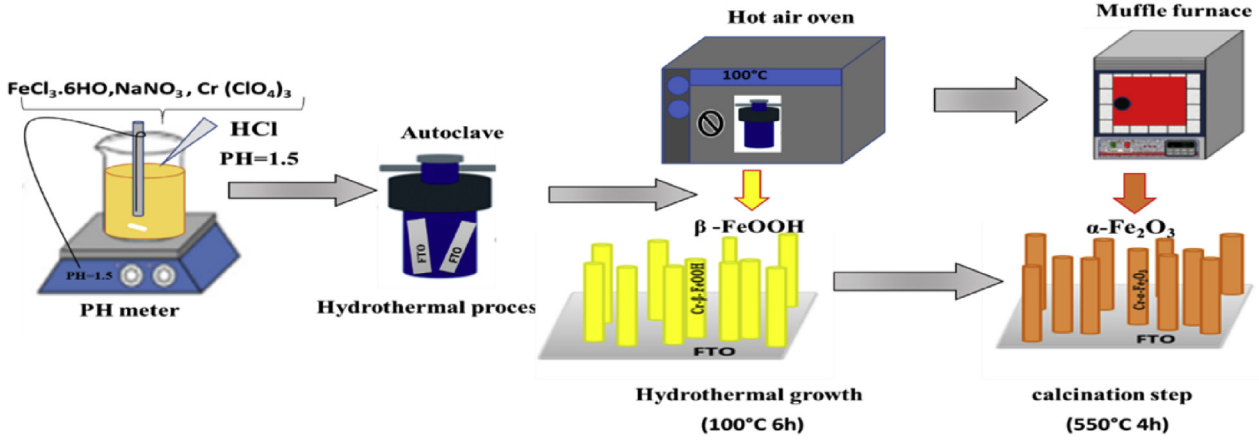

Fig. 1. Schematic illustration of Cr-doped hematite photoanodes synthesized by the hydrothermal method.

of the samples was calculated as follows:

$$\mathrm{IPCE}(\%) = \frac{1240 \cdot i_{photocurrent}\ (\mu A/cm^2)}{\lambda(\mathrm{nm}) \cdot j_{photons}(\mu W/cm^2)} * 100\% \quad (3)$$

Were $i_{photocurrent}$ is the photocurrent densities, λ(nm) is wavelength of the incident light and $j_{photons}$ is the measured irradiance.

3. Results and discussion

3.1. Morphological characterization

3.1.1. FESEM analysis

The morphology of undoped and Cr-doped **α-**Fe_2O_3 samples obtained under hydrothermal conditions was monitored by FESEM images (Fig. 2). Fig. 2 shows a typical morphology of hematite nanorod (NR) arrays grown on the FTO substrates by the hydrothermal process. Top view images show clearly that hematite NRs are uniformly distributed on the substrate and oriented upward with respect to the substrate. While others are detached from the substrate, being free standing and horizontal. Each hematite NR looks like a grain of rice as can be seen in Fig. 2 (a, b, c, d, and e (200 nm)) of the as-prepared sample, enabling the identification of a typical nanoparticle formation. On the other hand, top-view analysis of Cr-doped **α-**Fe_2O_3 electrodes synthesized during hydrothermal treatment 550 °C for 4 h showed that this substrate is formed by rods. The effect of different Cr-doped **α-**Fe_2O_3 did not affect the morphology of the iron oxide nanoparticles.

3.1.2. HRTEM analysis

The morphology of α-Fe_2O_3 nanostructure films was characterized by TEM and HRTEM. Fig. 3 (a, b) shows a low magnification TEM image of the α-Fe_2O_3 nanostructures analyzed shows that the as-synthesized NRs exhibit a smooth surface and a relatively uniform diameter along the axial direction, using the high-resolution transmission electron microscopy (HRTEM) technique Fig. 3 (c, d, e, f) shows a clear interplanar distance of 2.24 nm, matching the $d_{\mathbf{110}}$ spacing of pure hexagonal hematite. The NRs tend to have a parallel alignment, owing to weak Van der Waals attraction. The inset displays the electron diffraction (ED) pattern, which was taken of the entire area. The diffraction ring indicates the polycrystalline nature of α-Fe_2O_3 and is highly consistent with the XRD results (Fig. 4). Furthermore, the elemental mapping images (Fig. 3B) of the Fe (K_α), O (K_α), Cr(K_α) nanorod reveal that the Cr dopants are distributed over all the nanostructures without any segregation on the surface or inside the crystals.

3.2. Structural characterization

Fig. 4 shows the XRD patterns of doped and undoped hematite films. The diffraction peaks match the JCPDS Card No. 33–0664. Diffraction peaks located at 2θ = 24.2°, 33.1°, 35.6°, 40.9°, 49.5°, 54.1° and 64°correspond to (012), (104), (110), (113), (024), (116) and (300) diffraction planes, respectively. No peak corresponding to mixed oxides or impurities was detected in any of the samples. Hematite (**α-**Fe_2O_3) belongs to the space group R-3c (167) with the lattice parameters a = 5.036 Å, b = 5.036 Å, and c = 13.74 Å. This result proves that after being heated in air at 550 °C for 4 h, the precursor was completely converted from FeOOH to a pure α-Fe_2O_3 rhombohedral phase. Hence, undoped and Cr-doped hematite films have the same crystal structure as **α-**Fe_2O_3.

The crystallite size of the samples was calculated using the Debye–Scherer formula:

$$D = \frac{(K\lambda)}{(\beta cos\theta)} \quad (4)$$

where λ = 1.5405 Å is the wavelength of Cu K_α radiation, β, the full width at half maximum (FWHM) of the main diffraction peak in radian, θ, the Bragg angle and k, the Scherrer's constant equal to 0.90.

Table 2 displays the calculated crystallite sizes for hematite

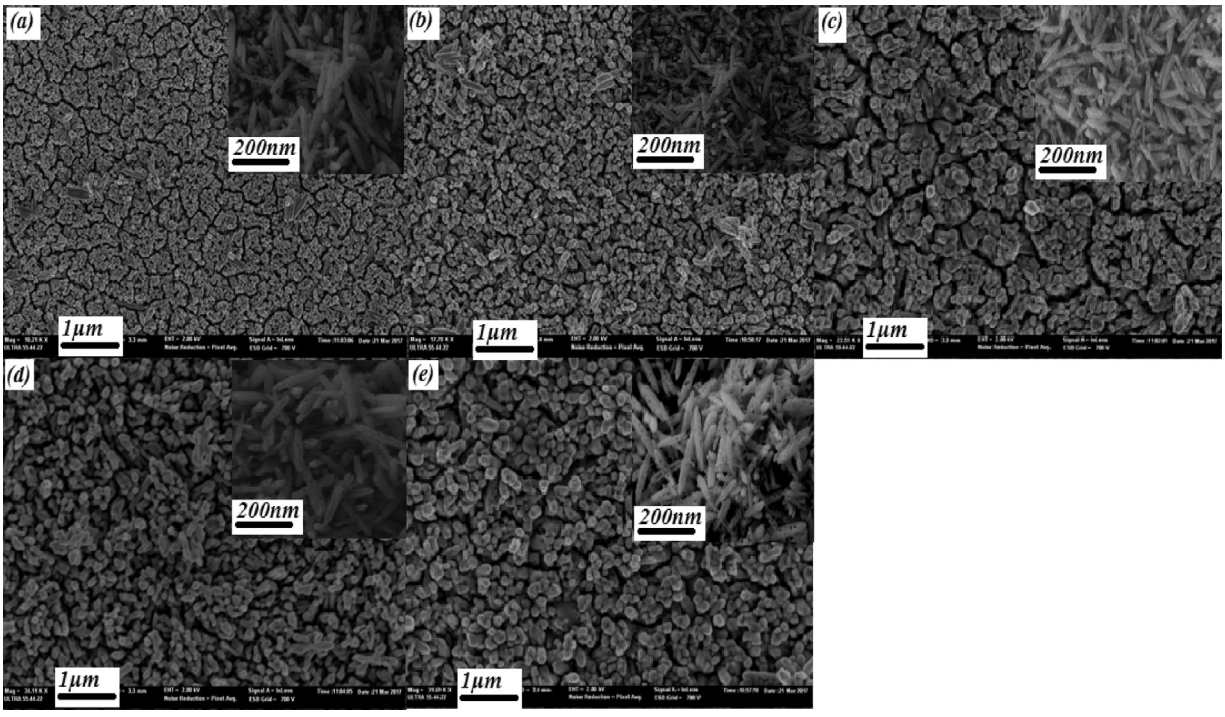

Fig. 2. FESEM of hydrothermal deposited α-Fe_2O_3 (a) undoped, (b) 4 at.% Cr, (c) 8 at.% Cr, (d) 16 at.% Cr, and (e) 20 at.% Cr (1 μm and 200 nm).

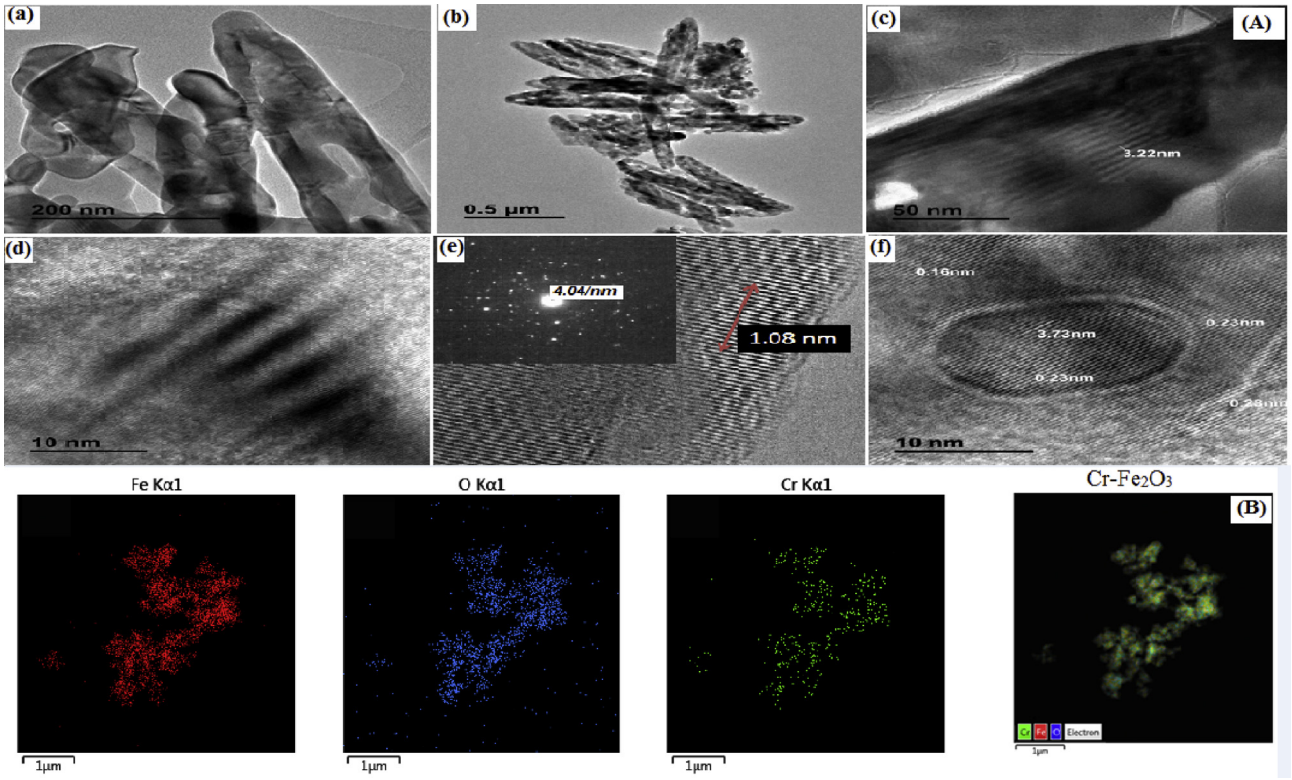

Fig. 3. (A) HRTEM of hydrothermally deposited undopedα-Fe_2O_3, (B) Element Mapping images of the Cr-Fe_2O_3 photoanode.

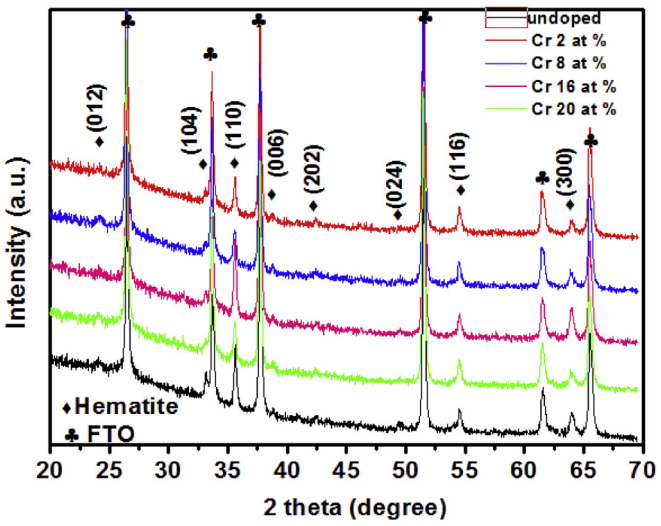

Fig. 4. XRD patterns of α-Fe_2O_3 and Cr-doped α-Fe_2O_3 films at different Cr concentrations.

samples doped at different Cr concentrations for the most intense peaks that correspond to (012) and (110) diffraction planes. The average crystallite size was found to decrease from 44 nm to 11.7 nm for (012) and 40.6 nm–4.8 nm for (110) as Cr doping varied from 0% to 20%, leading to a gradual decline of the intensity of the (012) and (110) XRD lines (See Fig. 4). The shift to higher angles observed for XRD peaks as Cr content increases (Table 2) confirms the replacement of Fe^{2+} ions (ion radius = 0.74 Å) by the smaller Cr^{3+} ions (ion radius = 0.69 Å). This replacement results in a contraction of the **α-**Fe_2O_3 lattice. It is also worth noting that EDX and optical analysis confirmed Cr-doping.

3.3. EDX analysis

Elemental analysis of the **α-**Fe_2O_3 thin films was done by Energy Dispersive X-ray analysis (EDX) spectra (Fig. 5). The L line of the Fe element peaks at 0.6398 keV, while the K-line of oxygen peaks at 0.525 keV. The atomic percentages of Fe, Cr, and O in undoped and Cr-doped **α-**Fe_2O_3 are shown in Fig. 5. The excess of oxygen (detected by EDX) could have arisen from SnO_2, as all Cr-doped films keep the hematite structure, it can be assumed that the films do not deviate excessively from the stoichiometric composition. The calculated atomic ratio of Fe and O is approximately equal

Table 2
Variation of the crystallite size of undoped and Cr-doped α-Fe_2O_3 vs Cr content.

Sample ID	2 θ(°) Peak (012)	Crystallite Size [nm]	2 θ(°) Peak (110)	Crystallite Size [nm]
Fe_2O_3	24.13	44.0	33.14	40.6
Fe_2O_3: Cr 4%	24.21	31.6	33.24	31.5
Fe_2O_3: Cr 8%	24.28	23.2	33.26	23.1
Fe_2O_3: Cr 16%	24.30	17.7	33.28	18.6
Fe_2O_3: Cr 20%	24.32	11.7	33.33	4.8

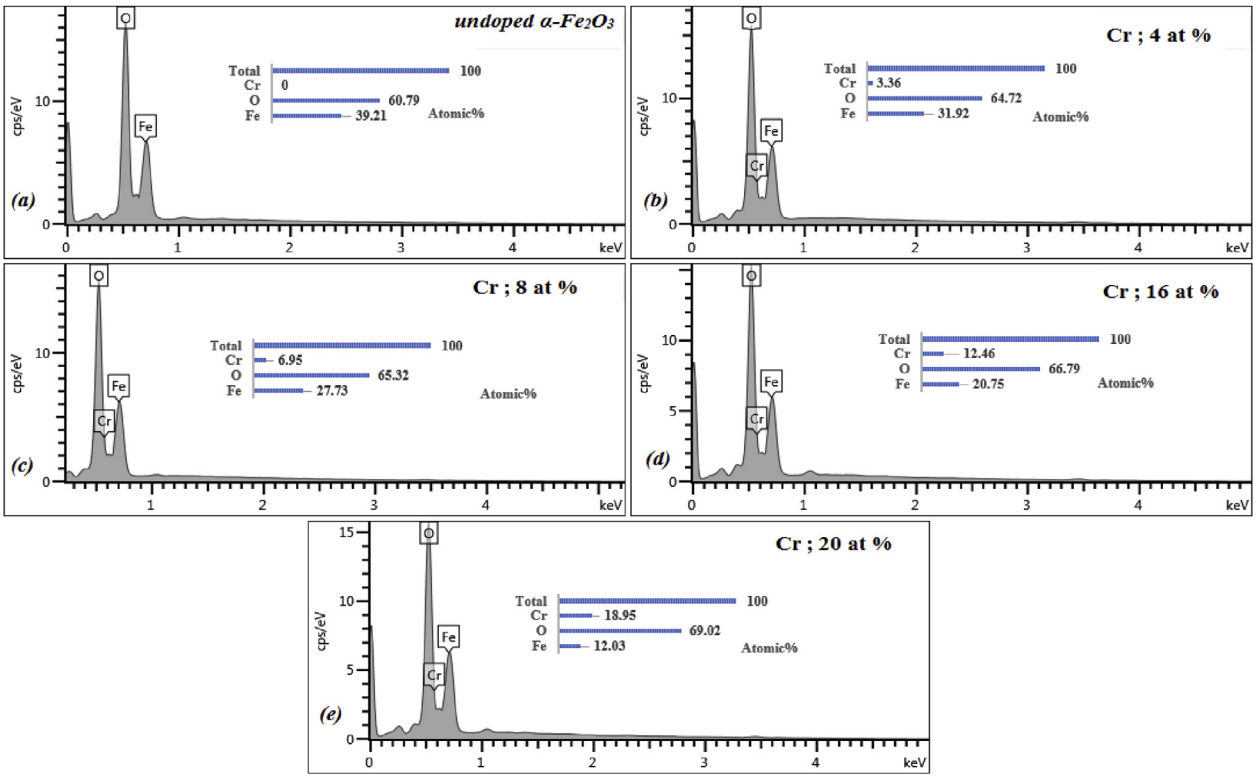

Fig. 5. EDX spectrum of (a) undoped α-Fe_2O_3, (b) 4 at.% Cr-doped α-Fe_2O_3, (c) 8 at.% Cr-doped α-Fe_2O_3 (d) 16 at.% Cr-doped α-Fe_2O_3 and (e) 20 at.% Cr-doped α-Fe_2O_3.

to 2:3, which agrees with the stoichiometric composition of α-Fe_2O_3, indicating that the films are rather thick so that only oxygen coming from the hematite is detected. On the other hand, the Cr concentration in the films is different from that existing in the precursor solution.

3.4. Optical characterization of Cr-doped Fe_2O_3 thin films

Fig. 6 shows the optical transmission spectra in the wavelength range of 450–800 nm. The films displayed a transparency above 65% with an excitation wavelength above 600 nm. With increasing Cr content, the absorption edge (550–700 nm) shifted towards the longer wavelength region. It appears that **α-Fe_2O_3** has a high absorbance in the blue region, indicating its applicability as an absorbing material in this wavelength range (Fig. 7).

The effect of Cr-doping on the band-gap energy of the synthesized films was determined from the Tauc plot. The band-gap energy (E_g) is estimated from the optical transmission spectra by calculating the absorption coefficient as follows [30]:

$$\alpha = \frac{1}{d}\ln\left(\frac{1}{T}\right) \quad (5)$$

The relation between the absorption coefficient and the incident light energy hν is approximated as [62]:

$$\alpha h\nu = A\,(h\nu - Eg)^{n} \quad (6)$$

where ***α*** is the absorption coefficient, ***A*** is a constant, ***h*** is the

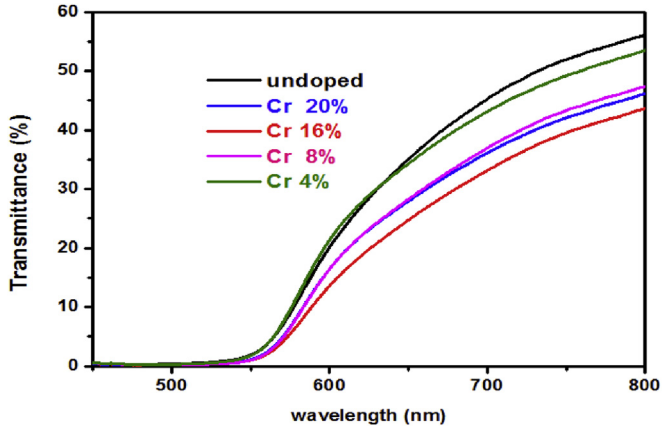

Fig. 6. Transmittance spectra of undoped and Cr doped α-Fe_2O_3.

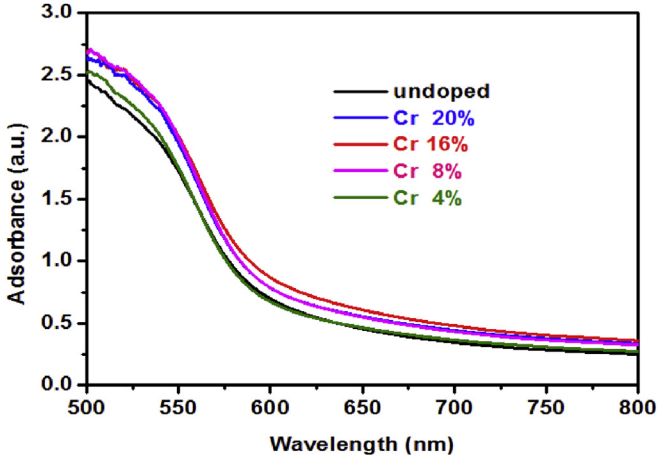

Fig. 7. Absorbance spectra of undoped and Cr doped α-Fe_2O_3.

Planck's constant, ν is the photon frequency, E_g is the optical bandgap, and n is equal to 1/2 for direct bandgap transitions and 2 for indirect ones. Fig. 8 shows the Tauc plot for direct bandgap transitions for undoped and Cr-doped **α-**Fe_2O_3 films. The optical band-gap energy of undoped **α-**Fe_2O_3 films was estimated to be 2.154 eV, slightly lower than that of bulk **α-**Fe_2O_3 (2.3 eV). It can be observed that the optical band-gap of Cr-doped **α-**Fe_2O_3 remains in the range of 2.05 eV–2.1 eV (Table 3).

3.5. Photoelectrochemical properties of the Cr-doped α-Fe_2O_3 electrode

The photocurrent response was measured under visible light irradiation. To improve the photocurrent response of **α-**Fe_2O_3 films the charge carrier transport must be enhanced in bulk and on the surface to reduce carrier recombination at both sites. All measurements were made in 1 M NaOH [63,64] electrolyte and under a potential bias of 0.4 V.

Furthermore, we conducted chronoamperometric measurements under repeated light-on and light-off conditions for all hematite films with and without Cr doping. As shown in Fig. 9, the photocurrent of hematite is low and all Cr-doped hematite films exhibit higher photocurrents than undoped ones. Hematite films with 16 at. % of Cr displays the highest photocurrent, which is consistent with the UV–vis.

The results clearly demonstrate that the photocurrent density generated from the Cr-doped α-Fe_2O_3 electrode is significantly higher than that of undoped electrodes due to the presence of an easier electron transport mechanism. In fact, structural studies showed that XRD peaks exhibited a slight shift towards higher diffraction angles as Cr doping increases, which indicates that Fe^{3+} ions were replaced by smaller Cr^{4+} ions. Accordingly, Cr (Cr^{4+}) acts as an electron donor in the **α-**Fe_2O_3 matrix, thus confirming the substitution of Fe^{3+} by Cr^{4+} ions.

In fact, Cr doping increases the donor concentration and enhances the charge carrier transportation by increasing the electric field across the space charge layer. The growth of the donor concentration would reduce the width of the space charge layer; hence, the charge carriers within the region should be efficiently separated before recombination. On the other hand, a higher concentration of dopant would provide more efficient defect-scattering/recombination inhibiting the increased separation efficiency, which might also explain the variation of the photocurrent density with the doping levels.

Table 3
Optical band-gap for α-Fe_2O_3 thin films having different Cr-doping.

α-Fe_2O_3: Cr-doping	Cr 0%	Cr 4%	Cr 8%	Cr 16%	Cr 20%
Bandgap energy (Eg) (eV)	2.15	2.09	2.08	2.05	2.07

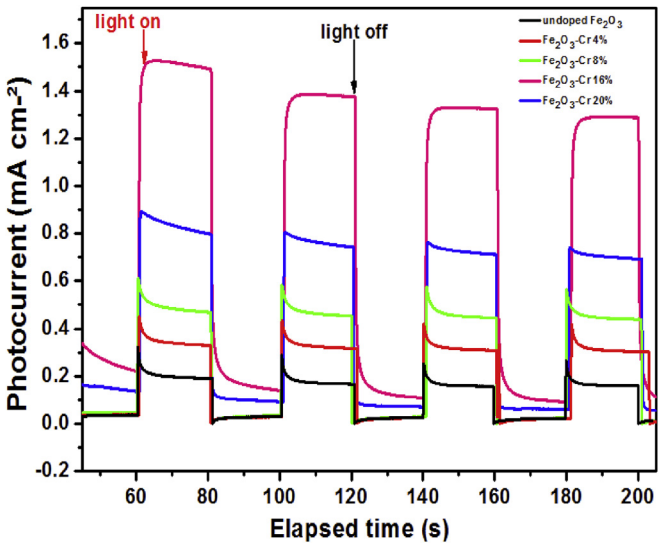

Fig. 9. Photocurrent intensity for Cr-doped Fe_2O_3 electrodes under on/off illumination, measured in 1 M NaOH electrolyte with a bias potential of +0.4 V, under successive illumination cycles.

Fig. 10 shows the performance of doped samples as compared to undoped sample. Significant performance enhancements were observed upon doping throughout the illumination wavelengths. The performance of the 4 at.% Cr-doped films is 4 times higher than that of the undoped sample. The IPCE of 16 at.% Cr-doped films measured at 400 nm with an applied bias of +0.4 V (vs. Ag/AgCl) is 6%, which corresponds to a thirty-fold improvement over the undoped hematite. The higher photon energy was absorbed in the outmost layers of hematite and therefore, the photogenerated holes

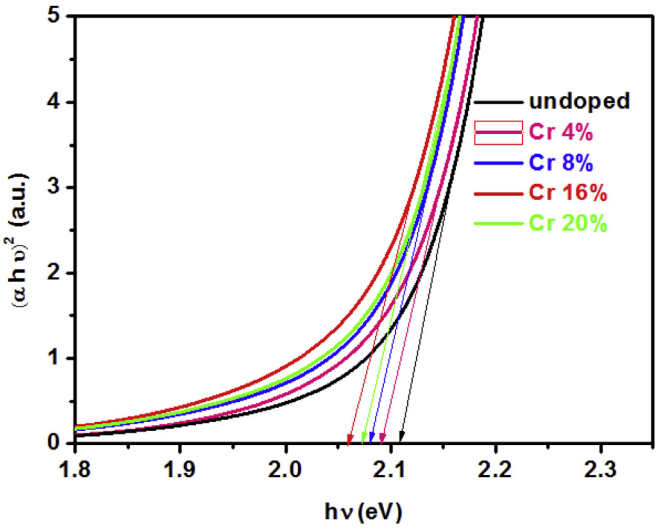

Fig. 8. Tauc plot of undoped and Cr-doped α-Fe_2O_3.

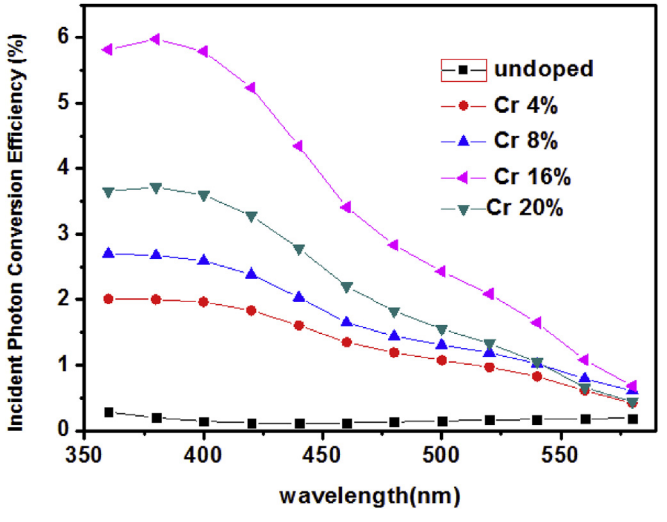

Fig. 10. IPCE for undoped and Cr-doped α-Fe_2O_3 films at an applied potential of +0.4 V (vs. Ag/AgCl) in1 M NaOH.

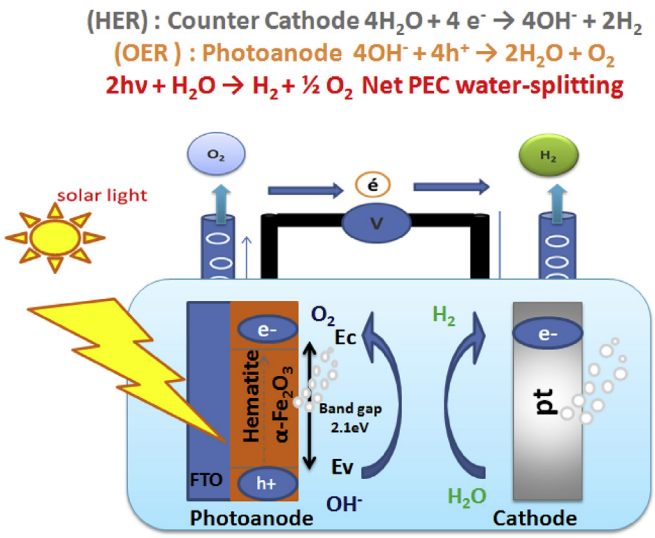

Fig. 11. Energy diagram of the n-type hematite photoanode and schematic illustration of the photoelectrochemical water splitting on photoanode and cathode.

have a shorter diffusion path to reach the surface where they will contribute in H_2O oxidation reaction. An anodic applied bias will increase the collection efficiency of the electrons, and an IPCE improvement can be seen in Fig. 10. Furthermore, the applied bias will enable H_2O reduction at the Pt counter-electrode by overcoming the mismatch (0.4 V (vs. Ag/AgCl)) between the hematite conduction band edge level and the reversible hydrogen potential (see Fig. 11). The improved IPCE performance is implausible to be related to an increase in the absorption of the doped samples since no significant change was obtained in the absorption spectra of the different Cr-doped samples (see Fig. 7).

4. Conclusions

Cr-doped α-Fe_2O_3 films were successfully deposited on FTO-coated glass substrates using the hydrothermal method and an annealing process. The concentration of the incorporated Cr atoms (Cr^{4+} ions) was controlled by varying the concentration of the $Cr(ClO_4)_3$ precursor solution, (i.e., the concentration of the dopant in the sample can be controlled by adjusting the electrolyte composition). The Cr dopant served as an ionized donor and was found to increase the carrier density of the α-Fe_2O_3 films. The major effect of Cr atoms is the improvement of the conductivity and the charge transport properties of the α-Fe_2O_3 films. The photoactivity of the iron oxide was improved by co-deposition with Cr. The best performing samples have a doping rate of 16 at% Cr, which in turn has an IPCE of 6% at 400 nm, with an applied potential of +0.4 V (vs Ag/AgCl). These IPCE values were thirty times higher than that of the undoped sample. Hence, a greater fraction of the photon-generating electron–hole pairs is available for surface redox chemistry. The apparent optimum at 16 at.% Cr doping may balance these competing effects most effectively and yield the best PCE performance. The Cr-doped α-Fe_2O_3 films provide potential applications in photocatalysis for water splitting or in photoelectrical devices.

Acknowledgements

This work was supported by the Ministry of Higher Education and Scientific Research, Tunisia and Ministerio de Economía y Competitividad (ENE2016-77798-C4-2-R) and Generalitat Valenciana (Prometeus 2014/044).

References

[1] A. B.Murphy, P.R. F.Barnes, L.K. Randeniya, I.C. Plumb, Grey, M.D. Horne, J.A. Glasscock, Int. J. Hydrogen Energy 31 (14) (2006) 1999–2017.
[2] Z.B. Chen, T.F. Jaramillo, T.G. Deutsch, A. Kleiman-Shwarsctein, A.J. Forman, N. Gaillard, R. Garland, K. Takanabe, C. Heske, M. Sunkara, E.W. McFarland, K. Domen, E.L. Miller, J.A. Turner, H.N. Dinh, J. Mater. Res. 25 (2010) 3.
[3] K. Sivula, F.L. Formal, M. Grätzel, ChemSusChem 4 (2011) 432–449.
[4] T.W. Hamann, Dalton Trans. 41 (2012) 7830–7834.
[5] V.M. Aroutiounian, V.M. Arakelyan, G.E. Shahnazaryan, H.R. Hovhannisyan, H.L. Wang, J.A. Turner, Sol. Energy 81 (2007) 1369.
[6] J.S. Jang, J. Lee, H. Ye, F.R.F. Fan, A.J. Bard, J. Phys. Chem. C 113 (2009) 6719.
[7] Y.S. Hu, A. Kleiman-Shwarsctein, A.J. Forman, D. Hazen, J.N. Park, E.W. McFarland, Chem. Mater 20 (2008) 3803.
[8] I. Cesar, A. Kay, J.A.G. Martinez, M. Gratzel, J. Am. Chem. Soc. 128 (2006) 4582.
[9] S. Saremi-Yarahmadi, K.G.U. Wijayantha, A.A. Tahir, B. Vaidhyanathan, J. Phys. Chem. C 113 (2009) 4768.
[10] Y.Q. Liang, C.S. Enache, R. van de Krol, Int. J. Photoenergy 2008 (2008) 1.
[11] I. Cesar, K. Sivula, A. Kay, R. Zboril, M. Gratzel, J. Phys. Chem. C 113 (2009) 772.
[12] Y.S. Hu, A. Kleiman-Shwarsctein, G.D. Stucky, E.W. McFarland, Chem. Commun. (2009) 2652.
[13] F. Morin, J. Phys. Rev. 83 (1951) 1005.
[14] J.S. Jang, J. Lee, H. Ye, F.R.F. Fan, A.J. Bard, J. Phys. Chem. C 113 (2009) 6719.
[15] A. Kleiman-Shwarsctein, M.N. Huda, A. Walsh, Y.F. Yan, G.D. Stucky, Y.S. Hu, M.M. Al Jassim, E.W. McFarland, Chem. Mater. 22 (2010) 510.
[16] A. Bak, W. Choi, H. Park, Appl. Catal. B 110 (2011) 207.
[17] A. Kleiman-Shwarsctein, Y.S. Hu, A.J. Forman, G.D. Stucky, E.W. McFarland, J. Phys. Chem. C 112 (2008) 15900.
[18] V.M. Aroutiounian, V.M. Arakelyan, G.E. Shahnazaryan, G.M. Stepanyan, E.A. Khachaturyan, H. Wang, J.A. Turner, Sol. Energy 80 (2006) 1098.
[19] K. Gurunathan, P. Maruthamuthu, Int. J. Hydrogen Energy 20 (1995) 287.
[20] G.K. Reddy, K. Gunasekara, P. Boolchand, P.G. Smirniotis, J. Phys. Chem. C 115 (2011) 920.
[21] R. Schrebler, L. Ballesteros, A. Burgos, E.A. Dalchiele, J. Electrochem. Soc. 158 (2011) D500.
[22] C.L. Chun, D.R. Baer, D.W. Matson, J.E. Amonette, R.L. Penn, Environ. Sci. Technol. 44 (2010) 5079.
[23] J. Velev, A. Bandyopadhyay, W.H. Butler, S. Sarker, Phys.Rev. B 71 (2005), 205208.
[24] A.A. Akl, Appl. Surf. Sci. 233 (2004) 307.
[25] C.D. Park, J. Walker, R. Tannenbaum, A.E. Stiegman, J. Frydrych, L. Machala, ACS Appl.Mater.Int. 1 (2009) 1843.
[26] A. Watanabe, H. Kozuka, J. Phys. Chem. B 107 (2003) 12713.
[27] A. Memar, W.R.W. Daud, S. Hosseini, E. Eftekhari, L.J. Minggu, Sol. Energy 84 (2010) 1538.
[28] C.J. Jia, L.D. Sun, Z.G. Yan, L.P. You, F. Luo, X.D. Han, Y.C. Pang, Z. Zhang, C.H. Yan, Angew. Chem. Int.Ed. 44 (2005) 4328.
[29] K. Sue, T. Sato, S. Kawasaki, Y. Takebayashi, S. Yoda, T. Furuya, T. Hiaki, Ind. Eng. Chem. Res. 49 (2010) 8841.
[30] E.L. Miller, D. Paluselli, B. Marsen, R.E. Rocheleau, Thin Solid Films 466 (2004) 307.
[31] Z.H. Zhang, M.F. Hossain, T. Miyazaki, T. Takahashi, Environ. Sci. Technol. 44 (2010) 4741.
[32] M. Aronniemi, J. Saino, J. Lahtinen, ThinSolidFilms 516 (2008) 6110.
[33] W. Widiyastuti, R. Balgis, F. Iskandar, K. Okuyama, Chem. Eng. Sci. 65 (2010) 1846.
[34] A. Duret, M. Gratzel, J. Phys. Chem. B 109 (2005), 17184.
[35] C.J. Sartoretti, B.D. Alexander, R. Solarska, W.A. Rutkowska, J. Augustynski, R. Cerny, J. Phys. Chem. B 109 (2005) 13685.
[36] S. Saremi-Yarahmadi, K.G.U. Wijayantha, A.A. Tahir, B. Vaidhyanathan, J. Phys. Chem. C 113 (2009) 4768.
[37] A. Kay, I. Cesar, M. Gratzel, J. Am. Chem. Soc. 128 (2006), 15714.
[38] Y.S. Hu, A. Kleiman-Shwarsctein, A.J. Forman, D. Hazen, J.N. Park, E.W. McFarland, Chem. Mater. 20 (2008) 3803.
[39] A. Kleiman-Shwarsctein, M.N. Huda, A. Walsh, Y.F. Yan, G.D. Stucky, Y.S. Hu, M.M. Al-Jassim, E.W. McFarland, Chem. Mater. 22 (2010) 510.
[40] R.L. Spray, K.S. Choi, Chem. Mater 21 (2009) 3701.
[41] A. Bak, W. Choi, H. Park, Appl. Catal. B 110 (2011) 207.
[42] U. Bjorksten, J. Moser, M. Gratzel, Chem. Mater. 6 (6) (1994) 858–863.
[43] H.L. Wang, J.A. Turner, J. Electrochem. Soc. 157, (11) (2010) F173–F178.
[44] L. Vayssieres, J.H. Guo, J. Nordgren, J. Nanosci. Nanotechnol. 1 (4) (2001) 385–388.
[45] L. Li, Y. Yu, F. Meng, Y. Tan, R.J. Hamers, S. Jin, Nano Lett. 12 (2) (2012) 724–731.
[46] M. Grätzel, Photoelectrochemical cells, Nature 414 (2001), 15 NOVEMBER.
[47] A. Boudjemaa, S. Boumaza, M. Trari, R. Bouarab, A. Bougueliac, Physical and photoelectrochemical characterizations of a-Fe_2O_3.Application for hydrogen production, Int. J. Hydrogen Energy 34 (2009) 4268–4274.
[48] A. Boudjemaa, M. Trari, Photo-catalytic hydrogen production over Fe_2O_3 based catalysts, Int. J. Hydrogen Energy 35 (2010) 7684–7689.
[49] J.H. Kennedy, K.W. Frese Jr., J. Electrochem. Soc. 125 (5) (1978) 709–714.
[50] M.P. Dare-Edwards, J.B. Goodenough, A. Hamnett, P.R. Travelling, J. Chem. Soc. Faraday Trans. I 79 (1983) 2027–2041.
[51] A. Mao, G.Y. Han, J.H. Park, J. Mater. Chem. 20 (2010) 2247–2250.

[52] C.J. Sartoretti, B.D. Alexander, R. Solarska, W.A. Rutkowska, J. Augustynski, R. Cerny, J. Phys. Chem. B 109 (28) (2005) 13685–13692.
[53] J.A. Glasscock, P.R.F. Barnes, I.C. Plumb, N. Savvides, J. Physical Chem. C 111 (44) (2007) 16477–16488.
[54] Yichuan Ling, Gongming Wang, Damon A. Wheeler, Jin Z. Zhang, Yat Li, Nano Lett. 11 (5) (2011) 2119–2125.
[55] Yanming Fu, Chung-Li Dong, Zhaohui Zhou, Wan-Yi Lee, Jie Chen, Penghui Guo, Liang Zhao, ShaohuaShen, Phys. Chem. Chem. Phys. 18 (2016) 3846–3853.
[56] S. Kumari, A.P. Singh, Sonal, D. Deva, R. Shrivastav, S. Dass, V.R. Satsangi, Int. J. Hydrogen Energy 35 (2010) 3985–3990.
[57] W.B. Ingler Jr., S.U.M. Khan, Thin Solid Films 461 (2004) 301–308.
[58] W.B. Ingler Jr., J.P. Baltrus, S.U.M. Khan, J. Am. Chem. Soc. 126 (2004) 10238–10239.
[59] L. Vayssieres, N. Beermann, S.E. Lindquist, A. Hagfeldt, Controlled aqueous chemical growth of oriented three-dimensional crystalline nanorod arrays: application to iron(III) oxides, Chem. Mater. 13 (2001) 233–235.
[60] A. Annamalai, P.S. Shinde, A. Subramanian, J.Y. Kim, J.H. Kim, S.H. Choi, J.S. Lee, J.S. Jang, J. Mater. Chem. A 3 (2015) 5007–5013.
[61] Mingyang Li, Ziyang Zhang, Feiyi Lyu, Xinjun He, Zhihao Liang, Muhammad-Sadeeq Balogun, Xihong Lu, Ping-Ping Fang, Yexiang Tong, Electrochim. Acta 186 (2015) 95–100.
[62] M.R. Belkhedkar, A.U. Ubale, Int. J. Mater. Chem. 4 (2014) 109–116.
[63] S.S. Shinde, R.A. Bansode, C.H. Bhosale, K.Y. Rajpure, J. Semicond. 32 (2011), 013001.
[64] Flavio L. Souza, Kirian P. Lopes, Pedro A.P. Nascente, Edson R. Leite, Sol. Energy Mater. Sol. Cells 93 (2009) 362–368.

Journal of The Electrochemical Society, **165** (2) H30-H38 (2018)
0013-4651/2018/165(2)/H30/9/$37.00 © The Electrochemical Society

Influence of a Compact α-Fe_2O_3 Layer on the Photovoltaic Performance of Perovskite-Based Solar Cells

F. Bouhjar,[1,2,3,z] M. Mollar,[1] Shafi Ullah,[1] B. Marí,[1] and B. Bessaïs[3]

[1] *Institut de Disseny i Fabricació (IDF) , Departament de Física Aplicada, Universitat Politècnica de València, 46022 València, Spain*
[2] *Photovoltaic Laboratory, Research and Technology Centre of Energy, Borj-Cedria Science and Technology Park, 2050 Hammam-Lif, Tunisia*
[3] *University of Tunis, Tunis, Tunisia*

In this study, uniform and dense iron oxide α-Fe_2O_3 thin films were used as an electron-transport layer (ETL) in $CH_3NH_3PbI_3$-based perovskite solar cells (PSCs), replacing the Titanium dioxide (TiO_2) ETL conventionally used in planar heterojunction perovskite solar cells. The α-Fe_2O_3 films were synthesized using an electrodeposition method for the blocking layer and a hydrothermal method for the overlaying layer, while 2,2',7,7'-tetrakis (N, N'-di-p-methoxyphenylamine)-9,9' spirobifluorene (spiro-OMeTAD) was employed as a hole conductor in the solar cells. Based on the above synthesized α-Fe_2O_3 films the photovoltaic performance of the PSCs was studied. The α-Fe_2O_3 layers were found to have a significant impact on the photovoltaic conversion efficiency (PCE) of the PSCs. This was attributed to an efficient charge separation and transport due to a better coverage of the perovskite on the α-Fe_2O_3 films. As a result, the PCE measured under standard solar conditions (AM 1.5G, 100 mW cm^{-2}) reached 5.7%.
 [DOI: 10.1149/2.1131802jes]

Manuscript submitted August 15, 2017; revised manuscript received November 30, 2017. Published January 25, 2018.

To date, organometallictrihalide perovskites $CH_3NH_3PbX_3$ (X is iodine or a mixture of iodine, chlorine and bromine) have been considered as the most promising light absorption materials for solar energy conversion because of their wide absorption range,[1] high extinction coefficient,[2] ambipolar charge transport,[3] and long electron–hole diffusion length.[4] Recently, Perovskite-based solar cells (PSCs) have attracted increased attention due to their superior performance and ease of fabrication. Indeed, spectacular progress in improving photovoltaic performance has been achieved in this field, and the power conversion efficiency (PCE) of PSCs has been greatly increased, surpassing 20%.[5–10].

To further understand the material properties and the mechanisms of the functioning device, simplified planar heterojunction structured devices have become the focus of many research efforts.[11] PSCs are usually composed of a fluorine-doped tin oxide (FTO) conductive substrate, a compact electron-selective layer (ESL), a mesoporous scaffold layer (optional), an organic–inorganic hybrid perovskite layer, a hole-transporting material (HTM), and a metallic electrode.[12]

The quality of the ESL and perovskite layers is indispensable in obtaining efficient PSCs[13] and it plays an important role in reducing the structural and electronic defects in the films, which in turn can significantly affect the device performance. In the case of PSCs, much emphasis has been placed on perovskite film processing and alternative hole transport materials, due to the high cost of 2,2',7,7'-tetrakis-(N,N-di-p-methoxyphenamine)-9,9'-spiro-bifluorene (spiro-OMeTAD).[14] On the other hand, less attention has been paid to processing ESLs. Frequently integrated in PSCs as a promising ESL material, TiO_2 is a semiconductor with a wide band gap.[15] However, TiO_2 has low electron mobility, which might create unbalanced charge transport in the perovskite.[16] In addition, this compact layer often requires high-temperature sintering at 450–500°C prior to use[17–19] making it incompatible with flexible substrates and easy fabrication. Indeed, Snaith et al.[14] suggested that oxygen vacancies in the TiO_2 electrode are activated by UV light, which increase charge traps causing the degradation of the PCEs of the PSCs. Therefore, many efforts have been made to use other n-type inorganic nanocrystals as alternative electron conductors in PSCs.

Several n-type inorganic nanocrystals such as ZnO,[20] SnO,CdSe,[21] CdS, and α-Fe_2O_3 have been considered as possible substitute of TiO_2, and have displayed considerable power conversion efficiency.[22,23] Among all of the alternative materials, α-Fe_2O_3 has been widely used as an anode material for super capacitors.[24] It is one of the most common n-type materials, and the most stable iron oxide with n-type semiconducting properties under ambient conditions. It has been used as the photoanode in dye-sensitized solar cells to enhance the electron transfer rate;[25] however its use as an electron transporting replacing TiO_2 has not yet been reported. Thus, we employed low-cost α-Fe_2O_3 as ETL material instead of TiO_2 in planar perovskite cells. The charge accumulation at the perovskite/α-Fe_2O_3 interface is significantly reduced and hence effective in reducing the hysteresis.[26] Furthermore, the fabricated solar cells show a good stability upon exposure to ambient air without any encapsulation. The studied materials for perovskite solar cells are $CH_3NH_3PbI_3$,$CH_3NH_3PbI_{3-x}Cl_x$, $CH_3NH_3PbBr_3$,$CH_3NH_3Pb(I_{1-X}Br_x)_3$, $HC(NH_2)_2PbI_3$,$HC(NH_2)_2Pb(I_{1-X}Br_x)_3$, and $CH_3NH_3SnI_3$. In Table I, the reported performances are summarized in terms of material $CH_3NH_3PbI_3$ and cell configuration. HTM materials are also important for high efficiency perovskite solar cells, where the most studied HTM is spiroMeOTAD, but polymertic HTMs such as the thiophene derivative P3HT and tryarylamine-based PTAA have also been tested. In addition, inorganic HTMs such as NiO, CuI, and CuSCN are confirmed to be suitable for perovskite solar cells.

The present report mainly focuses on the deposition of a compact α-Fe_2O_3 film, and its impact on the growth of the perovskite layer, providing a comprehensive understanding of the properties of the α-Fe_2O_3/perovskite interface. The α-Fe_2O_3 films are fabricated using an electrodeposition method for the blocking layer and a hydrothermal method for the overlying layer. Then the as-synthesized α-Fe_2O_3 films are used for PSCs. The impact of the growth of the α-Fe_2O_3 film on the properties of the α-Fe_2O_3/perovskite interface and on the performance of PSCs is investigated. Morphologically uniform α-Fe_2O_3 film let's achieve a PCE of 5.7%. These results show the application possibility of α-Fe_2O_3 in PSCs, and provide the principle for the choice of the electron transport layer for efficient PSCs.

Experimental

Synthesis of α-Fe_2O_3 thin films.—*Under layer fabrication (α-Fe_2O_3 (A)).*—The experimental set-up used to prepare α-Fe_2O_3 thin films consisted of a computer-controlled potentiostat/galvanostat and a classic three electrodes electrochemical cell. The electrochemical cell was filled with a solution containing 5 mM $FeCl_3$ +5 mM KF+ 1 M H_2O_2 +0.1 M KCl as supporting electrolyte in deionized water. The working electrode was a substrate composed of fluorine-doped tin oxide (FTO) coated glass having a sheet resistance of 10 Ω; the

[z] E-mail: feriel88bouhjar@gmail.com

Table I. Photovoltaic performance of perovskite ($MAPbI_3$) solar cells. J_{sc}, V_{oc} and FF stand for short-circuit current density, open-circuit voltage, and fill factor respectively.

Materials	Cell configuration	J_{sc}[mA/cm^2]	V_{oc} [V]	FF	PCE (%)	Ref
$MAPbI_3$	mesoporous-TiO_2/$MAPbI_3$/spiro-MeOTAD	17.6	0.888	0.62	9.7	27
	$MAPbI_3$/PCBM	10.32	0.60	0.63	3.9	28
	mesoporous-TiO_2 /$MAPbI_3$/P3HT-MWNT	14.8	0.76	0.57	6.45	29
	rutile TiO_2 nanorod/$MAPbI_3$/spiro-MeOTAD	15.6	0.955	0.63	9.4	30
	mesoporous-ZrO_2/$MAPbI_3$/spiro-MeOTAD	17.3	1.07	0.59	10.8	31
	NiO/MAPbI /$PCBM_3$	13.24	1.040	0.69	9.51	32
	mesoporous-TiO_2/$MAPbI_3$/CuI	17.8	0.55	0.62	6.0	33
	Fe_2O_3/$MAPbI_3$/ spiro-MeOTAD	11.27	1.55	0.33	5.7	Our work

previous substrate was cleaned in an ultrasonic acetone bath for 10 min, then rinsed in distilled water and dried. Pt and Ag/AgCl electrodes were used as a counter electrode and a reference electrode, respectively. The films were deposited by cathodic electrodeposition. The deposition potential was fixed at −0.15 V and the deposited charge was 1.2 C for all samples in order to have a thickness of approximately 40–60 nm for all Fe_2O_3 films. A thermostat fixed the solution temperature at 298 K. After deposition, the films were rinsed with distilled water. To obtain the desired α-Fe_2O_3 phase, the deposited films were annealed in air at 650°C for 2 h. The transition between phases, from β-FeOOH (yellow) to **α-**Fe_2O_3 (red–brown) is shown in Fig. 1.

On layer fabrication (α-Fe_2O_3 (B)).—Nanostructured **α-**Fe_2O_3 (B) thin films were obtained after annealing hydrothermally deposited iron films on a smooth α-Fe_2O_3 surface (A). The bath was done by filling a 30 mL recipient, with a 20 mL aqueous solution containing 0.15 M of $FeCl_3.6H_2O$ and 1 M $NaNO_3$ at pH 1.5 (adjusted by HCl), leading to the deposition of iron hydroxides (FeOOH). Iron films were deposited on the **α-**Fe_2O_3 (A) substrate from an iron precursor solution ($FeCl_3.6H_2O$).[34–36] A piece of FTO/**α-**Fe_2O_3 (A) was put into the autoclave, then heated at 100°C for 6 h and naturally cooled down to ambient temperature. Under hydrothermal conditions, this solution enables the interaction of Fe^{3+} ions with OH^-, producing iron oxide nuclei, as described by

$$Fe^{3+}{}_{(aq)} + 3OH^-{}_{(aq)} \rightarrow \beta\text{-}FeOOH_{(s)} + H_2O_{(l)} \quad [1]$$

As a result, a uniform layer of β-FeOOH grows on the FTO substrate. The akageneite-coated substrate was then washed with deionized water and subsequently sintered in air at 550°C for 4 h. During the annealing process, the β-FeOOH converts into α-Fe_2O_3. The phase transition from β-FeOOH (yellow) to **α-**Fe_2O_3 (red–brown) is shown in Fig. 2. During the phase transition, the occurring chemical reaction is due to the thermal treatment, it can be represented by

$$2\beta\text{-}FeOOH_{(s)} \rightarrow Fe_2O_{3(s)} + H_2O_{(L\,or\,G)} \quad [2]$$

Fabrication of the perovskite-based solar cell ($CH_3NH_3PbI_3$ or $MAPbI_3$).—The $MAPbI_3$ perovskite precursor solution was prepared from an equimolar of Methylammonium iodide (CH_3NH_3I or MAI)/Lead (II) iodide(PbI_2), in a 40% dimethylformamide (DMF) solution with ratios 1:1 (1:1 mol %) for MAI: PbI_2 and then stirred for 2 h at 70°C. The mixture was deposited onto (FTO) covered glass by spin-coating at 3500 rpm for 11 s. A drop of toluene was added after 2–4 s before the end then dried at 5000 rpm for 30 s. The resulting perovskite layers were then annealed at 100°C for 1 h. Before the deposition process, the FTO glass substrates were cleaned with ethanol, isopropanol, and water for 15 min, and then dried with clean dry air. The reaction results in the formation of a compact and flat crystalline MAI-DMFPbI_2 intermediate phase film.

$$PbI_2\text{-}MAI\text{-}DMF \rightarrow MAPbI_3 + DMF \uparrow \quad [3]$$

The intermediate phase film is successfully converted into a crystalline perovskite film by annealing at 100°C, as shown in Eq. 3. The DMF is removed in the intermediate phase film, leaving a compact and flat morphology (Fig. 3).

The hole-transporting layer (HTM) was then deposited via spin-coating using a 0.788 M solution of 2,2',7,7'-tetrakis-(N, N-di-p-methoxyphenylamine)9,9'-spirobifluorene (spiro-OMeTAD) in

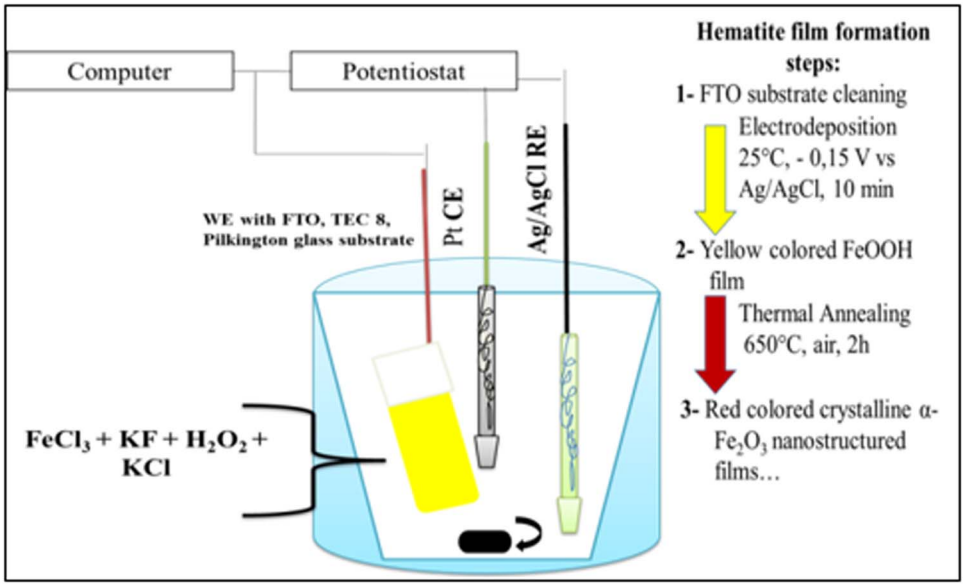

Figure 1. Schematic representations of a typical three-electrode electrochemical cell.

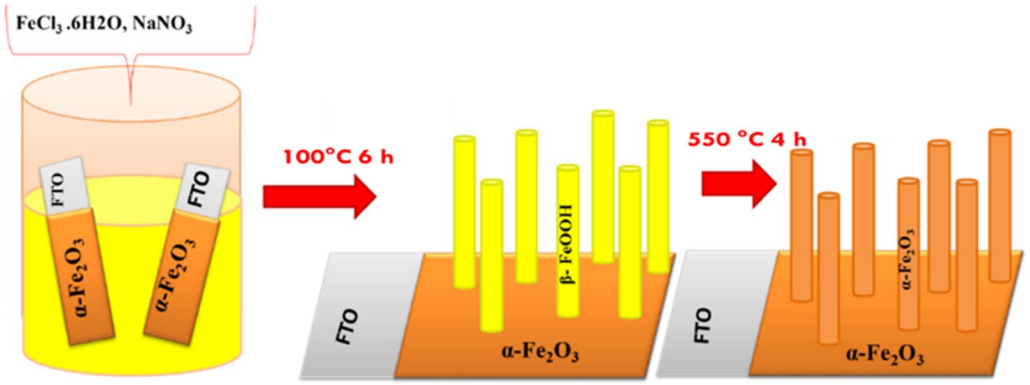

Figure 2. Schematic representations of the syntheses methods adopted for α-Fe_2O_3 hematite photoanode film electrodeposited on α-Fe_2O_3 (A) substrate.

chlorobenzene, with additives of 0.0184 M lithium bis (trifluoromethanesulfonyl) imide (added in 0.61M acetonitrile solution) and 0.0659 M 4-tert-butylpyridine. The HTM was spin coated at 4500 rpm for 30 s inside a drybox. Finally, the top anode (a 50 nm-thick gold (Au) film) contact was deposited by thermal evaporation under a vacuum of ∼10–6 Torr, yielding an active area of 0.2 cm^2, to complete the creation of the device (inset in Fig. 4).

Figure 4B shows the energy level diagram for the different solar cell components, depicting the conduction band of α-Fe_2O_3, conduction and valence bands of $CH_3NH_3PbI_3$ perovskite, and position of the highest occupied molecular orbital (HOMO) of Spiro-OMeTAD as HTM. In this scheme, the electrons and holes generated in $CH_3NH_3PbI_3$ can be energetically injected into the α-Fe_2O_3 and HTM phases respectively.[37,38]

Results and Discussion

Structural characterization.—The crystal structure of α-Fe_2O_3 and α-Fe_2O_3/perovskite thin films was investigated by X-ray diffraction (XRD) using a Rigaku Ultima IV diffractometer in the Bragg-Brentano configuration (the X-ray radiation is $\lambda_{CuK\alpha}$ = 1.54060 Å). Figure 5a shows the XRD patterns of α-Fe_2O_3 (A), α-Fe_2O_3 (B), and a α-Fe_2O_3/α-Fe_2O_3bilayer deposited on FTO substrates. The diffractograms of the α-Fe_2O_3/α-Fe_2O_3 and the FTO substrates are also shown. The XRD lines of the α-Fe_2O_3 films are observed at 2θ = 24.1°, 33.1°, 35.6°, 40.9°, 49.4°, 54.0°, and 64°, corresponding to the (012), (104), (110), (113), (024), (116), and (300) planes of the hematite phase, respectively. The dominant lines correspond to the (104) and (110) planes. The diffraction lines of the trigonal structure of α-Fe_2O_3 matches well with the reference pattern of the JCPDS card file no 33-0664, which corresponds to the space group R3c (167) with lattice parameters a = b = 5.03 nm and c = 13.74 nm.

Figure 5b shows the X-Ray diffractograms for the $MAPbI_3$ and α-Fe_2O_3 (A)/α-Fe_2O_3 (B)/ $MAPbI_3$/FTO thin films. XRD lines are located at 15°, 20°, 24.4°, 28.4°, 31.8°, 40.6°, and 43°. $MAPbI_3$ thin films crystallize and stabilize into the same cubic structure (Fig. 5c). The most intense diffraction line located below 15° corresponds to the (100) diffraction plane and the lines located at about 20°, 30°, and 34° are related to the (110), (200), and (210) orientation planes, respectively. One may also observe two diffraction lines located at 26.5° and 33.7°corresponding to the FTO substrates. For the α-Fe_2O_3 (A)/α-Fe_2O_3 (B)/$MAPbI_3$/FTO layers, all lines match the α-Fe_2O_3 (A), α-Fe_2O_3 (B), and $MAPbI_3$ patterns except those marked with a solid dark point that come from the FTO substrate.

Morphological characterization.—The microstructural and elemental analyses were characterized using a Zeiss ULTRA 55 model scanning electron microscope (FESEM) equipped with an energy dispersive spectroscopy (EDS) system. Figure 6 displays the FESEM images of (a) α-Fe_2O_3(A), (b) α-Fe_2O_3 (B), (c) α-Fe_2O_3(A)/α-Fe_2O_3 (B), (d) $MAPbI_3$, (e) α-Fe_2O_3(A)/α-Fe_2O_3(B)/$MAPbI_3$ and (f) the solar cell deposited on FTO substrates, respectively. Figure 6a shows vertically grown segregated nanostructured islands made up of small Fe_2O_3 (A) nanoparticles, showing some grain size dispersion. Figure 6b shows the microstructure of the as-prepared sample. The later allows us to point out the formation of typical anisotropic-like nanoparticles, mainly composed of nanostructured rods, which is a characteristic of the mesoporous film. Figure 6c depicts the morphology of α-Fe_2O_3/α-Fe_2O_3bilayer that reveals nanostructured aggregates having a grain size of approximately 20 nm. The α-Fe_2O_3(B) grains deposited on α-Fe_2O_3(A) are larger than those deposited on FTO. Figure 6d shows that the $MAPbI_3$ film is composed of dense and homogenous fibre-like crystals with the presence of voids due to solvent evaporation. Figure 6e shows that the fibre-like $MAPbI_3$ films deposited on α-Fe_2O_3(A)/α-Fe_2O_3(B) have dissimilar shapes and sizes. Figure 6f shows the α-Fe_2O_3(A)/α-Fe_2O_3(B)/$MAPbI_3$/spiro-OMeTAD/Au, where the $MAPbI_3$ film becomes uniform with a denser morphology. Figure 7 shows the vertical cross section of the FESEM image

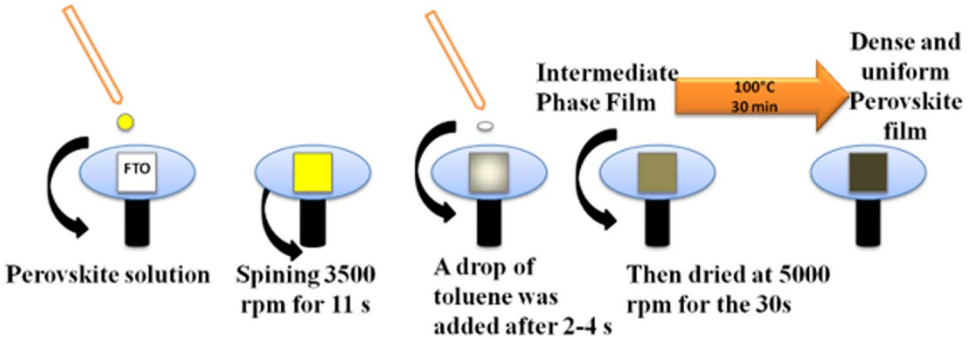

Figure 3. Solvent engineering procedure for preparing the uniform and dense perovskite film.

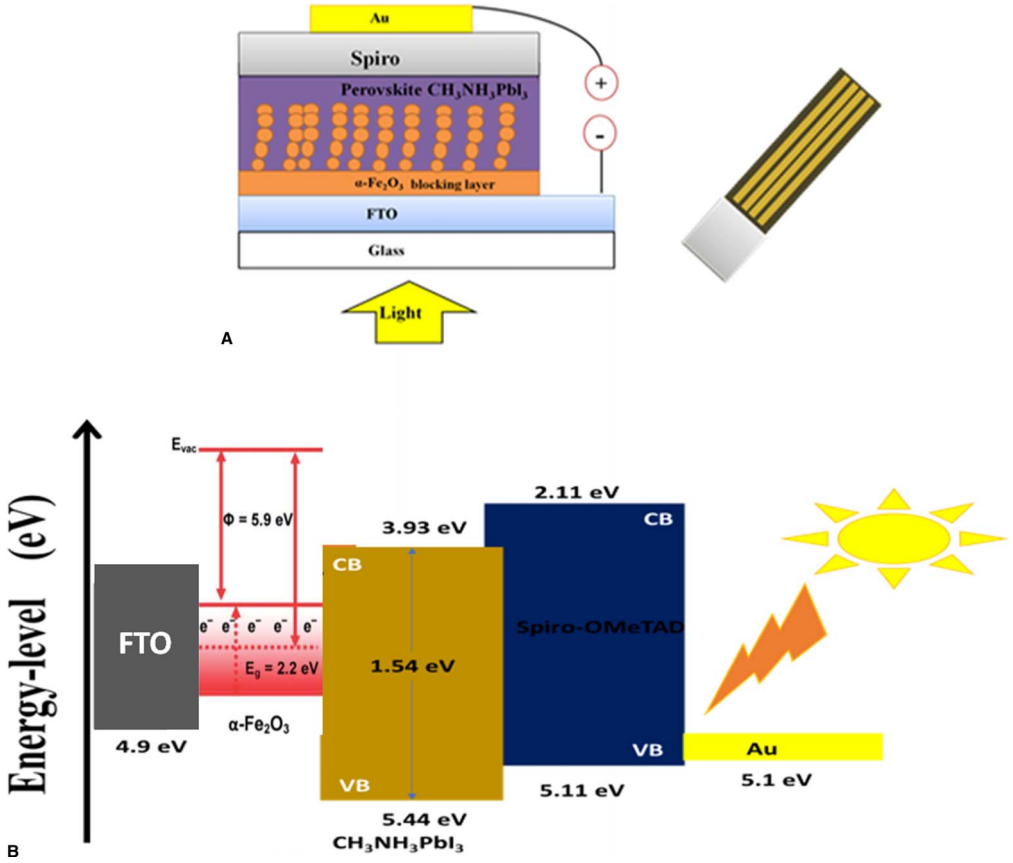

Figure 4. A: Scheme of the perovskite solar cell. B: Energy-level diagram for each component of the device.

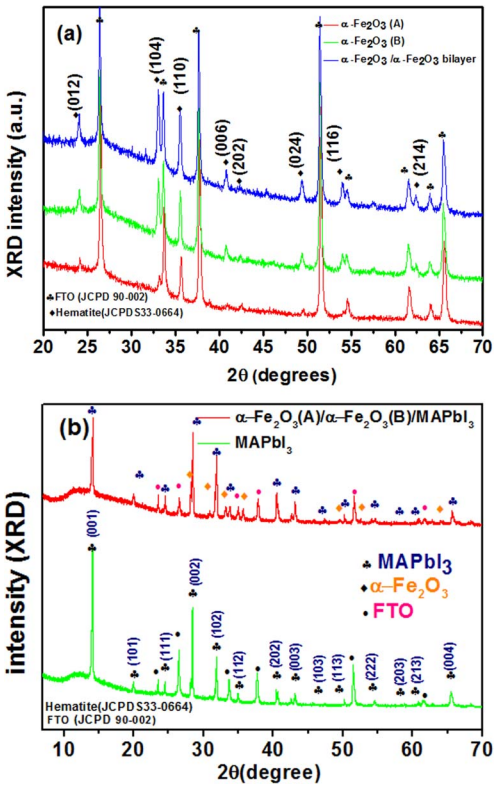

Figure 5. (a) XRD spectra of α-Fe_2O_3(A), α-Fe_2O_3(B) and α-Fe_2O_3/α-Fe_2O_3bilayer. (b). XRD patterns of $MAPbI_3$ and α-Fe_2O_3(A)/α-Fe_2O_3(B)/$MAPbI_3$/FTO. (c). Scheme of $MAPbI_3$ perovskite crystallization.

of the entire structure (α-Fe_2O_3 (A)/ α-Fe_2O_3 (B)/ $MAPbI_3$/spiro-OMeTAD/Au) deposited on FTO. The thickness of the cell is about 4.8 μm.

EDX analyses.—Figure 8A shows a EDX elemental analysis of the deposited $MAPbI_3$, α-Fe_2O_3(A)/α-Fe_2O_3(B), α-Fe_2O_3(A)/α-Fe_2O_3(B)/$MAPbI_3$. The line observed at 0.72 keV corresponds to the L line of Fe, and the oxygen K line is peaking at 0.525 keV. The calculated atomic ratio of Fe and O is approximately equal to 2:3, which well agrees with the stoichiometric composition of α-Fe_2O_3. The percentage of each element was calculated from EDX analyses (Fig. 8). The element ratio of the $MAPbI_3$ film is shown in Fig. 8A (a); two featured lines peaking at 2.48 and 3.98 keV are assigned to the Pb and I elements, respectively. The EDX presented in Fig. 8A (a) shows that Pb and I are well distributed on a large energy scale. Figures 8A (c-d) show the elemental composition of the solar cell and confirm the presence of each element formingthe cell. The line observed at 2.3 keV corresponds to the M line of the gold (Au) contacts.

Figure 8B shows the spatial distribution of α-Fe_2O_3+$MAPbI_3$, where Pb and I are three-dimensionally well-distributed in the α-Fe_2O_3 film. The atomic percentage calculated from the EDX analyses indicates that the Pb to I ratio is 1:3. Compared to the Fe atomic ratio, Pb has a relatively lower atomic percentage indicating that the perovskite sensitizer does not densely cover theα-Fe_2O_3 surface. It can be concluded that the α-Fe_2O_3 composites can uniformly encapsulate the $CH_3NH_3PbI_3$ crystals.

Optical characterization of α-Fe_2O_3 thin films.—The band gap energy was determined from the optical absorption by recording the transmission spectra using a UV-Visible spectrophotometer (Ocean Optics HR4000) coupled with an integrating sphere (to collect both specular and diffuse transmittance). Figure 9 shows the transmission spectra of the α-Fe_2O_3/α-Fe_2O_3 bilayer, from which the optical band

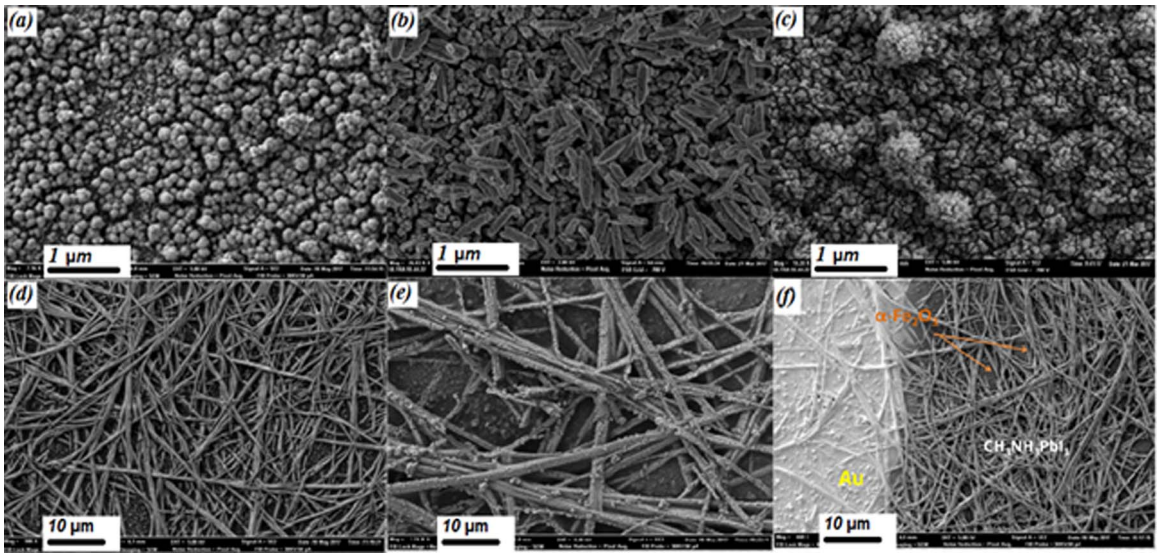

Figure 6. FESEM images of (a) α- Fe_2O_3(A), (b) α-Fe_2O_3(B), (c) α- Fe_2O_3(A)/α-Fe_2O_3(B), (d) $MAPbI_3$, (e) α-Fe_2O_3(A)/α-Fe_2O_3(B)/$MAPbI_3$ and (f) solar cell.

gap energies can be determined. The transmittance spectrum of the α-Fe_2O_3/α-Fe_2O_3 bilayer shows a high optical transmission ratio: above 30% in the visible range. A significant increase in absorption below 533 nm can be assigned to the intrinsic band gap absorption of the α-Fe_2O_3/α-Fe_2O_3 bilayer.

According to the solid band theory, the relation between the absorption coefficient **α** and the energy of the incident light ***hν*** is given by[39]

$$\alpha h\nu = A(h\nu - Eg)^n \quad [4]$$

where **α** is the absorption coefficient, ***A*** is a constant, ***h*** is the Planck's constant, **ν** is the incident photon frequency, ***Eg*** is the optical band gap, and ***n*** is equal to 2 for a direct transition, and to 1/2 for an indirect transition. Figure 9 depicts the Tauc plot of α-Fe_2O_3/α-Fe_2O_3 bilayer. One may point out a direct band gap energy of about 2.3 eV, smaller than that of bulk α-Fe_2O_3 (2.3 eV).

Figure 10 shows the transmission and the absorbance of the$MAPbI_3$ perovskite thin film. The main features of the transmission spectra are the existence of a sub-band gap absorption tail followed by a strong rise of the absorption, which corresponds to excitonic absorption, and then a transition from the valence band to the conduction band. When excitonic absorption dominates the absorption spectrum, the classical relationship between the coefficients (α) and the band gap energy (Eg) is commonly used for calculating the direct band gap of a semiconductor

$$(\alpha.h\nu)^2 = A\,(E\text{-}Eg) \quad [5]$$

where E is the incident photon energy and A is a constant.[40] Note the direct band gap energy of about 1.58 eV. Figure 11 shows the corresponding Tauc plot for MAPbI3 perovskite thin films.

Photoelectrochemical properties of α-Fe_2O_3 electrodes.—The PEC measurements were performed in a quartz cell to enable light reaching the photoelectrode surface. The surface area of the light-exposed working electrode was about 0.25 cm^2. The electrolyte used in all PEC measurements is 1 M NaOH (pH = 13.6). The electrolyte is

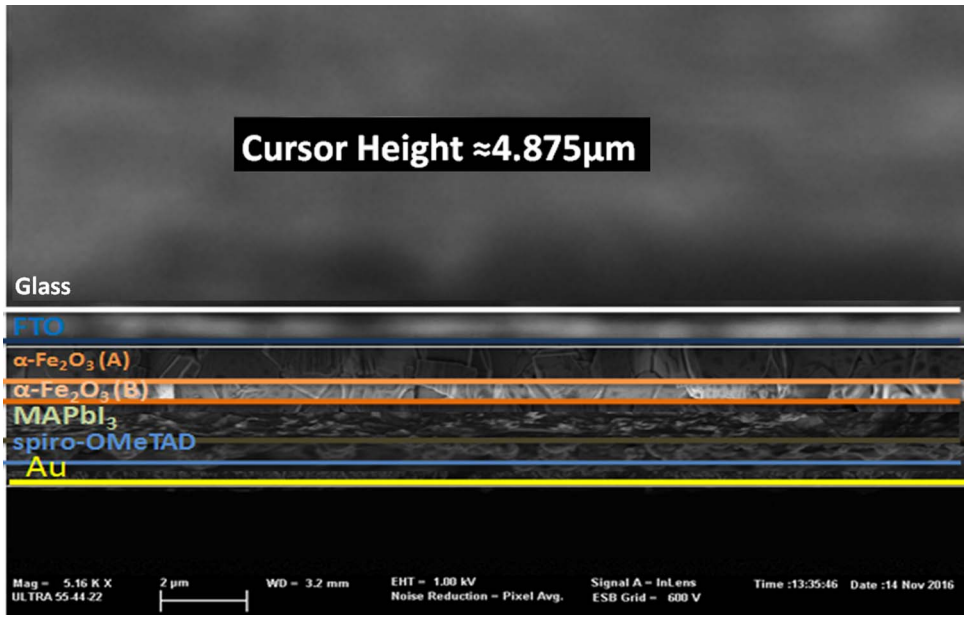

Figure 7. Vertical cross section of (a) α-Fe_2O_3(A), (b) α-Fe_2O_3/α-Fe_2O_3 thin films.

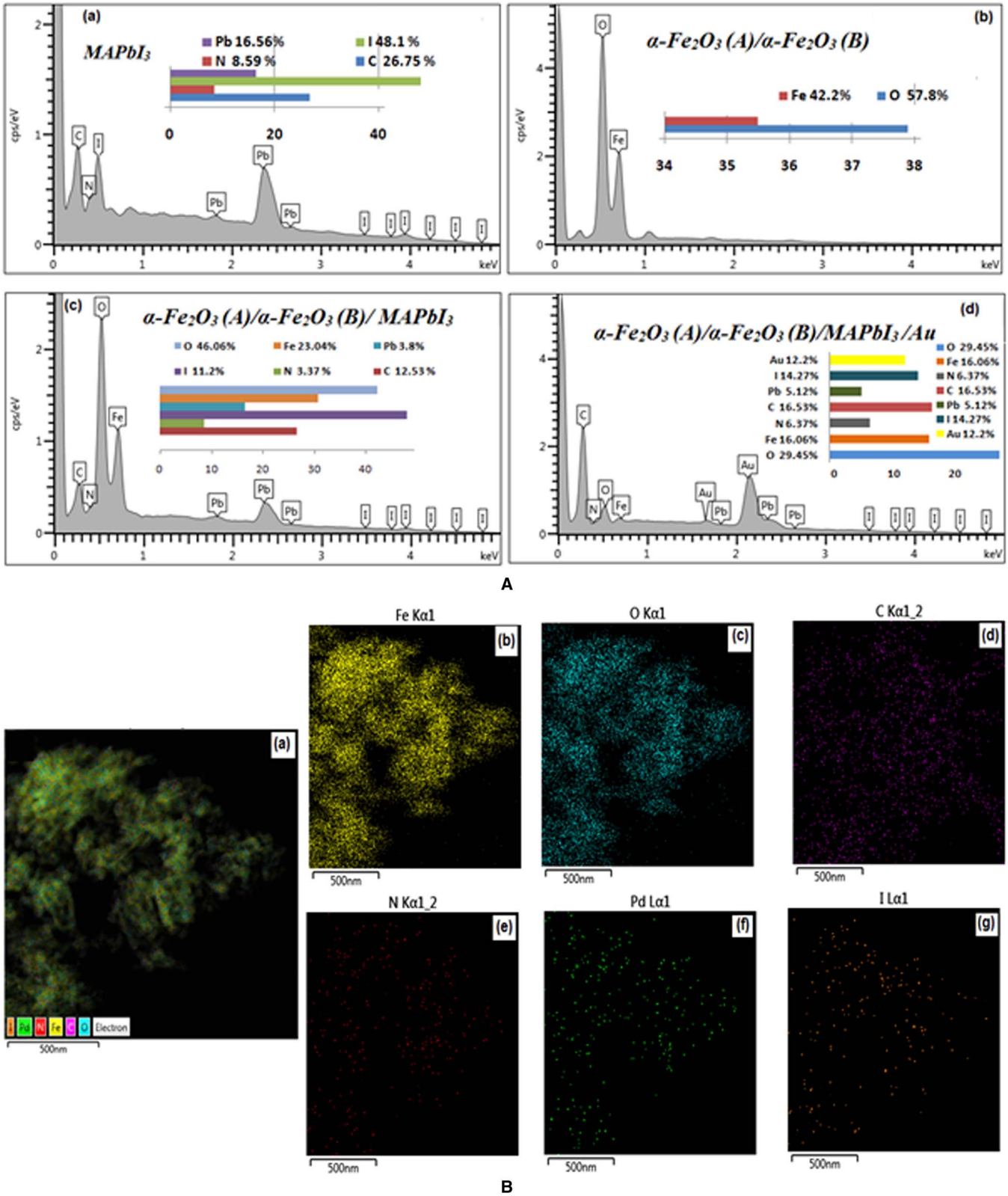

Figure 8. A: EDX spectrum for (a) $MAPbI_3$, (b) α-Fe_2O_3(A)/α-Fe_2O_3(B), (c) α-Fe_2O_3(A)/α-Fe_2O_3(B)/$MAPbI_3$, and (d) solar cell. B: EDX mapping for (a) α-Fe_2O_3(A)/α-Fe_2O_3(B)/$MAPbI_3$, (b) Fe map, (c) O map, (d) C map, (e) N map, (f) Pb map and (g) I map.

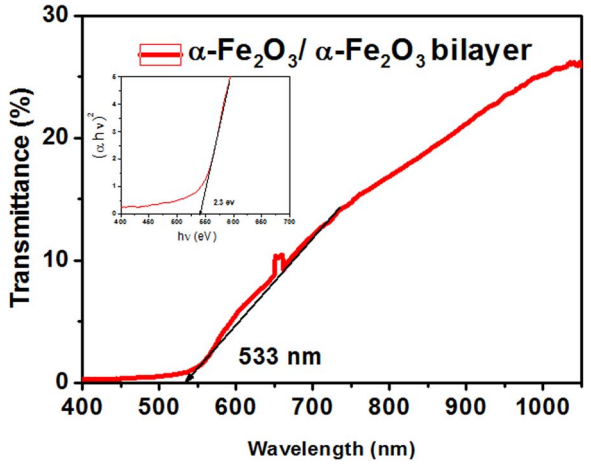

Figure 9. Transmission and Tauc plot (inset) of α-Fe_2O_3/α-Fe_2O_3 bilayer.

purged with nitrogen gas prior to experiments to prevent any possible reaction with dissolved oxygen at the counter-electrode. A potentiostat/galvanostat Autolab PGSTAT302N (Metrohm, Netherlands) with a Pt rod counter electrode and an Ag/AgCl saturated in 3 M KCl reference electrode was used. The films are illuminated with a 300 W Xenon lamp (PLSSXE300/300UV) equipped with a UV cut-off filter ($\lambda > 420$ nm). The set-up was completed with an automatic shutter and

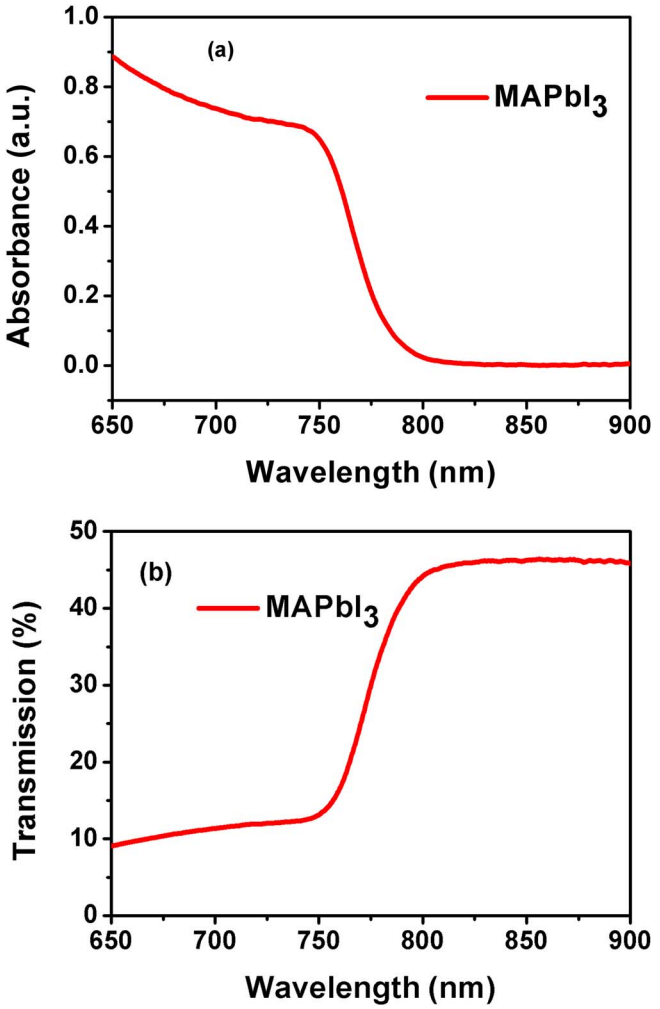

Figure 10. Absorbance (a) and Transmission (b) plots of perovskite thin films.

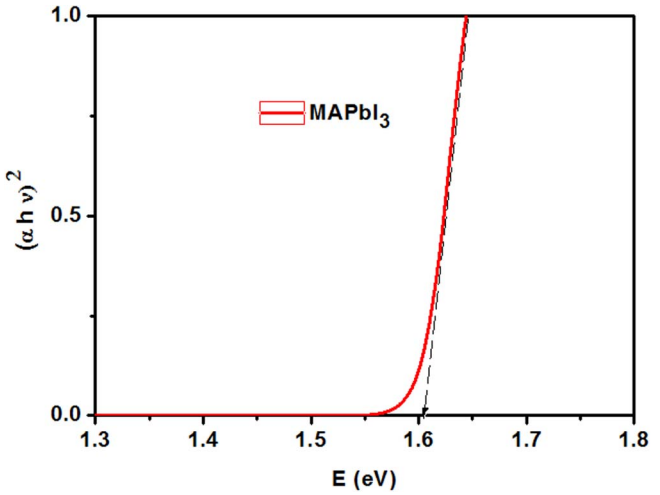

Figure 11. Taucplot of the perovskite thin films.

a filter box. The whole system was controlled by homemade software. The chronoamperometry curves of the films were also obtained at +0.1 V, both in the dark and under illumination with a light intensity of about 1 SUN (100 mW cm^{-2}) at the sample surface.

For wavelength-dependent photocurrent measurements a monochromator giving a ~20 nm bandpass from 360 to 680 nm was used together with cut off filters to eliminate secondary -harmonics. To be able to detect low photocurrent intensity, the set-up was completed with a photo-chopper and a lock-in amplifier (signal recovery). The absolute intensity of the incident excitation light was measured with a radiometer/photometer (international light). The incident photon to electron conversion efficiency (IPCE) of the samples was calculated as follows

$$\mathrm{IPCE}\,(\%) = \frac{1240 \cdot i_{photocurrent}\ \left(\mu A/cm^2\right)}{\lambda\,(\mathrm{nm}) \cdot j_{photons}\ \left(\mu W/cm^2\right)} * 100\% \qquad [6]$$

where $i_{photocurrent}$ is the photocurrent densities, λ(nm) is wavelength of the incident light and $j_{photons}$ is the measured irradiance.

The photocurrent density–voltage (J–V) characteristics of the α-Fe_2O_3(A)/α-Fe_2O_3(B)/$MAPbI_3$ solar cell were registered using a potentiostat/galvanostatAutolab PGSTAT302 under AM 1.5 G illumination (50 mW cm^{-2}) provided by a calibrated solar simulator (using a standard silicon solar cell before measurement).

The photocurrent intensities under pulsed light were measured using a chronoamperometric technique (Fig. 12). All measurements

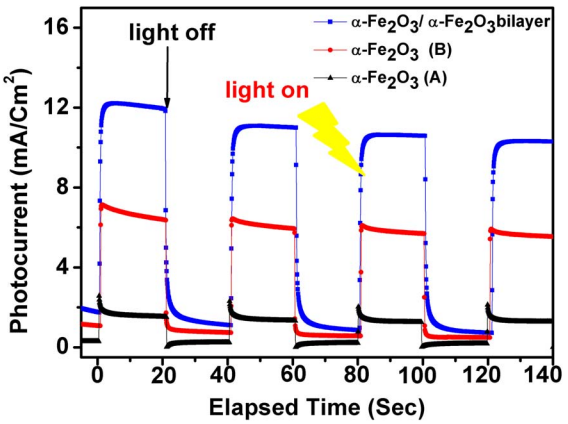

Figure 12. Photocurrent intensity for α-Fe_2O_3(A), α-Fe_2O_3(B) and α-Fe_2O_3/α-Fe_2O_3 (bilayer) electrodes under successive on/off illumination cycles, measured in 1 M NaOH electrolyte under a bias potential of +0.1 V.

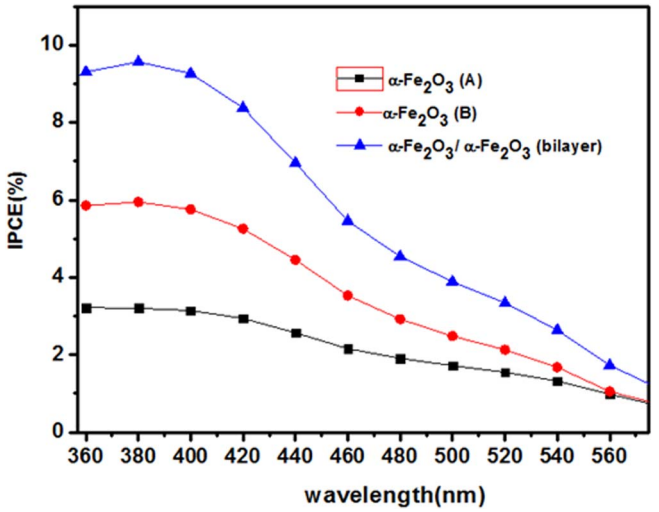

Figure 13. IPCE for α-Fe_2O_3(A), α-Fe_2O_3(B) and α-Fe_2O_3/α-Fe_2O_3(bilayer) at 0.4 V (vs. Ag/AgCl) applied potential in N_2 degassed 1 M NaOH.

were made in 1 M NaOH[41,42] electrolyte and under a potential bias of 0.1 V. Figure 12 shows the variation of the photocurrent density according to the elapsed time during on/off cycles. In the steady state, the α-Fe_2O_3(A)/FTO electrode shows a photocurrent density of about 3 mA/cm^2. However, the α-Fe_2O_3/α-Fe_2O_3/FTO bilayer shows a photocurrent density of about 12 mA/cm^2, which is 4 and 2 times greater than that of the α-Fe_2O_3(A)/FTO and α-Fe_2O_3(B)/FTO electrodes, respectively. The photocurrent density dropped in the first two cycles and then was steady and quasi-reproducible after several on–off cycles of light illumination. There was no overshoot at the beginning or at the end of the on–off cycle, meaning that the direction of the electron diffusion is free from grain boundaries, which can create traps to hinder electron movement and slow down the photocurrent generation.[43]

Figure 13 shows the action spectra for the best performing α-Fe_2O_3/α-Fe_2O_3/FTO bilayer samples compared to the α-Fe_2O_3(A), α-Fe_2O_3(B) films. Significant performance gains were observed upon all throughout the illumination wavelengths. The best performing samples were α-Fe_2O_3/ α-Fe_2O_3/FTO bilayer, which had IPCEs at 400 nm of 9%, with an applied potential of 0.4V v.s Ag/AgCl. These IPCE values were 3 times higher than the α-Fe_2O_3 (A) and α-Fe_2O_3 (B) samples for the α-Fe_2O_3/ α-Fe_2O_3/FTO bilayer samples. The high-energy photons are absorbed in the outermost layers of hematite and therefore, the photogenerated holes have a shorter diffusion path to reach the surface where they will participate in oxidative chemical reaction. A positively applied potential will increase the collection efficiency of the electrons and the IPCE increases, as shown in Fig. 13. Furthermore, the applied bias will facilitate hydrogen production at the Pt counter electrode by shifting its negative potential to overcome the approximately 0.4 V (vs. Ag/AgCl) difference between the hematite flat band potential and the hydrogen redox level.

Photocurrent density–voltage(J-V) of the solar cell device.—Figure 14 depicts the dark and under illumination (J–V) characteristics of the α -Fe_2O_3(A)/α-Fe_2O_3(B)/$MAPbI_3$/Au solar cell. From the J–V curves, we can deduce open-circuit voltage (V_{oc}) and short-circuit current density (J_{sc}). These parameters are summarized in Table II. The power conversion efficiency (η (%)) and Fill factor (FF (%)) are

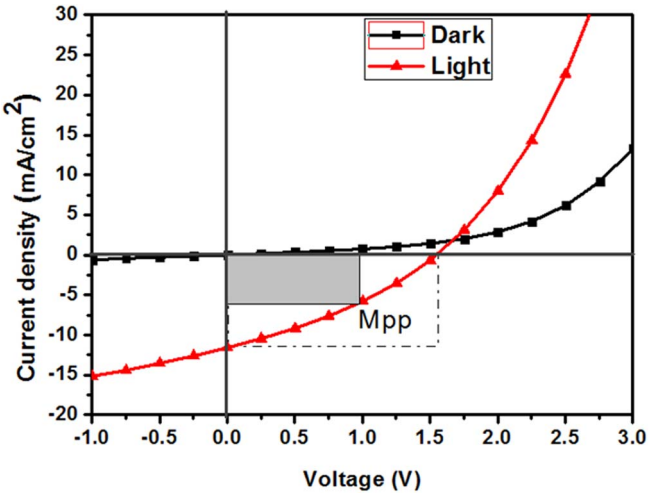

Figure 14. J-V curve solar cell devices in the dark and illumination.

calculated from

$$FF = \frac{I_{max} V_{max}}{I_{sc} V_{oc}} \quad [7]$$

$$\eta\,(\%) = \frac{I_{sc} V_{oc} FF}{P_{input}} * 100 \quad [8]$$

where, P_{input} is the power of the incident light, I_{max} and V_{max} are the current andvoltage corresponding to the maximum power point (Mpp),I_{sc} is the short-circuit current, and V_{oc} is the open-circuit potential, both can be extracted from the (J-V) curves. However, under illumination, the current magnitude of the cell increases up promptly. The current becomes stronger and increases more rapidly. This is because the conductivity of α-Fe_2O_3 is improved with the incorporation of perovskite. It should be emphasized that proper perovskite can greatly enhance the separation of electron-hole pairs. The device exhibited an encouraging solar conversion efficiency of 5.76%, with its open-circuit voltage (Voc) of 1.55 V, short-circuit current density (Jsc) of 11.27 mA/cm^2, and fill factor (FF) of 33%.

Conclusions

In this study, we measured the performance of PSCs based on α-Fe_2O_3 as the electron transport material, perovskite as the light harvester, and spiroMeOTAD as the hole transporting material. The α-Fe_2O_3 thin film was prepared by the electrodeposition and the hydrothermal processes. The perovskite layer was synthesized on the surface of the α-Fe_2O_3 thin film using the spin coating method. It was found that the growth of the α-Fe_2O_3 thin film has a clear influence on the uniform formation of the perovskite layer. Dense α-Fe_2O_3 thin films with appropriate grain sizes can ensure uniform coverage of the perovskite film, forming a better contact between the α-Fe_2O_3 film and the perovskite layer, which is able to not only facilitate the charge transport, but also to reduce charge recombination of the α-Fe_2O_3/perovskite interface. The photoelectrochemical performance of the nanostructured α-Fe_2O_3/α-Fe_2O_3 bilayer is higher than that of FTO/α-Fe_2O_3 (A) and FTO/α-Fe_2O_3 (B). Water splitting performance was evaluated and the highest photocurrent density of 12 mA/cm^2 v.s Ag/AgCl was exhibited for the α-Fe_2O_3/α-Fe_2O_3 bilayer photoelectrode, which had IPCEs at 400 nm of 9%, with an applied potential

Table II. Photovoltaic parameters of Perovskite solar cells.

Sample	V_{oc}[V]	J_{sc} [mA cm^{-2}]	V_{max} [V]	J_{max} [mA cm^{-2}]	Fill factor [%]	η [%]
Perovskite solar cells	1.55	11.27	0.99	5.7	33%	5.76%

of 0.4V v.s Ag/AgCl. The dependence of the photovoltaic properties of PSCs on α-Fe_2O_3 is carefully examined. The stability of PSCs is also studied. The best-performing device with a PCE of 5.76%, a V_{oc} of 1.55 V, a J_{sc} of 11.27 mA cm^{-2}, and a FF of 33% is demonstrated. This effect can be ascribed to the dense perovskite films that lead to full coverage of the α-Fe_2O_3 film, forming a better contact with the α-Fe_2O_3 thin film. In addition, the best performing device is also the most stable among all the devices presented. Therefore, we can state that the contact between α-Fe_2O_3 and the perovskite layer is the critical factor that determines the photovoltaic performance of PSCs. Moreover, the results indicate the great potential of α-Fe_2O_3 as an electron transport material, which provides high variety for perovskite-based solar cell design.

Acknowledgments

This work was supported by the Ministry of High Education and Scientific Research, Tunisia and Ministerio de Economía y Competitividad (ENE2013-46624-C4-4-R) and Generalitatvalenciana (Prometeus 2014/044).

References

1. Y. Ogomi, A. Morita, S. Tsukamoto, T. Saitho, N. Fujikawa, Q. Shen, T. Toyoda, K. Yoshino, S. S. Pandey, T. Ma, and S. Hayase, *J. Phys. Chem. Lett.*, **5**, 1004 (2014).
2. S. Kazim, M. K. Nazeeruddin, M. Grätzel, and S. Ahmad, *Angew. Chem., Int. Ed.*, **53**, 2812 (2014).
3. J. M. Ball, M. M. Lee, A. Hey, and H. J. Snaith, *Energy Environ. Sci.*, **6**, 1739 (2013).
4. Q. Dong, Y. Fang, Y. Shao, P. Mulligan, J. Qiu, L. Cao, and J. Huang, *Science*, **347**, 967 (2015).
5. A. Kojima, K. Teshima, Y. Shirai, and T. Miyasaka, *J. Am. Chem. Soc.*, **131**, 6050 (2009).
6. M. M. Lee, J. Teuscher, T. Miyasaka, T. N. Murakami, and H. J. Snaith, *Science*, **338**, 643 (2012).
7. M. Liu, M. B. Johnston, and H. J. Snaith, *Nature*, **501**, 395 (2013).
8. H. Zhou, Q. Chen, G. Li, S. Luo, T.-B. Song, H.-S. Duan, Z. Hong, J. You, Y. Liu, and Y. Yang, *Science*, **345**, 542 (2014).
9. W. S. Yang, J. H. Noh, N. J. Jeon, Y. C. Kim, S. Ryu, J. Seo, and I. Seok, *Science*, 2015, **348**, 1234.
10. N.-G. Park, *J. Phys. Chem. Lett.*, **4**, 2423 (2013).
11. H. T. Peng, W. H. Sun, Y. L. Li, W. B. Yan, P. R. Yu, H. P. Zhou, Z. Q. Bian, and C. H. Huang, *J. Photonics Energy*, **6**, 022002 (2016).
12. Q. S. Dong, Y. T. Shi, K. Wang, Y. Li, S. F. Wang, H. Zhang, Y. J. Xing, Y. Du, X. G. Bai, and T. L. Ma, *J. Phys. Chem. C*, **119**, 10212 (2015).
13. Q. Wu, W. Zhou, and Q. Liu, *ACS Appl. Mater. Interfaces*, **8**, 34464 (2016).
14. H. J. Snaith, *J. Phys. Chem. Lett.*, **4**, 3623 (2013).
15. J. H. Noh, H. I. Sang, and H. H. Jin, *Nano Lett.*, **13**, 1764 (2013).
16. A. Dymshits, L. Iagher, and L. Etgar, *Materials*, **9**, 60 (2016).
17. J. T. W. Wang, J. M. Ball, and E. M. Barea, *Nano lett*, **14**,24 (2013).
18. J. M. Ball, M. M. Lee, A. Hey, and H. J. Snaith, *Energy Environ. Sci.*, **6**, 1739 (2013).
19. M. J. Carnie, C. Charbonneau, M. L. Davies, J. Troughton, T. M. Watson, K. Wojciechowski, H. Snaith, and D. A. Worsley, *Chem. Commun.*, **49**, 7893 (2013).
20. Q. Zhang, C. S. Dandeneau, X. Zhou, and C. Cao, *Adv. Mater.*, **21**, 4087 (2009).
21. L. Wang, W. F. Fu, Z. W. Gu, C. C. Fan, X. Yang, H. Y. Li, and H. Z. Chen, *J. Mater. Chem. C*, **2**, 9087 (2014).
22. D.-Y. Son, J.-H. Im, H.-S. Kim, and N.-G. Park, *J. Phys. Chem. C*, **118**, 16567 (2014).
23. M. H. Kumar, N. Yantara, and S. Dharani, *Chem. Commun*, **49**, 11089 (2013).
24. H. Wang, Z. Xu, H. Yi, H. Wei, Z. Guo, and X. Wang, *Nano Energy*, **7**, 86 (2014).
25. H. Niu, S. Zhang, Q. Ma, S. Qin, L. Wan, J. Xu, and S. Miao, *RSC Adv.*, **3**, 17228 (2013).
26. D. H. Song, M. H. Jang, M. H. Lee, J. H. Heo, J. K. Park, S. J. Sung, D. H. Kim, K. H. Hong, and S. H. Im, "A discussion on the origin and solutions of hysteresis in perovskite hybrid solar cells." *J. Phys. D: Appl. Phys.*, **49**, 473001 (11pp) (2016).
27. H.-S. Kim, C. R. Lee, J. H. Im, K. B. Lee, T. Moehl, A. Marchioro, S. J. Moon, R. H. Baker, J. H. Yum, J. E. Moser, M. Grätzel, and N. G. Park, *Sci. Rep.*, **2**, 591 (2012).
28. J. Y. Jeng, Y. F. Chiang, M. H. Lee, S. R. Peng, T. F. Guo, P. Chen, and T. C. Wen, *Adv. Mater.*, **25**, 3727 (2013).
29. M. H. Kumar, N. Yantara, S. Dharani, M. Graetzel, S. Mhaisalk, P. P. Boix, and N. Mathews, *Chem. Commun.*, **49**, 11089 (2013).
30. H. S. Kim, J. W. Lee, N. Yantar, P. P. Boi, S. A. Kulkarni, S. Mhaisalkar, M. Gratzel, and N.-G. Park, *Nano Lett*, **13**, 2412 (2013).
31. D. Bi, S. J. Moon, L. Häggman, G. Boschloo, L. Yang, E. M. J. Johansson, M. K. Nazeeruddin, M. Grätzel, and A. Hagfeldt, *RSC Adv*, **3**, 18762 (2013).
32. K. C. Wang, J. Y. Jeng, P. S. Shen, Y. C. Chang, E. W. G. Diau, C. H. Tsai, T. Y. Chao, H. C. Hsu, P. Y. Lin, P. Chen, and T.-F. Guo T. C. Wen, *Sci. Rep.*, **4**, 4756 (2014).
33. J. A. Christians, R. C. M. Fung, and P. V. Kamat, *J. Am. Chem. Soc.*, **136**, 758 (2014).
34. L. Vayssieres, N. Beermann, S. E. Lindquist, and A. Hagfeldt, "Controlled aqueous chemical growth of oriented three-dimensional crystalline nanorod arrays: application to iron(III) oxides," *Chem. Mater.*, **13**, 233 (2001).
35. A. Annamalai, P. S. Shinde, A. Subramanian, J. Y. Kim, J. H. Kim, S. H. Choi, J. S. Lee, and J. S. Jang, "Bifunctional TiO_2 underlayer for α-Fe_2O_3nanorod based photoelectrochemical cells: enhanced interface and Ti^{4+} doping," *J. Mater. Chem. A*, **3**, 5007 (2015).
36. M. Li, Z. Zhang, F. Lyu, X. He, Z. Liang, M. S. Balogun, X. Lu, P. P. Fang, and Y. Tong, "Facile Hydrothermal Synthesis of Three Dimensional Hematite Nanostructures with Enhanced Water Splitting Performance," *Electrochimica Acta*, **186**, 95 (2015).
37. J. Cui, H. Yuan, J. Li, X. Xu, Y. Shen, H Lin, and M. Wang, "Recent progress in efficient hybrid leadhalide perovskite solar cells," *Sci. Technol. Adv. Mater.*, **16**, 036004 (14pp) (2015).
38. Y. V. Kaneti, Q. M. D. Zakaria, Z. Zhang, C. Chen, J Yue, M. Liu, X. Jiang, and A. Yua, "Solvothermal synthesis of ZnO-decorated a-Fe_2O_3 nanorods with highly enhanced gas-sensing performance toward n-butanol," *J. Mater. Chem. A*, **2**, 13283 (2014).
39. M. R. Belkhedkar and A. U. Ubale, *International Journal of Materials and chemistry*, **4**, 109 (2014).
40. R. J. Elliott, *Phys. Rev.*, **108**, 1384 (1957).
41. S. S. Shinde, R. A. Bansode, C. H. Bhosale, and K. Y. Rajpure, *Journal of Semiconductors*, **32**, 013001 (2011).
42. F. L. Souza, K. P. Lopes, P. A. P. Nascente, and E. R. Leite, *Solar Energy Materials & SolarCells*, **93**, 362 (2009).
43. M. Sookhakian, Y. M. Amin, S. Baradaran, M. T. Tajabadi, A. MoradiGolsheikh, and W. J. Basirun, *Thin Solid Films*, 204 (2014).

Journal of Solid State Electrochemistry
https://doi.org/10.1007/s10008-018-3946-7

ORIGINAL PAPER

Ultrathin-layer α-Fe_2O_3 deposited under hematite for solar water splitting

Feriel Bouhjar[1,2,3] · Brahim Bessaïs[1] · Bernabé Marí[2]

Received: 28 December 2017 / Revised: 9 March 2018 / Accepted: 12 March 2018

Abstract

This work proposes a new strategy to prepare a hematite (α-Fe_2O_3) bilayer photoanode by hydrothermally depositing α-Fe_2O_3 (B) on the α-Fe_2O_3 (A) films prepared by electrochemical deposition. Compact smooth surfaced α-Fe_2O_3 (A) films were electrochemically deposited on FTO (SnO_2:F) substrates from an aqueous bath. The α-Fe_2O_3 (A), α-Fe_2O_3 (B), and α-Fe_2O_3/α-Fe_2O_3 bilayer films' characteristics were defined by X-ray diffraction (XRD) measurements, field emission scanning electron microscopy (FESEM), and energy-dispersive X-ray (EDX) spectroscopy. Pure crystalline α-Fe_2O_3 (B) films with a typical anisotropic-like nanoparticle formation, which exhibited nanostructured rods covering the substrate and formed the characteristic mesoporous film morphology, were hydrothermally deposited on α-Fe_2O_3 (A) films prepared by electrochemical depositing in a solution bath at 25 °C and a potential of − 0.15 V. The photocurrent measurements exhibited increased intrinsic surface states (or defects) at the α-Fe_2O_3 (A)/α-Fe_2O_3 (B) interface. The photoelectrochemical performance of the α-Fe_2O_3 (A)/α-Fe_2O_3 (B) structure was examined by chronoamperometry, which found that the α-Fe_2O_3 (A)/α-Fe_2O_3 (B) structure exhibited greater photoelectrochemical activity than the α-Fe_2O_3 (A) and α-Fe_2O_3 (B) thin films. The highest photocurrent density was obtained for the bilayer α-Fe_2O_3 (A)/α-Fe_2O_3 (B) films in 1 M NaOH electrolyte. This great photoactivity was ascribed to the highly active surface area, and to the externally applied bias that favored the transfer and separation of photogenerated charge carriers in α-Fe_2O_3 (A)/α-Fe_2O_3 (B). The improved photocurrent density was attributed to an appropriate band edge alignment of semiconductors and to enhanced light absorption by both semiconductors. The best performing samples were α-Fe_2O_3 (A)/α-Fe_2O_3 (B), which reached the maximum incident photon conversion efficiencies (IPCE) of 400 nm at the potential of 0.1 V. In this case, the IPCE values were 3-fold higher than those of the α-Fe_2O_3 (A) and α-Fe_2O_3 (B) films.

Keywords α-Fe_2O_3 · Interface · Electrochemical deposition · Hydrothermal deposition · XRD analysis · FESEM analysis · Optical properties · Photoelectrochemical properties

Introduction

Recently, a great deal of attention has been paid to heterogeneous deposition on high-pressure structures such as Fe_2O_3, GaN, TiO_2, and ZnO to form a heterojunction. These semiconductor substrates are essential in many electrical, photoelectrical, and catalytic applications and generally require interface area enlargement. In thermodynamic terms, the water-splitting reaction is an uphill process that requires a minimum energy of 1.23 eV, while the Gibbs free energy change is $\Delta G^\circ = 237.2$ kJ mol^{-1} or 2.46 eV per H_2O molecule [1].

Nevertheless, it also requires a high over-potential because of non-idealities in real operations and water-splitting reaction complexity. The water-splitting process comprises two necessary steps because it is not quite as straightforward as ripping apart the three atoms in H_2O. To achieve a full reaction, the participation of two H_2O molecules is required, which are separated through oxidation and reduction in accordance with the following reduction and oxidation half-reactions [2].

✉ Feriel Bouhjar
feriel88bouhjar@gmail.com

[1] Photovoltaic Laboratory, Research and Technology Centre of Energy, Borj-Cedria Science and Technology Park, BP 95, 2050 Hammam-Lif, Tunisia

[2] Institut de Disseny i Fabricació (IDF) - Departament de Física Aplicada, Universitat Politècnica de València, Camí de Vera s/n, 46022 Valencia, Spain

[3] University of Tunis, Tunis, Tunisia

Published online: 22 March 2018

Reduction reaction:

$$2H^+ + 2e^- \rightarrow H_2 (E^\circ_{red} = 0.00\ \text{V/RHE}) \quad (1)$$

Oxidation reaction:

$$2H_2O + 4h^+ \rightarrow O_2 + 4H^+ (E^\circ_{ox} = -1.23\ \text{V/RHE}) \quad (2)$$

Overall reaction:

$$2H_2O \rightarrow 2H_2 + O_2 (\Delta E = -1\ .23\ \text{V/RHE}) \quad (3)$$

where RHE indicates a reversible hydrogen electrode (RHE).

Since four-electron water oxidation is the rate-limiting step in the overall water-splitting reaction, the development of high-efficiency photoanodes for O_2 evolution capable of overcoming the high over-potential required to perform this reaction is a major obstacle that must be overcome [3].

One of the most promising photoanode candidates is hematite (α-Fe_2O_3) because it has a narrow bandgap of ~2.1–2.2 eV and allows ~16.0% of theoretical solar-to-hydrogen (STH) efficiency for photoelectrochemical (PEC) water splitting [4–6]. Moreover, α-Fe_2O_3 has many further advantages over other narrow bandgap semiconductors, of which some have excellent stability in alkaline solutions, earth abundance, and non-toxicity [3–7]. Moreover, α-Fe_2O_3 has extremely poor electrical conductivity with a hole diffusion length of 2–4 nm [8] and suffers from a high-charge carrier's recombination. Therefore, hematite exhibits very poor PEC performance. This makes the future success of α-Fe_2O_3 photoanodes in PEC water splitting somewhat questionable since α-Fe_2O_3 itself can hardly achieve a good enough PEC efficiency for its potential practical use and necessitates modification to achieve improved PEC performance.

The following overview is that of the synthesis, modification, and characterization of the nanostructured α-Fe_2O_3 thin film, which is provided by emphasizing charge carrier dynamics and PEC properties [9]. Recently, a growing number of studies have focused on the α-Fe_2O_3 heterostructures that incorporate a second material to improve charge separation, charge collection, and surface catalysis. Notably, much greater PEC activities have been achieved with such α-Fe_2O_3 heterostructure-based photoanodes than with their single-component counterparts, and α-Fe_2O_3 (B) is promising as a hole-conducting material thanks to its transparency within the visible light spectrum range, considerable hole conductivity [10], and chemical stability [11]. Grätzel et al. developed a new way to enhance the water-splitting efficiency of hematite by introducing an ultrathin underlayer at the interface of SnO: F (FTO) substrate and the hematite thin film [12, 13]. This mechanism consisted in blocking the electrons from transferring back from the FTO to hematite films, and a charger combination at the FTO/hematite interface with an ultrathin underlayer of wide bandgap or insulating materials, which is a serious issue for the nanostructured photoanodes with only a weak interfacial electric field [13]. The underlayer needs to be thin enough (e.g., 10–50 nm thick) to allow electron tunneling from hematite to FTO, and to ensure photocurrent generation. Various materials prepared by the ALD method, such as TiO_2, have been investigated for their properties to be used for the underlayer: TiO_2, for example, significantly shifts the photocurrent onset to 1.1 or 1.3 V vs. RHE and increases the photocurrent by one order of magnitude [12, 13]. Table 1 shows a review of the achievements made in some typical α-Fe_2O_3-based semiconducting heterojunctions found in the literature. The data in Table 1 include the kind of heterostructures, the fabrication method, the suggested charge transfer for electrons and holes, and the main photoelectrical properties of these heterostructures. These data are compared with the electrochemically and hydrothermal-deposited α-Fe_2O_3/α-Fe_2O_3 heterojunction described herein.

In this study, a new bilayered nanostructure was synthesized by electrochemical deposition (A), which consisted in a top layer of nanorods produced by hydrothermal deposition (B), and a layer of nanoparticles underneath it (see Fig. 1). This new double-layered nanostructure combines the nanostructure's better photoelectrochemical properties. α-Fe_2O_3 (B) films were deposited on a smooth α-Fe_2O_3 surface (A). The characterization of these films was carried out by FESEM and X-ray diffraction (XRD) techniques. The nanostructure's morphological and electrochemical properties correlated with the results of the water-splitting tests to evaluate the performance of this new nanostructure as a photocatalyst for hydrogen production. The results of this study suggest improved performance for the iron oxide nanostructures used as photocatalyst in processes such as water splitting.

Experimental

Underlayer fabrication (α-Fe_2O_3 (A))

The experimental setup used to prepare α-Fe_2O_3 thin films consisted of a computer-controlled potentiostat/galvanostat and a classical three-electrode electrochemical cell. The electrochemical cell was filled with a solution that contained 5 mM $FeCl_3$ + 5 mM KF + 1 M H_2O_2 + 0.1 M KCl in deionized water. The working electrode was an FTO-coated glass with a sheet resistance of 10 Ω sq; substrates were cleaned in an ultrasonic acetone bath for 10 min before being rinsed in distilled water and dried. Ag/AgCl electrodes and Pt were used as a reference electrode and a counter electrode, respectively. Thin films were deposited by cathodic electrodeposition. The deposition potential was fixed at − 0.15 V, and the deposited charge was 1.2 C for all the samples, which gives a

Table 1 Hematite-based heterostructures including fabrication methods, suggested charge transfer, and photoelectrochemical characteristics

Heterostructure	Fabrication method	Suggested charge transfer		Photoelectrochemistry	Ref.
		Electron	Hole		
$WO_3/\alpha\text{-}Fe_2O_3$	Sol–gel	$WO_3 \rightarrow \alpha\text{-}Fe_2O_3$	None	Photocurrent 22 μA cm^{-2} at 0.8 V vs. Ag/AgCl (500-W Xe lamp); electrolyte 0.2 M Na_2SO_4 (pH = 7.5)	[14]
$WO_3/\alpha\text{-}Fe_2O_3$	Spin coating and spray pyrolysis	None	None	Photocurrent 22 mA cm^{-2} at 0.8 V vs. Ag/AgCl; electrolyte 0.05 M PBS (pH = 7)	[15]
$ZnO/\alpha\text{-}Fe_2O_3$	Hydrothermal and spin coating	$\alpha\text{-}Fe_2O_3 \rightarrow ZnO$	$ZnO \rightarrow \alpha\text{-}Fe_2O_3$	Photocurrent 1.6 mA cm^{-2} at 0.6 V vs. Ag/AgCl; electrolyte 1 M NaOH	[16]
$\alpha\text{-}Fe_2O_3$: Ti/Cu_2O	Spray pyrolysis	$Cu_2O \rightarrow \alpha\text{-}Fe_2O_3$: Ti	$\alpha\text{-}Fe_2O_3$: $Ti \rightarrow Cu_2O$	Photocurrent 2.60 mA cm^{-2} at 0.95 V vs. SCE (Xe lamp, 150 mW cm^{-2}); electrolyte 0.1 M NaOH	[17]
$\alpha\text{-}Fe_2O_3/CuSCN$	Electrodeposition	$CuSCN \rightarrow \alpha\text{-}Fe_2O_3$	$\alpha\text{-}Fe_2O_3 \rightarrow CuSCN$	Photocurrent 2.90 mA cm^{-2} at 0.59 V vs. Ag/AgCl (Xe lamp 150 W); electrolyte 0.1 M NaOH (pH = 13.9)	[18]
$\alpha\text{-}Fe_2O_3/\alpha\text{-}Fe_2O_3$	Hydrothermal and electrodeposition	$\alpha\text{-}Fe_2O_3(A) \rightarrow \alpha\text{-}Fe_2O_3(B)$	$\alpha\text{-}Fe_2O_3(B) \rightarrow \alpha\text{-}Fe_2O_3(A)$	Photocurrent 3 mA cm^{-2} at 0.1 V vs. Ag/AgCl (Xe lamp 100 W); electrolyte 0.1 M NaOH (pH = 13.9)	Our work

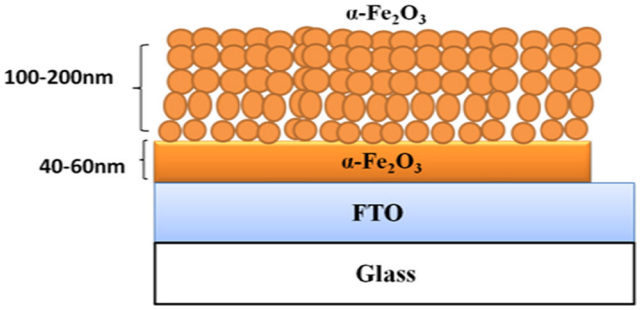

Fig. 1 Schematic cross-sectional view of the FTO glass, compact α-Fe_2O_3, and α-Fe_2O_3 under layer

thickness of about 40–60 nm for the electrodeposited Fe_2O_3 films. The solution temperature was set at 298 K (Fig. 2). After deposition, films were rinsed with distilled water. To obtain the desired α-Fe_2O_3 phase, the deposited films were annealed in a furnace in air at 650 °C for 2 h.

Overlayer fabrication (α-Fe_2O_3 (B))

Nanostructured α-Fe_2O_3 (B) thin films were obtained after annealing hydrothermally deposited iron films on a smooth α-Fe_2O_3 surface (A). The bath consisted of an aqueous solution that with a 30-mL capacity, filled with 20 mL aqueous solution with 0.15 M of $FeCl_3 \cdot 6H_2O$ and 1 M $NaNO_3$, pH 1.5 (adjusted by HCl), which led to the deposition of iron hydroxides (FeOOH) [19]. Iron films were deposited on the α-Fe_2O_3 (A) substrate from an iron precursor solution ($FeCl_3 \cdot 6H_2O$). A piece of FTO/α-Fe_2O_3 (A) was placed inside the autoclave to be then heated at 100 °C for 6 h in an oven and could cool down to ambient temperature. Under hydrothermal conditions, this solution enables the interaction of Fe^{3+} ions with OH^- by producing iron oxide nuclei, as described in Eq. (4):

$$Fe^{3+}{}_{(aq)} + 3OH^-{}_{(aq)} \rightarrow \beta\text{-}FeOOH_{(s)} + H_2O \quad (4)$$

Finally, a uniform layer of β-FeOOH on the FTO substrate was obtained. The akageneite-coated substrate was then washed with deionized water and was subsequently sintered in air at 550 °C for 4 h in a furnace. After the annealing process, β-FeOOH was converted into α-Fe_2O_3. The phase transition went from β-FeOOH (yellow) to α-Fe_2O_3 (red–brown, inset in Fig. 3). The chemical reaction that was expected to occur during phase transition due to thermal treatment can be represented by Eq. (5):

$$2\beta\text{-}FeOOH_{(s)} \rightarrow Fe_2O_{3(s)} + H_2O_{(L\ or\ G)} \quad (5)$$

Materials characterization

The crystal structure of the α-Fe_2O_3 (A), α-Fe_2O_3 (B), and α-Fe_2O_3(A)/α-Fe_2O_3 (B) thin films was investigated by X-ray

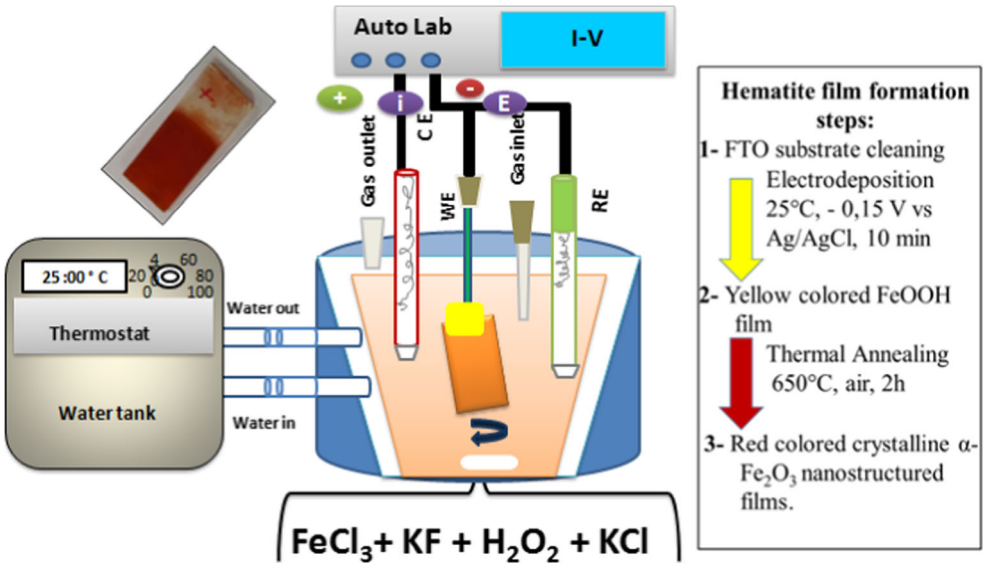

Fig. 2 Schematic representations of a typical three-electrode electrochemical cell and an image of the α-Fe_2O_3 film electrodeposited on the FTO substrate

diffraction (XRD) in a Rigaku Ultima IV diffractometer in the Bragg-Bentano configuration with CuKα radiation (λ = 1.54060 Å).

The microstructural and elemental analyses were characterized by a Zeiss ULTRA 55 model scanning electron microscope (SEM) with an attached energy-dispersive spectroscopy (EDS) system.

To determine bandgap energy, optical absorption was determined by recording the transmission spectra with a UV-Visible spectrophotometer (Ocean Optics HR4000) coupled to an integrating sphere to collect both specular and diffuse transmittances.

Photoelectrochemical and electrochemical analyses

PEC measurements were taken in a quartz cell to facilitate light reaching the photoelectrode surface. The light-exposed working electrode surface was 0.25 cm^2. The electrolyte used in all PEC measurements was 1.0 M NaOH (pH 13.6). The electrolyte was purged with gas nitrogen before the experiments to prevent any possible reaction with dissolved oxygen at the counter electrode. A potentiostat/galvanostat Auto lab PGSTAT302N (Metrohm, Netherlands) with an Ag/AgCl saturated in a 3 M KCl reference electrode and a Pt rod counter electrode was used. Films were illuminated by a 300-W Xenon lamp (PLSSXE300/300UV). The setup was completed with an automatic shutter and a filter box. The whole system was controlled by a homemade software. The chronoamperometry curves of thin films were obtained at + 0.1 V in the dark and under illumination with an intensity of about 1 SUN (100 mW cm^{-2}) on the sample surface [20, 21]. For the wavelength-dependent photocurrent measurements, a monochromator giving a ~ 20-nm bandpass from 360 to 680 nm was used together with cutoff filters to remove secondary harmonics. The incident photon to electron conversion efficiency (IPCE) of samples was calculated as follows:

$$\mathrm{IPCE}(\%) = \frac{1240 \cdot i_{\mathrm{photocurrent}}(\mu\mathrm{A/cm^2})}{\lambda(\mathrm{nm}) \cdot j_{\mathrm{photons}}(\mu\mathrm{W/cm^2})} \cdot 100\% \qquad (6)$$

where $i_{\mathrm{photocurrent}}$ is the photocurrent densities, λ(nm) is the incident light wavelength, and j_{photons} is the measured irradiance.

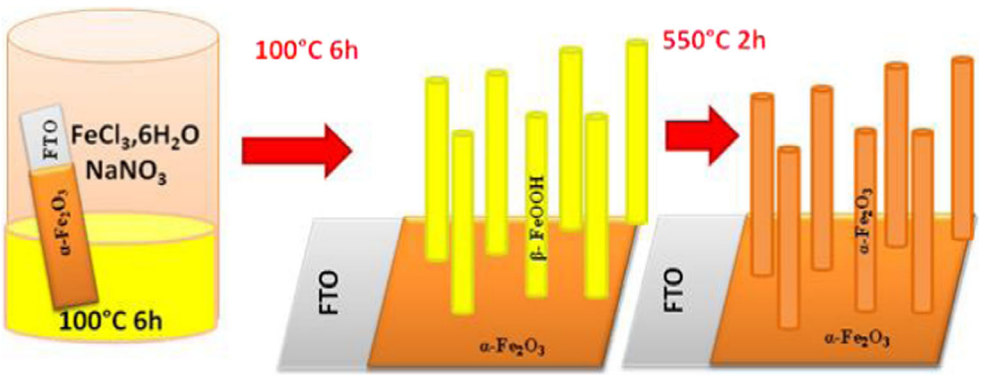

Fig. 3 Schematic representations of the synthesis methods adopted for α-Fe_2O_3 hematite photoanode film electrodeposited on α-Fe_2O_3 (A) substrate

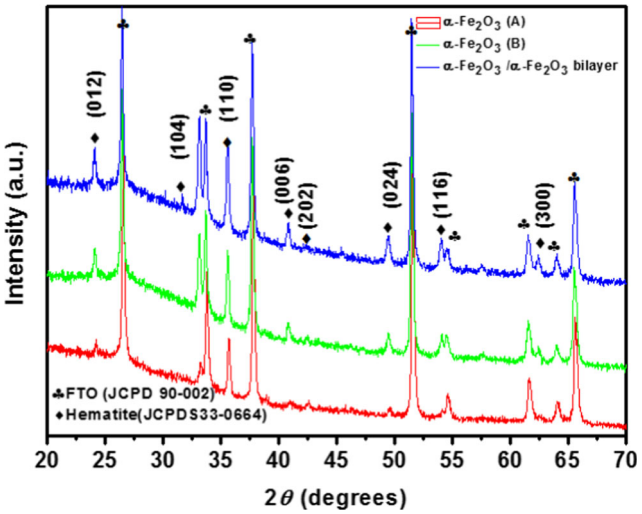

Fig. 4 X-ray diffractogram of the α-Fe_2O_3 (A), α-Fe_2O_3 (B), and α-Fe_2O_3/α-Fe_2O_3 bilayers

Electrochemical impedance spectra (EIS) were recorded at a DC potential of 0.1 V vs. Ag/AgCl in 1.0 M NaOH solution and an AC potential frequency range of 100,000–0.1 Hz with an amplitude of 10 mV. The Z View software was used for fitting the experimental EIS data to the equivalent circuit model.

Results and discussion

Structural characterization

Figure 4 shows the XRD patterns of the α-Fe_2O_3 (A), α-Fe_2O_3 (B), and α-Fe_2O_3/α-Fe_2O_3 bilayers deposited on the FTO substrates. The diffractograms of the α-Fe_2O_3/α-Fe_2O_3 bilayer and the FTO substrates are also shown.

The XRD peaks of the α-Fe_2O_3 films were observed at $2\theta = 24.1°$, 33.1°, 35.6°, 40.9°, 49.4°, 54.0°, and 64°, which respectively corresponded to the (012), (104), (110), (113), (024), (116), and (300) planes of the hematite phase. The dominant peaks corresponded to the (104) and (110) planes. The diffraction peaks of the trigonal structure of α-Fe_2O_3 well matched reference pattern JCPDS card file no. 33-0664, which corresponded to space group R3c (167) with lattice parameters $a = b = 5.03$ nm and $c = 13.74$ nm. No other phases of α-Fe_2O_3 were observed in the pattern.

Morphological characterization

Figure 5a–c displays the FESEM images of the α-Fe_2O_3 (A), α-Fe_2O_3 (B), and α-Fe_2O_3/α-Fe_2O_3 bilayer films deposited on the FTO substrates, respectively. Figure 4a shows the vertically grown segregated nanostructured islands made up of small α-Fe_2O_3 (A) nanoparticles, with some dispersion in grain sizes observed.

Figure 5b shows a typical morphology of hematite nanorods (NRs) (α-Fe_2O_3 (B)) grown on the FTO substrates by the hydrothermal process. Top view images show clearly that hematite NRs are uniformly distributed on the substrate and oriented upward with respect to the substrate. While others are detached from the substrate, being free standing and horizontal. The as-prepared hematite NRs look like rice grains (Fig. 5b), enabling the identification of a typical nanoparticle formation.

Figure 6 shows cross-sectional FESEM images of the α-Fe_2O_3 (A), α-Fe_2O_3 (B), and α-Fe_2O_3/α-Fe_2O_3 bilayer thin films deposited on α-Fe_2O_3 (B). The α-Fe_2O_3 (A) film (Fig. 6a) was found to be ultrathin (55 nm thick), while the α-Fe_2O_3 (B) film is ~ 196 nm thick. The α-Fe_2O_3/α-Fe_2O_3 bilayer was found to be about ~ 251 nm thick (Fig. 6c).

EDX analyses

The elemental analysis of the deposited α-Fe_2O_3/α-Fe_2O_3 bilayer was achieved by the energy-dispersive X-ray (EDX) analysis. The EDX spectra of the α-Fe_2O_3/α-Fe_2O_3 bilayer thin films are shown in Fig. 7. The line observed at 0.72 keV corresponds to the L line of Fe, and the oxygen K line peaks at 0.525 keV. The calculated atomic Fe/O ratio approximately equals 2:3, which well agrees with the stoichiometric composition of α-Fe_2O_3. The percentages of each element calculated from EDX are shown in the inset of Fig. 7.

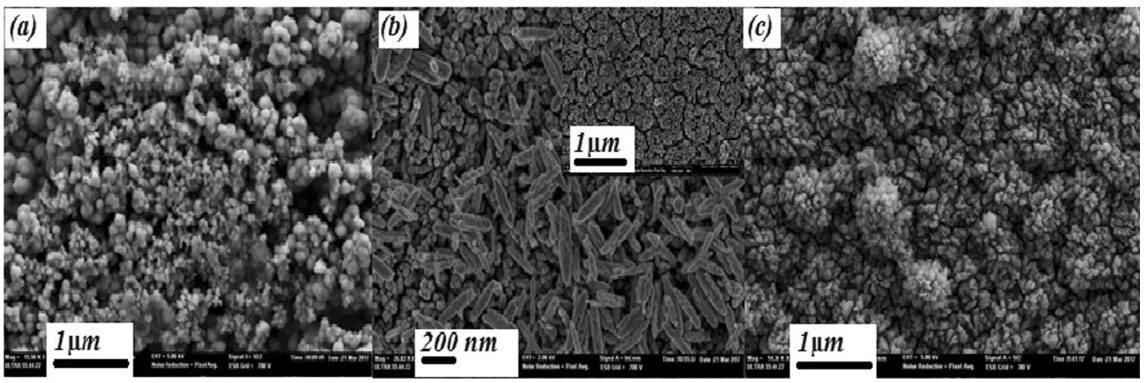

Fig. 5 FESEM images of α-Fe_2O_3 (A) (**a**), α-Fe_2O_3 (B) (**b**), and α-Fe_2O_3 (A)/α-Fe_2O_3 (B) (**c**)

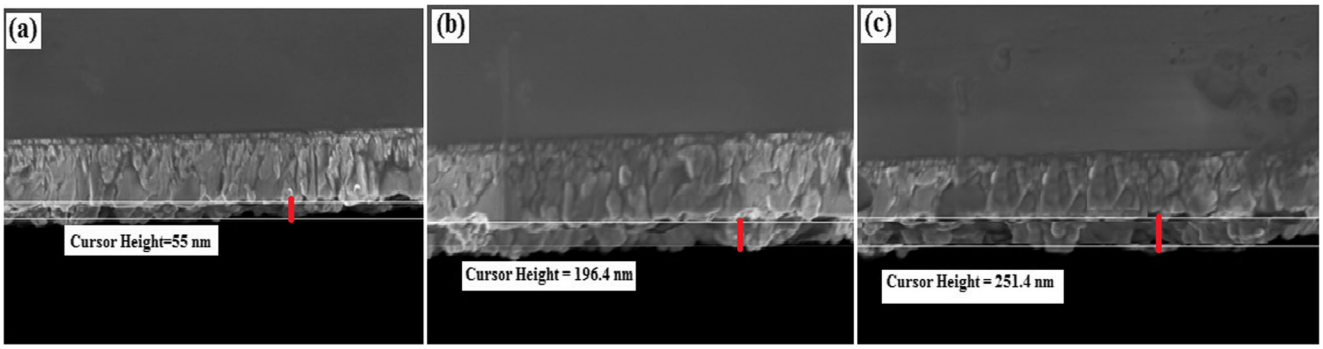

Fig. 6 Cross-sectional FESEM images of α-Fe_2O_3 (A) (**a**), α-Fe_2O_3 (A) (**b**), and α-Fe_2O_3/α-Fe_2O_3 (**c**) bilayer thin films

Optical characterization of the Fe_2O_3 thin films

Figure 8a shows the transmission spectra of the α-Fe_2O_3/α-Fe_2O_3 bilayer thin film, from which the optical bandgap energies can be determined. The transmittance spectrum of the α-Fe_2O_3/α-Fe_2O_3 bilayer has an optical transmission value above 30% within the visible range. A significant increase in absorption below 533 nm can be assigned to the intrinsic bandgap absorption of the α-Fe_2O_3/α-Fe_2O_3 bilayer. To calculate the optical bandgap energy *Eg* of thin films, the absorption coefficient can be estimated as follows [22]:

$$\alpha = \frac{1}{d}\ln\left(\frac{1}{T}\right) \tag{7}$$

According to the solid band theory, the relation between absorption coefficient α and the energy of incident light $h\nu$ is given by [23]:

$$\alpha h\nu = A(h\nu - Eg)^n \tag{8}$$

where α is the absorption coefficient, A is a constant, h is the Planck's constant, ν is the photon frequency, Eg is the optical bandgap, and n equals 2 for the direct transition, while it equals 1/2 for the indirect transition. Figure 8b depicts the Tauc plot ($(\alpha h\nu)^2$ vs. $h\nu$) of films α-Fe_2O_3 (A) and α-Fe_2O_3 (B). According to the Tauc plot, we can make out a direct bandgap energy of about 2.3 eV for α-Fe_2O_3 (A) and 2.1 eV for α-Fe_2O_3 (B), which is smaller than that of bulk α-Fe_2O_3 (2.3 eV). (*Eg* (A)-*Eg* (B) = ε; see Fig. 11).

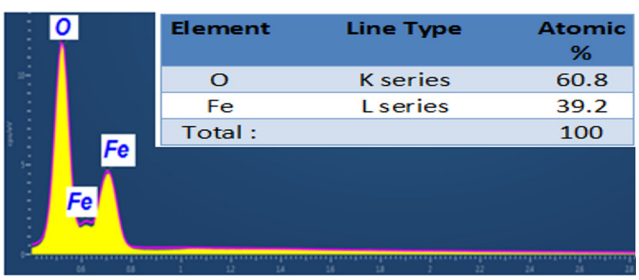

Fig. 7 EDX spectrum for α-Fe_2O_3/α-Fe_2O_3 bilayer

Photoelectrochemical properties of the α-Fe_2O_3 electrode

The photocurrent intensities under pulsed light were measured by a chronoamperometry technique (Fig. 9). All the measurements were taken in the 1 M NaOH [24, 25] electrolyte and with a potential bias of 0.1 V. Figure 9 shows the variation in the photocurrent density vs. the elapsed time during the switch on/off light for both. In the stable state, the α-Fe_2O_3 (A)/FTO electrode shows a photocurrent density of about 0.5 mA/cm^2. However, the α-Fe_2O_3/α-Fe_2O_3/FTO bilayer displays a photocurrent density of approximately 3 mA/cm^2, which is 6-fold bigger than that of the α-Fe_2O_3/FTO (A), and 3-fold that of the α-Fe_2O_3/FTO (B) electrodes. The photocurrent density dropped in the first two cycles to then become steady and quasi-reproducible after several on–off light illumination cycles, with no overshoot at the beginning or the end of the on–off cycle. These results indicate that the direction of the electron diffusion is free of grain boundaries, which can create traps to hinder electron movement and slow down photocurrent generation [26].

Figure 10 shows the spectra for the excellent performing α-Fe_2O_3/α-Fe_2O_3/FTO bilayer samples compared to the α-Fe_2O_3 (A) and α-Fe_2O_3 (B) sample. Meaningful performance gains were observed during the illumination wavelengths. For the α-Fe_2O_3 (A) films, performance was 3-fold greater than that of the α-Fe_2O_3 (B) sample. At 400 nm, the IPCE at a used bias of 0.1 V (vs. Ag/AgCl) was 3.25%, which corresponded to a 3-fold improvement over the α-Fe_2O_3/α-Fe_2O_3/FTO bilayer. Higher photon energy was absorbed on the outmost layers of hematite and, therefore, the photogenerated holes had a smaller diffusion way to reach the surface, where they participated in H_2O oxidation reaction. An anodic used bias would increase the collection efficiency of electrons, and an IPCE amelioration can be seen in Fig. 10.

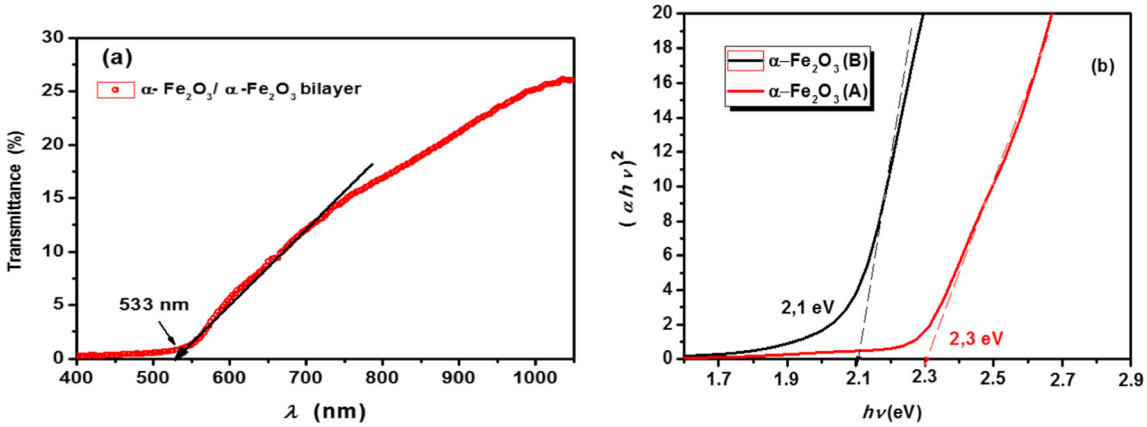

Fig. 8 **a** Transmittance of the α-Fe_2O_3/α-Fe_2O_3 bilayer. **b** Tauc plot of α-Fe_2O_3 (A) and α-Fe_2O_3 (B)

Moreover, the applied bias would allow H_2O reduction at the Pt counter electrode by overcoming the mismatch (0.1 V (vs. Ag/AgCl)) between the hematite conduction band edge level and the reversible hydrogen potential.

Let us analyze the effect of the different thickness for layers A (55 nm) and B (196 nm) and bilayer A + B (251 nm). The absorption coefficient for α-Fe_2O_3 at 500 nm is about 1.5×10^{-5} cm^{-1}. This means that the number of photons absorbed for α-Fe_2O_3 layers with 55 and 196 nm thick are respectively 30 and 95%. Indeed, this argument is valid to explain the increase in IPCE between A and B films. However, the overall thickness of the bilayer A + B is about 251 nm and, in that case, the number of photons absorbed at 500 nm is about 98%, which is quite similar to that absorbed by sample B and does not justify the improved PEC efficiency of the bilayer with respect to layer B. So, an additional mechanism must be considered to explain the PEC improvement in A + B bilayer.

To gain further insight into the charge transfer process, electrochemical impedance spectroscopy was performed at + 0.1 V vs. Ag/AgCl in 1 M NaOH solution (Fig. 11) [27]. Figure 11a shows the experimental and fitted results. The latter (solid lines) have been obtained by assimilating the whole system as the equivalent electrical circuit displayed in Fig. 11b. The radius of the arcs of the Nyquist plots for the α-Fe_2O_3 (A)/α-Fe_2O_3 (B) bilayer was found to be much smaller than that for both α-Fe_2O_3 (A) and α-Fe_2O_3 (B) films, indicating that the α-Fe_2O_3 (A)/α-Fe_2O_3 (B) bilayer has a higher charge transfer efficiency.

The α-Fe_2O_3 (A)/α-Fe_2O_3 (B) bilayer makes the charge transfer efficiency (Fig. 11) and charge separation more efficient in the bilayer photoanodes (Fig. 12) as compared to the α-Fe_2O_3 (A) and α-Fe_2O_3 (B) films; a dramatic enhancement of the photocurrent density occurred as shown in Fig. 9.

Table 2 displays the results of the fit of Nyquist plots to the equivalent electrical model. As expected, the charge transfer resistance increases proportionally to the layers' thickness because they behave as resistor connected in series. The capacitance is inversely proportional to the thickness of the dielectric; therefore, the thicker the dielectric, the smaller the capacitance. In the case of the bilayer, both capacitors are connected in series, and then the equivalent capacitance is always smaller

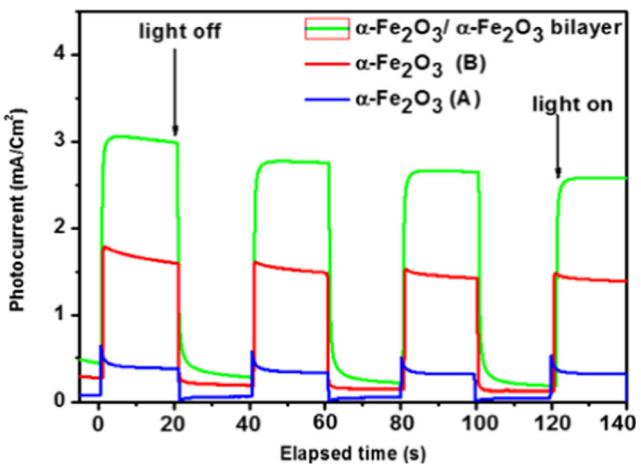

Fig. 9 Photocurrent intensity for the α-Fe_2O_3 (A), α-Fe_2O_3 (B), and α-Fe_2O_3/α-Fe_2O_3 (bilayer) electrodes under successive on–off illumination cycles. Measurements were made in the 1 M NaOH electrolyte with a bias potential of + 0.1 V

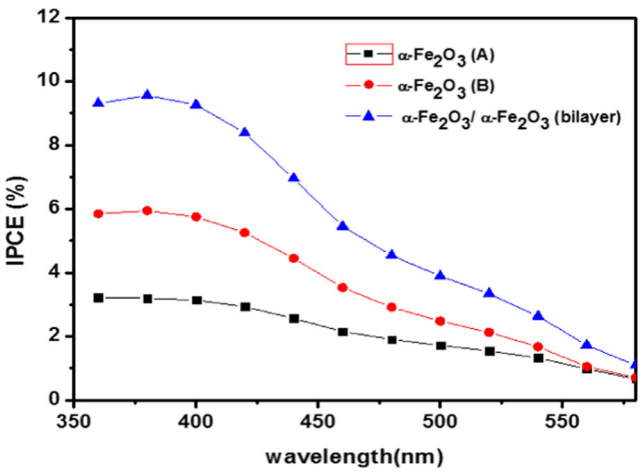

Fig. 10 IPCE for α-Fe_2O_3 (A), α-Fe_2O_3 (B), and α-Fe_2O_3/α-Fe_2O_3 (bilayer) at the 0.1 V (vs. Ag/AgCl) applied potential in N_2 degassed 1 M NaOH

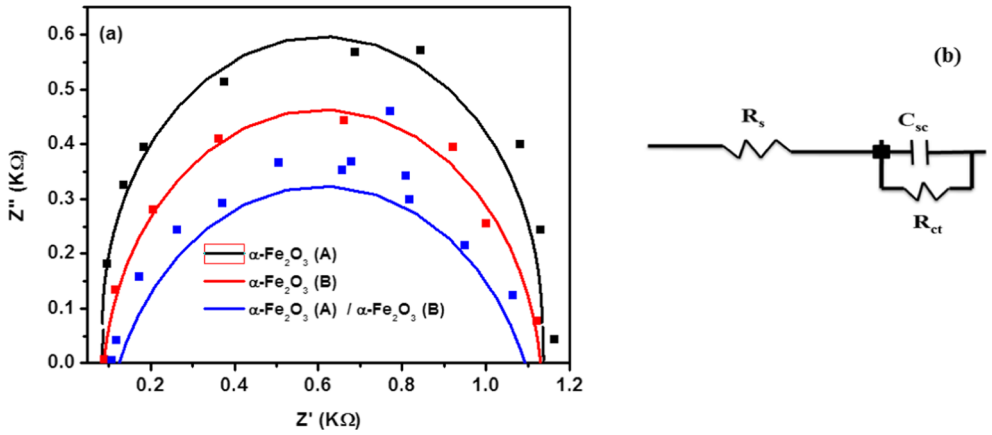

Fig. 11 **a** Nyquist plots for α-Fe_2O_3 (A), α-Fe_2O_3 (B), and α-Fe_2O_3 (A)/α-Fe_2O_3 (B) bilayer. Measurements were conducted in 1.0 M NaOH solution at + 0.1 V vs. Ag/AgCl at room temperature. **b** Equivalent circuit used to fit Nyquist plots. R_s, solution resistance; R_{ct}, charge transfer resistance; C_{SC}, the space charge layer capacitance

than the individual capacitances. For comparison purposes, the IPCE values at 380 nm are also shown in Table 2. As mentioned before, due to their respective thicknesses, the numbers of photons absorbed by the bilayer are quite like those absorbed by the α-Fe_2O_3 (B) films. Therefore, an additional mechanism is required to explain the PEC improvement for the bilayer.

To shed light on the origin of the improved PEC efficiency, we have measured the open circuit photovoltage curves of the photoanodes in the dark and under illumination. Open circuit photovoltage for all three layers was measured in 1.0 M NaOH solution and is shown in Fig. 12. Under illumination, the open circuit photovoltage for thicker sample α-Fe_2O_3 (B) layer is slightly higher than that of α-Fe_2O_3 (B) layer. However, the α-Fe_2O_3 (A)/α-Fe_2O_3 (B) bilayer shows nearly three-times larger open circuit photovoltage as compared to the individual α-Fe_2O_3 films. Similar results were obtained by Q. Yu et al. by using a hematite homojunction without foreign doping. Q. Yu et al. [28] suggest an enlarged band bending at the photoanode/electrolyte interface as the responsible mechanism at the origin of the enhanced electron-hole separation, which further results in an

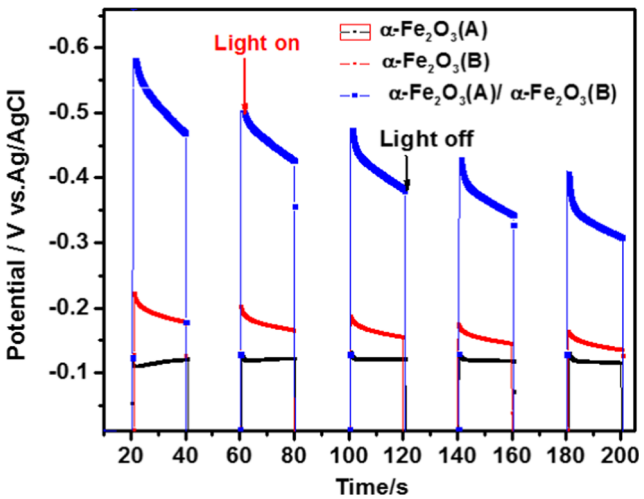

Fig. 12 Open circuit potentials of α-Fe_2O_3 (A) layer, α-Fe_2O_3 (B), and α-Fe_2O_3/α-Fe_2O_3 photoanodes

improved PEC efficiency. In our case, the different methods used for preparing α-Fe_2O_3 (A) and α-Fe_2O_3 (B) layers could give rise to layers with different Fermi level positions and an enhanced electron-hole separation [29].

Improvement mechanism of PEC properties by inserting an underlayer into the α-Fe_2O_3 thin film

We reviewed the above explanations, and how the α-Fe_2O_3 underlayers influenced the PEC properties of a hematite thin film, as shown in Scheme 10. The light diffusion length in hematite was in the order of 100 nm ($\alpha = 1.6 \times 10^7$ m^{-1} at 500 nm) [30], whereas the hole transmission length in hematite was very short (20 nm [31]; 2–4 nm [32]).

For the simple FTO hematite photoanode, the photogenerated holes created in the bulk would recombine with electrons before reaching the semiconductor/electrolyte interface to oxide water (indicated as (II) and (VI) in Fig. 13a). The photogenerated electrons could transfer in the external electric field to FTO (denoted as (III) in Fig. 13a). However, these electrons could readily transfer back (indicated as (IV) in Fig. 13a) to the hematite film, where they would recombine with holes (referred as (V) in Fig. 13a). Therefore, when the α-Fe_2O_3underlayer was interjected, it would work as a good wall to overpower the electrons back transfer (process (IV) in Fig. 13b) due to the lightweight conduction band offset (ε) of

Table 2 Parameters obtained from EIS measurements of the α-Fe_2O_3 (A), α-Fe_2O_3 (B), and α-Fe_2O_3/α-Fe_2O_3 photoanodes

Samples	Charge transfer resistance, R_{ct} (kΩ)	Space charge layer capacitance, C_{SC} (μF)	Solution resistance, R_s (kΩ)	IPCE at 380 nm (%)
α-Fe_2O_3 (A)	0.896	348	0.099	3
α-Fe_2O_3 (B)	1.048	236	0.018	6
α-Fe_2O_3 (A)/α-Fe_2O_3 (B)	2.085	195	0.021	9

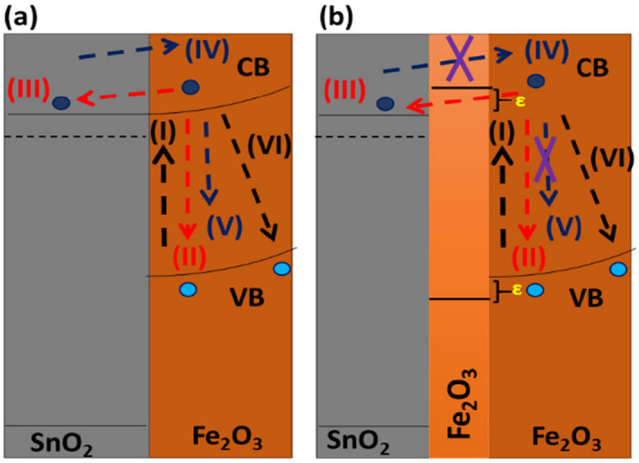

Fig. 13 **a** Schematic drawing of the FTO/α-Fe_2O_3 interface showing an unhindered electron transfer. **b** Blocking the effect of the α-Fe_2O_3 (A) underlayer on electrons transfer and the recombination process. The photogeneration and major recombination of electrons and holes are as follows: (I) photogeneration of electron and hole pairs; (II) direct recombinations of the photogenerated electrons and holes in α-Fe_2O_3; (III) forward transfer of electrons in the external electric field; (IV) electrons back transfer via diffusion; (V) recombinations of back transfer electrons and holes in the VB of α-Fe_2O_3; and (VI) recombinations of electrons in the CB of α-Fe_2O_3 with holes at the interface of the α-Fe_2O_3/electrolyte

α-Fe_2O_3 (A) to either FTO or hematite. The recombination of the process (V) in Fig. 13b would be well-suppressed.

Furthermore, the α-Fe_2O_3underlayer physically separated the hematite film from FTO, which also helped to repress the interfacial charge recombination. These actions would benefit by improving the photocurrent reaction of the photoanodes. However, the blocking effect of the α-Fe_2O_3 underlayer was not only for the electrons back transfer, but also for the electrons forward transfer, i.e., the photoelectrons that transfer from hematite to FTO. With increasing α-Fe_2O_3 underlayer thickness, the process (III) in Fig. 13b would also be suppressed. Therefore, the thin underlayer was needed to allow the forward electron transfer from α-Fe_2O_3 to FTO, while the dense underlayer would be good for the blocking effect. An optimal thickness for the α-Fe_2O_3 underlayer would exist that would balance the blocking function and the electron tunneling rate. The effects of the α-Fe_2O_3 layer worked separately for the photogenerated electrons and holes and donate to the separation of charge carriers.

Conclusions

Semiconducting materials, such as α-Fe_2O_3 (A) and α-Fe_2O_3 (B), were successfully electrodeposited on FTO substrates. This enabled us to study the energy behavior of both semiconductors and the α-Fe_2O_3/α-Fe_2O_3/FTO bilayer performance about photoelectrochemical applications. FESEM showed that α-Fe_2O_3 (B) could easily grow thicker to cover α-Fe_2O_3 (A). The photoelectrochemical performance of the nanostructured α-Fe_2O_3/α-Fe_2O_3 bilayer was better than that of FTO/α-Fe_2O_3 (A) and FTO/α-Fe_2O_3 (B). Water-splitting performance was evaluated and the highest photocurrent density of 3 mA/cm^2 vs. Ag/AgCl was exhibited for the α-Fe_2O_3/α-Fe_2O_3 bilayer photoelectrodes. The improved photocurrent density was attributed to two main combined factors: (i) generation of an electric field on the layer that suppressed the recombination of the photogenerated charge carriers and (ii) the application of an adequate external bias by favoring the transfer and separation of the photogenerated charge carriers on the α-Fe_2O_3/α-Fe_2O_3 bilayer. Enhanced photocurrent density has also been attributed to an appropriate band edge alignment of semiconductors that enhances light absorption in both semiconductors. The best performing samples were those of the α-Fe_2O_3/α-Fe_2O_3/FTO bilayer, which had IPCEs at 400 nm of 9%, with an applied potential of 0.1 V vs. Ag/AgCl. These IPCE values were 3-fold higher than those of the α-Fe_2O_3 (A) and α-Fe_2O_3 (B) samples for the α-Fe_2O_3/α-Fe_2O_3/FTO bilayer samples.

Funding information This work was supported by the Ministry of High Education and Scientific Research (Tunisia), Research and Technology Centre of Energy (CRTEn) Borj-Cedria, and the Spanish Ministerio de Economia y Competitividad (ENE2016-77798-C4-2-R), and the Generalitat valenciana (Prometeus 2014/044).

References

1. Brimblecombe R, Dismukes GC, Swiegers GF, Spiccia L (2009) Molecular water-oxidation catalysts for photoelectrochemical cells. Dalton Trans 0:9374–9384
2. Prévot MS, Sivula K (2013) Photoelectrochemical tandem cells for solar water splitting. J Phys Chem C 117(35):17879–17893
3. Valdés Á, Brillet J, Grätzel M, Gudmundsdóttir H, Hansen HA, Jónsson H, Klüpfel P, Kroes GJ, Formal FL, Man IC, Martins RS, Nørskov JK, Rossmeisl J, Sivula K, Vojvodic A, Zäch M (2012) Solar hydrogen production with semiconductor metal oxides: new directions in experiment and theory. Phys Chem Chem Phys 14(1):49–70
4. Murphy AB, Barnes PRF, Randeniya LK, Plumb IC, Grey IE, Horne MD, Glasscock JA (2006) Efficiency of solar water splitting using semiconductor electrodes. Int J Hydrog Energy 31(14):1999–2017
5. Chen Z, Jaramillo TF, Deutsch TG, Kleiman-Shwarsctein A, Forman AJ, Gaillard N, Garland R, Takanabe K, Heske C, Sunkara M, McFarland EW, Domen K, Milled EL, Dinh HN (2010) Accelerating materials development for photoelectrochemical hydrogen production: standards for methods, definitions, and reporting protocols. J Mater Res 25(01):3–16
6. Sivula K, Formal FL, Grätzel M (2011) Solar water splitting progress using hematite (α-Fe_2O_3) photoelectrodes. ChemSusChem 4(4):432–449
7. Dauth A, Love JA (2012) Synthesis and reactivity of 2-azametallacyclobutanes. Dalton Trans 41:7830–7834
8. Kennedy JH, Frese KW (1978) Photooxidation of water at α-Fe_2O_3 electrodes. J Electrochem Soc 125(5):709–714
9. Wheeler DA, Wang G, Ling Y, Li Y, Zhang JZ (2012) Nanostructured hematite: synthesis, characterization, charge carrier

dynamics, and photoelectrochemical properties. Energy Environ Sci 5(5):6682–6702
10. Regan BO, Schwartz DT (1995) Efficient photo-hole injection from adsorbed cyanine dyes into electrodeposited copper (I) thiocyanate thin films. Chem Mater 7(7):1349–1354
11. Li B, Wang L, Kang B, Wang P, Qiu Y (2006) Review of recent progress in solid-state dye-sensitized solar cells. Sol Energy Mater Sol Cells 90(5):549–573
12. Formal FL, Grätzel M, Sivula K (2010) Controlling photoactivity in ultrathin hematite films for solar water-splitting. Adv Funct Mater 20(7):1099–1107
13. Hisatomi T, Dotan H, Stefik M, Sivula K, Rothschild A, Grätzel M, Mathews N (2012) Enhancement in the performance of ultrathin hematite photoanode for water splitting by an oxide underlayer. Adv Mater 24(20):2699–2702
14. Luo W, Yu T, Wang Y, Li Z, Ye J, Zou Z (2007) Enhanced photocurrent–voltage characteristics of WO_3 /Fe_2O_3 nano-electrodes. J Phys D Appl Phys 40(4):1091–1096
15. Boudoire F, Toth R, Heier J, Braun A, Constable EC (2014) Photonic light trapping in self-organized all-oxide microspheroids impacts photoelectrochemical water splitting. Energy Environ Sci 7(8):2680–2688
16. Hsu YK, Chen YC, Lin YG (2015) Novel ZnO/Fe_2O_3 core–shell nanowires for photoelectrochemical water splitting. ACS Appl Mater Interfaces 7(25):14157–14162
17. Sharma D, Upadhyay S, Verma A, Satsangi VR, Shrivastav R, Dass S (2015) Nanostructured Ti-Fe_2O_3/Cu_2O heterojunction photoelectrode for efficient hydrogen production. Thin Solid Films 574:125–131
18. Bouhjar F, Ullah S, Chourou ML, Mollar M, Marí B, Bessaïs B (2017) Electrochemical fabrication and characterization of p-CuSCN/n-Fe_2O_3 heterojunction devices for hydrogen production. J Electrochem Soc 164:936–945
19. Bouhjar F, Mollar M, Chourou ML, Marí B, Bessaïs B (2018) Hydrothermal synthesis of nanostructured Cr-doped hematite with enhanced photoelectrochemical activity. Electrochim Acta 260: 838–846
20. Jaramillo TF, Baeck SH, Kleiman-Shwarsctein A, Choi KS, Stucky GD, McFarland EW (2005) Automated electrochemical synthesis and photoelectrochemical characterization of $Zn_{1-x}Co_xO$ thin films for solar hydrogen production. J Comb Chem 7(2):264–271
21. Jaramillo TF, Baeck SH, Kleiman-Shwarsctein A, McFarland EW (2004) Combinatorial electrochemical synthesis and screening of mesoporous ZnO for photocatalysis. Macromol Rapid Commun 25(1):297–301
22. Miller EL, Paluselli D, Marsen B, Rocheleau RE (2004) Low-temperature reactively sputtered iron oxide for thin film devices. Thin Solid Films 466(1-2):307–313
23. Belkhedkar MR, Ubale AU (2014) Preparation and characterization of α-Fe_2O_3 thin films grown by successive ionic layer adsorption and reaction method. Mater Chem 4:109–116
24. Shinde SS, Bansode RA, Bhosale CH, Rajpure KY (2011) Physical properties of hematite α-Fe_2O_3 thin films: application to photoelectrochemical solar cells. J Semicond 32:0–8
25. Souza FL, Lopes KP, Nascente PAP, Leite ER (2009) Nanostructured hematite thin films produced by spin-coating deposition solution: application in water splitting. Sol Energy Mater Sol Cells 93(3):362–368
26. Sookhakian M, Amin YM, Baradaran S, Tajabadi MT, Golsheikh AM, Basirun WJ (2014) A layer-by-layer assembled graphene/zinc sulfide/polypyrrole thin-film electrode via electrophoretic deposition for solar cells. Thin Solid Films 552:204–211
27. Qing Y, Xianguang M, Tao W, Peng L, Jinhua Y (2015) Hematite films decorated with nanostructured ferric oxyhydroxide as photoanodes for efficient and stable photoelectrochemical water splitting. Adv Funct Mater 25:2686–2692
28. Qing Y, Xianguang M, Li S, Guigao L, Peng L, Jinhua Y (2016) Hematite homojunctions without foreign element doping for efficient and stable overall water splitting. RSC Adv 6:62263–62269
29. Miao Z, Takashi H, Yongbo K, Jiao Z, Min L, Akihide I, Qingxin J, Hiroshi N, Tsutomu M, Mamiko N, Naoya S, Ryo N, Chisato K, Hidetaka S, Masao K, Akihiko K, Taro Y, Kazunari D (2015) Surface modification of CoO_x loaded $BiVO_4$ photoanodes with ultrathin p-type NiO layers for improved solar water oxidation. J Am Chem Soc 137:5053–5060
30. Gardner RFG, Sweett F, Tanner DW (1963) The electrical properties of alpha ferric oxide-II. J Phys Chem Solids 24(10):1183–1196
31. Dare-Edwards MP, Goodenough JB, Hamnett A, Trevellick PR (1983) Electrochemistry and photoelectrochemistry of iron(II1) oxide. J Chem SOC Faraday Trans I 79(9):2027–2041
32. Cesar I, Sivula K, Kay A, Zboril R, Grätzel M (2009) Influence of feature size, film thickness, and silicon doping on the performance of nanostructured hematite photoanodes for solar water splitting. J Phys Chem C 113(2):772–782

Synthesis of in-gap band CuGaS 2 :Cr absorbers and numerical assessment of their performance in solar cells

Article *in* Solar Energy Materials and Solar Cells · July 2017

DOI: 10.1016/j.solmat.2017.06.062

CITATION
1

READS
75

5 authors, including:

Shafi Ullah
Universitat Politècnica de València
15 PUBLICATIONS **9** CITATIONS
SEE PROFILE

Hanif Ullah
Universitat Politècnica de València and Fuua…
19 PUBLICATIONS **27** CITATIONS
SEE PROFILE

Feriel Bouhjar
Universitat Politècnica de València
12 PUBLICATIONS **4** CITATIONS
SEE PROFILE

Bernabé Marí Soucase
Universitat Politècnica de València
189 PUBLICATIONS **1,789** CITATIONS
SEE PROFILE

Solar Energy Materials and Solar Cells 180 (2018) 322–327

Contents lists available at ScienceDirect

Solar Energy Materials and Solar Cells

journal homepage: www.elsevier.com/locate/solmat

Synthesis of in-gap band $CuGaS_2$:Cr absorbers and numerical assessment of their performance in solar cells

Shafi Ullah, Hanif Ullah, Feriel Bouhjar, Miguel Mollar, Bernabé Marí*

Departament de Física Aplicada-IDF, Universitat Politècnica de València, Camí de Vera s/n, 46022 València, Spain

ARTICLE INFO

Keywords:
$CuGaS_2$
Thin film solar cells
Intermediate band solar cell
Numerical simulation
Photoconversion efficiency
SCAPS

ABSTRACT

$CuGaS_2$ thin films were obtained by sulfurization of $CuGaSe_2$. $CuGaSe_2$ thin films were first electrodeposited from aqueous solutions containing $CuCl_2$, $GaCl_3$, and H_2SeO_3 and subsequently annealed at 400 °C for 10 min in forming gas atmosphere and in the presence of molecular sulfur. This sulfurization process resulted in the complete conversion of $CuGaSe_2$ into $CuGaS_2$. The formation of $CuGaS_2$ was proven by X-Ray diffraction and optical spectroscopy. Diffraction peaks of $CuGaS_2$ shifted to higher angles than those observed for $CuGaSe_2$ films, and the optical band gap shifted to blue rising from 1.66 eV for $CuGaSe_2$ to 2.2 eV for $CuGaS_2$. When Cr ions were added to the initial electrolyte, the final $CuGaS_2$ films exhibited a broad in-gap absorption band centred at 1.63 eV that can be attributed to Cr atoms at the Ga sites. The performance of solar cells based on $CuGaS_2$:Cr absorbers containing an in-gap absorption band was then estimated by numerical simulation using Solar Cell Capacitance Simulator Software. Both quantum efficiency and short circuit current of simulated Mo/$CuGaS_2$:Cr/CdS/ZnO solar cells rose proportionally to the amount of Cr present in the $CuGaS_2$:Cr absorbers. As a result, the photo conversion efficiency of the simulated devices changed from 14.7% for $CuGaS_2$ to 34% for $CuGaS_2$:Cr absorbers. Nevertheless, when neutral defects related to Cr-doping were introduced in the absorber layer, the positive effect of the enhancement of photon harvesting due to IGB was compensated by a decline in the carrier collection and the overall efficiency of the device diminished considerably.

1. Introduction

CIGS chalcopyrite semiconductors are among the most promising materials to be used in high-performance photovoltaic devices due to their direct bandgap, which can be tuned between 1.1 for $CuInSe_2$ and 2.2 eV for $CuGaS_2$. Also, their cost-effectiveness and easy processing are well known. Recently, CIGS thin-film photovoltaic devices reached a record solar efficiency of 22.3% [1]. Among thin film technologies, CIGS solar cells have achieved highest conversion efficiencies at laboratory scale [2,3]. Efforts to seek an economical and scalable method for the production of stoichiometric CIGS thin-films have been made to allow the commercialization of these devices. Among several techniques, electrodeposition has demonstrated to produce CIGS devices with high efficiency [4]. Currently efforts are being made with regard to theoretical studies and also to improve inexpensive deposition strategies for the chalcopyrite absorber layer [5].

The band gap energy of semiconductor materials plays a key role in the performance of photovoltaic devices [6]. According to the Shockley–Queisser limit, the optimal band gap energy of a single band gap PV device was calculated to be about 1.4 eV [7]. Therefore, it would be unreasonable to use $CuGaS_2$ thin film as absorber in photovoltaic devices based on one junction due to their high band gap which is about 2.2 eV. However, this energy matches the optimal band gap to host an in-gap band (IGB) (also known as intermediate band) intended to absorb photons with energies lower than the gap. In the proposed IGB material, electrons can follow two ways to be promoted from the valence band to the conduction band: a) absorbing a photon with a higher energy than the band gap, and b) through the absorption of two photons with energy below the bandgap. The absorption of one photon promotes one electron from the valence band to the partially filled IGB and then the electron is transferred from this IGB to the conduction band after the absorption of a second photon, allowing a more efficient use of the solar spectrum in photovoltaic devices. This type of solar cell would be able to utilize the solar spectrum more efficiently, resulting in a theoretical efficiency limit of 63.2% [8], which is significantly higher than the 40.7% limit of conventional single band-gap photovoltaic cells [7]. Such devices would possess higher open circuit voltages and increased short circuit currents due to the higher band gap energy of the absorbing material and the greater absorption coming from sub-band gap photons, resulting in an increase of the overall efficiency [9].

* Corresponding author.
E-mail address: bmari@fis.upv.es (B. Marí).

http://dx.doi.org/10.1016/j.solmat.2017.06.062
Received 10 February 2017; Received in revised form 26 June 2017; Accepted 28 June 2017
Available online 06 July 2017
0927-0248/

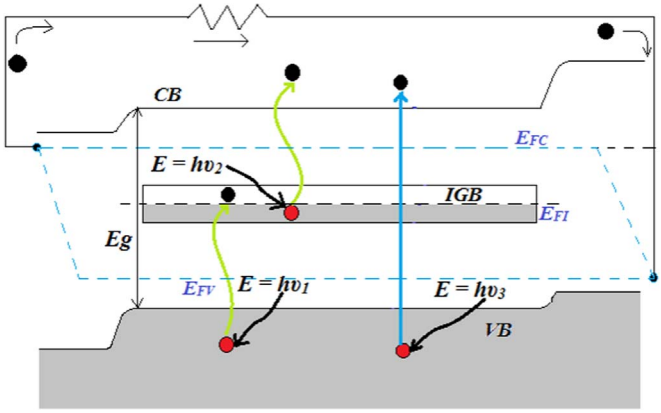

Fig. 1. The electronic structure and design of an IGB solar cell.

The in-gap absorption band concept is based on an adjustment of the electronic structure of a semiconductor, by introducing a partially filled absorption band inside the gap, as presented in the Fig. 1. This IGB divides the band gap into smaller energy units, sub-band gaps. The IGB then acts as a stepping stone for low-energy photons and allows the promotion of electrons from the Valence Band to the Conduction Band using two photons with energies below the band gap.

The semi-filled IGB will function as an electron receiver as well as an electron supplier. The electronic structure of an IGB photovoltaic device will in other words allow absorption of three photons at the same time. The multi-absorption creates higher density of electron-hole pairs available for increasing the electric current without lowering the open voltage of the cell. As a result, the efficiency of the cell rises due to the enlarged energy output per unit of incoming radiation.

High expectations have been placed in this theoretically model of wide-spectrum absorption of chalcopyrite by introducing various dopants (Ti, V, Cr, Ni, etc.) [10]. The partially-filled IGB can provide empty states to receive the electrons pumped by photon $h\upsilon_1$ and further pump the electrons from there by photon $h\upsilon_2$. The solar response is significantly extended to lower energy photons, especially in the near-infrared region. As a consequence, the multi-photon absorption of two sub-band gaps (EV and EC) improves the photocurrent operationally without photo-voltage degradation.

According to the literature [11], chrome substituting Ga in $CuGaS_2$ chalcopyrite lattices would generate an IGB separated from both valence and the conduction bands. When the transition metal (Cr) IGB introduced into the $CuGaS_2$ lattice, it produces a partially filled band separated from both conduction and the valence bands that allows promoting an electron-hole pair through a two photons absorption process with sub-band gap energies. Therefore, the use of an IGB absorber would allow harvesting higher amounts of solar photons.

The main determination of the present work is to dope $CuGaS_2$ thin films with the transition-metal Cr to create a suitable IGB absorber [12]. Herein, we report the synthesis and optical characterization of $CuGaS_2$ and $CuGaS_2$:Cr thin films containing an IGB associated to Cr. $CuGaS_2$ thin films were produced by sulfurization of previously electrodeposited $CuGaSe_2$ films. The replacement of Se by S was completely carried out after sulfurization. Optical analysis showed that the band gap shifted from 1.66 for $CuGaSe_2$ to 2.20 eV for $CuGaS_2$.with the sulfurization, the position of X-Ray diffractogram peaks also shifted from 27 to 29 degrees. The effectiveness of Cr-doping was inferred from the presence of Cr in $CuGaS_2$ layers detected by microanalysis and the optical detection of an in-gap absorption band. Furthermore, the behaviour of photovoltaic devices based on $CuGaS_2$ absorbers, with and without an IGB was calculated by specific Solar Cell Capacitance Simulation (SCAPS) software [13].

2. Experimental

$CuGaSe_2$ layers were electrodeposited from an electrolyte solution containing 2 mMol L^{-1} $CuCl_2$, 4 mmol L^{-1} H_2SeO_3, 10 mmol L^{-1} $GaCl_3$, 50 mmol L^{-1} KSCN, 100 mmol L^{-1} NH_4Cl and 300 mmol L^{-1} LiCl. The precursor solution pH was adjusted between 2.3 and 2.4 by adding hydrochloric acid (HCl) and potassium hydroxide (KOH). For better stability of the deposition bath solution, LiCl was used as a supporting electrolyte, also improving the quality of the deposited layers.

Electrodeposition was performed on a standard 3-electrode electrochemical cell. The $CuGaSe_2$ thin films were deposited onto a 1 μm thick Mo-coated soda lime glass substrate acting as a working electrode, a platinum wire was used as counter electrode and Ag/AgCl as a reference electrode.

For doping purposes, Cr^{3+} ions were added to the electrolyte described above. 150 mMol L^{-1} of Cr $(ClO_4)_3$ was dissolved in 40 mL of the electrolyte aqueous solution. The pH of the final solution was adjusted between 2.3 and 2.4 using concentrated HCl. Electrodeposition produced Cr-doped $CuGaSe_2$ films and these films, which were subsequently sulfurized following the sulfurization procedure described below.

$CuGaS_2$ layers were obtained after subsequent sulfurization of previously electrodeposited $CuGaSe_2$ layers. A complete replacement of the selenium by sulfur, transforming the precursor $CuGaSe_2$ wurtzite film into a $CuGaS_2$ chalcopyrite film took place in a quartz tube kept inside a cylindrical oven at a 400 °C temperature for 10 min in a forming gas atmosphere.

The crystal structure of $CuGaSe_2$ and $CuGaS_2$ thin films were investigated by X-Ray Diffraction (XRD) with a Rigaku Ultima IV diffractometer in the Bragg-Brentano configuration using CuKα radiation (λ = 1.54060 Å). The chemical composition was analysed by means of Energy Dispersive Spectroscopy (EDS) with a FESEM Zeiss model Ultra55.

Numerical simulations were performed using SCAPS, which is a one dimensional computer software to simulate electrical characteristics of thin film heterojunction solar cells. SCAPS was developed for CIGS and CdTe thin film solar cells but it has been applied to other thin film materials [14]. $CuGaS_2$:Cr absorber layers with different Cr contents were used in the simulation. Besides, the effect of neutral defects related to Cr-doping on the performance of solar cells was also studied and discussed.

3. Results and discussion

Fig. 2 shows the XRD patterns of $CuGaSe_2$ and $CuGaS_2$ thin films at their different preparation stages: (a) electrodeposited $CuGaSe_2$ thin films and (b) sulfurized $CuGaSe_2$ thin films annealed for 10 min at 450 °C. The diffractogram obtained for $CuGaSe_2$ thin films matches the tetragonal crystal system JCPDS No. 075-0104 pattern well. The major peaks were located at 27.9°, 45.7°/46.2° and 54.3°/55.2° corresponding to (1 1 2), (2 2 0)/(2 0 4) and (3 1 2)/(1 1 2) diffraction planes, respectively.

The sulfurization process of the electrodeposited $CuGaSe_2$ films took place after a short annealing time in the presence of molecular sulfur, resulting in the formation of the $CuGaS_2$ chalcopyrite phase as revealed by the XRD pattern of sulfurized films [Fig. 2(b)]. The XRD peaks shifted to higher angles with the sulfurization process. The main XRD peak corresponding to (1 1 2) diffraction peaks shifted from 27.9 to 29.0 degrees. Furthermore, the peaks corresponding to (2 2 0) and (2 0 4) and (3 1 2) and (1 1 6) diffraction planes observed for annealed $CuGaSe_2$ films also shifted to higher angles for sulfurized films. These XRD peaks match the JCPDS No. 75-0103 pattern corresponding to $CuGaS_2$ films. This diffraction pattern confirms the replacement of Se atoms by S atoms after sulfurization, and consequently, $CuGaSe_2$ thin films were transformed into $CuGaS_2$ [15–17].

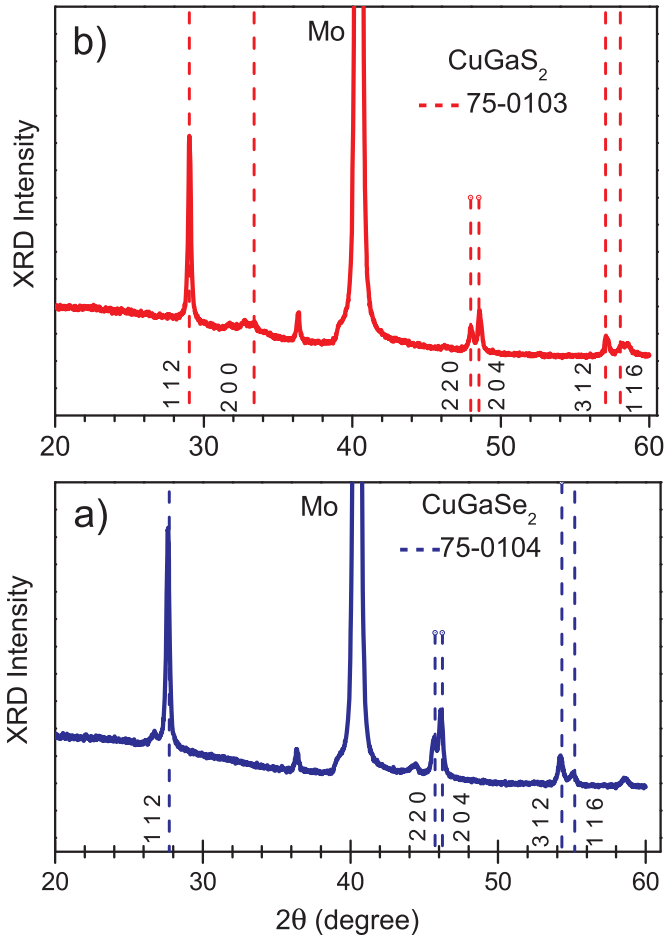

Fig. 2. XRD patterns of $CuGaSe_2$ and $CuGaS_2$ films: (a) $CuGaSe_2$ after annealing at 400 °C in forming gas atmosphere, and (b) after sulfurization in molecular sulfur for 10 min at 400 °C.

Both $CuGaSe_2$ and $CuGaS_2$ films exhibited a tetragonal crystalline structure. The XRD patterns of $CuGaSe_2$ and $CuGaS_2$ thin films display a highly crystalline structure offering the possibility of being used for photovoltaic devices with high conversion efficiency [18].

EDS was used to estimate the composition of deposited $CuGaSe_2$ and $CuGaS_2$ films. Fig. 3(a), (b) shows the EDS spectra of annealed $CuGaSe_2$ and $CuGaSe_2$ films doped with chrome. Main X-ray peaks belong to Cu, Ga, Se and Mo, produced by the substrate. In Cr-doped $CuGaSe_2$ films, three lines located at 0.5, 5.5 and 6.0 keV, respectively, support the presence of chrome in these samples. After sulfurization the lines related to Se practically disappear, which means that the substitution of selenium by sulfur has taken place [19]. Only a residual part of selenium (below 1%) remains after 10-min sulfurization. The content of chrome in doped films always remains between 1% and 2%, irrespective of the amount of Cr^{3+} added to the starting electrolyte, which means that the Cr:Ga ratio ranges from 4% to 8%.

Fig. 4 shows the normalized absorbance for $CuGaSe_2$, $CuGaS_2$ and $CuGaS_2$:Cr thin films, respectively. According to Fig. 4(a), the cut-off wavelength for $CuGaSe_2$ is about 746 nm, which corresponds to a band gap of 1.6 eV. Fig. 4(b) displays the normalized absorbance for $CuGaS_2$ films after sulfurization treatment. The cut-off wavelength for $CuGaS_2$ films shifts to a lower wavelength (563 nm), which means a higher energy band gap (2.2 eV). Fig. 4(c) shows the normalized absorbance for $CuGaS_2$:Cr thin films. An additional characteristic with respect to undoped $CuGaS_2$ films is evidenced: in $CuGaS_2$:Cr films, a wide absorption band centred at 760 nm (1.63 eV) appears. This absorption band can be assigned to a sub-band related to Cr-doping. According to theoretical studies, the substitution Ga^{3+} by some transition metals like Cr would give rise to a partially filled absorption band into $CuGaS_2$ chalcopyrite structures, which would then support the promotion of electrons from the valence band to the conduction band through a two-photon absorption procedure [20].

The proposed in-gap-band concept has gained a great deal of attention in the field of third generation solar cell research. The IGB position should neither overlap with the valence band (VB) nor with the conduction band (CB). Such an in-gap-band does not only absorb photons having an energy higher than that of the band gap (Eg) but also permits the absorption of photons corresponding to sub-band gap, which are capable of promotion electrons from the VB to the IGB and then from the IGB to the CB [21]. The IGB associated to Cr-doped $CuGaS_2$ may allow a higher current to be obtained at the voltage corresponding to the energy gap value, which is described in detail in the simulation part.

4. Numerical simulation of solar cells based on $CuGaS_2$:Cr absorbers

The performance of photovoltaic devices based on IGB-absorbers has been numerically simulated using SCAPS. The simulated photovoltaic device consists of the following sequence of layers: Mo/$CuGaS_2$:Cr/CdS/ZnO corresponding to back contact, absorber, buffer and window layers, respectively.

In the simulation we used the experimental absorption coefficient measured for $CuGaS_2$:Cr considering that 5% of Ga was substituted by Cr. To further estimate the effectiveness of the Cr-related IGB, we proportionally increased the Cr content to 10% and 20% and then studied its effect on the performance of the solar cell.

Fig. 5 shows the energy band diagram for Mo/$CuGaS_2$:Cr/CdS/ZnO thin film solar cells. The diagram plots various key electron energy levels as the Fermi level and the energy band edges. The band gap of pure $CuGaS_2$ is 2.2 eV, which is appropriate for hosting an IGB separated from both conduction and valence bands. Cr doping originates an IGB centred at 1.63 eV, which enhances the absorption and allows boosting the efficiency of the device.

Fig. 6 shows the External Quantum Efficiency (EQE) under AM1.5 illumination for $CuGaS_2$:Cr solar cells with a different Cr content ranging from 0% to 20%. The EQE is the ratio of the amount of charge carriers collected by the solar cell with respect to the amount of incident photon energy on the solar cell. The EQE for pure $CuGaS_2$ falls to 0 for wavelengths longer than 620 nm, which corresponds to the band gap of the absorber (2.2 eV). However, due to the absorption of the IGB, a rise in EQE is observed within the range of 620–1000 nm. This increase in EQE is related to the absorption of sub-band-gap photons associated to the IGB and the general rule is: the higher the Cr content, the higher the EQE in the region below the band gap. The key goal of this research was to improve the performance of solar cells by inserting an IGB to cover a wider wavelength range.

Fig. 7 shows the J-V characteristic of solar cells for $CuGaS_2$ absorbers with various Cr contents. Under AM1.5 illumination, the short circuit current (J_{sc}) depends on the Cr content in the $CuGaS_2$ absorber layer. The short circuit current increases with regard to the Cr percentage. For Cr 0%, the $CuGaS_2$ absorber gives J_{sc} = 12.6 mA/cm^2, and J_{sc} increases proportionally to the Cr content of up to 29.41 mA/cm^2 for Cr 20%, Cr 5%, 10%, and 20%, which means that the remaining Ga atoms are 95%, 90% and 80% with respect to Ga atoms in pure $CuGaS_2$ absorbers assuming that all Cr atoms are substituting Ga atoms. Unfortunately, this cannot be inferred from EDS analysis.

Table 1 displays the main photovoltaic parameters for the studied devices in relation to the Cr content. Both, the open circuit voltage (Voc = 1.34 V) and the fill factor (FF = 89.5) remain constant with the amount of Cr. However, the short circuit current (Jsc) dramatically increases with the Cr content, and as a result the photo conversion efficiency (PCE) increases from 14.73% for the $CuGaS_2$ absorber layer without Cr to 34.00% for $CuGaS_2$:Cr (20%) absorbers. This increase in

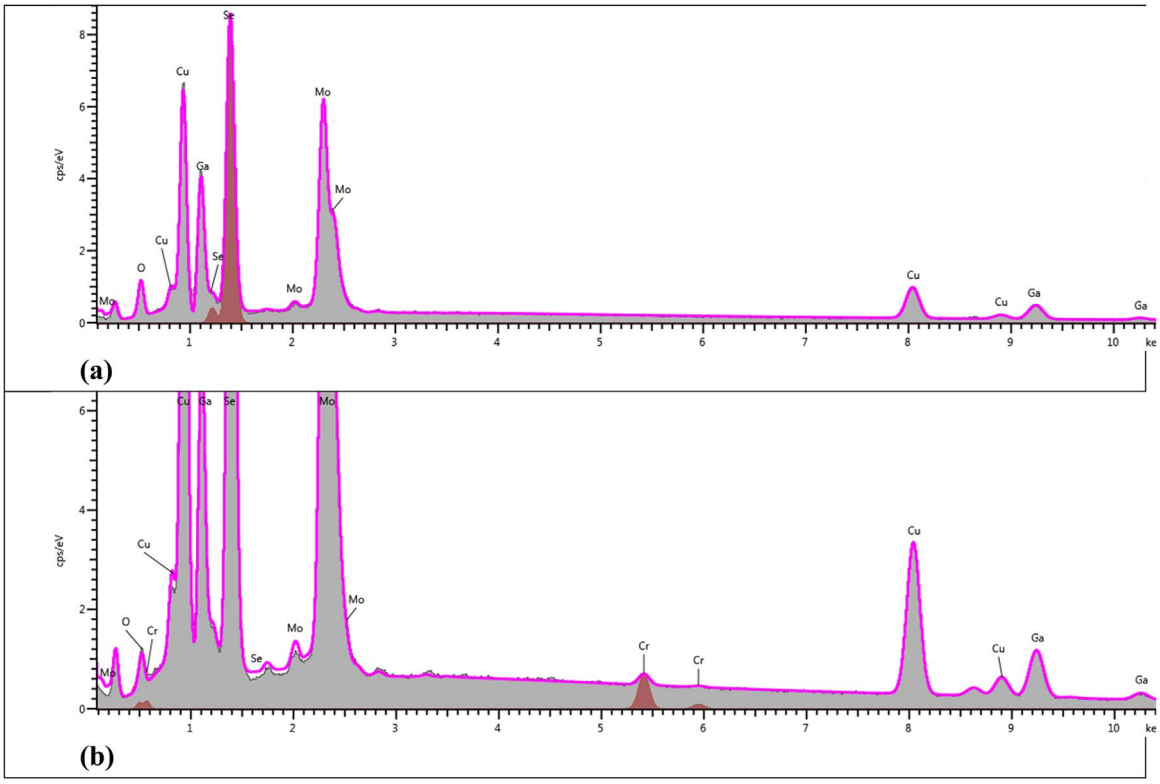

Fig. 3. EDS spectrum for: a) annealed $CuGaSe_2$, b) $CuGaSe_2$ doped with Cr.

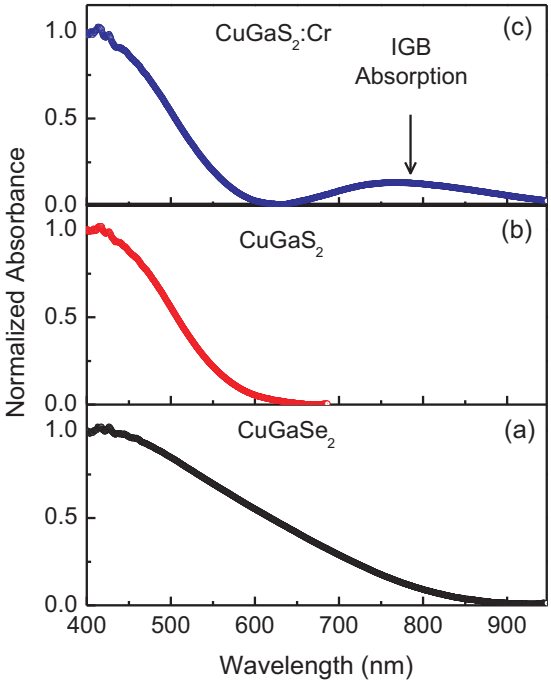

Fig. 4. Comparison of the absorbance of $CuGaSe_2$, $CuGaS_2$ and $CuGaS_2$:Cr thin films. The broad absorption band observed for $CuGaS_2$:Cr, centred at 760 nm, is attributed to the Cr-related in-gap band.

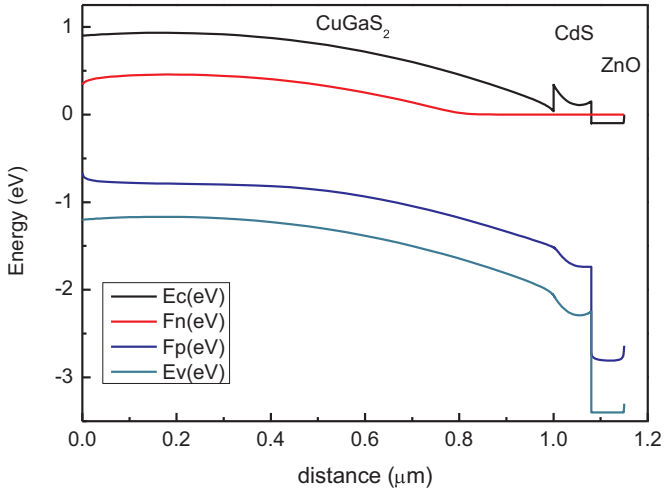

Fig. 5. Band diagram of the Mo/$CuGaS_2$/CdS/ZnO thin film solar cell.

the PCE is directly related to the effectiveness of the intermediate band for absorbing photons with energies below the band gap.

In the $CuGaS_2$ lattice, Cr atoms should act as a neutral defect and would then hinder the movement of the carriers. Therefore, Cr doping adds two effects; a) increasing the photon harvesting through the related IGB, and b) hindering the carriers drift as the doping modifies the crystal lattice. In order to take into account both effects, we calculated the photovoltaic parameters for the $CuGaSe_2$:Cr devices for an increasing concentration of neutral defects.

Fig. 8 shows the J-V curves for PV devices based on $CuGaSe_2$:Cr absorbers with an increasing concentration of Cr-related neutral defects. Several features can be seen in these J-V curves: a) increasing neutral defects results in a drop of Voc, b) Jsc is also decreased as the number of neutral defects increases. As a result, PCE drops drastically with the amount of neutral defects. The photovoltaic parameters of such devices in relation to the neutral defects concentration are summarized in Table 2.

By introducing neutral defects, the relationship between the PCE and defects is inverse. When the neutral defect concentration increases from 10^{16} to 10^{20} cm^{-3}, the PCE decreases from 34% to 2.3%, which means that the performance of the photovoltaic device is very sensitive to neutral defects. Cr-doping improves photon harvesting and,

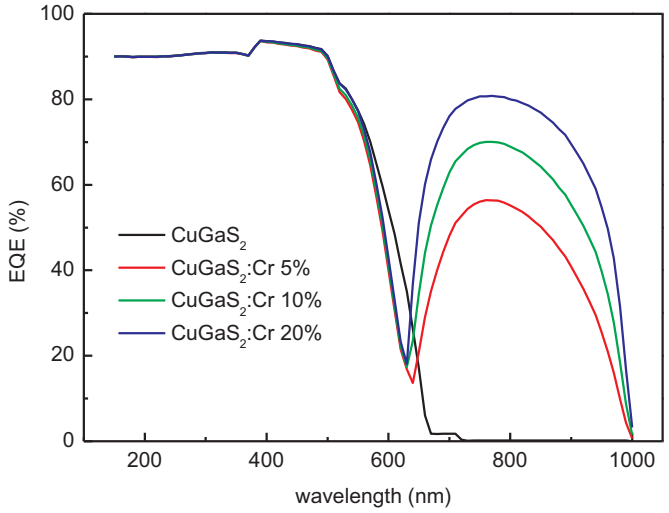

Fig. 6. EQE for Mo/$CuGaS_2$:Cr/CdS/ZnO solar cells with different Cr contents under standard AM1.5 illumination.

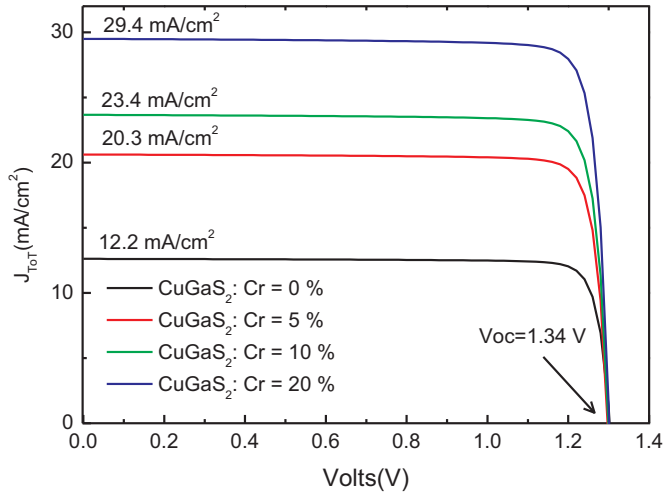

Fig. 7. J-V characteristics of $CuGaS_2$:Cr thin film solar cells with various Cr contents.

Table 1
Output parameters of the modeled Mo/$CuGaS_2$:Cr/CdS/ZnO thin film solar cell with various Cr content.

Cr (%)	Voc (Volt)	Jsc (mA/cm^2)	FF (%)	PCE (%)
0	1.344	12.22	89.7	14.73
5	1.339	20.31	89.5	24.35
10	1.341	23.38	89.5	28.07
20	1.343	29.41	89.5	34.00

consequently, the short circuit current but, simultaneously, spreads the concentration of neutral defects that obstruct the extraction of carriers to the external load.

5. Conclusions

$CuGaS_2$ thin films were obtained by sulfurization at 400 °C for 10 min of previously electro-deposited $CuGaSe_2$ precursor films. The shift observed in X-ray diffraction peaks and the widening of the optical bandgap from 1.66 to 2.20 eV confirm the conversion of $CuGaSe_2$ into $CuGaS_2$.

After partial substitution of Ga by Cr atoms, an absorption band below the gap is observed. This in-gap-band is centred at about 1.63 eV above the valence band. Apart from transitions from the VB to the CB,

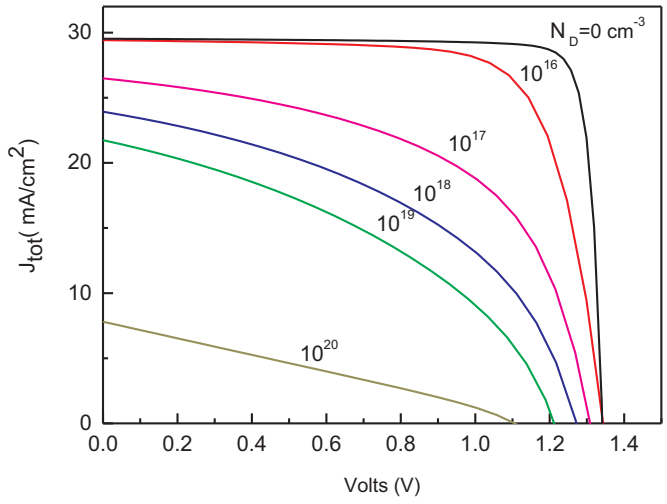

Fig. 8. J-V characteristics of solar cells based on $CuGaS_2$:Cr 20% absorbers with different amounts of neutral defects.

Table 2
Output parameters of the modeled Mo/$CuGaS_2$Cr/CdS/ZnO thin film solar cell with neutral defects.

Neutral Defects (cm^{-3})	Voc (Volt)	Jsc (mA/cm^2)	FF (%)	PEC (%)
0	1.34	29.41	89.70	34.00
10^{16}	1.34	29.32	70.90	30.29
10^{17}	1.30	26.48	51.71	17.80
10^{18}	1.27	23.92	42.70	12.97
10^{19}	1.21	21.74	38.82	10.21
10^{20}	1.10	7.80	26.34	2.26

the IGB band in $CuGaS_2$:Cr films allows the absorption of two sub-band gap photons and promotes electrons from the VB to the CB via the intermediate IGB. As a result, the absorption coefficient of the IGB absorber extends to a longer wavelength region.

Using the experimental absorption coefficient obtained for $CuGaS_2$:Cr films with 5% of Ga atoms being substituted by Cr, we performed numerical simulations to assess the behaviour of a solar cell based on $CuGaS_2$:Cr absorbers for various amounts of Cr. The absorption due to the IGB dramatically increases the short circuit current of the solar cell, and the photo conversion efficiency also grows from 14.7% for the $CuGaS_2$ absorber layer without Cr to 34% for the $CuGaS_2$:Cr absorber layer with 20% Cr content. However, as the amount of neutral defects related to Cr increases, the efficiency of devices diminishes, showing that the PCE for IGB-absorbers is very sensitive to the presence of neutral defects.

Acknowledgments

This work was supported by Ministerio de Economía y Competitividad (ENE2016-77798-C4-2-R) and Generalitat Valenciana (Prometeus 2014/044).

References

[1] M. Mezher, R. Garris, L.M. Mansfield, K. Horsley, L. Weinhardt, D.A. Duncan, C. Heske, Electronic structure of the Zn (O, O, S)/Cu (In, Ga) Se_2 thin-film solar cell interface, Prog. Photovolt.: Res. Appl. 24 (2016) 1142–1148.
[2] A. Carrete, M. Placidi, A. Shavel, A.P. Rodríguez, A. Cabot, Spray-deposited CuIn1 − xGaxSe2 solar cell absorbers: influence of spray deposition parameters and crystallization promoters, Phys. Status Solidi (a) 212 (1) (2015) 67–71.
[3] V.S. Saji, I.H. Choi, C.W. Lee, Progress in electrodeposited absorber layer for CuIn (1 − x)GaxSe2 (CIGS) solar cells, Sol. Energy 85 (11) (2011) 2666–2678.
[4] S. Aksu, S. Pethe, A.K. Shwarsctein, S. Kundu, M. Pinarbasi, Advances in Electroplating-Based CIGS Solar Cell Fabrication. In: Proceedings of the 38th IEEE Photovotaics Specialists Conference, 2012, pp. 3092–3097.
[5] V.S. Saji, S.M. Lee, C.W. Lee, CIGS thin film solar cells by electrodeposition, J.

Korean Electrochem. Soc. 14 (2) (2011) 61–70.
[6] W. Wang, J. Yang, X. Zhu, J. Phillips, Intermediate-band solar cells based on dilute alloys and quantum dots, Front. Optoelectron. China 4 (1) (2011) 2–11.
[7] W. Shockley, H.J. Queisser, Detailed balance limit of efficiency of p-n junction solar cells, J. Appl. Phys. 32 (3) (1961) 510–519.
[8] A. Luque, A. Martí, increasing the efficiency of ideal solar cells by photon induced transitions at intermediate levels, Phys. Rev. Lett. 78 (26) (1997) 5014–5017.
[9] P. Palacios, K. Sánchez, J.C. Conesa, P. Wahnón, First principles calculation of isolated intermediate bands formation in a transition metal-doped chalcopyrite-type semiconductor, Phys. Status Solidi (a) 203 (6) (2006) 1395–1401.
[10] C. Tablero, D.F. Marron, Analysis of the electronic structure of modified CuGaS2 with selected substitutional impurities: prospects for intermediate-band thin-film solar cells based on Cu-containing chalcopyrites, J. Phys. Chem. C 114 (2010) 2756–2763.
[11] P. Palacios, K. Sánchez, J.C. Conesa, J.J. Fernández, P. Wahnón, Theoretical modelling of intermediate band solar cell materials based on metal-doped chalcopyrite compounds, Thin Solid Films 515 (15) (2007) 6280–6284.
[12] I. Aguilera, P. Palacios, P. Wahnón, Enhancement of optical absorption in Ga-chalcopyrite-based intermediate-band materials for high efficiency solar cells, Sol. Energy Mater. Sol. Cells 94 (11) (2010) 1903–1906.
[13] M. Burgelman, J. Verschraegen, S. Degrave, P. Nollet, Modeling thin-film PV devices, Prog. Photovolt.: Res. Appl. 12 (2-3) (2004) 143–153.
[14] H. Ullah, B. Marí, Numerical analysis of SnS based polycrystalline solar cells, Superlattices Microstruct. 72 (2014) 148–155.
[15] D. Kim, Y. Kwon, D. Lee, S. Yoon, S. Lee, B. Yoo, The effect of sulfurization temperature on CuIn (Se, S)2 solar cells synthesized by electrodeposition, J. Electrochem. Soc. 162 (1) (2015) D36–D41.
[16] W.W. Hou, B. Bob, S.H. Li, Y. Yang, Low-temperature processing of a solution-deposited CuInSSe thin-film solar cell, Thin Solid Films 517 (24) (2009) 6853–6856.
[17] J. Lee, W. Lee, N.K. Shrestha, D.Y. Lee, I. Lim, S.H. Kang, S.H. Han, Influence of encapsulated electron active molecules of single walled-carbon nanotubes on superstrate-type Cu (In, Ga) Se2 solar cells, Mater. Chem. Phys. 144 (1) (2014) 49–54.
[18] J. Yang, D. Lee, K. Huh, S. Jung, J. Lee, H. Lee, G. Kim, Influence of surface properties on the performance of Cu(In, Ga)(Se, S)2 thin-film solar cells using Kelvin probe force microscopy, RSC Adv. 5 (51) (2015) 40719–40725.
[19] S. Ullah, M. Mollar, B. Marí, Electrodeposition of CuGaSe2 and CuGaS2 for photovoltaic applications, J. Solid State Electrochem. 20 (8) (2016) 2251–2257.
[20] P. Palacios, I. Aguilera, P. Wahnón, J.C. Conesa, Thermodynamics of the formation of Ti-and Cr-doped CuGaS2 intermediate-band photovoltaic materials, J. Phys. Chem. C 112 (25) (2008) 9525–9529.
[21] H. Ullah, S. Ullah, B. Marí Soucase, Baseline of numerical simulations for ZnTe based thin-film solar cells. International Conference on Energy Systems and Policies (ICESP), 2014, pp. 1–6.

Research Article

iMedPub Journals
www.imedpub.com

Insights in Analytical Electrochemistry
ISSN 2470-9867

2018
Vol.4 No.1:8

DOI: 10.21767/2470-9867.100028

Single Step Electrodeposited Kesterite Cu_2ZnSnS_4 (CZTS) Thin Films at Low Annealing Temperatures

Bernabe Mari[1*], Miguel Mollar[1], Amany El Nahrawy[2], Suzan Saber[1,2,3], Nagwa Khattab[2], Ali Eid[2], Mohamed Abo-Aly[3] and Feriel Bouhjar[1,4,5]

[1]Design and Manufacturing Institute, Polytechnic University of Valencia, Camino de Vera s/n 46022 Valencia, Spain

[2]National Research Center, 33 El Bohouth St. (former El Tahrir St.), Dokki, Giza, Cairo, Egypt

[3]Chemistry Department, Faculty of Science, Ain Shams University, Cairo, Egypt

[4]Photovoltaic Laboratory, Research and Technology Centre of Energy, Borj-Cedria Science and Technology, Tunisia

[5]Universite de Tunis EL Manar, Campus Universitaire Farhat Hached, Rommana, Tunis, Tunisia

[*]**Corresponding author:** Bernabe Mari, Design and Manufacturing Institute, Polytechnic University of Valencia, Camino de Vera s/n 46022 Valencia, Spain, Tel: 585-395-5586; E-mail: bmari@fis.upv.es

Rec date: February 20, 2018; **Acc date:** March 05, 2018; **Pub date:** March 13, 2018

Citation: Mari B, Mollar M, Nahrawy AE, Saber S, Khattab N, et al. (2018) Single Step Electrodeposited Kesterite Cu_2ZnSnS_4 (CZTS) Thin Films at Low Annealing Temperatures. Insights Anal Electrochem Vol.4 No.1:8

Abstract

This paper reports on the growth of quaternary Cu_2ZnSnS_4 (CZTS) thin films by a single step electrochemical deposition followed by annealing at low temperature. The influence of different annealing atmospheres at constant annealing times (t=45 min) and fixed preparation controlling parameters; i.e., starting materials (precursor metal salts) solution concentration, time of deposition and electrodeposition potential. Structural, compositional, morphological and optical properties as well as photoelectrochemical properties were studied. The films sulfurized during 2 hours, showed a prominent kesterite phase with a nearly stoichiometric composition. Samples were characterized by X-ray diffraction (XRD), scanning electron microscopy (SEM), EDS and UV-VIS-NIR spectrometry. X-ray diffraction and confirmed the formation of pure kesterite CZTS films. SEM shows that films are compact with dense morphology and homogeneous distribution. EDS analyzed the elemental constituents of the quaternary Cu_2ZnSnS_4 with an apparent Cu deficiency and S rich for the sulfurized samples. From optical study, the energy gap was indexed for the sulfurized samples. Eg=1.52 eV. Under illumination sulfurized CZTS films exhibits negative photocurrent and positive photovoltage values confirming the p-type character of the films.

Keywords: Cu_2ZnSnS_4; Single step electrodeposition; Thin films; Sulfurization

Introduction

At present, photovoltaic solar cell investigations have rapidly increased due to the higher demand of cleaner energy consumption. In this sense, chalcogenides semiconductors exhibit unique optical, electrical and chemical properties [1-5]. Consequently, in the last years, these compounds have attracted the attention of the scientific community. In particular, the thin film technology has been heavily promoted by the interest in CdTe and CIGS-based solar cells [6-8]. However, these materials contain scarce elements in the earth's crust, such as In, Te and Ga and toxic ones as Cd and Se [9,10]. Cu_2ZnSnS_4 system (CZTS) that crystallizes kesterite structure is one of the most promising absorber materials for solar cells, because of its low band gap around 1.5 eV and its high absorption coefficient (104 cm^{-1}) [11]. In addition, the absence of toxic elements and incorporation of low cost, abundant and environmentally friendly elements as Zn and Sn, instead of In and Ga [12]. Currently, 12.6% of efficiency record has been achieved using hydrazine-based solution. Shockley–Queisser photon balance calculations display 32.2% of theoretical conversion limit for CZTS solar cells [13]. Thus, it is important to highlight that the CZTS efficiency could improve noticeably and becomes closer to CIGS efficiency (20.1%). In the past, several chemical routes for CZTS synthesis have been studied as well as their thin film deposition [14].

There are various preparation methods of CZTS divided into two main parts; (1) physically vacuum deposition techniques like sputtering [15,16], evaporation [17-19] and pulsed laser deposition (PLD) [20]; (2) chemically based non-vacuum deposition techniques such as electrodeposition [21,22], hydrazine-based solution [23] and sol gel-based methods [24]. Electrodeposition technique is with favorable unique advantages that are low-cost, large area plating, convenient

industrial process, so electrodeposition is highly competitive degree than other manufacturing techniques for CZTS synthesis. Three electrode cell processes are characterized by four main deposition techniques depending upon the starting precursor species of ions. (1) stacked elemental layer approach (SEL), (2) metal alloy electrodeposition (MAE), (3) electrophoretic deposition (EPD), and (4) quaternary electrodeposition (QED).

In each case, a post-deposition annealing step in the presence of a molecular conductor source (chalcogenide) to enhance the growth process. Each process possesses their own merits and drawbacks, and all of them have drawn significant attention as comfortable methods for large area CZTS thin film deposition.

Here, we propose a single-step electrochemical deposition method (SED) to deposit quaternary elements of copper, zinc, tin and sulfur onto ITO substrates. The as deposited CZTS films were further thermally treated in different atmospheres argon and sulfur, respectively; at different temperatures in order to enhance the crystallinity of the prepared films. The physical properties, microstructure and morphology of the as deposited and treated ones were studied by X-ray diffraction. The best structure with the smallest crystal size was further studied by scanning electron microscopy and EDS. Optical properties were measured in order to calculate the band gap energy and the absorption coefficient. Photoelectrochemical properties were studied also for the sulfurized samples.

Experimental

Methods

CZTS thin-film precursor is grown by single-step electrodeposition using -1.05 V versus saturated calomel electrode (SCE) at RT for 45 min. The CZTS thin films were electrodeposited potentiostatically on ITO substrates. Substrate cleaning process is performed in an ultrasonic using some organic solvents (soap, ethanol, acetone, 15 min each step) in order to obtain uniform and good adherent deposition. Electrochemical baths were formed of an aqueous solution containing $CuSO_4$ (20 mM), $ZnSO_4$ (10 mM), $SnSO_4$ (20 mM) and $Na_2S_2O_3$ (0.2 M).

Tartaric acid is used to adjust pH of the solution at 5.0 and tri-sodium citrate ($Na_3C_6H_5O_7$) was as complexing agent. The precursor films formed were annealed in Ar atmosphere and in sulfur atmosphere **(Table 1)**.

Table 1 Preparation parameters for Cu2ZnSnS4 as grown, annealed in Ar atmosphere and sulfurized.

Annealing atmospheres	Temperature (°C)	Annealing Time (Min)	Potential (V)	pH	Deposition Time (S)
Cu_2ZnSnS_4 - sulfurized	400	45	-1.05	5.0	2700
Cu_2ZnSnS_4 - Annealed in Ar	450	45	-1.05	5.0	2700
Cu_2ZnSnS_4 -as-grown	-	-	-1.05	5.0	2700

Materials characterization

The crystal structure of CZTS is investigated by XRD (Rigaku Ultima IV diffractometer in the Bragg-Bentano configuration) using the CuK_α radiation (λ=1.54060 Å). The microstructural and elemental analyses were characterized using a Zeiss ULTRA 55 model scanning electron microscope (SEM) equipped with an energy dispersive spectroscopy (EDS) system. To determine the band gap energy was estimated from the optical absorption, which was measured by recording the transmission spectra using a UV-Visible spectrophotometer (Ocean Optics HR4000) coupled to an integrating sphere (in order to collect both specular and diffuse transmittance).

Photo electrochemical and electrochemical analyses

The PEC measurements were performed in a quartz cell to facilitate the light reaching the photo electrodes surface. The light exposed surface of the working electrode is 0.25 cm^2. The electrolyte used in all PEC measurements is 0.1 M Na_2SO_4. A potentiostat/galvanostat Autolab PGSTAT 302 N (Metrohm, Netherlands) with a Pt rod counter-electrode and an Ag/AgCl saturated in 3 M KCl reference electrode was used. The chronoamperometry curves of the films were also obtained in dark and under illumination with an intensity of about 1 SUN (100 mW cm^{-2}) at the film surface.

Results and Discussion

Structural properties

The X-ray diffraction (XRD) patterns of Cu_2ZnSnS_4 quaternary alloy nanostructures as deposited, annealed in Ar and in sulfur atmosphere are shown in **Figure 1**. There are five peaks attributed to the diffractions of the (112), (101), (110), (105), and (312) planes, at 2θ=28.35°, 44.05°, 46.68°, 47.31°, 55.54° and 28.27°, 44.05°, 47.32°, 47.42°, 55.96°, respectively for Cu_2ZnSnS_4 annealed in sulfur and in Ar atmospheres. The Cu_2ZnSnS_4 (CZTS) nanostructures were found to consist of the tetragonal structure kesterite phase, with the (112), (105), (220) and (312) diffraction peaks corresponding to those of JSPDS card 26-0575.

XRD patterns shown in **Figure 1** with diffraction angle 2θ varied from 10 to 60 degrees. The observed peaks are attributed to both CZTS and ITO. However, the XRD pattern of the as deposited CZTS film shows the ITO characteristic peaks

only. After annealing in Ar atmosphere (without sulfur) the XRD pattern corresponds to the kesterite CZTS phase in addition to ITO peaks. Those annealed in sulfur atmosphere indicates a good crystallized kesterite phase and disappear of ITO peaks referring to successful growth of CZTS kesterite phase.

There is no peak for secondary phases in contrast to some reports states that copper sulfide, tin sulfide, and copper tin sulfide compounds exist as intermediates during sulfurization. Those secondary phase sulfides always form mixtures with CZTS at low sulfurization temperatures whereas they did not appear in the prepared CZTS films. This result is due to the selective process of precursor starting materials, sensitivity control of solution pHs and complexing agent concentration dependence. Careful equilibrium between temperature and annealing atmosphere thus in absence of sulfur we have increased the temperature of annealing to 450°C. In the same time, we have decreased annealing temperature in presence of sulfur to 400°C. Both annealing process were done for 45 min which is also in decrease with comparison to other stated work where the annealing temperature is set for 1 h or more.

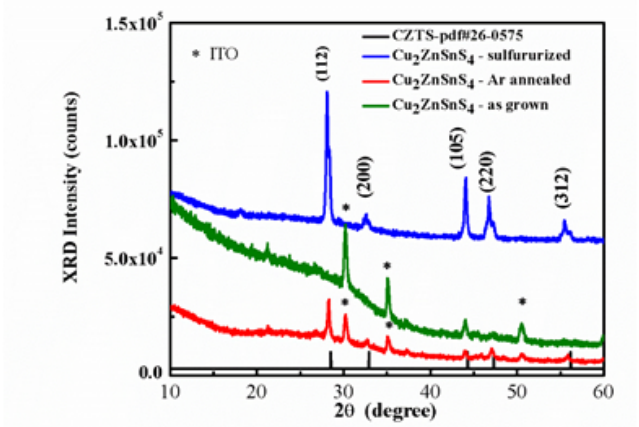

Figure 1 XRD patterns of the CZTS films as deposited, annealed at 450°C, 400°C in Ar and sulfur atmosphere, respectively for 45 min.

As the annealing process were done in different atmospheres as a function of time stability, lead to an optimized resultant CZTS kesterite phase. Crystallite size was calculated according to Scherer's formula:

$D=k\lambda/\beta\cos\theta$

where β is the Full Width at Half Maximum (FWHM), λ wavelength of X-rays with value is 1.5418 A, K is Scherer's constant depending on the crystallite shape and is close to 1 (K=0.9 was used) and θ is the Bragg angle at the center of the peak. **Table 2** displays the crystallite sizes for CZTS films annealed in Ar and in sulfur atmospheres, respectively.

Table 2 Crystallite size measurement of Cu_2ZnSnS_4 annealed in Ar atmosphere and sulfurized films.

Sample	Crystallite size (nm)
Cu_2ZnSnS_4 - Annealed in Ar	27.8
Cu_2ZnSnS_4 - sulfurized	17.3

It is worth to notice that the crystallite size of kesterite phase Cu_2ZnSnS_4 sulfurized ones has larger crystallite size than those annealed in Argon atmosphere. The annealing process in Argon atmosphere were held at 450°C which lead to complete kesterite phase formation with all kesterite indexed peaks in addition to those of ITO used substrate. In the mean while those grown in sulfur atmosphere shown sharp indexed peaks for kesterite phase only and no substrate ITO representative peaks.

Optical properties

Figure 2 shows the transmittance and absorbance spectra for the CZTS thin films as-grown and sulfurized, respectively. As can be seen the transmittance for the sulfurized sample is higher in all the studied wavelength range, meaning that the reflectance of the surface has decreased after the sulfurization process.

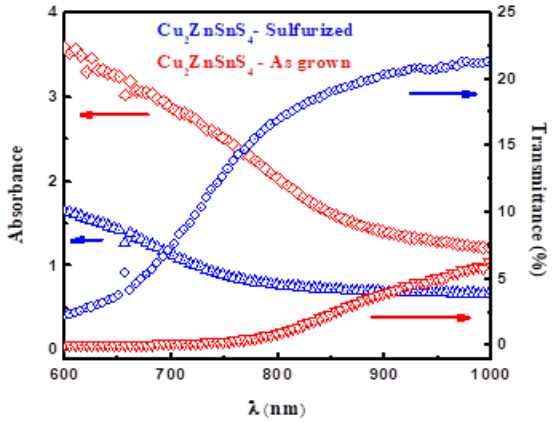

Figure 2 Absorbance and transmittance spectra for kesterite Cu_2ZnSnS_4, As-grown (red) and Sulfurized (blue) thin films.

For a direct-band-gap semiconductor, the optical band gap energy can be evaluated by the expression $(\alpha h)^2=A(h-Eg)$, where Eg is the optical band gap energy, A is an energy independent constant, h is the Planck constant, υ is frequency, and n is an index that characterizes the optical absorption process and is theoretically equal to 1/2 for the direct allowed transitions.

All the CZTS thin film samples exhibited broad absorption in the visible region. The band gaps were obtained by plotting $(\alpha h\upsilon)^2$ versus the photon energy in eV. Extrapolation of the straight line to zero absorption coefficient (α=0) allows estimation of Eg.

Figure 3 shows the Tauc plot of Cu_2ZnSnS_4 kesterite thin films before annealing the (as grown) and sulfurized samples in

sulfur atmosphere. The band gaps of the as grown films were 1.83 eV and 1.52 eV for the sulfurized ones which is close to the reviewed CTZS band gap values.

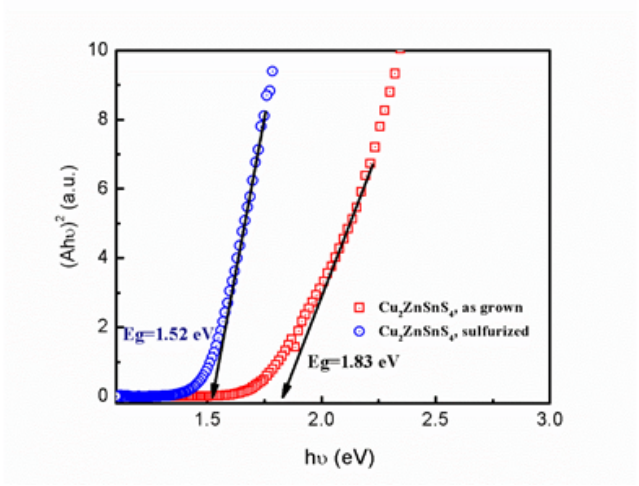

Figure 3 Tauc plot of $(Ahv)^2$ versus (hv) for kesterite Cu_2ZnSnS_4, As-grown and Sulfurized thin films.

Scanning electron microscopy

Figure 4 shows Scanning Electron Microscopy (SEM) images of the sulfurized CZTS films at different magnifications. Scanning Electron Microscopy is one of the predominant techniques to survey the surface of the samples. The SEM analysis reveals that the grown films revealing good crystallinity in agreement with XRD data. Uniform, homogenous, well-covered and good adherence agglomeration of grains with the films. No secondary phases have been detected in contrast to annealing in sulfur atmosphere at low temperatures like, ZnS, SnS, CuSnS and CuS.

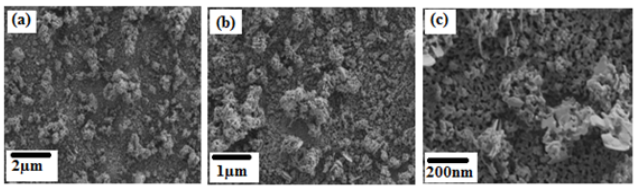

Figure 4 SEM images for kesterite thin films Cu_2ZnSnS_4-sulfurized at different magnifications.

The growth temperature determines growth of CZTS films presence of sulfur enhance the crystallinity of the films. The films deposited at 400°C in sulfur atmosphere show homogeneity with smooth islands or small grains owing to combination of CZTS formed in Ar atmosphere and sulfur. The smooth region is related to the stoichiometry of the pure kesterite CZTS formed phase with (Cu:Zn:Sn:S=2:1:1:4) ratio of constituent films which is highly required to develop efficient thin film solar cells. The SEM images of the sulfurized CZTS films grown with optimum growth conditions show very uniform grain sizes.

EDS analysis

The composition of the as-deposited sample was evaluated by a quantitative EDS analysis. **Figure 5** shows a typical EDS spectrum revealing peaks of Cu, Zn, Sn and S, due to the deposited CZTS thin film. It is also obviously noticed that no presence of any additionally peaks arising from substrate ITO.

The fundamental properties of CZTS have proven to be suitable to serve as an active layer in solar cell devices. In the Cu-based chalcogenides the Cu content is of key importance, that it is strongly affects morphological, structural and electrical properties of the films. Therefore, as a first optimization for experimental conditions to synthesize CZTS, we studied structural and morphological properties of CZTS thin films as well as corresponding solar cell parameters by varying the content of Cu. Controlling the amount of copper lead to varying all other constituent elements, which in turn lead to varying all other elemental ratios: i.e., Zn/Sn, (Cu/(Zn +In) and (S/metal) ratios.

Figure 5 shows a typical EDS spectrum of sulfurized films. Peaks corresponding to the four components Cu, Zn, Sn, and S of CZTS films are evident in ECS spectrum.

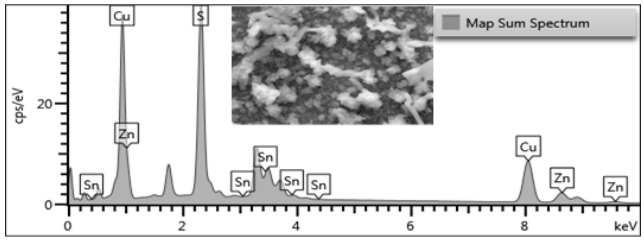

Figure 5 EDS elemental composition analysis for sulfurized Cu_2ZnSnS_4 kesterite thin films.

The composition of the studied samples is presented in the **Table 3** and their relative positions are indicated in the phase diagram **(Figure 5)**. The calculated ratios [Cu]/([Zn]+[Sn])=0.5 and [Zn]/[Sn]=1.4, where the [s]/([metal]) ratio is equal to 1.65; which is clearly the most effected one due to the high ratio of sulfur more than 50%. The apparent composition of the elements is 12.59 at%, 14.79 at%, 10.27 at% and 62.32 at % for Cu, Zn, Sn, and S elements, respectively. In general, it has been observed that sulfurized films are moderately poor in Cu and rich in S. The calculated [Cu]/([Zn]+[Sn])=0.5 and [Zn]/[Sn]=1.4, where the [s]/([metal]) ratio is equal to 1.65; which is clearly the most effected one due to the high ratio of sulfur more than 50%.

Table 3 Compositional analysis of sulfurized Cu_2ZnSnS_4 kesterite thin films.

Elements composition atomic (%)	Elemental composition ratio

	Cu (%)	Zn (%)	Sn (%)	S (%)	Cu/Zn +Sn	Zn/S n	S/ metal
Cu_2ZnSnS_4	12.59	14.79	10.27	62.35	0.5	1.4	1.65

Photo electrochemical measurements of CZTS

Photo electrochemistry has been employed to explore the semiconducting properties of sulfurized Cu_2ZnSnS_4. When semiconductor electrodes are exposed to periodic illumination, the current driven is affected by the creation of electron-hole pairs, which alters the concentration of minority carriers and thereby promotes processes governed by these carriers. During photoexitation both photopotential and photocurrent can be observed, even at open circuit potential. The photo excited electrons and holes are separated in the space charge layer, and are driven by the electric field in opposite directions. This migration induces an inverse potential in the electrode (photopotential), reducing the potential difference across the space charge layer and retarding the migration of the carriers. In the case of p-type semiconductors, the Fermi level of the semiconductor decreases (the electrode potential increases) when the band edge level bends downward in the space charge layer. Moreover a negative photocurrent is registered when photogenerated electrons move across the space charge region towards the electrode/electrolyte interface and increase the cathodic current [11].

Figure 6 shows the photocurrent registered at open circuit potential and the photopotential developed across the sulfurized CZTS at 400°C. The cathodic nature of the photocurrent and the positive value of the photopotential confirm the p-type character of the sulfurized CZTS film.

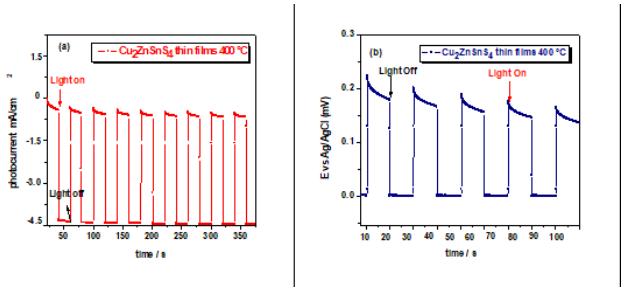

Figure 6 (a) Photocurrent and (b) Photopotential response of sulfurized Cu_2ZnSnS_4 thin films (T=400°C) using chopped light (10 sec on/10 sec off) in 0.1 M Na_2SO_4 solution.

Conclusion

Cu_2ZnSnS_4 thin films with kesterite structure were successfully synthesized using single step electrodeposition process. Annealing process in Argon and sulfur atmosphere were studied as function of time, as the time was fixed where in Argon atmosphere the temperature was held higher than those in sulfur atmosphere.

Characterization techniques have revealed the formation of pure kesterite phase for the prepared Cu_2ZnSnS_4 films in both argon and sulfur atmosphere. XRD structure study showed indexed peaks for Cu_2ZnSnS_4 thin films with kesterite structure with average crystal size about 17 nm.

The morphological study for the sulfurized samples indicates that both films are polycrystalline with a uniform homogenous surface morphology suitable for solar cell applications. The elemental EDS analysis promotes that the prepared sulfurized films with Cu poor, Zn and S rich Cu_2ZnSnS_4 sulfurized kesterite films. For the photoelectrochemical performance of the Cu_2ZnSnS_4 the photocurrent registered at open circuit potential and the photopotential developed across the sulfurized CZTS at 400°C improve the cathodic nature of the photocurrent and the positive value of the photopotential confirms the p-type character of the film.

Acknowledgements

This work was supported by the Culture, Affairs and Missions Sector, Ministry of Higher Education and Scientific Research (Egypt) and Ministerio de Economia y Competitividad (Spain) (ENE2016-77798-C4-2-R) and Generalitat valenciana (Prometeus 2014/044).

References

1. Repins I, Beall C, Vora V, DeHart C, Kuciauskas D, et al. (2012) Co-evaporated $Cu_2ZnSnSe_4$ films and devices. Sol Energy Mater Sol Cells 101: 154-159.
2. Dudchak IV, Piskach LV (2003) Phase equilibria in the Cu_2SnSe_3–$SnSe_2$–ZnSe system. J Alloys Compd 351: 145-150.
3. Chen S, Gong XG, Walsh A, Wei SH (2009) Electronic structure and stability of quaternary chalcogenide semiconductors derived from cation cross-substitution of II-VI and I-III-VI compounds. Phys Rev B 79: 165211.
4. Persson C (2010) Electronic and optical properties of Cu_2ZnSnS_4 and $Cu_2ZnSnSe_4$. J Appl Phys 107: 053710.
5. Shin B, Gunawan O, Zhu Y, Bojarczuk NA, Chey SJ, et al. (2013) Thin film solar cell with 8.4% power conversion efficiency using an earth-abundant Cu_2ZnSnS_4 absorber. Prog Photovoltaics 21: 72-76.
6. Siebentritt S (2013) Why are kesterite solar cells not 20% efficient? Thin Solid Films 535: 1-4.
7. Watjen JT, Engman J, Edoff M, Bjorkman CP (2012) Direct evidence of current blocking by ZnSe in $Cu_2ZnSnSe_4$ solar cells. Appl Phys Lett 100: 173510.
8. Scragg JJ, Wätjen JT, Edoff M, Ericson T, Kubart T, et al. (2012) A Detrimental Reaction at the Molybdenum Back Contact in Cu_2ZnSn (S, Se_4) Thin-Film Solar Cells. J Am Chem Soc 134: 19330-19333.
9. Ahn S, Jung S, Gwak J, Cho A, Shin K, et al. (2010) Determination of band gap energy (Eg) of $Cu_2ZnSnSe_4$ thin films: On the discrepancies of reported band gap values. Appl Phys Lett 97: 021905.
10. Redinger A, Hoenes K, Fontane X, Roca VI, Saucedo E, et al. (2011) Detection of a ZnSe secondary phase in coevaporated Cu_2 $ZnSnSe_4$ thin films. Appl Phys Lett 98: 101907.

11. Scragg JJ, Berg DM, Dale PJ (2010) A 3.2% efficient Kesterite device from electrodeposited stacked elemental layers. J Electroanal Chem 646: 52-59.

12. Lee SG, Kim J, Woo HS, Jo Y, Inamdar AI, et al. (2014) Structural, morphological, compositional, and optical properties of single step electrodeposited Cu_2ZnSnS_4 (CZTS) thin films for solar cell application. Curr Appl Phys 14: 254-258.

13. Gunaicha PP, Gangam S, Roehl JL, Khare SV (2014) Structural, energetic and elastic properties of Cu_2ZnSn (SxSe1-x) 4 (x=1, 0.75, 0.5, 0.25, 0) alloys from first-principles computations. Sol Energy 102: 276-281.

14. Seol JS, Lee SY, Lee JC, Nam HD, Kim KH (2003) Sol Energy Mater Sol Cells 75: 155.

15. Katagiri H, Jimbo K, Maw WS, Oishi K, Yamazaki M, et al. (2009) Thin Solid Films 517: 2455-2460.

16. Fernandes PA, Salome PMP, Cunha AFDA (2011) Cu_2ZnSnS_4 solar cells prepared with sulphurized dc-sputtered stacked metallic precursors. Thin Solid Films 519: 7382-7385.

17. Vora N, Blackburn J, Repins I, Beall C, To B, et al. (2012) Phase identification and control of thin films deposited by co-evaporation of elemental Cu, Zn, Sn, and Se. J Vac Sci Technol 30: 051201.

18. Shin B, Gunawan O, Zhu Y, Bojarczuk NA, Chey SJ, et al. (2013) Thin film solar cell with 8.4% power conversion efficiency using an earth-abundant Cu_2ZnSnS_4 absorber. Prog Photovoltaics Res Appl 21: 72.

19. Repins I, Beall C, Vora N, Dehart C, Kuciauskas D, et al. (2012) Sol Energy Mater Sol Cells 101: 154.

20. Knutson TR, Hanson PJ, Aydil ES, Penn RL (2014) Synthesis of Cu_2ZnSnS_4 thin films directly on to conductive substrates via selective thermolysis using microwave energy. Chem Commun 50: 5902.

21. Scragg JJ, Berg DM, Dale PJ (2010) A 3.2% efficient Kesterite device from electrodeposited stacked elemental layers. J Electroanal Chem 646: 1-2.

22. Schurr R, Hölzing A, Jost S, Schock HW (2009) The crystallisation of Cu_2ZnSnS_4 thin film solar cell absorbers from co-electroplated Cu-Zn-Sn precursors. Thin Solid Films 517: 2465-2468.

23. Todorov TK, Reuter KB, Mitzi DB (2010) High-efficiency solar cell with Earth-abundant liquid-processed absorber. Adv Mater 22: E156-159.

24. Fahrettin Y (2011) Nanostructure Cu_2ZnSnS_4 Thin Film Prepared By Sol-gel For Optoelectronic Applications. Solar Energy 85: 2518–2523.